

EUROPEAN ORGANIZATION FOR NUCLEAR RESEARCH

CERN-EP/2003-007

21 July 2003

# Searches for supersymmetric particles in $e^+e^-$ collisions up to 208 GeV and interpretation of the results within the MSSM

DELPHI Collaboration

## Abstract

DELPHI data collected at centre-of-mass energies up to 208 GeV have been analysed to search for charginos, neutralinos and sfermions in the framework of the Minimal Supersymmetric Standard Model (MSSM) with R-parity conservation. No evidence for a signal was found in any of the channels. The results of each search were used to derive limits on production cross-sections and particle masses. In addition, the combined result of all searches excludes regions in the parameter space of the constrained MSSM, leading to limits on the mass of the Lightest Supersymmetric Particle and other supersymmetric particles.

Accepted by Eur. Phys. J. C

J.Abdallah<sup>25</sup>, P.Abreu<sup>22</sup>, W.Adam<sup>51</sup>, P.Adzic<sup>11</sup>, T.Albrecht<sup>17</sup>, T.Alderweireld<sup>2</sup>, R.Alemany-Fernandez<sup>8</sup>, T.Allmendinger<sup>17</sup>, P.P.Allport<sup>23</sup>, U.Amaldi<sup>29</sup>, N.Amapane<sup>45</sup>, S.Amato<sup>48</sup>, E.Anashkin<sup>36</sup>, A.Andreazza<sup>28</sup>, S.Andringa<sup>22</sup>, N.Anjos<sup>22</sup>, P.Antilogus<sup>25</sup>, W-D.Apel<sup>17</sup>, Y.Arnooud<sup>14</sup>, S.Ask<sup>26</sup>, B.Asman<sup>44</sup>, J.E.Augustin<sup>25</sup>, A.Augustinus<sup>8</sup>, P.Baillon<sup>8</sup>, A.Ballestrero<sup>46</sup>, P.Bambade<sup>20</sup>, R.Barbier<sup>27</sup>, D.Bardin<sup>16</sup>, G.Barker<sup>17</sup>, A.Baroncelli<sup>39</sup>, M.Battaglia<sup>8</sup>, M.Baubillier<sup>25</sup>, K-H.Becks<sup>53</sup>, M.Begalli<sup>6</sup>, A.Behrmann<sup>53</sup>, E.Ben-Haim<sup>20</sup>, N.Benekos<sup>32</sup>, A.Benvenuti<sup>5</sup>, C.Berat<sup>14</sup>, M.Berggren<sup>25</sup>, L.Berntzon<sup>44</sup>, D.Bertrand<sup>2</sup>, M.Besanccon<sup>40</sup>, N.Besson<sup>40</sup>, D.Bloch<sup>9</sup>, M.Bлом<sup>31</sup>, M.Bluj<sup>52</sup>, M.Bonesini<sup>29</sup>, M.Boonekamp<sup>40</sup>, P.S.L.Booth<sup>23</sup>, G.Borisov<sup>21</sup>, O.Botner<sup>49</sup>, B.Bouquet<sup>20</sup>, T.J.V.Bowcock<sup>23</sup>, I.Boyko<sup>16</sup>, M.Bracko<sup>43</sup>, R.Brenner<sup>49</sup>, E.Brodet<sup>35</sup>, P.Bruckman<sup>18</sup>, J.M.Brunet<sup>7</sup>, L.Bugge<sup>33</sup>, P.Buschmann<sup>53</sup>, M.Calvi<sup>29</sup>, T.Camporesi<sup>8</sup>, V.Canale<sup>38</sup>, F.Carena<sup>8</sup>, N.Castro<sup>22</sup>, F.Cavallo<sup>5</sup>, M.Chapkin<sup>42</sup>, Ph.Charpentier<sup>8</sup>, P.Checchia<sup>36</sup>, R.Cherici<sup>8</sup>, P.Chliapnikov<sup>42</sup>, J.Chudoba<sup>8</sup>, S.U.Chung<sup>8</sup>, K.Cieslik<sup>18</sup>, P.Collins<sup>8</sup>, R.Contri<sup>13</sup>, G.Cosme<sup>20</sup>, F.Cossutti<sup>47</sup>, M.J.Costa<sup>50</sup>, B.Crawley<sup>1</sup>, D.Crennell<sup>37</sup>, J.Cuevas<sup>34</sup>, J.D'Hondt<sup>2</sup>, J.Dalmau<sup>44</sup>, T.da Silva<sup>48</sup>, W.Da Silva<sup>25</sup>, G.Della Ricca<sup>47</sup>, A.De Angelis<sup>47</sup>, W.De Boer<sup>17</sup>, C.De Clercq<sup>2</sup>, B.De Lotto<sup>47</sup>, N.De Maria<sup>45</sup>, A.De Min<sup>36</sup>, L.de Paula<sup>48</sup>, L.Di Ciaccio<sup>38</sup>, A.Di Simone<sup>39</sup>, K.Doroba<sup>52</sup>, J.Drees<sup>53,8</sup>, M.Dris<sup>32</sup>, G.Eigen<sup>4</sup>, T.Ekelof<sup>49</sup>, M.Ellert<sup>49</sup>, M.Elsing<sup>8</sup>, M.C.Espirito Santo<sup>22</sup>, G.Fanourakis<sup>11</sup>, D.Fassouliotis<sup>11,3</sup>, M.Feindt<sup>17</sup>, J.Fernandez<sup>41</sup>, A.Ferrer<sup>50</sup>, F.Ferro<sup>13</sup>, U.Flagmeyer<sup>53</sup>, H.Foeth<sup>8</sup>, E.Fokitis<sup>32</sup>, F.Fulda-Quenzer<sup>20</sup>, J.Fuster<sup>50</sup>, M.Gandelman<sup>48</sup>, C.Garcia<sup>50</sup>, Ph.Gavillet<sup>8</sup>, E.Gazis<sup>32</sup>, R.Gokiel<sup>8,52</sup>, B.Golob<sup>43</sup>, G.Gomez-Ceballos<sup>41</sup>, P.Goncalves<sup>22</sup>, E.Graziani<sup>39</sup>, G.Grosdidier<sup>20</sup>, K.Grzelak<sup>52</sup>, J.Guy<sup>37</sup>, C.Haag<sup>17</sup>, A.Hallgren<sup>49</sup>, K.Hamacher<sup>53</sup>, K.Hamilton<sup>35</sup>, S.Haug<sup>33</sup>, F.Hauler<sup>17</sup>, V.Hedberg<sup>26</sup>, M.Hennecke<sup>17</sup>, H.Herr<sup>8</sup>, J.Hoffman<sup>52</sup>, S-O.Holmgren<sup>44</sup>, P.J.Holt<sup>8</sup>, M.A.Houlden<sup>23</sup>, K.Hultqvist<sup>44</sup>, J.N.Jackson<sup>23</sup>, G.Jarlskog<sup>26</sup>, P.Jarry<sup>40</sup>, D.Jeans<sup>35</sup>, E.K.Johansson<sup>44</sup>, P.D.Johansson<sup>44</sup>, P.Jonsson<sup>27</sup>, C.Joram<sup>8</sup>, L.Jungermann<sup>17</sup>, F.Kapusta<sup>25</sup>, S.Katsanevas<sup>27</sup>, E.Katsoufis<sup>32</sup>, G.Kernel<sup>43</sup>, B.P.Kersevan<sup>8,43</sup>, U.Kerzel<sup>17</sup>, A.Kiiskinen<sup>15</sup>, B.T.King<sup>23</sup>, N.J.Kjaer<sup>8</sup>, P.Kluit<sup>31</sup>, P.Kokkinias<sup>11</sup>, C.Kourkoumelis<sup>3</sup>, O.Kouznetsov<sup>16</sup>, Z.Krumstein<sup>16</sup>, M.Kucharczyk<sup>18</sup>, J.Lamsa<sup>1</sup>, G.Leder<sup>51</sup>, F.Ledroit<sup>14</sup>, L.Leinonen<sup>44</sup>, R.Leitner<sup>30</sup>, J.Lemonne<sup>2</sup>, V.Lepeltier<sup>20</sup>, T.Lesiak<sup>18</sup>, W.Liebig<sup>53</sup>, D.Liko<sup>51</sup>, A.Lipniacka<sup>44</sup>, J.H.Lopes<sup>48</sup>, J.M.Lopez<sup>34</sup>, D.Loukas<sup>11</sup>, P.Lutz<sup>40</sup>, L.Lyons<sup>35</sup>, J.MacNaughton<sup>51</sup>, A.Malek<sup>53</sup>, S.Maltezos<sup>32</sup>, F.Mandl<sup>51</sup>, J.Marco<sup>41</sup>, R.Marco<sup>41</sup>, B.Marechal<sup>48</sup>, M.Margoni<sup>36</sup>, J-C.Marin<sup>8</sup>, C.Mariotti<sup>8</sup>, A.Markou<sup>11</sup>, C.Martinez-Rivero<sup>41</sup>, J.Masik<sup>12</sup>, N.Mastroyiannopoulos<sup>11</sup>, F.Matorras<sup>41</sup>, C.Matteuzzi<sup>29</sup>, F.Mazzucato<sup>36</sup>, M.Mazzucato<sup>36</sup>, R.Mc Nulty<sup>23</sup>, C.Meroni<sup>28</sup>, W.T.Meyer<sup>1</sup>, E.Migliore<sup>45</sup>, W.Mitaroff<sup>51</sup>, U.Mjoernmark<sup>26</sup>, T.Moa<sup>44</sup>, M.Moch<sup>17</sup>, K.Moenig<sup>8,10</sup>, R.Monge<sup>13</sup>, J.Montenegro<sup>31</sup>, D.Moraes<sup>48</sup>, S.Moreno<sup>22</sup>, P.Morettini<sup>13</sup>, U.Mueller<sup>53</sup>, K.Muenich<sup>53</sup>, M.Mulders<sup>31</sup>, L.Mundim<sup>6</sup>, W.Murray<sup>37</sup>, B.Muryn<sup>19</sup>, G.Myatt<sup>35</sup>, T.Myklebust<sup>33</sup>, M.Nassiakou<sup>11</sup>, F.Navarria<sup>5</sup>, K.Nawrocki<sup>52</sup>, R.Nicolaïou<sup>40</sup>, M.Nikolenko<sup>16,9</sup>, A.Oblakowska-Mucha<sup>19</sup>, V.Obraztsov<sup>42</sup>, A.Olshevski<sup>16</sup>, A.Onofre<sup>22</sup>, R.Orava<sup>15</sup>, K.Osterberg<sup>15</sup>, A.Ouraou<sup>40</sup>, A.Oyanguren<sup>50</sup>, M.Paganoni<sup>29</sup>, S.Paiano<sup>5</sup>, J.P.Palacios<sup>23</sup>, H.Palka<sup>18</sup>, Th.D.Papadopoulos<sup>32</sup>, L.Pape<sup>8</sup>, C.Parkes<sup>24</sup>, F.Parodi<sup>13</sup>, U.Parzefall<sup>8</sup>, A.Passeri<sup>39</sup>, O.Passon<sup>53</sup>, L.Peralta<sup>22</sup>, V.Perepelitsa<sup>50</sup>, A.Perrotta<sup>5</sup>, A.Petrolini<sup>13</sup>, J.Piedra<sup>41</sup>, L.Pieri<sup>39</sup>, F.Pierre<sup>40</sup>, M.Pimenta<sup>22</sup>, E.Piotti<sup>8</sup>, T.Podobnik<sup>43</sup>, V.Poireau<sup>8</sup>, M.E.Pol<sup>6</sup>, G.Polok<sup>18</sup>, P.Poropat<sup>47</sup>, V.Pozdniakov<sup>16</sup>, N.Pukhaeva<sup>2,16</sup>, A.Pullia<sup>29</sup>, J.Rames<sup>12</sup>, L.Ramler<sup>17</sup>, A.Read<sup>33</sup>, P.Rebecchi<sup>8</sup>, J.Rehn<sup>17</sup>, D.Reid<sup>31</sup>, R.Reinhardt<sup>53</sup>, P.Renton<sup>35</sup>, F.Richard<sup>20</sup>, J.Ridky<sup>12</sup>, M.Rivero<sup>41</sup>, D.Rodriguez<sup>41</sup>, A.Romero<sup>45</sup>, P.Ronchese<sup>36</sup>, E.Rosenberg<sup>1</sup>, P.Roudeau<sup>20</sup>, T.Rovelli<sup>5</sup>, V.Ruhmann-Kleider<sup>40</sup>, D.Ryabtchikov<sup>42</sup>, A.Sadovsky<sup>16</sup>, L.Salmi<sup>15</sup>, J.Salt<sup>50</sup>, A.Savoy-Navarro<sup>25</sup>, U.Schickerath<sup>8</sup>, A.Segar<sup>35</sup>, R.Sekulin<sup>37</sup>, M.Siebel<sup>53</sup>, A.Sisakian<sup>16</sup>, G.Smadja<sup>27</sup>, O.Smirnova<sup>26</sup>, A.Sokolov<sup>42</sup>, A.Sopczak<sup>21</sup>, R.Sosnowski<sup>52</sup>, T.Spassov<sup>8</sup>, M.Stanitzki<sup>17</sup>, A.Stocchi<sup>20</sup>, J.Strauss<sup>51</sup>, B.Stugu<sup>4</sup>, M.Szczechowski<sup>52</sup>, M.Szeptycka<sup>52</sup>, T.Szumlak<sup>19</sup>, T.Tabarelli<sup>29</sup>, A.C.Taffard<sup>23</sup>, F.Tegenfeldt<sup>49</sup>, J.Timmermans<sup>31</sup>, L.Tkatchev<sup>16</sup>, M.Tobin<sup>23</sup>, S.Todorovova<sup>12</sup>, B.Tome<sup>22</sup>, A.Tonazzo<sup>29</sup>, P.Tortosa<sup>50</sup>, P.Travnicek<sup>12</sup>, D.Treille<sup>8</sup>, G.Tristram<sup>7</sup>, M.Trochimczuk<sup>52</sup>, C.Troncon<sup>28</sup>, M-L.Turluer<sup>40</sup>, I.A.Tyapkin<sup>16</sup>, P.Tyapkin<sup>16</sup>, S.Tzamarias<sup>11</sup>, V.Uvarov<sup>42</sup>, G.Valenti<sup>5</sup>, P.Van Dam<sup>31</sup>, J.Van Eldik<sup>8</sup>, A.Van Lysebetten<sup>2</sup>, N.van Remortel<sup>2</sup>, I.Van Vulpen<sup>8</sup>, G.Vegni<sup>28</sup>, F.Veloso<sup>22</sup>, W.Venus<sup>37</sup>, P.Verdier<sup>27</sup>, V.Verzi<sup>38</sup>, D.Vilanova<sup>40</sup>, L.Vitale<sup>47</sup>, V.Vrba<sup>12</sup>, H.Wahlen<sup>53</sup>, A.J.Washbrook<sup>23</sup>, C.Weiser<sup>17</sup>, D.Wicke<sup>8</sup>,

J.Wickens<sup>2</sup>, G.Wilkinson<sup>35</sup>, M.Winter<sup>9</sup>, M.Witek<sup>18</sup>, O.Yushchenko<sup>42</sup>, A.Zalewska<sup>18</sup>, P.Zalewski<sup>52</sup>, D.Zavrtanik<sup>43</sup>, V.Zhuravlov<sup>16</sup>, N.I.Zimin<sup>16</sup>, A.Zintchenko<sup>16</sup>, M.Zupan<sup>11</sup>

<sup>1</sup>Department of Physics and Astronomy, Iowa State University, Ames IA 50011-3160, USA

<sup>2</sup>Physics Department, Universiteit Antwerpen, Universiteitsplein 1, B-2610 Antwerpen, Belgium and IIHE, ULB-VUB, Pleinlaan 2, B-1050 Brussels, Belgium

and Faculté des Sciences, Univ. de l'Etat Mons, Av. Maistriau 19, B-7000 Mons, Belgium

<sup>3</sup>Physics Laboratory, University of Athens, Solonos Str. 104, GR-10680 Athens, Greece

<sup>4</sup>Department of Physics, University of Bergen, Allégaten 55, NO-5007 Bergen, Norway

<sup>5</sup>Dipartimento di Fisica, Università di Bologna and INFN, Via Irnerio 46, IT-40126 Bologna, Italy

<sup>6</sup>Centro Brasileiro de Pesquisas Físicas, rua Xavier Sigaud 150, BR-22290 Rio de Janeiro, Brazil

and Depto. de Física, Pont. Univ. Católica, C.P. 38071 BR-22453 Rio de Janeiro, Brazil

and Inst. de Física, Univ. Estadual do Rio de Janeiro, rua São Francisco Xavier 524, Rio de Janeiro, Brazil

<sup>7</sup>Collège de France, Lab. de Physique Corpusculaire, IN2P3-CNRS, FR-75231 Paris Cedex 05, France

<sup>8</sup>CERN, CH-1211 Geneva 23, Switzerland

<sup>9</sup>Institut de Recherches Subatomiques, IN2P3 - CNRS/ULP - BP20, FR-67037 Strasbourg Cedex, France

<sup>10</sup>Now at DESY-Zeuthen, Platanenallee 6, D-15735 Zeuthen, Germany

<sup>11</sup>Institute of Nuclear Physics, N.C.S.R. Demokritos, P.O. Box 60228, GR-15310 Athens, Greece

<sup>12</sup>FZU, Inst. of Phys. of the C.A.S. High Energy Physics Division, Na Slovance 2, CZ-180 40, Praha 8, Czech Republic

<sup>13</sup>Dipartimento di Fisica, Università di Genova and INFN, Via Dodecaneso 33, IT-16146 Genova, Italy

<sup>14</sup>Institut des Sciences Nucléaires, IN2P3-CNRS, Université de Grenoble 1, FR-38026 Grenoble Cedex, France

<sup>15</sup>Helsinki Institute of Physics, P.O. Box 64, FIN-00014 University of Helsinki, Finland

<sup>16</sup>Joint Institute for Nuclear Research, Dubna, Head Post Office, P.O. Box 79, RU-101 000 Moscow, Russian Federation

<sup>17</sup>Institut für Experimentelle Kernphysik, Universität Karlsruhe, Postfach 6980, DE-76128 Karlsruhe, Germany

<sup>18</sup>Institute of Nuclear Physics, Ul. Kawiory 26a, PL-30055 Krakow, Poland

<sup>19</sup>Faculty of Physics and Nuclear Techniques, University of Mining and Metallurgy, PL-30055 Krakow, Poland

<sup>20</sup>Université de Paris-Sud, Lab. de l'Accélérateur Linéaire, IN2P3-CNRS, Bât. 200, FR-91405 Orsay Cedex, France

<sup>21</sup>School of Physics and Chemistry, University of Lancaster, Lancaster LA1 4YB, UK

<sup>22</sup>LIP, IST, FCUL - Av. Elias Garcia, 14-1º, PT-1000 Lisboa Codex, Portugal

<sup>23</sup>Department of Physics, University of Liverpool, P.O. Box 147, Liverpool L69 3BX, UK

<sup>24</sup>Dept. of Physics and Astronomy, Kelvin Building, University of Glasgow, Glasgow G12 8QQ

<sup>25</sup>LPNHE, IN2P3-CNRS, Univ. Paris VI et VII, Tour 33 (RdC), 4 place Jussieu, FR-75252 Paris Cedex 05, France

<sup>26</sup>Department of Physics, University of Lund, Sölvegatan 14, SE-223 63 Lund, Sweden

<sup>27</sup>Université Claude Bernard de Lyon, IPNL, IN2P3-CNRS, FR-69622 Villeurbanne Cedex, France

<sup>28</sup>Dipartimento di Fisica, Università di Milano and INFN-MILANO, Via Celoria 16, IT-20133 Milan, Italy

<sup>29</sup>Dipartimento di Fisica, Univ. di Milano-Bicocca and INFN-MILANO, Piazza della Scienza 2, IT-20126 Milan, Italy

<sup>30</sup>IPNP of MFF, Charles Univ., Areal MFF, V Holešovickach 2, CZ-180 00, Praha 8, Czech Republic

<sup>31</sup>NIKHEF, Postbus 41882, NL-1009 DB Amsterdam, The Netherlands

<sup>32</sup>National Technical University, Physics Department, Zografou Campus, GR-15773 Athens, Greece

<sup>33</sup>Physics Department, University of Oslo, Blindern, NO-0316 Oslo, Norway

<sup>34</sup>Dpto. Fisica, Univ. Oviedo, Avda. Calvo Sotelo s/n, ES-33007 Oviedo, Spain

<sup>35</sup>Department of Physics, University of Oxford, Keble Road, Oxford OX1 3RH, UK

<sup>36</sup>Dipartimento di Fisica, Università di Padova and INFN, Via Marzolo 8, IT-35131 Padua, Italy

<sup>37</sup>Rutherford Appleton Laboratory, Chilton, Didcot OX11 0QX, UK

<sup>38</sup>Dipartimento di Fisica, Università di Roma II and INFN, Tor Vergata, IT-00173 Rome, Italy

<sup>39</sup>Dipartimento di Fisica, Università di Roma III and INFN, Via della Vasca Navale 84, IT-00146 Rome, Italy

<sup>40</sup>DAPNIA/Service de Physique des Particules, CEA-Saclay, FR-91191 Gif-sur-Yvette Cedex, France

<sup>41</sup>Instituto de Fisica de Cantabria (CSIC-UC), Avda. los Castros s/n, ES-39006 Santander, Spain

<sup>42</sup>Inst. for High Energy Physics, Serpukov P.O. Box 35, Protvino, (Moscow Region), Russian Federation

<sup>43</sup>J. Stefan Institute, Jamova 39, SI-1000 Ljubljana, Slovenia and Laboratory for Astroparticle Physics,

Nova Gorica Polytechnic, Kostanjevicka 16a, SI-5000 Nova Gorica, Slovenia

and Department of Physics, University of Ljubljana, SI-1000 Ljubljana, Slovenia

<sup>44</sup>Fysikum, Stockholm University, Box 6730, SE-113 85 Stockholm, Sweden

<sup>45</sup>Dipartimento di Fisica Sperimentale, Università di Torino and INFN, Via P. Giuria 1, IT-10125 Turin, Italy

<sup>46</sup>INFN, Sezione di Torino, and Dipartimento di Fisica Teorica, Università di Torino, Via P. Giuria 1, IT-10125 Turin, Italy

<sup>47</sup>Dipartimento di Fisica, Università di Trieste and INFN, Via A. Valerio 2, IT-34127 Trieste, Italy

and Istituto di Fisica, Università di Udine, IT-33100 Udine, Italy

<sup>48</sup>Univ. Federal do Rio de Janeiro, C.P. 68528 Cidade Univ., Ilha do Fundão BR-21945-970 Rio de Janeiro, Brazil

<sup>49</sup>Department of Radiation Sciences, University of Uppsala, P.O. Box 535, SE-751 21 Uppsala, Sweden

<sup>50</sup>IFIC, Valencia-CSIC, and D.F.A.M.N., U. de Valencia, Avda. Dr. Moliner 50, ES-46100 Burjassot (Valencia), Spain

<sup>51</sup>Institut für Hochenergiephysik, Österr. Akad. d. Wissenschaft., Nikolsdorfergasse 18, AT-1050 Vienna, Austria

<sup>52</sup>Inst. Nuclear Studies and University of Warsaw, Ul. Hoza 69, PL-00681 Warsaw, Poland

<sup>53</sup>Fachbereich Physik, University of Wuppertal, Postfach 100 127, DE-42097 Wuppertal, Germany

† deceased

# 1 Introduction

Supersymmetry (SUSY) [1] is at present one of the most attractive possible extensions of the Standard Model (SM) and its signatures could be observed at LEP through a large variety of different channels. This paper presents searches for the pair-production of charginos, neutralinos, sleptons and squarks. The searches were performed and interpreted in the most model-independent way possible in terms of production cross-sections and masses. The results were interpreted in the framework of constrained SUSY models, with the different search channels complementing each other in constraining the parameter space.

The data collected by the DELPHI experiment in  $e^+e^-$  collisions at centre-of-mass energies ( $\sqrt{s}$ ) up to 208 GeV were used. No signal was found in any of the channels, and limits were set at 95% confidence level (CL).

The paper is organised as follows. In section 2 the basic supersymmetry framework is described: the general phenomenology is discussed in section 2.1, and implications of more constrained models used for interpreting the data are given in section 2.2. The DELPHI detector is described in section 3, and in section 4 the data sets and event generators are reviewed. In section 5 the general analysis framework is described, the analysis methods are briefly mentioned and the specific searches for sleptons, squarks, charginos and neutralinos are discussed. The results of each search are separately presented and interpreted in section 6. In section 7 the results are combined and interpreted in the framework of constrained SUSY scenarios with gravity-induced breaking of supersymmetry (SUGRA). A brief summary is given in section 8.

Previous results published by DELPHI can be found in references [2] to [9].

# 2 SUSY framework

The searches presented in this paper were performed in the framework of the Minimal Supersymmetric extension of the Standard Model (MSSM) [1].  $R$ -parity<sup>1</sup> conservation is assumed, implying that the Lightest Supersymmetric Particle (LSP) is stable and SUSY particles (“sparticles”) are pair-produced. In addition, they decay directly or indirectly into the LSP. In this paper the lightest neutralino,  $\tilde{\chi}_1^0$ , is assumed to be the weakly interacting LSP, which escapes detection giving signatures of missing energy and momentum.

The searches for sparticle production were developed with minimal assumptions, and the selections employed depended primarily on the masses of the particles involved. In particular, the sensitivity of the searches depends on the visible energy released in the decay process. In direct decays into the LSP, this visible energy is largely determined by the mass difference ( $\Delta M$ ) between the decaying sparticle and the LSP. In indirect (cascade) decays, other mass differences can also be important.

The MSSM has a large number of free parameters in addition to the SM ones. The most model-independent interpretation of the results is in terms of the masses and cross-sections explicitly involved, for each production channel. A common interpretation of the results from the various searches can also be performed and used to exclude regions of the model parameter space. This, however, requires a manageable number of free parameters. For this reason, assumptions must be made and specific scenarios defined

---

<sup>1</sup> $R$ -parity is a multiplicative quantum number defined as  $R = (-1)^{3(B-L)+2S}$  where  $B$ ,  $L$  and  $S$  are the baryon number, the lepton number and the spin of the particle, respectively. SM particles have  $R=+1$  while their SUSY partners have  $R = -1$ .

for such an interpretation. The general phenomenology of the searches will be discussed in section 2.1, followed by a description of the implications of more specific scenarios in section 2.2.

## 2.1 General phenomenology

### Squarks and Sleptons

The “sfermions”, squarks and sleptons, are the scalar partners of the SM fermions. The left- and right-handed chiral states of each SM fermion,  $f_L$  and  $f_R$ , have as SUSY partners two scalars, usually labelled  $\tilde{f}_L$  and  $\tilde{f}_R$ .

Sleptons and squarks could be pair-produced at LEP via  $e^+e^-$  annihilation into  $Z/\gamma$ , leading to  $\tilde{f}_R\tilde{f}_R$  or  $\tilde{f}_L\tilde{f}_L$  final states. Selectrons could also be produced through  $t$ -channel neutralino exchange. The selectron cross-section depends critically on the neutralino mass, and destructive interference can make it very small. The  $t$ -channel contribution also introduces the possibility of  $\tilde{e}_L\tilde{e}_R$  and  $\tilde{e}_R\tilde{e}_L$  production.

If the unification of sfermion masses at a high mass scale typical of Grand Unified Theories (GUT) is assumed, smaller masses and cross-sections for a given universal mass parameter are typically expected for the partners of right-handed fermions. Under this assumption, the kinematic accessibility of first and second family sfermions at LEP depends only on their assumed common mass at the unification scale. Squarks are in general expected to be heavier than sleptons. However, for sfermions of the third family the large Yukawa couplings lower the masses, as large mixing between left and right states may occur. In this case, the lighter mass states of third family sleptons and squarks,  $\tilde{\tau}_1$  (stau),  $\tilde{b}_1$  (sbottom) and  $\tilde{t}_1$  (stop), are candidates for the lightest charged supersymmetric particle.

In large regions of the SUSY parameter space the dominant decay of the sfermions is to the corresponding fermion and the lightest neutralino,  $\tilde{f} \rightarrow f\tilde{\chi}_1^0$ . In the case of the stop, the decay  $\tilde{t} \rightarrow t\tilde{\chi}_1^0$  is not kinematically allowed at LEP, and the dominant two-body decay channel is expected to be  $\tilde{t} \rightarrow c\tilde{\chi}_1^0$  ( $\tilde{t} \rightarrow b\tilde{\chi}_1^\pm$  being disfavoured by existing limits on the chargino mass). If  $m_{\tilde{\nu}} < M_{\tilde{t}_1}$ , the three-body decay  $\tilde{t}_1 \rightarrow b\ell\tilde{\nu}$  may compete with the  $c\tilde{\chi}_1^0$  decay.

Thus final state topologies with a pair of acoplanar<sup>2</sup> leptons or jets and missing energy are the relevant ones in the search for sleptons and squarks, respectively, and the total energy of the detectable final state particles (and thus the sensitivity of the search) depends primarily on the mass difference between the sfermion and the LSP.

### Charginos and Neutralinos

In the MSSM there are four neutralinos,  $\tilde{\chi}_i^0, i = 1, 4$  (numbered in order of increasing mass) and two charginos  $\tilde{\chi}_i^\pm, i = 1, 2$  which are linear combinations of the SUSY partners of neutral and charged gauge and Higgs bosons (gauginos and higgsinos). The lightest states can be mainly gaugino or higgsino, or strongly mixed (for similar gaugino and higgsino mass parameters).

Neutralinos (charginos) could be pair-produced at LEP via  $s$ -channel  $Z$  ( $Z/\gamma$ ) exchange or  $t$ -channel exchange of a selectron (sneutrino). The  $t$ -channel contribution can be important if the slepton is light. The interference with the  $s$ -channel diagram is constructive in the case of neutralinos, but destructive in the case of charginos.

<sup>2</sup>In this context, acoplanar means that the direction of one of the leptons/jets is not in the plane defined by the direction of the other lepton/jet and the beam line. Throughout this paper, the acoplanarity angle between two particles or jets is defined as the complementary (with respect to  $180^\circ$ ) of the angle between their directions in the plane transverse to the beam direction.

Expected decays are  $\tilde{\chi}_i^0 \rightarrow \tilde{\chi}_1^0 f \bar{f}$  and  $\tilde{\chi}_j^\pm \rightarrow \tilde{\chi}_1^0 f \bar{f}'$ . If the sfermions are heavy, these decays proceed via Z or W exchange. However, sfermion emission may also contribute if the sfermions are light, increasing the partial width for decays into the corresponding fermions, and two-body decays into  $f \bar{f}$  can dominate if kinematically allowed. The one-loop decay  $\tilde{\chi}_2^0 \rightarrow \tilde{\chi}_1^0 \gamma$  can be important in specific regions of the parameter space when other decays are suppressed.

Thus the sfermion mass spectrum may significantly affect both the production cross-section and the decay modes of charginos and neutralinos, and many final state topologies are possible.

In the case of chargino pair-production, the final state is expected to be four jets if both charginos decay hadronically, two jets and one lepton if one chargino decays into  $\ell \nu \tilde{\chi}_1^0$ , and leptons only if both charginos decay into leptons. The branching ratio of  $\tilde{\chi}_1^\pm \rightarrow \tilde{\chi}_2^0 f \bar{f}'$  can be sizable, in particular in the regions of the parameter space where  $\tilde{\chi}_2^0 \rightarrow \tilde{\chi}_1^0 \gamma$  is important. In this case, the above topologies are accompanied by photons.

If the mass difference  $\Delta M$  between the chargino and the LSP is very small the visible energy released in the decay is very small, making the signal hard to detect. The simultaneous production of a photon by initial state radiation (ISR) can be used to explore such regions, as this allows a very efficient background rejection (at the expense of a small signal cross-section). Still smaller mass differences imply a long lifetime of the chargino, which can then be identified as a heavy stable charged particle or one with a displaced decay vertex.

In the case of the detectable  $\tilde{\chi}_1^0 \tilde{\chi}_k^0$  neutralino production channels (*i.e.* excluding  $\tilde{\chi}_1^0 \tilde{\chi}_1^0$ ), the most important signatures are expected to be acoplanar pairs of jets or leptons with high missing energy and momentum. Although  $\tilde{\chi}_1^0 \tilde{\chi}_2^0$  and  $\tilde{\chi}_1^0 \tilde{\chi}_3^0$  are expected to dominate in most of the parameter space, channels like  $\tilde{\chi}_2^0 \tilde{\chi}_3^0$  and  $\tilde{\chi}_2^0 \tilde{\chi}_4^0$  must also be considered for a complete coverage. These give rise to cascade decays with multiple jets or leptons in the final state, possibly accompanied by photons from  $\tilde{\chi}_2^0 \rightarrow \tilde{\chi}_1^0 \gamma$ .

## 2.2 Constraining the parameter space

In this paper the results are combined and interpreted in the framework of constrained SUSY scenarios with gravity-induced SUSY breaking. To make the model more predictive, the unification of some parameters at a high mass scale typical of Grand Unified Theories (GUT) can be assumed [10]. The MSSM parameters and the assumptions that can be relevant in the interpretation of the results are listed below:

- $\tan \beta$ , the ratio of the vacuum expectation values of the two Higgs doublets;
- $\mu$ , the Higgsino mixing mass parameter;
- $M_1, M_2, M_3$ , the  $U(1) \times SU(2) \times SU(3)$  gaugino masses at the electroweak (EW) scale: when gaugino mass unification at the GUT scale is assumed, with a common gaugino mass  $\mathbf{m}_{1/2}$ , the relation between  $M_1$  and  $M_2$  is  $M_1 = \frac{5}{3} M_2 \tan^2 \theta_W \sim 0.5 M_2$ , with the assumption that  $M_i/\alpha_i$  ( $i = 1, 2, 3$ ) is renormalization group invariant, fulfilled at the one-loop level;
- $M_{\tilde{f}}$ , the sfermion masses: under the assumption of sfermion mass unification,  $\mathbf{m}_0$  is the common sfermion mass at the GUT scale;
- the pseudoscalar Higgs mass,  $\mathbf{m}_A$ , on which the masses in the Higgs sector depend: if scalar mass unification is assumed,  $m_A$  at the EW scale can be derived from  $m_0$ ;
- the trilinear couplings,  $\mathbf{A}_f$ , determining the mixing in the sfermion families: the third family trilinear couplings are the most relevant ones,  $\mathbf{A}_\tau, \mathbf{A}_b, \mathbf{A}_t$ , and under

the assumption of universal parameters at high mass scale there is a common trilinear coupling  $\mathbf{A}$ , to which  $A_\tau$ ,  $A_b$  and  $A_t$  at the EW scale can be related.

Mass mixing terms at the EW scale given by  $m_\tau(A_\tau - \mu \tan \beta)$ ,  $m_b(A_b - \mu \tan \beta)$  and  $m_t(A_t - \mu / \tan \beta)$  are considered for  $\tilde{\tau}$ ,  $\tilde{b}$  and  $\tilde{t}$ , respectively. The mass splitting grows with the mixing terms, and for large  $|\mu|$  this can give light  $\tilde{\tau}_1$  and  $\tilde{b}_1$  states if  $\tan \beta$  is large, or a light  $\tilde{t}_1$  for small  $\tan \beta$ .

In the model referred to as the “Constrained MSSM” (CMSSM) in the following, sfermion and gaugino mass unification are assumed. The parameter set is then reduced to  $M_2$ ,  $m_0$ ,  $\tan \beta$ ,  $\mu$ ,  $m_A$  and three  $A_f$  couplings. This is the model considered in section 7.

Further tightening the assumptions, the individual  $A_f$  couplings can be replaced by a universal coupling  $A$  and  $m_A$  can be related to the other parameters by assuming scalar (including Higgs bosons) mass unification. Requiring in addition the correct reproduction of the EW symmetry scale, which fixes the absolute value of  $\mu$ , defines the minimal MSSM with gravity-induced SUSY breaking (mSUGRA).

The direct results of the searches are first derived and presented in the most model-independent way possible. Under the assumptions described above, the results are then used to constrain the SUSY parameters. Presently, the strongest constraints on SUSY models come from the MSSM Higgs searches [11].

Chargino production is the most important direct SUSY detection channel for large regions of the parameter space. However, if sfermions are light (corresponding to a small  $m_0$  scenario), or if the parameters take particular values, the chargino production cross-section can be greatly suppressed or undetectable final states can dominate (in particular for small mass splittings). The most relevant of these cases are the following:

### Large $m_0$

For large  $m_0$ , the sfermions are heavy and have little influence on the observable phenomenology. The chargino pair-production cross-section is large and the chargino is excluded nearly up to the kinematic limit. The search for charginos in non-degenerate scenarios has been applied down to  $\Delta M = M_{\tilde{\chi}_1^\pm} - M_{\tilde{\chi}_1^0} = 3 \text{ GeV}/c^2$ . The region  $\Delta M < 3 \text{ GeV}/c^2$  is covered by the search requiring an ISR photon and by the searches for long-lived charginos. Moreover, small values of  $\Delta M$  occurring in scenarios without gaugino mass unification [12] have also been investigated.

At small  $\tan \beta$  ( $\tan \beta < 1.2$ ), neutralino searches can extend the sensitivity of the searches beyond the kinematic limit for chargino production. This concerns the region of (small) negative  $\mu$  and  $M_2 > 60 \text{ GeV}/c^2$ . In particular, searches for neutralino cascade decays are crucial for investigating the  $M_2 < 120 \text{ GeV}/c^2$  region, where the  $\tilde{\chi}_1^0 \tilde{\chi}_2^0$  cross-section is small.

### Small $m_0$

If  $m_0$  is small, light sfermions affect the chargino and neutralino production cross-sections. In particular, the decrease of  $m_0$  causes the chargino production cross-section to drop in the region where the gaugino components dominate (small  $M_2$  and large  $|\mu|$ ). Down to  $m_0 \simeq 200 \text{ GeV}/c^2$ , the cross-section remains large enough to allow chargino exclusion nearly up to the kinematic limit. For smaller  $m_0$ , the neutralino production cross-section is very much enhanced, and neutralino searches become sensitive instead.

If  $m_0$  is very small ( $m_0 \simeq 100 \text{ GeV}/c^2$ ), sleptons can be sufficiently light to affect drastically the decay patterns of charginos and neutralinos, and nearly invisible final states can become dominant in some cases. However, for such small  $m_0$  and small  $M_2$  (below  $200 \text{ GeV}/c^2$ ) sleptons can also be searched for in direct pair-production.

If  $M_{\tilde{\chi}_1^\pm} > m_{\tilde{\nu}}$  and the mass difference  $M_{\tilde{\chi}_1^\pm} - m_{\tilde{\nu}}$  is small, the chargino decay chain  $\tilde{\chi}_1^\pm \rightarrow \tilde{\nu} \ell \rightarrow \nu \tilde{\chi}_1^0 \ell$  is dominant, and leads to an experimentally undetectable final state (the only visible final state lepton has very low momentum). However, in this case the search for selectrons can be used to constrain the sneutrino mass (under the assumption of unification) and thus the chargino mass.

It can also happen, in scenarios with large mixing among sfermions and large  $\tan \beta$  and  $M_2$ , that “blind spots” occur in the chargino detection sensitivity due to  $\tilde{\chi}_1^\pm \rightarrow \tilde{\tau} \nu \rightarrow \tau \tilde{\chi}_1^0 \nu$  with a small mass difference  $M_{\tilde{\tau}} - M_{\tilde{\chi}_1^0}$ . In this case,  $\tilde{\chi}_1^0 \tilde{\chi}_2^0$  or  $\tilde{\chi}_2^0 \tilde{\chi}_2^0$  production with  $\tilde{\chi}_2^0 \rightarrow \tilde{\tau} \tau$  are the only detectable channels. A specific search was designed for this case.

### 3 Detector description

The DELPHI detector is described in detail in [13]. The central tracking system consisted of a Time Projection Chamber (TPC), supplemented by a system of silicon tracking detectors and drift chambers. These included the Vertex Detector (VD), closest to the beam pipe, the Inner Detector (ID) and the Outer Detector (OD). These were situated inside a solenoidal magnetic field of 1.2 T, parallel to the beam axis. The average momentum resolution for charged particles in hadronic final states was in the range  $\Delta p/p^2 \simeq 0.001 - 0.01 (\text{GeV}/c)^{-1}$ .

The electromagnetic (EM) calorimeters were symmetric around the plane perpendicular to the beam ( $\theta = 90^\circ$ )<sup>3</sup>, with the High density Projection Chamber (HPC) extending from  $88.7^\circ$  to  $43.1^\circ$  (barrel region), the Forward Electromagnetic Calorimeter (FEMC) from  $36^\circ$  down to  $9^\circ$ , overlapping with the Small angle Tile Calorimeter (STIC), the DELPHI luminometer, which covered the range  $1.7^\circ \leq \theta \leq 10.6^\circ$ . The region of poor electromagnetic calorimetry at a polar angle close to  $40^\circ$  was instrumented by scintillators (hermeticity taggers) [14] to tag photons.

The Hadron Calorimeter (HCAL) covered 98% of the solid angle. Muons with momenta above  $2 \text{ GeV}/c$  penetrated the HCAL and were recorded in sets of Muon drift chambers located in the barrel (MUB), forward (MUF) and surround<sup>4</sup> (MUS) regions of the detector.

### 4 Data samples and event generators

During the year 2000 DELPHI collected data in the centre-of-mass energy range from 201.5 to 208.8 GeV. The average centre-of-mass energy was  $\langle \sqrt{s} \rangle \simeq 206 \text{ GeV}$  and the total integrated luminosity amounted to about  $224 \text{ pb}^{-1}$ . In 1999 (1998) about  $227 \text{ pb}^{-1}$  ( $158 \text{ pb}^{-1}$ ) were collected at centre-of-mass energies around 192, 196, 200 and 202 GeV (189 GeV).

The data collected in the years 1999-2000 were analysed in the searches presented in this paper. In some cases the 1998 data were re-analysed for consistency with the improved methods now presented, as detailed in the description of the analyses. Combination with earlier results was performed to obtain cross-section upper limits and excluded regions in the model parameter space. Details for each channel are given in section 6.

<sup>3</sup>In DELPHI, a right-handed Cartesian coordinate system is used with the  $z$  direction defined by the direction of the electron beam, and the  $x$ -axis pointing towards the centre of the LEP ring. The origin is at the centre of the detector. The polar and azimuthal angles  $\theta$  and  $\phi$  are defined with respect to the  $z$  axis and  $\phi = 0$  corresponds to the  $x$ -direction, and the coordinate  $r$  is defined in the usual way as  $r = \sqrt{x^2 + y^2}$ . In this paper, polar angle ranges are always assumed to be symmetric with respect to the  $\theta = 90^\circ$  axis.

<sup>4</sup>The region between the barrel and end-cap parts of DELPHI not covered by the MUF and the MUB chambers.

Quality requirements on the status of the subdetectors most relevant for each analysis were applied, generically based on the status of the main tracking devices. Muon chambers or calorimeters were considered in channels where muon or electromagnetic shower detection was crucial. The luminosity loss was at most of the order of a few percent and was taken into account in the analyses.

On September 1<sup>st</sup> 2000, sector 6 of the TPC (corresponding to 1/12 of the TPC acceptance) failed beyond repair. This required modifications of the pattern recognition, and affected the quality of charged track reconstruction. Thus special care had to be taken for each search when analysing the data collected without TPC sector 6. The accumulated integrated luminosities with and without a working sector 6 are respectively  $164 \text{ pb}^{-1}$  and  $60 \text{ pb}^{-1}$  at average centre-of-mass energies around 206 GeV.

In order to increase the sensitivity for a discovery, the data collected in 2000 were divided into 4 regions of centre-of-mass energy as given in table 1.

$\sqrt{s}$ region of analysis		$\mathcal{L} (\text{pb}^{-1})$	$\langle \sqrt{s} \rangle (\text{GeV})$	
1	Sector 6 on	$\sqrt{s} \leq 205.75 \text{ GeV}$	78.3	204.9
2	Sector 6 on	$205.75 < \sqrt{s} \leq 207.5 \text{ GeV}$	78.8	206.7
3	Sector 6 on	$207.5 \text{ GeV} < \sqrt{s}$	7.2	208.0
4	Sector 6 off	all $\sqrt{s}$	60.0	206.5(*)

Table 1: Definition of the  $\sqrt{s}$  regions used to analyse the data collected in 2000. The three energy bins for the period in which the detector was fully operational are referred to in the text by their approximate average centre-of-mass energies: 205, 207 and 208 GeV. The “Sector 6 off” data are referred to as 206.5(\*)).

To evaluate the signal efficiencies and background contaminations, simulated events were generated using several different programs.

The background process  $e^+e^- \rightarrow q\bar{q}(n\gamma)$  was generated with PYTHIA 6.125 [15]. For  $\mu^+\mu^-(\gamma)$  and  $\tau^+\tau^-(\gamma)$ , DYMU3 [16] and KORALZ 4.2 [17] were used, respectively. The BHWIDE generator [18] was used for Bhabha events. Simulation of four-fermion final states was performed using EXCALIBUR [19] and grc4f [20].

Two-photon interactions giving hadronic final states were generated using TWOGAM [21], PHOJET [22] and PYTHIA 6.143 [15], while leptonic final states were generated using the generator of [23], including radiative corrections for the  $e^+e^-\mu^+\mu^-$  and  $e^+e^-\tau^+\tau^-$  final states.

SUSYGEN 2.2004 [24] was used to generate chargino, neutralino, slepton, and sbottom signal events and to calculate cross-sections and branching ratios for these channels. For the nearly mass-degenerate case, the chargino decays were modelled with the results of the computations of reference [12]. Stop events were generated according to the expected differential cross-sections using the BASES and SPRING program packages and taking special care in the modelling of the stop hadronisation [25].

In all cases except for stop generation, JETSET 7.4 [15], tuned to LEP1 data [26], was used for quark fragmentation.

The generated signal and background events were passed through the detailed simulation of the detector, DELSIM [13], and then processed with the same reconstruction and analysis programs as the real data. The faster DELPHI simulation code SGV [27] was also used for signal efficiency studies in some analyses. SGV is a model of the detector response which has been tuned to the data independently from DELSIM. For charged

particles the perigee parameters resulting from the physical process generation were modified to take into account parametrized effects of multiple scattering, detector resolutions and acceptance. For neutral particles geometric acceptance and parametrized calorimetric resolutions were taken into account. Bremsstrahlung and photon conversion in the tracking system were also simulated.

The numbers of simulated events from different background processes were several times the numbers in the real data.

## 5 Descriptions of the analyses

The analyses described below can be divided into two stages. The first stage was very similar for all searches and consisted of the selection of charged and neutral particles followed by an event preselection. These are described in sections 5.1.1 and 5.1.2. In the subsequent stage, the analyses differed according to the characteristics of the various signals. This is described in sections 5.2 to 5.5. In most searches several different topologies were considered, accounting for the different possible final states. Particle identification and reconstruction algorithms common to several searches are described in section 5.1.3. Different analysis techniques were chosen for the various searches: some analyses were based on successive requirements on individual event variables (“sequential cut analyses”), others used multidimensional techniques based on likelihood ratios or neural networks. These techniques are briefly discussed in section 5.1.4.

As discussed above, the sensitivity of the searches depends on the mass difference between the produced sparticles and the LSP, which determines the visible energy released in the process. Typically, for small  $\Delta M$  the signatures of sparticle production are similar to those of two-photon interactions ( $\gamma\gamma$  events). For high  $\Delta M$  sparticle production events resemble four-fermion final states such as  $W^+W^-$  and  $ZZ$ . For intermediate  $\Delta M$  values, the background is composed of several SM processes (in particular two-fermion ones). The coverage of all the relevant  $\Delta M$  regions often requires the combination of different searches or the optimisation of the selection criteria separately in each  $\Delta M$  interval. Sparticle searches for very low values of  $\Delta M$  are particularly challenging and required different preselections.

### 5.1 Basic selections and techniques

#### 5.1.1 Particle selection

The following quality requirements were applied to the charged and neutral particles observed in the detector.

Charged particles were required to have momentum  $p$  above 100 MeV/ $c$  and below  $0.75\sqrt{s}$ , a relative momentum error less than 100%, and to extrapolate back to within 5 cm of the main vertex in the transverse ( $r\phi$ ) plane and 10 cm/ $\sin\theta$  in the longitudinal ( $z$ ) direction. Similar but more stringent criteria were applied to particles whose tracks extrapolated to the TPC, but which gave no signal in the TPC. Whenever tracks reconstructed with TPC information were required in the subsequent analyses, at least five of the 16 pad rows had to contribute hits.

In the stau analysis (see section 5.2.3) charged particle tracks were required to have TPC information, or all three of the detectors VD, ID and OD used in the reconstruction of the track. In addition, only tracks with polar angle  $\theta > 15^\circ$  were kept.

In the nearly mass-degenerate chargino search (see section 5.4.2) there was no lower bound on the momentum for tracks at polar angle above  $25^\circ$ , while  $p > 150 \text{ MeV}/c$  was required otherwise. In addition, different impact parameter requirements were applied (6 cm and 12 cm in the transverse and longitudinal directions, respectively).

Energy clusters in the calorimeters were taken as neutral particles if not associated to a charged particle and if above an energy threshold which was 900 MeV for deposits in the hadron calorimeter and ranged from 300 to 500 MeV for deposits in the electromagnetic calorimeters (depending on the region of the detector). Cuts removing clusters created by radioactivity in the lead of the HPC or by particles from cosmic ray showers were also applied.

### 5.1.2 General event preselection

In the general preselection, events were kept if there were at least two charged particles, at least one of them had a transverse momentum above  $1.5 \text{ GeV}/c$ , and the transverse energy of the event<sup>5</sup> exceeded 4 GeV. This rejected mostly two-photon interactions (for which most of the energy is deposited in the forward regions of the detector), zero- or one-prong final states (like  $e^+e^- \rightarrow \gamma\gamma$ ,  $e\gamma \rightarrow e\gamma$ ) and beam-related backgrounds (such as beam-gas interactions).

For chargino searches in nearly mass-degenerate scenarios a different preselection was used: at least two charged particles were required, as well as one isolated electromagnetic cluster with transverse energy above a  $\sqrt{s}$ -dependent threshold close to 5 GeV and a mass recoiling against it above  $90 \text{ GeV}/c^2$ . Two-photon and beam-gas backgrounds were reduced by rejecting events with a large fraction of the detected energy in the forward region of the detector.

### 5.1.3 Particle identification and reconstruction algorithms

The following criteria for particle and event classification were common to the different searches.

Particle jets were reconstructed using three different approaches:

- The DURHAM [28] algorithm was used to cluster the particles into a fixed number of jets: two or four.
- The LUCLUS [15] algorithm was applied with the critical distance set to  $d_{\text{join}} = 10 \text{ GeV}/c$  or  $d_{\text{join}} = 2.5 \text{ GeV}/c$ . The final number of jets is, thus, variable (and lower in the first case).
- A specific algorithm optimised for the low multiplicity jets resulting from  $\tau$  decays was used for  $\tilde{\tau}$  pair-production searches. This method considered all possible ways of clustering the charged particles in the event into groups, always requiring the invariant mass to be below  $2 \text{ GeV}/c^2$ . Clearly identified leptons were considered as a single group, except for pairs of oppositely charged, well identified electrons close together which were allowed to be grouped with other particles, since they could come from a converted photon.

If possible, the event was clustered into two groups with invariant mass below  $2 \text{ GeV}/c^2$ . If no such combination existed, the one with the smallest number of groups was kept. When more than one way of obtaining two groups both with invariant mass below  $2 \text{ GeV}/c^2$  was found, the grouping yielding the lowest sum of masses was retained. Once the best grouping of the charged tracks was found, it

---

<sup>5</sup>The transverse energy is defined as the sum of the absolute values of the transverse momenta of all particles in the event:  $c \sum_i p_{\text{T}i}$ .

was attempted to associate the neutrals in the event to the particle groups. Also in this step, the grouping yielding the lowest sum of masses was chosen. However, as very few long-lived neutral hadrons are expected in  $\tau$ -decays, neutral hadronic clusters were not included in the groups, but treated as isolated neutrals. Also electromagnetic clusters which could not be merged into any of the groups without the invariant mass exceeding  $2 \text{ GeV}/c^2$ , were left as isolated neutrals. In addition, a special procedure was applied to identify and correct for neutral clusters that were likely to be either bremsstrahlung photons or a shower induced by an electron that was not correctly assigned to the track by the reconstruction program.

The charge of each cluster was taken as the sum of the charges of all its particles.

The thrust variable used in several analyses throughout this paper was computed using all the particles meeting the particle selection requirements.

Isolated leptons or photons in the event are often very important in distinguishing signal and background. In the present searches, the isolation criteria depended on the multiplicity of the event:

- In low multiplicity searches, charged particles were classified as isolated if the total charged energy, excluding the energy of the particle itself, within  $10^\circ$  of the track direction was below 2 GeV. Slightly tighter cuts in the impact parameters (1 cm and 5 cm in  $r\phi$  and  $z$ , respectively) and in the momentum error were also applied.
- In high multiplicity searches, a photon was considered isolated if its angular separation from any neutral or charged particle was greater than  $15^\circ$ . A lepton was tagged as isolated if its angular separation from all the jets (computed without the lepton using the LUCLUS algorithm with  $d_{join} = 40 \text{ GeV}/c$ ) was greater than  $20^\circ$ .

The identification of a track as a muon, electron, or hadron was “tight”, “loose”, or “veto” (or none at all). Tight identification was unambiguous. A particle could simultaneously be loosely identified as several different species. Excluded particle species were vetoed.

The identification of muons was provided primarily by the DELPHI standard algorithm described in [13], which relies on the association of charged particles to signals in the muon chambers and the HCAL.

Electron and photon identification was performed by the algorithm described in [29] which combines deposits in the EM calorimeters with tracking information and takes possible radiation and interaction effects into account by a clustering procedure in an angular region around the main shower. In the  $\tilde{\tau}$  analysis (see section 5.2.3), the clustering procedure was not used for tracks in the barrel region of the detector, since it tended to treat charged pions from  $\tau$  decays wrongly, if they were accompanied closely by neutral pions. In low multiplicity topologies a very loose electron identification based on the ratio  $E/p$  between the energy deposited in the EM calorimeter and the momentum of the associated charged track was also used.

Below, whenever the identification level is not specified, it is implied to be “tight” for electrons and “loose” for muons. In the case of electrons, “tight” identification basically adds some isolation requirements to the identification ones.

$e/\gamma$  separation inside the acceptance of the STIC luminometer was performed on a statistical basis, using the veto information of the two planes of the scintillator counters placed in front of it.

In the stau analysis a particle was considered as a tight hadron if it was not classified as a muon or electron and had an associated energy in the hadron calorimeter exceeding 50% of its momentum, or else was considered as a loose hadron if it had hadronic energy

associated and it was not tightly identified as a muon or electron. If both the electromagnetic and hadronic energies were small (less than 1 and 6 GeV, respectively), and the difference between the hadronic energy and the track momentum was above 10 GeV, the particle was assigned both the loose muon and loose hadron code.

Decays of b-quarks were tagged using a probabilistic method based on the impact parameter of tracks with respect to the main vertex [30].  $\mathcal{P}_E^+$  stands for the corresponding probability estimator for tracks with positive impact parameter, the sign of the impact parameter being defined by the jet direction. The combined probability  $\mathcal{P}_{\text{comb}}$  included additional contributions from properties of reconstructed secondary vertices.

All searches made use of the information from the hermeticity taggers [14] to reject events with photons in the otherwise insensitive region at polar angles around  $40^\circ$ . If there were active taggers not associated to reconstructed jets, the event was rejected if the tagger was located in the direction of the missing momentum. In the stau analysis, where neutrinos from tau decays made the estimation of the direction of the missing momentum unreliable, events containing active and isolated taggers were rejected irrespective of the direction of the missing momentum.

#### 5.1.4 Analysis techniques

##### Likelihood ratio method

In the likelihood ratio method used, several discriminating variables are combined into one on the basis of their one-dimensional probability density functions (pdf's). If the variables used are independent, this gives the best possible background suppression for a given signal efficiency [31]. For a set of variables  $\{x_i\}$ , the pdf's of these variables are estimated by normalised frequency distributions for the signal and the background samples. We denote the pdf's of these variables  $f_i^S(x_i)$  for the signal events and  $f_i^B(x_i)$  for the background events submitted to the same selection criteria. The likelihood ratio function is defined as  $\mathcal{L}_{\mathcal{R}} = \prod_{i=1}^n \frac{f_i^S(x_i)}{f_i^B(x_i)}$ . Events with  $\mathcal{L}_{\mathcal{R}} > \mathcal{L}_{\mathcal{R}_{\text{cut}}}$  are selected as candidate signal events. The choice of variables and the value of  $\mathcal{L}_{\mathcal{R}_{\text{cut}}}$  were optimised using simulated event samples by minimising the signal cross-section that was expected to be excluded at 95% confidence level in the absence of a signal.

##### Neural networks

A neural network provides a different way of defining one discriminating variable from multidimensional distributions of event variables given as inputs. The neural network used below (see section 5.3) contains three layers of nodes: the input layer where each neuron corresponds to a discriminating variable, the hidden layer, and the output layer which is the response of the neural network. The program used in the squark analysis was **SNNS** [32]. A “feed-forward” architecture is implemented and the “back-propagation” algorithm is used to train the network with simulated events. An independent validation sample was also used not to overtrain the network. A way of enhancing the efficiency of the network without increasing too much the number of its parameters is to define a separate output node for each type of event that the neural network should separate. More details are given in section 5.3.

## 5.2 Slepton searches

Supersymmetric partners of electrons, muons and taus were searched for. In this paper, data collected at centre-of-mass energies between 189 and 208 GeV were analysed, and were combined with previous results [2].

The track selection and the general event preselection described in sections 5.1.1 and 5.1.2, respectively, were used. The analyses were then performed in two stages. Firstly, a loose selection was used to obtain a sample of low multiplicity events. Events with less than ten charged particles and a visible invariant mass above  $4.5 \text{ GeV}/c^2$  were retained for further analysis. Different selections were then applied in each of the three channels.

### 5.2.1 Selectron searches

To search for selectrons, the general topology required was two acoplanar electrons and missing energy. All candidates with exactly two well reconstructed and isolated particles (according to the definition described in section 5.1.3), oppositely charged and with momentum above  $1 \text{ GeV}/c$ , were first selected. One of the two charged particles was required to be tightly identified as an electron, and the event was rejected if the other was identified as a muon.

At this stage of the selection the sample consisted mainly of Bhabha and two-photon events. Satisfactory agreement was observed between the data and simulated background, as shown in figure 1<sup>6</sup>.

A series of tighter cuts reduced the SM background further. As two-photon events are predominantly at low polar angles and with low momentum, the visible energy was required to be greater than 15 GeV, the energy deposited in the low angle STIC calorimeter less than 4 GeV and the total transverse momentum with respect to the beam axis greater than  $5 \text{ GeV}/c$ . To reduce the number of Bhabha events an upper limit on the visible energy of 100 GeV was imposed, while also requiring that the neutral energy not associated to the charged particle tracks be less than 30 GeV. Events were also rejected if there were more than four neutral clusters in total, each with energy above 500 MeV. Bhabha events are coplanar and with a large opening angle, hence it was demanded that the opening angle between the two tracks be lower than  $165^\circ$  and the acoplanarity be greater than  $15^\circ$ . Constraints were also imposed on the momenta of the two particles, requiring that both tracks had momentum greater than  $2 \text{ GeV}/c$ .

### 5.2.2 Smuon searches

Smuon pair-production with decays to muon plus neutralino is expected to give acoplanar muons and missing energy. All candidates with exactly two well reconstructed and isolated particles (according to the definition given in section 5.1.3), oppositely charged and with momentum above  $1 \text{ GeV}/c$ , were first selected. At least one of the particles had to be loosely identified as a muon. It was further required that neither particle be identified as an electron. The selected sample consisted mainly of two-photon events and fair agreement between real data and simulated background was observed (see figure 2; the slight discrepancies visible in figure 2(d), in the tail of the two-photon distribution at about  $40 \text{ GeV}/c$ , and for high momenta, are in kinematic regions rejected in the next step of the analysis).

To reduce the SM background further, a series of tighter cuts were applied. To remove two-photon events, the visible energy was required to be greater than 10 GeV. Also, the

<sup>6</sup>In order to show the different background contributions, the largely dominant Bhabha background was suppressed in these plots by demanding that the opening angle between the two tracks was below  $176^\circ$ .

energy in the STIC had to be less than 1 GeV. It was also demanded that the transverse momentum be greater than 5  $\text{GeV}/c$ . To remove  $e^+e^- \rightarrow \mu^+\mu^-$  events, an upper limit of 120 GeV on the visible energy was imposed, whilst also requiring the unassociated neutral energy to be less than 10 GeV, with no more than two neutral clusters. This background was further suppressed by accepting only events in which the opening angle between the tracks was less than  $165^\circ$  and the acoplanarity was greater than  $15^\circ$ . To reduce  $t$ -channel  $W$  pair contamination, events were rejected if the positively charged muon was within  $40^\circ$  of the  $e^+$  beam direction, or the negatively charged muon was within  $40^\circ$  degrees of the  $e^-$  beam direction.

### 5.2.3 Stau searches

Events with two acoplanar taus and high missing energy can be the signature of stau pair-production. Due to the scalar nature of the stau, the two taus are produced centrally in the detector. To select this topology, the particles in the events were grouped into clusters according to the algorithm described in section 5.1.3. Events with exactly two particle clusters (possibly accompanied by isolated neutral particles) were considered further if they contained at least one charged particle with momentum above 1  $\text{GeV}/c$  and a relative error less than 30%. This particle had to be isolated (no neutral or charged particles in a cone of  $20^\circ$  half-angle around it), or above  $30^\circ$  in polar angle, and its calorimetric energy could not exceed the momentum by more than three times the expected error on the calorimetric measurement. A comparison of data and simulated SM background at this stage <sup>7</sup> is shown in figure 3. It was further required that there were no more than six charged particles in the event and that the total charge was 0 or  $\pm 1$ .

Tight and loose electrons, muons and hadrons were defined as described in section 5.1.3. In addition, if a particle had a loose identification for one species, and was vetoed for the other two, it was considered as tightly identified. If a track pointed to a gap in the electromagnetic calorimetry, it was considered as a loose electron. Tracks with no identification information were treated as loose electrons. Neutral clusters passing the criteria of section 5.1.1 were used if their angle to the beam was above  $15^\circ$ . Furthermore, no identified hadronic secondary interactions inside the tracking system were allowed.

Beyond this point, the analysis differed depending on whether a stau with mass above or below  $m_Z/2$  was searched for.

#### Search for staus with large mass

To suppress the two-photon background, it was required that the total transverse momentum imbalance exceeded 4  $\text{GeV}/c$ , the total calorimetric energy below  $30^\circ$  in polar angle did not exceed 20% of the beam momentum and the total momentum of the event was within the region  $\theta(\Sigma\vec{p}) > 30^\circ$ .

To reduce the background from radiative return to the  $Z$ , none of the clusters was allowed to have a total momentum ( $p^{\text{JET}}$ ) above 70% of the beam momentum, the momentum of isolated photons had to be less than 10% of the beam momentum, and the acoplanarity was required to be above  $12^\circ$ . To reject  $e^+e^- \rightarrow Z/\gamma \rightarrow \tau^+\tau^-$  events where the decay of one  $\tau$  yielded visible products with large momentum, while the decay of the

<sup>7</sup>In order to show the contribution of all classes of background, the largely dominant Bhabha background was suppressed in these plots by demanding that the missing transverse momentum was above 4  $\text{GeV}/c$ , and that the acoplanarity was above  $1^\circ$ .

other  $\tau$  yielded soft products, the momentum transverse to the thrust axis was required to exceed  $0.7 \text{ GeV}/c$ .

This selection was supplemented by cuts that depended on the region of the  $(M_{\tilde{\tau}}, M_{\text{LSP}})$  plane considered. At any given point in the plane, it was demanded that the accepted events in that point were kinematically compatible with the corresponding signal: the maximal momentum the  $\tau$  can have in the lab frame, neglecting  $m_{\tau}$ , is  $p_{\text{max}} = \frac{\sqrt{s}}{4} (1 - [M_{\text{LSP}}/M_{\tilde{\tau}}]^2) (1 + \sqrt{1 - 4M_{\tilde{\tau}}^2/s})$ , which is also the end-point of the spectrum of the visible  $\tau$  - jet momentum. Hence  $p_{\text{high}}^{\text{JET}}$  (the larger of the two jet momenta) was required to be less than  $p_{\text{max}}$ .

For large  $\Delta M = M_{\tilde{\tau}} - M_{\text{LSP}}$ , the remaining background from two-photon events can be removed by requiring large transverse momentum imbalance. At smaller values of  $\Delta M$  such a cut would greatly reduce the signal detection efficiency. Therefore, if  $\Delta M$  was below (above)  $20 \text{ GeV}/c^2$  the total missing transverse momentum ( $\cancel{P}_t$ ) had to exceed  $0.8$  ( $1.2$ ) times the maximum transverse momentum a  $\gamma\gamma$  event could have without one of the beam-remnant electrons being deflected into the STIC (*i.e.* by an angle greater than  $\theta_{\text{max}} = 1.82^\circ$ ). This limit depended on the centre-of-mass energy:  $p_T^{\text{lim}} = \sqrt{s} \sin \theta_{\text{max}} / (1 + \sin \theta_{\text{max}}) = 0.031 \sqrt{s}$ <sup>8</sup>. In addition, in the region with  $\Delta M$  below  $20 \text{ GeV}/c^2$  there should be no calorimetric energy below  $30^\circ$ , and  $\theta(\Sigma \vec{p})$  had to exceed  $45^\circ$ .

At this stage of the analysis, the dominant remaining background at large  $\Delta M$  were  $W^+W^-$  events. Only events with both  $W$  bosons decaying leptonically were still present. Electrons and muons in  $W^+W^-$  events might come either directly from the  $W$ -decay, or indirectly from  $\tau$ -decays. In the former case, which is dominant, the momentum of the detected lepton tends to be higher than in the signal, where all electrons and muons would be indirect. In the latter case, the momentum spectrum of background and signal events is similar.

In order to reduce the background from  $W^+W^-$  events with leptons from direct  $W$  decays, it was demanded that the highest momentum of any tightly or loosely identified lepton in the event was less than  $(0.1\Delta M + 0.6)P_{W\text{min}}^{\text{lept}}$ , where  $P_{W\text{min}}^{\text{lept}}$  is the lowest momentum a lepton in the decay  $W \rightarrow \ell\nu$  can obtain in the lab-frame if the  $W$  is on-shell. In the region of large  $\Delta M$ , it was also demanded that there be no more than one tightly identified electron or muon in the event.

To suppress further the  $W^+W^-$  background, and in particular the component with leptons from indirect decays, the events were analysed as if they were indeed  $W^+W^-$  events. The  $\theta$  angle of the  $W$  yielding the cluster with positive charge was estimated ( $\theta_{W^+}$ ) and selections in the  $(\theta_{W^+}, p_{\text{high}}^{\text{JET}})$ -plane were used to discriminate the signal from this background<sup>9</sup>. The  $\theta_{W^+}$  was estimated as follows. If neither  $W$  decayed to a tau,  $\theta_{W^+}$  can be calculated exactly (albeit usually with two-fold ambiguity). The  $W$  decay to a muon or an electron could be distinguished from the decay to the  $\tau$  by the presence of a single track cluster with at least a loose lepton identification and a momentum above the lowest possible momentum for the charged lepton from the decay of an on-shell  $W$ . Decays that did not fulfil these requirements were assumed to be decays to  $\tau$ . If one of the  $W$  decayed to a  $\tau$  the solution for  $\theta_{W^+}$  is approximate, since the momentum of the  $\tau$  is unknown. In this case, the momentum of the initial  $\tau$  was estimated as the average momentum of taus from  $W$  decay, calculated for tau momenta above the measured jet

<sup>8</sup>The missing transverse momentum was estimated in four different ways: from the transverse momentum of the two jets, as that of all particles passing the quality cuts, as that of all reconstructed particles except those identified as bremsstrahlung photons, and as that of all reconstructed particles. The cut was applied on the smallest of these. This gave stability against possible errors in reconstruction and against the presence of noise or cosmics.

<sup>9</sup>At this stage of the analysis about 99 % of the events had a cluster with charge equal to +1 (this selection was not applied to events where there was no cluster with positive charge).

momentum. The direction of the momentum of the tau was taken as the measured jet direction.

The W pair-production process tends to have higher  $p_{high}^{\text{JET}}$  and  $\theta_{W^+}$ . In addition,  $p_{high}^{\text{JET}}$  and  $\theta_{W^+}$  are correlated in such processes, while they are independent in  $\tilde{\tau}$  production. Thus the signal selection criteria in the  $(\theta_{W^+}, p_{high}^{\text{JET}})$ -plane were:

$$\theta_{W^+} < \begin{cases} -3.0(x - 0.325) + A & \text{if } x < 0.325 \\ A & \text{if } 0.325 \leq x < 0.52 \\ -2.1(x - 0.52) + A & \text{if } x \geq 0.52 \end{cases}$$

where  $\theta_{W^+}$  is in radians and  $x = p_{high}^{\text{JET}}/p_{beam}$ , and  $A$  is a constant chosen to be 1.6 (2.1) for  $\Delta M$  below (above) 20  $\text{GeV}/c^2$ . The boundary of the selected region in the  $(\theta_{W^+}, p_{high}^{\text{JET}})$ -plane thus defined closely follows a curve of constant ratio between the probability density functions for signal and background (the likelihood ratio).

### Search for light staus without coupling to the Z

A light stau can be excluded to a large extent using LEP1 results, as discussed in section 6.3. This is however not possible when the coupling to the Z vanishes (the stau mixing angle gives the minimum cross-section). The large mass analysis described in the previous section loses its efficiency for stau masses below 15  $\text{GeV}/c^2$ . This is mainly due to the fact that the staus are highly boosted at such small masses, failing the acoplanarity cut.

Therefore a specific search was required for small  $M_{\tilde{\tau}}$  at the minimal cross-section mixing angle. Two search regions were identified: one optimised for very small masses,  $M_{\tilde{\tau}}$  below 10  $\text{GeV}/c^2$ , referred to as the “very small mass analysis”, and one for larger masses, optimized for  $M_{\tilde{\tau}}$  above 10  $\text{GeV}/c^2$  and  $\Delta M$  between  $m_{\tau}$  and 4  $\text{GeV}/c^2$  referred to as the “small mass analysis” (the large mass analysis shows good sensitivity for  $\Delta M$  above 4  $\text{GeV}/c^2$  down to  $M_{\tilde{\tau}} = 15 \text{ GeV}/c^2$ ).

The signal events in the relevant kinematic regions are characterised by containing two taus at large angles to the beam, and being softer than two-fermion events but slightly harder than  $\gamma\gamma$  events. Due to the sizable boost of the staus, the two jets tend to be rather back-to-back. Two-tau events were selected as described in the previous section, with the additional requirement that the topology was either 1-prong and 3-prong, or two 1-prongs. In the latter case, there should not be two tightly identified leptons of the same flavour in the event. To select central events, the polar angle of the most energetic particle in each detector hemisphere had to be above 50°, and the sine of the polar angle of each jet had to be above 0.8. The acollinearity was required to be above 0.4°,  $p_{max}^{\text{JET}}/p_{beam}$  had to be below 90%, and the total reconstructed mass of the visible system had to be above 4.5  $\text{GeV}/c^2$ . There had to be no energy in a 30° cone around the beam axis.

In the small mass region,  $\theta(\Sigma \vec{p})$  had to be above 55° in polar angle, the visible mass had to be below  $[15(\Delta M - m_{\tau}) - (M_{\tilde{\tau}} - 25)/3 - (\Delta M - m_{\tau})(M_{\tilde{\tau}} - 25)/2 + 15]$   $\text{GeV}/c^2$ , and  $\not{p}_t$  had to exceed  $\max(0.05, (\Delta M - m_{\tau})/4) p_T^{\text{lim}}$ .

In the very small mass region, it was required that  $\not{p}_t$  was above  $0.01 p_T^{\text{lim}}$ ,  $p_{max}^{\text{JET}}/p_{beam}$  was above 15%, and  $\theta(\Sigma \vec{p})$  was above 15° to the beam. The acollinearity had to be below 15°.

### 5.3 Squark searches

Supersymmetric partners of top and bottom quarks were searched for. The data collected at centre-of-mass energies from 189 to 208 GeV were analysed. The dominant decays of the stop and sbottom squarks are assumed to be  $\tilde{t}_1 \rightarrow c\tilde{\chi}_1^0$  and  $\tilde{b}_1 \rightarrow b\tilde{\chi}_1^0$ , respectively, and the final topology is two acoplanar jets and missing energy. In the non-degenerate scenario ( $\Delta M > 10 \text{ GeV}/c^2$ ), the neural network analysis has already been presented in [3]. This analysis has been extended down to  $\Delta M = 5 \text{ GeV}/c^2$ . In addition, a new analysis based on a sequential cut approach has been developed to search for stops nearly degenerate in mass with the LSP, investigating  $\Delta M$  values between 2 and  $10 \text{ GeV}/c^2$ . Moreover, this analysis has been extended to  $\Delta M$  values up to  $20 \text{ GeV}/c^2$  in order to cross-check the non-degenerate analysis.

The track selection and the general event preselection described in sections 5.1.1 and 5.1.2, respectively, were used.

#### 5.3.1 Non-degenerate scenarios

To select hadronic events, the number of charged particles reconstructed with TPC information was required to be greater than three, and the energy in the STIC to be less than 70% of the detected energy. The polar angle of the thrust axis had to be above  $20^\circ$ . The following event quality cuts were then applied. The percentage of good tracks, the ratio of the number of charged particle tracks after the particle selection to the number before, had to be greater than 35%. In addition, the scalar sum of charged particle momenta reconstructed with TPC information was required to be greater than 55% of the total energy in the event, and the total number of charged particles to be greater than six.

To remove radiative return events, the energy of the most energetic neutral particle was required to be less than 40 GeV. Additional cuts were then applied to restrict the selection to events with missing energy. The transverse missing momentum had to be greater than  $4 \text{ GeV}/c$ , the polar angle of the missing momentum had to be above  $20^\circ$  and the energy in a  $40^\circ$  cone around the z axis was required to be less than 40% of the total detected event energy. Finally, the visible mass of the events was required to be less than  $95 \text{ GeV}/c^2$ .

The number of events selected by this preselection was 2178 for  $2143 \pm 8$  expected (combined data from  $\sqrt{s} = 189$  to 208 GeV). Figure 4 shows a comparison between data and simulated events. At this level, for  $\Delta M > 10 \text{ GeV}/c^2$ , stop signal efficiencies ranged from 20% to 70% depending on the mass difference between the stop and the neutralino. Sbottom efficiencies were quite similar except at low  $\Delta M$  where, for example, the efficiency for  $M_{\tilde{b}_1} = 90 \text{ GeV}/c^2$  and  $M_{\tilde{\chi}_1^0} = 85 \text{ GeV}/c^2$  was close to zero, because the  $b$  quarks are produced almost at rest.

The final selection of events was performed using neural network techniques (see section 5.1.4). Separate searches were made for two different ranges of  $\Delta M$ :  $\Delta M > 20 \text{ GeV}/c^2$  and  $5 < \Delta M \leq 20 \text{ GeV}/c^2$ . Events were forced into two jets using the Durham algorithm. The neural network structure was as follows. There were ten input nodes (variables), ten hidden nodes (in one layer) and three output nodes. The ten input variables were: the ratio between the transverse missing momentum and the visible energy, the transverse energy, the visible mass, the softness defined as  $M_{\text{jet1}}/E_{\text{jet1}} + M_{\text{jet2}}/E_{\text{jet2}}$ , the acollinearity, the quadratic sum of the transverse momenta of the jets  $\sqrt{(P_t^{\text{jet1}})^2 + (P_t^{\text{jet2}})^2}$ , the acoplanarity, the sum of the first and third Fox-Wolfram moments, the polar angle of the missing momentum and finally the combined b-tagging event probability. For each

$\Delta M$  window a neural network with three output nodes was trained to discriminate the signal from the combined two-fermion and four-fermion backgrounds, and from the  $\gamma\gamma$  interactions leading to hadronic final states.

Although the three output nodes proved useful in training the network, the selection was made according to the output of the signal node only. Figure 5 shows the number of events as a function of the signal efficiency for the two mass analysis windows of the stop and the sbottom searches. The number of events in the data is in agreement with the SM background predictions over the full range of neural network outputs. The optimisation of the final cuts was performed by minimising the confidence level of the signal hypothesis expected in the absence of a signal. [33].

### 5.3.2 Nearly mass degenerate scenarios

Due to the large Yukawa coupling (see section 2.1), the stop ( $\tilde{t}_1$ ) and the sbottom ( $\tilde{b}_1$ ) can be light and nearly degenerate in mass with the LSP. The effective coupling of the stop to charm and neutralino results from loops and is thus small. In addition, the width of the decay  $\tilde{t} \rightarrow c\tilde{\chi}_1^0$  is proportional to  $M_{\tilde{t}}(1 - M_{\tilde{\chi}_1^0}^2/M_{\tilde{t}}^2)^2$ , and therefore proportional to  $\Delta M$ . So if  $\Delta M$  gets small enough, the stop acquires a sizable lifetime and may form a quasi-stable (decaying inside the tracking volume) or even stable stop hadron (see [34] for this case). The current analysis focusses on a stop decaying promptly into a charm particle and the LSP.

The event preselection required, in addition to the criteria described in section 5.1.2, that not more than 30% of the total visible energy was carried by particles with tracks seen in the VD and ID only. To eliminate Bhabha and leptonic  $\gamma\gamma$  backgrounds, the charged multiplicity was required to be greater than five. The  $\gamma\gamma$  background was further suppressed by requiring the energy in a forward cone of  $30^\circ$  around the beam direction to be at most 40% of the total visible energy and smaller than 2 GeV, and that no energy was deposited in the STIC calorimeter. To avoid the relatively low hadronic energy region, where the  $\gamma\gamma$  background is not well reproduced by the MC, the total transverse charged energy was required to be greater than 7 GeV, the total transverse energy of tracks reconstructed with TPC information and the total transverse momentum had to be greater than 4 GeV and 3.5 GeV/c, respectively, and the number of tracks with TPC information had to be at least four.

The agreement between data and MC after this preselection is shown in figure 6(a) to 6(d). Figure 6 also demonstrates that the two-fermion and four-fermion backgrounds dominate at this stage of the selection. The smaller contribution from two-photon interactions can be reduced at this level using for example the different polar angle distribution with respect to the signal.

A further selection was performed in order to reduce the remaining backgrounds. Events having mainly barrel activity were selected. This was achieved by requiring that the energy within a cone of  $60^\circ$  around the beam direction was less than 10 GeV and that the polar angle of the missing momentum was above  $45^\circ$ . Most of the remaining two- and four-fermion background was rejected by demanding that the transverse momentum of the most energetic particle was less than 10 GeV/c and that the total transverse energy was less than 40 GeV. Finally, the total transverse momentum was required to be greater than 5 GeV/c and the scaled acoplanarity<sup>10</sup> greater than  $20^\circ$ . This cut removed most of the remaining background from two-photon processes. The agreement between data and simulation after this selection is shown in figure 6(e,f).

<sup>10</sup>The scaled acoplanarity is the acoplanarity of the two jets multiplied by the sine of the minimum angle between a jet and the beam axis.

## 5.4 Chargino searches

### 5.4.1 Non-degenerate scenarios

The search for charginos in the non-degenerate scenarios covers the case when the mass difference  $\Delta M = M_{\tilde{\chi}_1^\pm} - M_{\tilde{\chi}_1^0}$  is above  $3 \text{ GeV}/c^2$ . In order to take all possible signatures of chargino decays into account, events were divided into four mutually exclusive topologies:

- the  $\ell\ell$  topology, with no more than five charged particles and no isolated photons;
- the  $jj\ell$  topology, with more than five charged particles, at least one isolated lepton and no isolated photons;
- the *jets* topology, with more than five charged particles and no isolated photons or leptons;
- the *rad* topology, with at least one isolated photon.

The signal events selected in a given topology are mostly events from the corresponding decay channel, but events from other channels may also contribute. For instance, for low  $\Delta M$  (and thus low visible energy) some events with hadronic decays are selected in the  $\ell\ell$  topology, and some mixed decay events with the isolated lepton unidentified enter into the *jets* topology. This migration effect tends to disappear as  $\Delta M$  increases. This effect was taken into account in the final efficiency and limit computations.

The signal events were simulated using 132 combinations of  $\tilde{\chi}_1^\pm$  and  $\tilde{\chi}_1^0$  masses for nine chargino mass values ( $M_{\tilde{\chi}_1^\pm} \approx 103, 102, 100, 98, 94, 85, 70, 50$  and  $45 \text{ GeV}/c^2$ ) and with  $\Delta M$  ranging from  $3 \text{ GeV}/c^2$  to  $80 \text{ GeV}/c^2$ . A total of 264000 chargino events (2000 per mass combination) was generated. The kinematic observables (acoplanarity<sup>11</sup>,  $E_{\text{vis}}$ ,  $\not{P}_t$ , etc.) of the signal events were studied in terms of their mean value and standard deviation, and six  $\Delta M$  regions were defined, each containing signal events with similar properties (see table 2).

In each of these 24 windows (four topologies, six  $\Delta M$  regions), a likelihood ratio function ( $\mathcal{L}_R$ , see section 5.1.4) was defined. The variables  $\{x_i\}$  used to build the  $\mathcal{L}_R$  functions in the present analysis were [4]: the visible energy ( $E_{\text{vis}}$ ), visible mass ( $M_{\text{vis}}$ ), missing transverse momentum ( $\not{P}_t$ ), polar angle of the missing momentum, number of charged particles, total number of particles, acoplanarity, acollinearity, ratio of electromagnetic energy to total detected energy, percentage of total energy within  $30^\circ$  of the beam axis, kinematic information concerning the isolated photons and leptons and the two most energetic charged particles, and finally the jet characteristics.

The generation of these 24 likelihood ratio functions was performed as follows:

- The signal distributions of all the variables  $\{x_i\}$  were built with signal events generated with parameter sets giving rise to charginos and neutralinos with masses in the corresponding  $\Delta M$  region. For each  $\Delta M$  region the events were classified according to the above topological cuts. The background distributions were built with background events passing the same topological cuts.
- Preselection cuts [35], different for each  $\Delta M$  region, were applied in order to reduce the backgrounds with largest cross-section (two-photon interactions and Bhabha events) and to generate the pdf's. The total background was reduced to 5% of the one passing the general event preselection (section 5.1.2). The pdf's were then generated as mentioned in section 5.1.4. Figure 7(8) shows the distributions of some event variables for the *jets*,  $\ell\ell$  and *rad* topologies for the 2000 data and simulation with the TPC sector 6 on (off).

<sup>11</sup>To compute the acoplanarity and acollinearity the particles were forced into two jets by the DURHAM algorithm.

- To reduce statistical fluctuations, a smoothing was performed by passing the 24 sets of pdf's for signal and background through a triangular filter [36].
- In each window all the combinations of the pdf's were tested, starting from a minimal set of four variables. Every combination defined an  $\mathcal{L}_R$  function and an  $\mathcal{L}_{R_{cut}}$ , as described in section 5.1.4, using the single channel formula [37]. The parameters entering this computation were the number of expected background events and the window efficiency of the chargino selection, defined as the mean efficiency of the chargino-neutralino mass sets belonging to the investigated window <sup>12</sup>. Figures 7(d) and 8(d) show the good agreement obtained between real and simulated events as a function of the likelihood ratio cut, for  $25 \leq \Delta M < 35 \text{ GeV}/c^2$  in the  $jj\ell$  topology.
- The combination of variables corresponding to the lowest excluded cross-section defined the  $\mathcal{L}_R$  function and the  $\mathcal{L}_{R_{cut}}$  of each window.

$\Delta M$ regions	
1	$3 \leq \Delta M < 5 \text{ GeV}/c^2$
2	$5 \leq \Delta M < 10 \text{ GeV}/c^2$
3	$10 \leq \Delta M < 25 \text{ GeV}/c^2$
4	$25 \leq \Delta M < 35 \text{ GeV}/c^2$
5	$35 \leq \Delta M < 50 \text{ GeV}/c^2$
6	$50 \text{ GeV}/c^2 \leq \Delta M$

Table 2: Definition of the  $\Delta M$  (mass difference between the chargino and lightest neutralino) regions for the chargino search in non-degenerate scenarios.

### 5.4.2 Nearly mass-degenerate scenarios

The search for charginos in the nearly mass-degenerate scenarios uses several different techniques, depending on the lifetime of the chargino, which in turn depends on the mass difference  $\Delta M$  between the chargino and the lightest neutralino (this is the only relevant dependence, at least in the heavy slepton hypothesis). When  $\Delta M$  is below the mass of the pion, the chargino lifetime is usually long enough to let it pass through the entire detector before decaying. This range of  $\Delta M$  can be covered by the search for long-lived heavy charged particles. For  $\Delta M$  of a few hundred  $\text{MeV}/c^2$  the chargino can decay inside the main tracking devices. Therefore, a search for secondary vertices or kinks can be used to cover this region. As the mass difference increases, the mean lifetime shortens until the position of the  $\tilde{\chi}_1^\pm$  decay can hardly be distinguished from the main event vertex. In this case, the tagging of an energetic ISR photon can help in exploring the  $\Delta M$  region between a few hundred  $\text{MeV}/c^2$  and  $3 \text{ GeV}/c^2$ . The selection criteria are similar to the ones used in the analysis of previous data, which have been described in [6].

#### Search for long lived charginos

Long lived charginos can either be “quasi-stable” (decay outside the tracking system) or decay “visibly” inside the tracking devices.

The search for heavy stable charged particles is described in [5]. The method used to identify heavy stable particles relied on the ionisation loss measurements in the TPC and

<sup>12</sup>The efficiency of one chargino-neutralino mass set is defined as the number of events satisfying  $\mathcal{L}_R > \mathcal{L}_{R_{cut}}$  divided by the total number of chargino events satisfying the topological cuts.

on the absence of signal in the DELPHI Cherenkov radiation detectors (RICH). Heavy stable charged particles crossing the detector would be seen in the tracking system and have as distinctive signature the absence of Cherenkov radiation and an anomalous energy loss in the TPC. Three different search windows were used in the search for heavy stable charginos:

- the charged particle had momentum above  $15 \text{ GeV}/c$ , and no photons in any of the two radiators of the RICH (liquid, refractive index  $n = 1.28$ , and gas,  $n = 1.0015$ ) were associated to the track;
- the charged particle had momentum above  $5 \text{ GeV}/c$ , high ionisation loss in the TPC, and no signal in the gas RICH;
- the charged particle had momentum above  $15 \text{ GeV}/c$ , a TPC ionisation loss not exceeding 70% of the expectation for a proton, and no signal in the gas RICH.

A fourth search window considered in [5] was not included, in order to treat the two hemispheres of the event independently.

If a heavy charged particle decays inside the central tracking devices (at a radius between 10 cm and 1 m) then both the incoming and the outgoing track can be reconstructed, and the angle between the tracks can be calculated. Such a search for kinks was originally designed to search for long-lived staus in the Gauge Mediated SUSY Breaking scenario [5]. A similar technique was applied to search for mass-degenerate charginos, with some specific features needed because the visible decay products carry very little momentum in the nearly mass-degenerate case. Details of the selection criteria can be found in [6]. Here only a brief and qualitative summary of the most important selection cuts is given.

A set of rather loose general requirements was applied in order to suppress the low energy background (beam-gas, beam-wall, etc), two-photon,  $e^+e^-$  and hadronic events. For each event passing the preselection cuts, all the charged particles were grouped in clusters according to their measured point closest to the interaction vertex. A cluster with only one track with momentum above  $20 \text{ GeV}/c$  was considered as a possible chargino candidate if it was compatible with a particle coming from the interaction point. For each single track cluster fulfilling the above conditions, a search was made for a second cluster possibly formed by the decay products of the  $\tilde{\chi}_1^+$  and defining a secondary vertex or kink with the chargino candidate.

Reconstructed secondary vertices could also be the result of particles interacting in the detector material, or having a particle trajectory reconstructed in two separate track segments. Additional requirements rejected these backgrounds in the events with an acceptable secondary vertex [5]. Finally, for an event to be accepted, at least one charged particle had to be found in each hemisphere (defined by the plane containing the beam spot and perpendicular to the line connecting the beam spot to the kink).

The search for events with tracks at large impact parameter described in [5] was not possible in this case: events with only two extremely soft charged particles with large impact parameter are difficult both to trigger on and to discriminate from machine related noise. Such events were however considered if a high  $p_t$  ISR photon was present, as explained in the next section.

### Search for charginos with ISR photons

The visible particles resulting from the decay of a chargino nearly mass-degenerate with the LSP have typically little energy and momentum. The trigger efficiency is low for such events, and there is a very large background from two-photon events. The ISR

photon tag improves detectability and, if the transverse energy of the photon is above a threshold which depends on the minimal polar angle acceptance of the experiment, it rejects most of the two-photon background.

After the preselection, which was summarised in 5.1.2, the following requirements were applied to the data and simulation samples.

- There had to be at least two and at most six good charged particles passing the quality criteria (see section 5.1.1), and no more than ten tracks in total.
- The transverse energy of the ISR photon candidate was required to be greater than  $(E_T^\gamma)^{\min} \simeq 0.03 \cdot \sqrt{s}$ .
- The mass recoiling against the photon had to be above  $2M_{\tilde{\chi}_1^\pm} - \delta M$ , where the term  $\delta M$  takes into account the energy resolution in the electromagnetic calorimeters.
- The photon had to be isolated by at least  $30^\circ$  with respect to any other charged or neutral particle in the event.
- The sum of the energies of the particles with polar angles within  $30^\circ$  of the beam axis ( $E_{30}$ ) was required to be less than 25% of the total visible energy. If the photon itself was below  $30^\circ$ , it was the ratio  $(E_{30} - E_\gamma)/(E_{\text{vis}} - E_\gamma)$  that was required to be below 0.25.
- If the ISR photon candidate was detected in the very forward calorimeter STIC, it must not be correlated with a signal in the scintillators placed in front of the STIC.
- $(E_{\text{vis}} - E_\gamma)/\sqrt{s}$  had to be below a kinematic threshold which depended on  $\Delta M$  and on  $M_{\tilde{\chi}_1^\pm}$  (and in any case below 6%).
- The ratio of the absolute value of the missing transverse momentum over the total transverse energy had to be above  $0.40/c$  if  $\Delta M > 300 \text{ MeV}/c^2$ , and above  $0.75/c$  for smaller  $\Delta M$ .
- If  $\Delta M > 1 \text{ GeV}/c^2$ , at least two charged particles in the event had to be consistent with coming from the beam interaction region.

Distributions of some of the variables used in the final selection are shown in figure 9 for data, simulated SM background, and simulated signal events. Although there is a certain overall qualitative agreement of the various distributions, there is already an excess of data. On the other hand, the two-photon generators used in the simulation lack the events which have small  $\gamma\gamma$  invariant mass, and in some cases (namely,  $\gamma\gamma \rightarrow e^+e^-$ ) no ISR generation is implemented at all. Moreover, background processes such as beam-gas interactions are not included in the simulation. As in previous publications [6], the most likely explanation of such disagreement is therefore a deficit of simulated background events rather than an excess of data from possible new physics. As no attempt will be made in the following to account for the backgrounds missing in the simulation, the limits that will be obtained are conservative.

## 5.5 Neutralino searches

The neutralino searches were designed to cover both  $\tilde{\chi}_k^0 \tilde{\chi}_1^0$  production with  $\tilde{\chi}_k^0 \rightarrow \tilde{\chi}_1^0 + f\bar{f}$ , with a signature of acoplanar jets or leptons, and channels of the type  $\tilde{\chi}_k^0 \tilde{\chi}_j^0$  with  $k$  or  $j > 2$ , which can lead to neutralino cascade decays. To maximise the sensitivity several searches were used, covering different topologies, namely:

- a search for acoplanar jet events, as from  $\tilde{\chi}_1^0 \tilde{\chi}_2^0$  with  $\tilde{\chi}_2^0 \rightarrow \tilde{\chi}_1^0 q \bar{q}$ ;
- a search for acoplanar lepton events, as from  $\tilde{\chi}_1^0 \tilde{\chi}_2^0$  with  $\tilde{\chi}_2^0 \rightarrow \tilde{\chi}_1^0 e^+e^-$  or  $\tilde{\chi}_2^0 \rightarrow \tilde{\chi}_1^0 \mu^+\mu^-$ ;

- a search for multijet events, as from  $\tilde{\chi}_i^0 \tilde{\chi}_j^0, i = 1, 2, j = 3, 4$  with  $\tilde{\chi}_j^0 \rightarrow \tilde{\chi}_2^0 q \bar{q}$  and  $\tilde{\chi}_2^0$  decaying to  $\tilde{\chi}_1^0 q \bar{q}$  or  $\tilde{\chi}_1^0 \gamma$ ;
- a search for multilepton events for the corresponding decays to lepton pairs;
- a search for cascade decays with tau leptons, e.g.  $\tilde{\chi}_2^0 \tilde{\chi}_1^0$  production with  $\tilde{\chi}_2^0 \rightarrow \tilde{\tau} \tau$  and  $\tilde{\tau} \rightarrow \tilde{\chi}_1^0 \tau$ ;
- a search for double cascade decays with tau leptons, e.g.  $\tilde{\chi}_2^0 \tilde{\chi}_2^0$  production with the same  $\tilde{\chi}_2^0$  decay chain as above.

The different searches, briefly described below, were designed to be mutually exclusive in order to allow easy combination of the results. Thus events selected in the likelihood-based searches for acoplanar leptons or jets of section 5.5.1 were explicitly rejected in the searches described in the subsequent sections. The track selection and the general event preselection described in sections 5.1.1 and 5.1.2, respectively, were used. The LUCLUS algorithm with  $d_{\text{join}} = 10$  GeV/ $c$  was used for jet clustering in the analyses described below, with the exceptions of the likelihood ratio acoplanar jets/leptons and double tau cascade searches, as explicitly mentioned in the corresponding sections (see section 5.1.3 for details on the jet clustering algorithms).

Data collected at centre-of-mass energies between 192 and 208 GeV were analysed, and were combined with previous results [7]. In the search for staus in  $\tilde{\chi}_2^0 \tilde{\chi}_2^0$  production, all data recorded at centre-of-mass energies between 189 and 208 GeV were analysed.

### 5.5.1 Acoplanar jets and acoplanar leptons searches

As mentioned above, the acoplanar jets and acoplanar leptons topologies are dominant in most of the parameter space. For these cases, a search based on the likelihood ratio method was performed and the sequential cut analyses described in [7] were used as a cross-check.

The characteristics of the neutralino decays are mainly determined by the value of  $\Delta M$ , here defined as the mass difference between the heavier of the produced neutralinos and the LSP ( $\tilde{\chi}_1^0$ ). The total energy of the visible final state particles,  $E_{\text{vis}}$ , was used to distinguish between regions of different signal and background characteristics in the optimisation of the selections.

#### Likelihood Ratio analysis

The first step of the analysis was to preselect the events dividing them into three mutually exclusive topologies: ee,  $\mu\mu$ , and  $q\bar{q}$ . The ee and  $\mu\mu$  topologies were defined as having exactly two isolated lepton candidates (see section 5.1.3). In the ee topology, at least one of these had to be a tightly identified electron, and neither identified as a muon. Similarly, the events in the  $\mu\mu$  topology were required to contain at least one isolated loose muon candidate and no isolated electron. The  $q\bar{q}$  topology was defined as events with more than five charged particles and no isolated photons or leptons.

In the second step, aimed at removing the dominant SM background processes, events which fulfilled all of the following criteria were selected:

- the polar angles of the most energetic neutral and charged particles were required to be above  $10^\circ$ ;
- the missing transverse momentum had to exceed  $2$  GeV/ $c$ , or  $4$  GeV/ $c$  if the visible energy was less than  $30$  GeV;
- both the acoplanarity and acollinearity had to be greater than  $3^\circ$ ;
- the total visible energy had to be lower than  $0.75\sqrt{s}$ .

The first two requirements remove the bulk of the  $\gamma\gamma$  events and off-momentum beam electrons. The third and fourth reject two-fermion processes. The last requirement removes mainly four-fermion events.

In the  $q\bar{q}$  topology an additional selection was applied to suppress further the large  $q\bar{q}(\gamma)$  background. This was based on the jets reconstructed using the Durham algorithm and forcing the number of jets to two. If the invariant mass of the event was within  $40 \text{ GeV}/c^2$  of the  $Z$  mass, the acoplanarity of the two jets was required to be at least  $10^\circ$ .

For different values of visible energy  $E_{\text{vis}}$  (typical of different values of  $\Delta M$ ), the kinematic properties of the signal were studied in terms of the mean value and standard deviation of several event variables. Five  $E_{\text{vis}}$  regions were defined, each containing signal events with similar properties and SM background composition. These regions are given in table 3, together with the corresponding dominant SM background.

$E_{\text{vis}}$ regions		Main SM bkg.
1	$5 \leq E_{\text{vis}} < 20 \text{ GeV}/c^2$	$\gamma\gamma$
2	$20 \leq E_{\text{vis}} < 50 \text{ GeV}/c^2$	$\gamma\gamma$ , 2-fermions
3	$50 \leq E_{\text{vis}} < 70 \text{ GeV}/c^2$	2-fermions
4	$70 \leq E_{\text{vis}} < 110 \text{ GeV}/c^2$	2- and 4-fermions
5	$110 \text{ GeV}/c^2 \leq E_{\text{vis}}$	4-fermions

Table 3: Definition of the visible energy regions of the neutralino search in the acoplanar leptons and jets topologies and corresponding dominant SM backgrounds.

In the last step of the analysis, for each of the 15 windows (three topologies, five  $E_{\text{vis}}$  regions) thus defined, a likelihood ratio function was computed. The variables used in the likelihood definition are listed below:

- global variables (all topologies): visible energy, transverse energy, missing momentum, energy and direction of the most energetic charged and neutral particles, transverse momentum with respect to the thrust axis, polar angle of the missing momentum, thrust value, thrust direction and acoplanarity;
- variables specific to the  $q\bar{q}$  topology: jet directions, energies, widths, invariant mass and  $y_{\text{cut}}$  value;
- variable specific to the ee and  $\mu\mu$  topologies, namely the invariant mass of the two charged particles.

For each variable used in the likelihood ratio function, the one-dimensional probability density function was defined according to the procedure described in sections 5.1.4 and 5.4.1, and events with  $\mathcal{L}_R > \mathcal{L}_{R\text{cut}}$  were selected as candidate signal events.

Some event variable distributions for real and simulated data before the likelihood selection are shown in figure 10. A fair agreement between data and the SM expectation is found. A low visible energy event is present in the ee topology (see figure 10(d)), in a region where low but non-zero background was expected from the SM (about 0.5 events with visible energy below 30 GeV expected from four-fermion processes). No significant disagreement between data and MC is found in any of the topologies.

### Sequential analysis

The detailed selection criteria for the selection based on sequential cuts are given in reference [7] and have not been changed. This analysis was used as a cross-check of the likelihood ratio results. At the final selection level, criteria optimised for different  $\Delta M$

regions were designed. They were used as independent selections in the derivation of the results.

### 5.5.2 Multijet search

The multijet search was optimised for cascade decays of neutralinos with large mass splittings, giving high energy jets. Events with energetic photons, characteristic of the decay  $\tilde{\chi}_2^0 \rightarrow \tilde{\chi}_1^0 \gamma$ , were treated separately. Events with a photon signature were selected on the basis of reconstructed photons with a polar angle above  $20^\circ$ , isolated by more than  $20^\circ$  from the nearest charged particle. If there was only one such photon its energy was required to be between 10 GeV and 40 GeV; if more than one photon was present, at least two had to have energy greater than 10 GeV.

This selection was similar to the acoplanar jet selection of the sequential analysis, but required a rather large transverse energy and allowed any number of reconstructed jets. Events selected by the searches for acoplanar leptons or acoplanar jets were explicitly rejected.

The detailed selection criteria are similar to the ones described in [7]. Background studies based on data of 1998 and an improved energy-flow reconstruction motivated several changes in the selection procedure. Three selection stages (preselection, intermediate selection and final selection) are defined and used in the figures and tables. In the following, the most important steps of this search are summarised.

At preselection level, at least five charged particles (passing the track selection described in section 5.1.1) were required, at least one of them with a transverse momentum exceeding  $2.5 \text{ GeV}/c$ . The transverse energy of the event had to be greater than 25 GeV, the visible energy was required to be less than  $0.65\sqrt{s}$ , and the missing momentum had to be less than  $0.4\sqrt{s}/c$ . There were several requirements aimed at selecting events with jets which were not dominated by single particles with large reconstructed energy. Figures 11(a,b) and 12(a,b) show the distributions of the visible mass divided by the centre-of-mass energy for real data and simulated background events passing the above selection.

At the intermediate selection level, radiative return to the Z, two-photon, and Bhabha background was reduced by excluding events with a neutral particle whose energy exceeded 60 GeV or with more than 40% of the visible energy within  $30^\circ$  of the beam direction. Also, the transverse momentum had to exceed  $6 \text{ GeV}/c$ . The total momentum and the most energetic shower in the event were both required not to be close to the beam direction. A comparison of the  $cpt/\sqrt{s}$  distributions for real data and simulated background following the above selection is shown in figures 11(c,d) and 12(c,d). The excess in data visible in 11(c) and 12(c) was found to be consistent with (low acoplanarity) radiative return to the Z events with misreconstructed missing momentum. In 12(c) the excess is larger. The reason for this is that in the year 2000 the missing momentum reconstruction suffered from the problems with sector 6 of the TPC and from the fact that the distortions in the TPC data had not yet been fully corrected for at the time of this analysis. The phase space region in question was removed by criteria imposed later in the selection, and the excess has no impact on the analysis results.

At the final level of the selection the acollinearity and scaled acoplanarity (in a forced 2-jet configuration) had to be greater than  $30^\circ$  and  $10^\circ$ , respectively. To reject  $W^+W^-$  background it was required that there be no charged particle with a momentum above  $30 \text{ GeV}/c$ , and no isolated lepton above  $10 \text{ GeV}/c$  or above  $4 \text{ GeV}/c$  with an isolation angle greater than  $20^\circ$ .

For events with a photon signature, the mass recoiling against the visible system was required to exceed 20% of the centre-of-mass energy and the scalar sum of momenta reconstructed with TPC information had to be less than 60% of the visible energy.

For the complementary sample, without a photon signature, several of the criteria above were made stricter in order to reject  $Z\gamma$  events. The recoil mass was required to exceed 40% of  $\sqrt{s}$  and the energy deposited in electromagnetic calorimeters had to be less than 40 GeV. No isolated neutrals with energy greater than 20 GeV were allowed and the average momentum of particles with tracks reconstructed in the TPC had to be less than 4  $\text{GeV}/c$ .

Figures 11(e,f) and 12(e,f) show the distribution of the scaled acoplanarity for real and simulated data after final selections, while figures 12(g,h) show  $cpt/\sqrt{s}$  for data with TPC sector 6 on. A satisfactory agreement between data and SM simulation is found. Four events are observed while three were expected from SM simulation.

### 5.5.3 Multilepton search

The multilepton search is sensitive to cascade decays involving leptons, which can dominate if there are light sleptons. This search was described in [7] and is briefly summarised here.

At the preselection level, well reconstructed low multiplicity events with missing energy and missing mass were selected. In particular, the total visible energy including badly reconstructed tracks (not passing the track selection described in section 5.1.1) was required to be less than 140 GeV, the number of charged particles was required to be at least two and at most eight, and events with more than four neutral particles were rejected. Figures 13(a) and 14(a) show a comparison between the visible mass divided by the centre-of-mass energy for real and simulated events passing the preselection.

The selection at the intermediate level served mainly to reject  $Z\gamma$ , two-photon, and Bhabha events by requiring significant transverse momentum and transverse energy ( $p_T > 8 \text{ GeV}/c$ ,  $E_{\text{vis}}^T > 25 \text{ GeV}$ ). The distributions of  $cpt/\sqrt{s}$  for real and simulated data, following the intermediate selection are compared in figures 13(c) and 14(c).

At the final selection level events with two or more charged particles were subjected to criteria designed to reject Bhabha events. In addition, the charge asymmetry for the two most energetic such particles was used to reject  $W$  pairs decaying leptonically. Events with four or more tracks were clustered into jets, and those with exactly two jets were rejected if their scaled acoplanarity was less than 15°. Figures 13(e) and 14(e) show the acoplanarity distribution for real and simulated data at this level.

### 5.5.4 Asymmetric tau cascade search

The tau cascade search is sensitive to  $\tilde{\chi}_1^0 \tilde{\chi}_2^0$  production with  $\tilde{\chi}_2^0 \rightarrow \tilde{\tau} \tau$  and  $\tilde{\tau} \rightarrow \tilde{\chi}_1^0 \tau$ , where the second  $\tau$  produced has very low energy. This search was described in [7] and is briefly summarised here.

At the preselection level, well reconstructed low multiplicity events with missing energy and missing mass were selected. The selection was the same as for the multilepton search (section 5.5.3), with the additional requirement of no more than two reconstructed jets. At least two of the charged particles had also to satisfy stricter criteria on reconstruction and impact parameters. The distributions of the visible mass divided by the centre-of-mass energy for real and simulated data at this level are shown in figures 13(b) and 14(b).

At the intermediate selection level, the highest and second highest momenta of charged particles were required to be below  $40 \text{ GeV}/c$  and  $25 \text{ GeV}/c$ , respectively, and at least one charged particle had to have a transverse momentum above  $2.5 \text{ GeV}/c$ . The criteria to reject  $Z\gamma$ , two-photon, and Bhabha events were similar to those used in the multilepton search, except for the removal of the requirement on the transverse energy. Figures 13(d) and 14(d) show the distributions of  $cp_T/\sqrt{s}$  for real and simulated data at the intermediate selection level.

At the final selection level, events with two or more isolated charged particles were required to have acollinearity and acoplanarity above  $60^\circ$ . The smaller of the two momenta had to be below 70% of the greater one, and below  $10 \text{ GeV}/c$ . For events with two reconstructed jets the scaled acoplanarity was required to be greater than  $20^\circ$ , and the acoplanarity and the acollinearity greater than  $60^\circ$ . The acoplanarity distributions for the resulting samples of real and simulated data events are shown in figures 13(f) and 14(f).

### 5.5.5 Double tau cascade search

The final state of  $\tilde{\chi}_2^0 \tilde{\chi}_2^0 \rightarrow \tilde{\tau}\tau\tilde{\tau}\tau$  differs from that of stau pair-production only in the presence of two soft taus from the stau decays. The search criteria for stau pairs (see section 5.2.3) could therefore be applied with slight modifications, as follows. Instead of exactly two  $\tau$ -candidates, at least three were required, but the momentum of the third most energetic one had to be less than 4% of the beam momentum. The maximum number of tracks in the event was increased from seven to eight, and, as the  $W^+W^-$  background is negligible, the requirement on  $p_{high}^{\text{JET}}$  versus  $\theta_{W^+}$  was removed. Since the only SM processes yielding final states with four taus are  $ZZ$ ,  $ZZ^*$  or  $Z\gamma^*$ , the invariant mass of the two most energetic  $\tau$ -candidates was required to be below  $40 \text{ GeV}/c^2$ , *i.e.* well below  $m_Z$ . Variables specific to the two-jet topology, *e.g.* acoplanarity, were evaluated using the two most energetic  $\tau$  candidates only, and the remaining requirements of the stau pair search were left unchanged. In the cases where these requirements differed for high and low  $\Delta M$ , the less stringent selection was applied here.

## 6 Results and limits

In this section the results of the event selections and the estimated signal efficiencies are presented for each channel. No evidence of a significant excess with respect to the SM expectation was found in any of the channels, and limits on masses and cross-sections were set. In a relatively model-independent approach, cross-section upper limits are derived. Lower limits on the sparticle masses are also obtained, under assumptions which depend on the channel and will be specified case by case. All limits quoted are at 95% confidence level (CL).

### 6.1 Limit computation

Depending on the searches, limits were derived using the multichannel Bayesian method [38] or the modified frequentist likelihood ratio method [33]. Both these approaches allow search results in multiple channels to be combined, taking into account efficiency, expected background, number of candidates and centre-of-mass energy in each channel.

In the Bayesian multichannel approach [38], the a posteriori probability density of the mean total number of signal events (assuming a uniform prior) is used to compute a 95% CL upper limit and compare it to the mean predicted for different signal assumptions. In the likelihood ratio approach, global multi-channel likelihood functions for the signal plus background and background-only hypotheses are evaluated for the experimental outcome [33]. One then defines the confidence level in the signal plus background hypothesis as the probability, under this hypothesis, to obtain a lower likelihood ratio than experimentally observed. In the modified frequentist approach used here this confidence level is renormalised by the probability to obtain a value below the observed one in the absence of a signal. All points where the resulting confidence in the signal,  $CL_s$ , is less than 5% are considered excluded. More details are given below channel by channel.

The two methods typically give similar results. Both methods take a posteriori knowledge about the background into account, and thus give physically reasonable and conservative results in the case of downward fluctuations of the background. Background fluctuations could nevertheless significantly affect the range of exclusion, and for this reason limits expected in the absence of a signal are also given below.

## 6.2 Systematic uncertainties

The excluded cross-section and mass ranges can be affected by the systematic uncertainties related to the SM background rate and signal efficiency determinations. These are mainly due to imperfections in:

- the description of the differential cross-sections;
- the modelling of fragmentation and hard gluon radiation;
- the modelling of the detector response.

The inaccuracy of the differential cross-section description for the various SM processes was studied extensively in the context of their measurement at LEP and is typically small, except for the hadronic  $\gamma\gamma$  background. Modelling of fragmentation and hard gluon radiation was studied both in the context of background and efficiency. It mainly affects the searches for the stop quark, due to the uncertainties in the modelling of the stop fragmentation. However, the largest contribution to the systematics on both background rate and efficiency determination arises from the modelling of the detector response. This was addressed in several ways, depending on the type of the final state searched for. Below, a review of all of these systematic effects is given. The methods used to address them are then discussed. Finally, the methods used to propagate those uncertainties in the limit computation are briefly presented.

### 6.2.1 Review of the main systematic sources

#### Description of the differential cross-sections:

The uncertainty on the differential cross-sections within the acceptance region of the most important SM processes is [25,39] less than 1% for  $W^+W^-$  production, around 0.5% for  $Z\gamma$ , 2% for  $ZZ$  and about 5%<sup>13</sup> for  $We\nu_e$  and  $Ze^+e^-$ . The uncertainty of the description of the  $Z\gamma^*$  process is typically 5%, reaching 20% in the region of very small masses of  $\gamma^*$ . While the uncertainties are small for two-photon interactions giving leptons (less than 5%), the description of the hadronic  $\gamma\gamma$  processes is subject to large uncertainties in some regions of the phase space. The effect was studied comparing various

<sup>13</sup>This number is valid in the phase-space regions where these processes are not  $\gamma\gamma$ -like.

two-photon generators [39]. In the squark analysis (see section 5.3) at the preselection level PYTHIA [15] results were cross-checked with TWOGAM [21] and differences up to 15% were observed, with PYTHIA giving a higher background. It has been shown [40] that the PYTHIA generator represents a more correct background estimation. A systematic uncertainty of 15% on the hadronic  $\gamma\gamma$  background was assumed. The impact of these uncertainties on the final background rate determination will depend on the importance of the two-photon background in the different cases. In most of the analyses presented in this paper the contribution of the hadronic  $\gamma\gamma$  process at the final selection level is negligible. The search for multi-jet final states without isolated photons from heavier neutralino decays (see section 5.5) may serve as an example. In this case, 40% of the background originates from the  $W^+W^-$  process, 40% from  $W\bar{e}\nu_e$  and  $ZZ$  processes, and 15% from  $Z\gamma$ . If the presence of photon(s) is required, 80% of the background originates from the  $Z\gamma$  process. In summary, the net uncertainties arising from the description of the above processes are of the order of a few percent at most.

#### Fragmentation and hard gluon radiation modelling:

The description of hard gluon radiation leads to uncertainties of at most 10% in the relevant parameter space, in particular for the rate of b-tagged four-jet events from the  $Z\gamma$  process. This is unimportant for most of analyses presented here. Fragmentation uncertainty related effects are typically of the order of 1%. However in the searches for the stop (see section 5.3), the stop hadronisation scheme is important and a dedicated generator was used for these studies. The stop hadronisation was performed non-perturbatively and the  $\epsilon$  parameter of the Peterson function, which regulates the stop fragmentation and hadronisation, was varied. The analysis was applied to the different signal samples thus obtained and the results were compared. The relative systematic error on the efficiency as a consequence of imperfect signal simulation was taken to be 7% for  $\Delta M > 10 \text{ GeV}/c^2$  and 10% for  $\Delta M \leq 10 \text{ GeV}/c^2$ . For the sbottom analysis, 7% was used for all  $\Delta M$ .

#### Modelling of the detector response:

The modelling of the detector response is the main source of systematics in the searches for new particles. The next section gives a review of the methods which were developed to address primarily the influence of this uncertainty on the SM background rate and efficiency determinations.

### 6.2.2 Methods to evaluate detector response systematics

#### The “re-weighting” method

This method estimates the systematic error on the number of selected background events from imperfect simulation of the detector response, as well as from possible large uncertainties in the modelling of the differential cross-section for two-photon processes. It propagates the difference between the data and the simulated background at preselection level to the final selection level for the variables relevant for the analysis.

The propagation is performed as follows. Each discriminating variable used in the event selection is histogrammed both for data and simulated background events at the preselection and final selection levels. From the preselection histograms a weight factor,  $N_{\text{Data}}/N_{\text{Back}}$ , is calculated for each bin containing at least 1 % of the total number of background events and a non-zero number of data events. For bins with zero data events,

it was checked that the SM expectation was in agreement with such an observation. These weight factors are then applied, bin by bin, to the background histograms at the final selection level. The contribution to the systematic error of each variable is then determined by subtracting the total number of selected background events from the total number of re-weighted background events at the final selection level.

The total positive (negative) systematic error of the number of background events is then computed as a quadratic sum over positive (negative) error contributions from the different variables:

$$\delta^\pm = \sqrt{\sum_{N_{\text{Back}}^{\text{RW}}(i) \gtrless N_{\text{Back}}} (N_{\text{Back}}^{\text{RW}}(i) - N_{\text{Back}})^2}$$

where  $N_{\text{Back}}^{\text{RW}}(i)$  is the total number of re-weighted background events from variable  $i$  and  $N_{\text{Back}}$  is the number of selected background events without re-weighting.

In this method the correlations between different variables are not taken into account, but, as the quadratic sum is performed over all error contributions, the total systematic error is overestimated. It was checked by the means of the Kolmogorov test that rescaling the distribution of any of the variables improves the agreement between the data and SM background for the other variables as well. Moreover, the statistical fluctuation in the bins of the histograms used to calculate the weight factors lead to an additional overestimation of the error. Another drawback of this method is that the total systematic error obtained grows with the number of studied variables.

The main advantages of this method are its simplicity and conservative error estimation. Because of its conservative nature, it was used in searches where the expected background is small, and background fluctuations have bigger effect on the expected limit than the systematic error. For example, in the squark analysis the systematic error on the background estimated with this method was 15-60 % (see section 6.5.1). This had only a small effect on the final mass/cross-section limits.

### The “shaking” method

The “shaking” method [41] attempts to correct at particle level the simulation description of the detector response and residual effects in the fragmentation. Changes in the particle multiplicity (by adding or removing particles) are made in the simulation, in such a way that the multiplicities of neutral and charged particles in bins of momentum and polar angle are well described for the hadronic data collected at the  $Z$  peak. The momentum and the polar angle of the added particles are randomly changed with respect to the parent particle, while staying in the same phase space region.

The method was tested in the study of the systematics of the  $ZZ$  cross-section measurement [41]. The multiplicity adjustment is of the order of 1%-2%. It leads to a better agreement between the data taken at energies above the  $Z$  peak and the SM background, typically predicting slightly higher observed missing energy and momentum.

The method can be used to study the uncertainty on the background and efficiency in hadronic high multiplicity topologies, with or without isolated leptons (or photons). In these topologies, the method gives an estimation of the systematic uncertainty including both the effect of “shaking” the variables and the consequences of additional reconstructed tracks which lie inside the cone for the isolated lepton or photon.

This method was used to study the systematic error of background and efficiency in hadronic neutralino topologies, and the systematic error on the chargino (non-degenerate

scenario) detection efficiency in the hadronic, semileptonic and radiative topologies. Tables 4 and 5 show, for chargino and neutralino searches respectively (sections 6.6.1 and 6.7), the relative difference between the efficiencies obtained with and without “shaking”. The values in table 4 correspond to high multiplicity hadronic and semi-leptonic final states and are averaged over several points with model parameters corresponding to the specific  $\Delta M$  region (see section 5.4.1 for the  $\Delta M$  region definition). The values shown in table 5 correspond to the different high multiplicity topologies in the neutralino search and they are averaged over the interesting range of masses.

$\Delta M$	1	2	3	4	5	6
<i>jets</i>	6.8 %	8.8 %	3.1 %	0.5 %	1.0 %	3.4 %
<i>jj<math>\ell</math></i>	12.9 %	4.1 %	0.5 %	0.4 %	0.0 %	0.9 %

Table 4: The relative difference in the chargino detection efficiency obtained with and without “shaking” in the year 2000 simulation with the detector fully operational. The values shown correspond to the different  $\Delta M$  regions of the hadronic (*jets*) and semi-leptonic (*jj $\ell$* ) topologies in the chargino production (see section 6.6.1).

topology	efficiency change
multijets without $\gamma$	2.9 %
multijets with $\gamma$	1.3 %
acoplanar jets	1.3 %

Table 5: The relative difference in the neutralino detection efficiency obtained with and without “shaking” in the year 2000 simulation with the detector fully operational. The values shown correspond to the different high multiplicity topologies in the neutralino production (see section 6.7) and they are averaged over the interesting range of masses.

Except for the lowest  $\Delta M$  regions in the chargino analysis, where systematic uncertainties due to tracking and neutral energy reconstruction have the largest effect, the variation in the detection efficiency is very small. The efficiencies for the “shaken” signal are typically larger than for the “unshaken” signal.

In hadronic neutralino topologies, the background estimated with the shaking method was typically 10% higher than the “unshaken” background. The variation of both background and efficiency is consistent with “shaking” predicting slightly higher observed missing energy.

#### Methods dedicated to low multiplicity topologies (“smearing” technique)

The uncertainty on the efficiency of the muon, electron and photon identifications is expected to be a dominant effect in the low multiplicity topologies requiring identified particles. Studies on back-to-back di-muon events and back-to-back di-electron events and photons from radiative return to the  $Z$  peak point to background errors and relative efficiency errors of the order of 3% each. The uncertainty on the track momentum reconstruction arising from the modelling of the detector response was also studied and a small effect was found, both on efficiency and background estimates. These estimates are relevant for neutralino and chargino leptonic topologies, and for all slepton searches.

### 6.2.3 Methods to propagate statistical and systematic uncertainties in the mass/cross-section limits

Systematic and statistical uncertainties on the parameters involved in the calculation of the limits (mainly, the uncertainties related to the SM background rate and signal efficiency determinations) were propagated into the final results using two methods. The analyses that rely on the modified likelihood ratio method adopted the procedure explained in [33]. For the analyses that use the multichannel method of [38], a different procedure based on the same Bayesian approach was chosen [42]. A probability distribution function (pdf) was assumed for the efficiency and the background for every signal channel. Such a pdf was assumed to be either gaussian or binomial, depending on the statistical accuracy of the estimations of the signal or background, and on the methods used to evaluate the uncertainty of the parameter.

The effect of including systematics in the computation of the limits can become relevant whenever there are large (order of 10% or more) relative errors on the efficiency and, in particular, on the expected background. The degradation of the limits is much less significant, however, than would be indicated by the simplistic and over-conservative approach of reducing all efficiencies and increasing all backgrounds by one standard deviation.

## 6.3 LEP1 limits

In this section limits on the masses of SUSY particles from LEP1 data [43] are briefly reviewed. In most cases the LEP1 limits have been superseded by LEP2 results, such as those presented in the present paper. However, for certain situations they are still relevant. This is particularly true for limits deriving from comparisons of the measured  $Z$  decay widths to SM expectations. Such limits are relatively insensitive to the details of the decays of SUSY particles, although they depend on the coupling of the sparticles to the  $Z$  (which is affected by the sparticle field composition).

From 1990 to 1995 LEP was run at centre-of-mass energies near the  $Z$  resonance. Model independent fits to all the lineshape and asymmetry data have been carried out, giving accurate values of the resonance parameters [44]. The total decay width of the  $Z$  boson was measured with a precision of about  $2.5 \text{ MeV}/c^2$ . Decay channels of the  $Z$  opened by new physics would increase the  $Z$  width. Thus the difference between the measured width and the SM value may be used to constrain SUSY models. If the new particles decay invisibly, limits can be derived in a straightforward manner from the comparison of the measured invisible width to the SM prediction. The combined LEP result gives  $\Gamma_{\text{inv}}^{\text{new}} < 2.0 \text{ MeV}/c^2$  at 95% confidence level [45]. Whether the new particles are visible or invisible, they will contribute to the measured values of the total width  $\Gamma_Z$ . Confronting the measured  $Z$  width with the SM expectation an upper limit on the extra partial width  $\Gamma^{\text{new}} < 3.2 \text{ MeV}/c^2$  was obtained [45]<sup>14</sup>.

From the limit on  $\Gamma_{\text{inv}}^{\text{new}}$ , a limit on the sneutrino mass of  $43.7 \text{ GeV}/c^2$  may be obtained [45]. A lower mass limit for the lightest chargino of approximately  $45 \text{ GeV}/c^2$ , independent of the field composition and of the decay modes, has been derived from the analysis of the  $Z$  width and decays. Limits for other sparticles depend both on masses and couplings. To a large extent left-handed sleptons below  $40 \text{ GeV}/c^2$  can also be excluded using the agreement of the  $Z$  decay width with the SM prediction [45].

The composition of the neutralinos affects their production cross-sections and the light states may decouple from the  $Z$ . The production then proceeds through  $t$ -channel

<sup>14</sup>In [46] a method designed to be more model-independent gives  $\Gamma^{\text{new}} < 6.3 \text{ MeV}/c^2$  using older data.

selectron exchange, giving a small cross-section if the selectrons are heavy. Hence no general limit on the LSP mass can be derived from LEP1.

For the third family, the production rates may be affected by potential large mixing of the weak eigenstates. For the stau mixing angle giving the minimal cross-section, the coupling to the  $Z$  vanishes and no exclusion is possible using this method<sup>15</sup>. Also for squarks, the LEP1 limits depend on the mixing angle. Left squarks below  $45 \text{ GeV}/c^2$  are excluded by the  $Z$  invisible width if they are nearly mass-degenerate with the LSP, decaying invisibly. If the decay is visible, the limit from the total width should be applied instead. Squarks with non-zero mixing cannot be excluded by this method, as the coupling to the  $Z$  varies and can vanish<sup>16</sup>.

Direct searches at LEP1 set mass limits above  $40 \text{ GeV}/c^2$  for sfermions in the case of a decay into a fermion and a neutralino, with  $\Delta M > 5 \text{ GeV}/c^2$  and provided the production cross-section is not suppressed due to  $t$ -channel contributions (in the case of selectrons) or to  $Z$  decoupling (in the case of third family sleptons and squarks).

## 6.4 Slepton searches

### 6.4.1 Smuon and selectron searches

#### Efficiencies and selected events

The efficiency for signal detection depends on the masses of the slepton and neutralino. The cuts used to reject the backgrounds resulted in typical signal efficiencies of 50% both for the selectron and the smuon channels.

The number of events selected at each energy in the data, together with the estimate of the background, is shown in tables 6 and 7 for the selectron and smuon analyses. It can be seen that the principal background arises from leptonic decays of  $W$  pairs.

The effect of systematic uncertainties on background and efficiency evaluation was studied with the “smearing” method (see section 6.2). The variations both in the detection efficiency and in the background were found to be of the order of 3% on average.

year	Selectrons			Smuons		
	1998	1999	2000	1998	1999	2000
2-fermion events	5.6	8.4	4.2	2.1	2.2	1.4
4-fermion events	29.7	40.9	34.4	18.8	25.5	20.8
$\gamma\gamma$ events	1.7	2.5	2.2	0.5	0.6	1.6
Total	37.0	51.8	40.8	21.4	28.3	23.8
Data	40	52	49	19	23	28

Table 6: Selectron and smuon candidates in the different data sets, together with the number of background events expected. The systematic uncertainties on the background were estimated to be of the order of 3% (see section 6.2).

#### Limits

<sup>15</sup>Selectron mass limits of the order of  $50 \text{ GeV}/c^2$  have been derived from single photon searches at early colliders, for a nearly massless photino LSP [47].

<sup>16</sup>A sufficiently light stop would contribute through loop corrections to the partial width  $\Gamma_{bb}$ .

$\sqrt{s}$ (GeV)	Selectron search					
	Preselection		Intermediate		Final	
	Data	MC	Data	MC	Data	MC
189	29460	$28558 \pm 7$	1925	$1937.0 \pm 2.1$	40	$37.0 \pm 0.4$
192	4797	$4649 \pm 7$	315	$319.7 \pm 2.1$	6	$7.0 \pm 0.4$
196	13705	$14046 \pm 9$	812	$847.2 \pm 2.8$	21	$17.8 \pm 0.6$
200	14709	$14653 \pm 8$	993	$1001.0 \pm 2.5$	14	$18.5 \pm 0.6$
202	7125	$7154 \pm 4$	474	$491.5 \pm 1.4$	11	$8.6 \pm 0.3$
205	13229	$12687 \pm 15$	832	$774.8 \pm 4.7$	22	$14.7 \pm 0.3$
207	12735	$13315 \pm 6$	810	$813.2 \pm 2.0$	13	$15.4 \pm 0.4$
208	1202	$1231 \pm 1$	78	$75.2 \pm 0.2$	3	$1.4 \pm 0.04$
206.5(*)	8963	$9655 \pm 6$	524	$495.6 \pm 1.8$	11	$9.4 \pm 0.5$
All	105295	$105948 \pm 23$	6763	$6755.2 \pm 7$	141	$129.8 \pm 1.3$
$\sqrt{s}$ (GeV)	Smuon search					
	Preselection		Intermediate		Final	
	Data	MC	Data	MC	Data	MC
189	18759	$18591 \pm 7$	5378	$5501.2 \pm 2.1$	19	$21.4 \pm 0.4$
192	2985	$3058 \pm 7$	854	$860.2 \pm 2.1$	3	$3.4 \pm 0.4$
196	8908	$8874 \pm 9$	2659	$2617.3 \pm 2.8$	8	$10.4 \pm 0.6$
200	9974	$10253 \pm 8$	2883	$3017.8 \pm 2.5$	6	$9.9 \pm 0.6$
202	4768	$4676 \pm 4$	1439	$1377.8 \pm 1.4$	6	$4.6 \pm 0.3$
205	8773	$8695 \pm 15$	2659	$2609.5 \pm 4.7$	7	$8.5 \pm 0.3$
207	9084	$9024 \pm 6$	2805	$2854.7 \pm 2.0$	11	$8.9 \pm 0.4$
208	820	$835 \pm 1$	253	$247.4 \pm 0.2$	0	$0.8 \pm 0.04$
206.5(*)	6411	$6549 \pm 6$	1696	$1621.6 \pm 1.8$	10	$5.6 \pm 0.5$
All	70482	$70555 \pm 2$	20626	$20707.5 \pm 2$	70	$73.4 \pm 0.4$

Table 7: Results of the selectron and smuon searches at the different selection levels and centre-of-mass energies. The number of events selected in data and expected from the SM simulation are given. Simulation errors are statistical; (\*) indicates the 2000 data taken with the sector 6 of the TPC off.

The results are presented in terms of excluded regions in the slepton-neutralino mass plane, obtained using all the analysed data sets combined with data taken previously at lower energies [2]. The method in [33] was used.

Limits on slepton masses can be derived using several assumptions. In the MSSM, right-handed sleptons are expected to have lower masses and lower cross-sections for a given mass. Hence the assumption was made that only right-handed selectrons and smuons are sufficiently low in mass to be pair produced at LEP. This leads to conservative mass limits.

Excluded regions in the slepton-neutralino mass plane were obtained taking into account the signal efficiencies for each slepton-neutralino mass point, the cross-section for right-handed slepton production and the branching ratios squared for the direct decay  $\tilde{\ell} \rightarrow \ell \chi_1^0$ , together with the number of data and background events kinematically compatible with the mass combination under test. The estimate of the SUSY cross-section and branching ratios for each mass point were determined with the SUSY parameters  $\tan \beta = 1.5$  and  $\mu = -200 \text{ GeV}/c^2$ . In addition, for the smuons a further exclusion curve was derived setting the branching ratio of  $\tilde{\mu} \rightarrow \mu \chi_1^0$  to 1.

Figure 15 shows the excluded region for  $\tilde{e}_R \tilde{e}_R$  production. For a mass difference between the selectron and the neutralino above  $5 \text{ GeV}/c^2$ , right-handed selectrons are excluded up to masses of  $98 \text{ GeV}/c^2$ , for a neutralino mass up to  $60 \text{ GeV}/c^2$ , beyond which the limit is weaker. For  $\Delta M \geq 15 \text{ GeV}/c^2$ , the excluded mass range is up to  $94 \text{ GeV}/c^2$ .

Figure 16 shows the excluded regions for  $\tilde{\mu}_R \tilde{\mu}_R$ . The excluded region is shown both taking the branching ratios for each mass point with the SUSY parameters  $\tan \beta = 1.5$  and  $\mu = -200 \text{ GeV}/c^2$  (lighter shaded region) and setting the branching ratio of  $\tilde{\mu} \rightarrow \mu \chi_1^0$  to 1 (darker shaded region). For the smuons the limit is determined at small neutralino masses, provided the mass difference between the smuon and the neutralino is above

5  $\text{GeV}/c^2$ . Assuming the branching ratio  $\text{BR}(\tilde{\mu} \rightarrow \mu \chi_1^0) = 1$ , masses up to 88  $\text{GeV}/c^2$  are excluded.

The effect of the systematic and statistical errors of background and efficiency on the mass limits was evaluated in a conservative way by changing the background and the efficiency by  $\pm 3\%$ . The resulting change in the limit was less than 1  $\text{GeV}/c^2$ .

#### 6.4.2 Stau search

##### Efficiencies and selected events

The efficiencies of the stau search have been determined using 5000 events for each point of a  $1 \text{ GeV}/c^2 \times 1 \text{ GeV}/c^2$  grid in the  $(M_{\tilde{\tau}}, M_{\text{LSP}})$  plane, using SGV (see section 4), and range from 20% to 30% for  $\Delta M > 20 \text{ GeV}/c^2$ . The results have been verified with the full DELSIM detector simulation and analysis chain (figure 17(a)). In the low mass search, the efficiency only needed to be evaluated at a limited number of points, and in particular at  $\Delta M = m_{\tau}$ . Therefore, the full detector simulation could be used at  $\Delta M = m_{\tau}$  for  $M_{\tilde{\tau}}$  between 2 and 45  $\text{GeV}/c^2$  (figure 17(b)). It was verified with SGV and, for a smaller number of  $M_{\tilde{\tau}}$  values, with DELSIM that the efficiencies were higher for higher  $\Delta M$ .

The systematic error on the efficiencies in the high  $\Delta M$  region was obtained by reversing the cuts designed to remove the  $\tau$ -pair and  $W^+W^-$  backgrounds, and comparing the number of selected events with the SM expectation. This method selected a sample which contained 97.6%  $W^+W^-$  and  $\tau$ -pair events, while a possible signal would not exceed 1%. In terms of the most important kinematic distributions, the events selected were nevertheless quite similar to a high  $\Delta M$  signal. The difference between data and the simulated SM processes was  $5 \pm 5\%$ , and 5% was taken as the estimate of the systematic uncertainty. For low  $\Delta M$ , the uncertainty was estimated by the maximal scatter of the efficiency obtained with SGV with respect to the values obtained with DELSIM, and amounted to 15%.

For the high mass stau-pair search, table 8 summarises the number of accepted events in the data together with the expected number of events from the different background channels. In all  $\Delta M$  regions, good agreement with the SM expectation was observed. Most of the selected SM events in the simulation contained either one or two  $\tau$ 's (17% and 67%, respectively). In two thirds of the events with less than two  $\tau$ 's, the lepton mistakenly taken as coming from a  $\tau$ -decay had low momentum, *i.e.* was indistinguishable from a secondary lepton from a  $\tau$ -decay. In the low mass analysis, a total of 196 events kinematically compatible with  $M_{\tilde{\tau}} = 25 \text{ GeV}/c^2$  and  $\Delta M = m_{\tau}$  were selected, and the SM background was estimated to be  $196.1^{+10.1}_{-4.1}$ . The contribution from  $\gamma\gamma \rightarrow \tau\tau$  to the background was 91%, and the remainder was other  $\gamma\gamma$  processes (8%) and  $\tau$ -pairs (1%). In the very low mass analysis, 59 events compatible with  $M_{\tilde{\tau}} = 5.5 \text{ GeV}/c^2$  and  $\Delta M = m_{\tau}$  were selected, while the SM background was estimated to be  $69.7 \pm 1.8$  events. The background was dominated by  $\tau$ -pairs (89%) and  $\gamma\gamma$  processes (7%). The remaining 4% came from four-fermion processes.

The systematic errors on the background estimates were obtained using the re-weighting method, as described in section 6.2.2.

##### Limits

Excluded regions in the  $(M_{\tilde{\chi}_1^0}, M_{\tilde{\tau}})$  plane were derived, combining the analysed data with previous data sets [2]. For each  $M_{\tilde{\tau}} - M_{\text{LSP}}$  mass combination, the predicted num-

$\sqrt{s}$ (GeV)	Preselection		Intermediate	
	Data	MC	Data	MC
189	2949	$2916 \pm 29$	80	$82 \pm 2$
192	473	$444 \pm 4$	14	$14 \pm 0$
196	1265	$1333 \pm 12$	36	$40 \pm 1$
200	1351	$1264 \pm 11$	41	$39 \pm 1$
202	716	$652 \pm 6$	12	$20 \pm 1$
205	1284	$1228 \pm 11$	38	$34 \pm 1$
207	1214	$1230 \pm 11$	33	$36 \pm 1$
208	132	$116 \pm 3$	3	$3 \pm 0$
206.5(*)	842	$857 \pm 8$	28	$26 \pm 1$
Total	10226	$10040 \pm 38$	285	$294 \pm 3$
Channel	Background composition			
$W^+W^-$	8 %		85 %	
4-fermion	0 %		2 %	
2-fermion	16 %		1 %	
bhabha	42 %		0 %	
$\gamma\gamma$	34 %		12 %	

$\sqrt{s}$ (GeV)	Final					
	High $\Delta M$		Medium $\Delta M$		Low $\Delta M$	
Data	MC	Data	MC	Data	MC	
189	16	$17.8 \pm 0.4 \begin{array}{l} +1.7 \\ -2.8 \end{array}$	10	$10.4 \pm 0.4 \begin{array}{l} +1.0 \\ -1.6 \end{array}$	0	$1.6 \pm 0.5 \begin{array}{l} +0.2 \\ -0.1 \end{array}$
192	5	$2.8 \pm 0.0 \begin{array}{l} +0.3 \\ -0.5 \end{array}$	2	$1.6 \pm 0.0 \begin{array}{l} +0.1 \\ -0.3 \end{array}$	0	$0.1 \pm 0.0 \begin{array}{l} +0.0 \\ -0.0 \end{array}$
196	7	$7.5 \pm 0.1 \begin{array}{l} +0.7 \\ -1.2 \end{array}$	3	$4.2 \pm 0.1 \begin{array}{l} +0.4 \\ -0.7 \end{array}$	0	$0.3 \pm 0.0 \begin{array}{l} +0.0 \\ -0.0 \end{array}$
200	11	$7.4 \pm 0.1 \begin{array}{l} +0.7 \\ -1.2 \end{array}$	9	$4.5 \pm 0.1 \begin{array}{l} +0.4 \\ -0.7 \end{array}$	0	$0.6 \pm 0.1 \begin{array}{l} +0.1 \\ -0.0 \end{array}$
202	1	$4.1 \pm 0.1 \begin{array}{l} +0.4 \\ -0.7 \end{array}$	1	$2.6 \pm 0.0 \begin{array}{l} +0.2 \\ -0.4 \end{array}$	0	$0.3 \pm 0.0 \begin{array}{l} +0.0 \\ -0.0 \end{array}$
205	6	$7.2 \pm 0.1 \begin{array}{l} +0.7 \\ -1.1 \end{array}$	4	$4.7 \pm 0.1 \begin{array}{l} +0.4 \\ -0.7 \end{array}$	1	$0.4 \pm 0.0 \begin{array}{l} +0.1 \\ -0.0 \end{array}$
207	9	$6.2 \pm 0.1 \begin{array}{l} +0.6 \\ -1.0 \end{array}$	5	$3.9 \pm 0.1 \begin{array}{l} +0.3 \\ -0.7 \end{array}$	2	$0.5 \pm 0.1 \begin{array}{l} +0.1 \\ -0.1 \end{array}$
208	0	$0.7 \pm 0.0 \begin{array}{l} +0.1 \\ -0.1 \end{array}$	0	$0.4 \pm 0.0 \begin{array}{l} +0.0 \\ -0.1 \end{array}$	0	$0.2 \pm 0.0 \begin{array}{l} +0.0 \\ -0.0 \end{array}$
206.5(*)	5	$4.8 \pm 0.1 \begin{array}{l} +0.5 \\ -0.7 \end{array}$	2	$3.0 \pm 0.1 \begin{array}{l} +0.3 \\ -0.5 \end{array}$	0	$0.5 \pm 0.0 \begin{array}{l} +0.0 \\ -0.0 \end{array}$
Total	60	$58.4 \pm 0.5 \begin{array}{l} +2.3 \\ -3.8 \end{array}$	36	$35.3 \pm 0.5 \begin{array}{l} +1.3 \\ -2.3 \end{array}$	3	$4.5 \pm 0.5 \begin{array}{l} +0.2 \\ -0.2 \end{array}$
Channel	Background composition					
$W^+W^-$	82 %		77 %		54 %	
4-fermion	3 %		4 %		2 %	
2-fermion	3 %		4 %		0 %	
bhabha	0 %		0 %		0 %	
$\gamma\gamma$	12 %		15 %		44 %	

Table 8: Stau candidates, together with the number of background events expected, at the different selection levels and centre-of-mass energies. The column labelled “High  $\Delta M$ ” corresponds to the point with  $M_{\tilde{\tau}}=80$   $\text{GeV}/c^2$  and  $M_{\text{LSP}}=0$   $\text{GeV}/c^2$ , the one labelled “Medium  $\Delta M$ ” to  $M_{\tilde{\tau}}=80$   $\text{GeV}/c^2$  and  $M_{\text{LSP}}=40$   $\text{GeV}/c^2$ , and the one labelled “Low  $\Delta M$ ” to  $M_{\tilde{\tau}}=65$   $\text{GeV}/c^2$  and  $M_{\text{LSP}}=60$   $\text{GeV}/c^2$ . The composition of the SM background for all centre-of-mass energies summed is also given; (\*) indicates the 2000 data taken with the sector 6 of the TPC off.

ber of observed SUSY events was compared with the observed number of kinematically compatible events in data and simulated background. The method presented in [33] was used and systematic errors were taken into account when calculating  $CL_s$ . The largest effect of the systematic uncertainty on the limit was observed at high  $\Delta M$ , but never exceeded  $800$   $\text{MeV}/c^2$ .

Figure 18 shows the  $\tilde{\tau}_R$  excluded region. Figure 19 shows the excluded regions in the case of the mixing corresponding to the minimal production cross-section. The cross-section has a minimum at mixing angle  $52^\circ$  at LEP2 energies [48]. In addition, the limit for  $\tilde{\tau}_L$  was also evaluated, and was found to be  $84.7$   $\text{GeV}/c^2$  (expected limit  $84.9$   $\text{GeV}/c^2$ ) for  $M_{\text{LSP}} = 0$   $\text{GeV}/c^2$ . The excess of candidates at low  $\Delta M$  for high stau-mass seen in both figures is compatible with a statistical fluctuation: the observed limit was

everywhere contained inside the 95% confidence band for the expected limit, calculated from the Poisson distributed background.

From the low mass search, at the minimum cross-section, the lower limit on the stau mass was  $26.3 \text{ GeV}/c^2$  for  $\Delta M = m_\tau$ ,  $31.7 \text{ GeV}/c^2$  for  $\Delta M = 3 \text{ GeV}/c^2$ , and  $40.5 \text{ GeV}/c^2$  for  $\Delta M = 4 \text{ GeV}/c^2$ . The corresponding expected limits were  $26.3 \text{ GeV}/c^2$ ,  $35.9 \text{ GeV}/c^2$ , and  $42.1 \text{ GeV}/c^2$ , respectively. The limit improves to  $29.6$  ( $31.1$ )  $\text{GeV}/c^2$  for  $\tilde{\tau}_R$  ( $\tilde{\tau}_L$ ), with an expected limit of  $30.0$  ( $31.9$ )  $\text{GeV}/c^2$ , for  $\Delta M = m_\tau$ . The low mass search does not exclude  $M_{\tilde{\tau}}$  below  $6.3 \text{ GeV}/c^2$  for  $\Delta M$  below  $3 \text{ GeV}/c^2$ . As shown in figure 20, to cover this region combination with the very low  $M_{\tilde{\tau}}$  search is needed.

In summary, a stau mass limit can be set at  $81.9$  to  $84.7 \text{ GeV}/c^2$  (depending on mixing) for mass differences between the stau and the LSP above  $15 \text{ GeV}/c^2$ . The same limits hold for LSP masses below  $68 \text{ GeV}/c^2$  and mass differences between the stau and the LSP above  $6 \text{ GeV}/c^2$ . The expected limit in the same region ranges from  $82.1$  to  $84.9 \text{ GeV}/c^2$ . The lowest stau mass allowed is  $26.3 \text{ GeV}/c^2$  (any mixing-angle and any  $\Delta M \geq m_\tau$ ).

## 6.5 Squark searches

### 6.5.1 Efficiencies and selected events

The efficiencies of the stop and sbottom signal selection are summarised in figure 21 for the non-degenerate scenario. Systematic uncertainties on the efficiency determination have been estimated as explained in section 6.2.1.

The number of events selected and the expected background at the final selection level are shown in table 9. The systematic uncertainties shown in the table have been estimated using the “re-weighting” method described in section 6.2.2. Moreover, in the mass limit computation, an additional relative uncertainty of 15% related to the determination of the hadronic  $\gamma\gamma$  contribution (see section 6.2.1) has been added.

In the nearly degenerate scenario, the efficiency for the stop signal is summarised in figure 22. The figure shows the variation of the efficiency for signal selection as a function of  $\Delta M$  for different stop mass hypotheses, for centre-of-mass energies of  $189$  and  $206 \text{ GeV}$ . Some examples of the detection efficiency obtained with this analysis are quoted below: for a  $\Delta M$  of  $2 \text{ GeV}/c^2$  and a stop mass of  $70 \text{ GeV}/c^2$ , an efficiency of 2.4% is obtained at  $\sqrt{s} = 189 \text{ GeV}$  and of 4.8% at  $\sqrt{s} = 206 \text{ GeV}$ . For a  $\Delta M$  of  $4 \text{ GeV}/c^2$  and a stop mass of  $80 \text{ GeV}/c^2$ , an efficiency of 4.0% is achieved at  $\sqrt{s} = 189 \text{ GeV}$  and of 7.7% at  $\sqrt{s} = 206 \text{ GeV}$ .

Table 10 gives the results for the nearly degenerate scenario in terms of number of events compared to the MC expectation after the preselection and at the final selection level. The systematic uncertainties were computed using the same method as for the non-degenerate case, and the same remark concerning the hadronic two-photon background applies.

### 6.5.2 Limits

Stop and sbottom cross-sections were calculated with the SUSYGEN program for two squark mixing angles. For purely left-handed squarks ( $\theta_{\tilde{q}} = 0^\circ$ ), the cross-section is maximal. The squark mixing angle which corresponds to the Z decoupling is  $56^\circ$  for the stop and  $68^\circ$  for the sbottom, and it corresponds approximately to the minimal cross-section. The program ALRMC [33] was used and systematic errors were taken into account in the definition of  $CL_s$ .

$\sqrt{s}$ (GeV)	Sbottom Analysis			
	$\Delta M \geq 20 \text{ GeV}/c^2$		$5 < \Delta M < 20 \text{ GeV}/c^2$	
	Data	MC	Data	MC
189	2	$0.43 \pm 0.08^{+0.12}_{-0.03}$	1	$0.47 \pm 0.20^{+0.19}_{-0.05}$
192	0	$0.05 \pm 0.01^{+0.02}_{-0.02}$	0	$0.06 \pm 0.02^{+0.01}_{-0.03}$
196	0	$0.17 \pm 0.04^{+0.03}_{-0.03}$	1	$0.22 \pm 0.08^{+0.02}_{-0.07}$
200	0	$0.14 \pm 0.03^{+0.02}_{-0.03}$	0	$0.27 \pm 0.08^{+0.05}_{-0.30}$
202	0	$0.07 \pm 0.02^{+0.03}_{-0.01}$	1	$0.13 \pm 0.04^{+0.04}_{-0.03}$
205	0	$0.49 \pm 0.05^{+0.05}_{-0.06}$	0	$0.43 \pm 0.17^{+0.05}_{-0.23}$
207	0	$0.36 \pm 0.04^{+0.07}_{-0.03}$	0	$0.38 \pm 0.17^{+0.13}_{-0.16}$
208	0	$0.05 \pm 0.01^{+0.07}_{-0.00}$	0	$0.04 \pm 0.02^{+0.06}_{-0.01}$
206.5(*)	0	$0.33 \pm 0.04^{+0.01}_{-0.10}$	0	$0.12 \pm 0.03^{+0.02}_{-0.05}$
Total	2	$2.10 \pm 0.12^{+0.17}_{-0.13}$	3	$2.12 \pm 0.34^{+0.25}_{-0.42}$

$\sqrt{s}$ (GeV)	Stop Analysis			
	$\Delta M \geq 20 \text{ GeV}/c^2$		$10 < \Delta M < 20 \text{ GeV}/c^2$	
	Data	MC	Data	MC
189	3	$2.28 \pm 0.22^{+0.78}_{-0.01}$	3	$0.87 \pm 0.21^{+0.28}_{-0.02}$
192	2	$0.92 \pm 0.11^{+0.17}_{-0.40}$	0	$0.27 \pm 0.07^{+0.01}_{-0.10}$
196	0	$2.35 \pm 0.22^{+0.34}_{-0.24}$	3	$0.78 \pm 0.15^{+0.08}_{-0.20}$
200	1	$2.14 \pm 0.13^{+0.07}_{-0.39}$	0	$0.91 \pm 0.16^{+0.13}_{-0.11}$
202	1	$1.16 \pm 0.07^{+0.49}_{-0.12}$	0	$0.49 \pm 0.08^{+0.18}_{-0.12}$
205	5	$2.00 \pm 0.11^{+0.34}_{-0.28}$	0	$0.75 \pm 0.18^{+0.07}_{-0.42}$
207	1	$2.32 \pm 0.11^{+0.43}_{-0.10}$	1	$0.78 \pm 0.18^{+0.16}_{-0.27}$
208	0	$0.19 \pm 0.01^{+0.26}_{-0.01}$	0	$0.08 \pm 0.02^{+0.14}_{-0.00}$
206.5(*)	1	$2.67 \pm 0.11^{+0.01}_{-0.89}$	0	$0.41 \pm 0.04^{+0.03}_{-0.18}$
Total	14	$16.03 \pm 0.41^{+1.2}_{-1.1}$	7	$5.34 \pm 0.41^{+0.43}_{-0.60}$

Table 9: Number of events selected by the squark analysis in the non-degenerate scenarios. The first errors are statistical and the second ones are systematic; (\*) indicates the 2000 data taken with the sector 6 of the TPC off.

Figures 23 and 24 show the  $(M_{\tilde{q}}, M_{\tilde{\chi}_1^0})$  regions excluded by the search for  $\tilde{t} \rightarrow c\tilde{\chi}_1^0$  and  $\tilde{b} \rightarrow b\tilde{\chi}_1^0$  decays, with the 100 % branching ratio assumption, both for purely left-handed states and for the states at the Z decoupling. Figure 25 shows the region excluded using only the nearly degenerate analysis for  $\Delta M$  values between 2 and 20  $\text{GeV}/c^2$ .

Table 11 shows the limit on the squark masses as a function of  $\Delta M$  obtained combining the two analyses. The introduction of the systematics in the confidence level calculation has no effect on these numbers. Stop masses lower than  $71 \text{ GeV}/c^2$  and sbottom masses lower than  $76 \text{ GeV}/c^2$  are excluded if  $\Delta M \geq 2 \text{ GeV}/c^2$  and  $\Delta M \geq 7 \text{ GeV}/c^2$ , respectively, for any squark mixing angle. These limits become  $75 \text{ GeV}/c^2$  and  $93 \text{ GeV}/c^2$  for purely left-handed squarks.

Stop (nearly degenerate) $\Delta M \leq 10 \text{ GeV}/c^2$				
$\sqrt{s}$ (GeV)	Preselection		Final	
	Data	MC	Data	MC
189	3717	3717	3	$2.72 \pm 0.34^{+0.78}_{-0.33}$
192	527	599	0	$0.33 \pm 0.12^{+0.10}_{-0.15}$
196	1620	1623	2	$1.02 \pm 0.21^{+0.12}_{-0.17}$
200	1667	1679	0	$1.12 \pm 0.22^{+0.27}_{-0.15}$
202	867	793	0	$0.64 \pm 0.16^{+0.26}_{-0.05}$
205	1469	1492	1	$1.32 \pm 0.33^{+0.14}_{-0.21}$
207	1423	1468	2	$1.33 \pm 0.33^{+0.35}_{-0.21}$
208	138	133	1	$0.12 \pm 0.10^{+0.17}_{-0.01}$
206.5(*)	1023	1133	0	$0.55 \pm 0.19^{+0.21}_{-0.16}$
Total	12451	12637	9	$9.15 \pm 0.72^{+0.99}_{-0.55}$

Table 10: Number of events selected in the stop analysis in the nearly degenerate scenario. The first errors are statistical and the second ones are systematic; (\*) indicates 2000 data taken with sector 6 of the TPC off.

	Sbottom		Stop	
	$\theta_{\tilde{b}} = 0$	$\theta_{\tilde{b}} = 68^\circ$	$\theta_{\tilde{t}} = 0$	$\theta_{\tilde{t}} = 56^\circ$
$\Delta M \geq 2 \text{ GeV}/c^2$	-	-	75	71
$\Delta M \geq 3 \text{ GeV}/c^2$	-	-	80	78
$\Delta M \geq 4 \text{ GeV}/c^2$	-	-	84	81
$\Delta M \geq 5 \text{ GeV}/c^2$	-	-	91	87
$\Delta M \geq 7 \text{ GeV}/c^2$	93	76	95	91
$\Delta M \geq 10 \text{ GeV}/c^2$	98	87	96	92
$\Delta M \geq 15 \text{ GeV}/c^2$	99	89	96	92

Table 11: Lower limits on squark masses (in  $\text{GeV}/c^2$ ) as a function of  $\Delta M$  from the squark analysis in the non-degenerate and nearly degenerate scenarios.

## 6.6 Chargino searches

### 6.6.1 Non-degenerate scenarios

#### Efficiencies and selected events

The efficiencies of the chargino selection in the four topologies were computed separately for the 132 MSSM points using the  $\mathcal{L}_R$  function and the  $\mathcal{L}_{R_{cut}}$  of the corresponding topology and  $\Delta M$  region. To pass from the efficiencies of the chargino selection in the four topologies to the efficiencies in the four decay channels, all the migration effects were computed for all the generated points of the signal simulation. Then the efficiencies of the selection in the four decay channels were interpolated in the  $(M_{\tilde{\chi}_1^\pm}, M_{\tilde{\chi}_1^0})$  plane using the same method as in [4]. These efficiencies as functions of  $M_{\tilde{\chi}_1^\pm}$  and  $M_{\tilde{\chi}_1^0}$  are shown in figure 26(27) for a mean centre-of-mass energy of 206(206.5) GeV with the TPC sector 6 on(off).

Table 12 gives the total number of events selected in data and expected from the SM simulation after the preselections and after the final selections, for the different centre-of-mass energies. The total number of background events expected in the different mass windows and topologies is shown in tables 13, 14 and 15, together with the number of events selected. In all the topologies, the number of selected events in the real data is compatible with the expectation from the background simulation.

The systematic errors shown in tables 13, 14 and 15 were obtained with the “re-weighting” method described in section 6.2.2.

$\sqrt{s}$ (GeV)	$\int \mathcal{L}$ (pb $^{-1}$ )	Preselection		Final sel.	
		Data	MC	Data	MC
192	25.4	1966	$2012 \pm 11$	21	$23.7 \pm 0.9$
196	76.2	5926	$5818 \pm 25$	85	$71.6 \pm 2.4$
200	84.0	6433	$6331 \pm 22$	60	$72.3 \pm 1.7$
202	40.4	3086	$2994 \pm 11$	26	$35.0 \pm 0.8$
205	78.3	5796	$5734 \pm 21$	56	$54.6 \pm 1.3$
207	78.8	5795	$5770 \pm 21$	63	$54.9 \pm 1.3$
208	7.2	530	$528 \pm 2$	3	$5.1 \pm 0.1$
206.5(*)	60.0	4119	$4356 \pm 16$	53	$58.7 \pm 1.8$
all		33651	$33543 \pm 50$	367	$375.9 \pm 4.0$

Table 12: Numbers of events selected in data and expected from the SM simulation in the non-degenerate chargino search at the preselection and at the final selection level, for the different centre-of-mass energies collected during the years 1999 and 2000; (\*) indicates the data collected with the TPC sector 6 off. Simulation errors are statistical.

1999 data, $\mathcal{L} = 227 \text{ pb}^{-1}$					
Topology:	$jj\ell$	$\ell\ell$	$\text{jets}$	rad	Total
$3 \leq \Delta M < 5 \text{ GeV}/c^2$					
Obs. events:	4	39	3	7	53
Expect. events:	$2.3 \pm 0.7^{+1.2}_{-0.1}$	$49.2 \pm 2.3^{+2.6}_{-5.7}$	$5.3 \pm 0.9^{+0.0}_{-2.7}$	$5.3 \pm 0.7^{+0.9}_{-0.2}$	$62.1 \pm 2.7^{+3.0}_{-6.3}$
$5 \leq \Delta M < 10 \text{ GeV}/c^2$					
Obs. events:	4	13	1	7	25
Expect. events:	$2.3 \pm 0.7^{+1.2}_{-0.1}$	$11.9 \pm 1.1^{+0.5}_{-3.0}$	$2.5 \pm 0.7^{+0.5}_{-0.7}$	$5.3 \pm 0.7^{+0.9}_{-0.2}$	$22.0 \pm 1.7^{+1.6}_{-3.1}$
$10 \leq \Delta M < 25 \text{ GeV}/c^2$					
Obs. events:	4	14	17	7	42
Expect. events:	$2.3 \pm 0.7^{+1.2}_{-0.1}$	$14.3 \pm 0.9^{+1.7}_{-3.1}$	$15.8 \pm 1.2^{+2.1}_{-1.4}$	$5.3 \pm 0.7^{+0.9}_{-0.2}$	$37.6 \pm 1.8^{+3.1}_{-3.4}$
$25 \leq \Delta M < 35 \text{ GeV}/c^2$					
Obs. events:	6	21	10	7	44
Expect. events:	$2.2 \pm 0.2^{+0.7}_{-0.0}$	$25.1 \pm 1.0^{+4.2}_{-3.5}$	$8.3 \pm 0.3^{+0.8}_{-0.0}$	$5.3 \pm 0.7^{+0.9}_{-0.2}$	$40.6 \pm 1.3^{+4.4}_{-3.5}$
$35 \leq \Delta M < 50 \text{ GeV}/c^2$					
Obs. events:	2	40	28	14	84
Expect. events:	$2.3 \pm 0.2^{+0.7}_{-0.1}$	$45.1 \pm 1.1^{+3.1}_{-4.2}$	$23.6 \pm 0.4^{+3.4}_{-0.4}$	$12.9 \pm 0.8^{+1.7}_{-0.2}$	$84.1 \pm 1.4^{+4.9}_{-4.2}$
$50 \leq \Delta M$					
Obs. events:	9	60	37	14	120
Expect. events:	$7.5 \pm 0.3^{+2.2}_{-0.3}$	$68.2 \pm 1.2^{+4.4}_{-6.9}$	$36.8 \pm 0.5^{+4.9}_{-0.4}$	$12.9 \pm 0.8^{+1.7}_{-0.2}$	$125.4 \pm 1.6^{+7.1}_{-6.9}$
TOTAL (logical OR. between different $\Delta M$ windows)					
Obs. events:	14	109	54	15	192
Expect. events:	$10.7 \pm 0.8$	$126.1 \pm 2.7$	$52.8 \pm 1.4$	$13.9 \pm 0.8$	$202.6 \pm 3.2$

Table 13: Number of events observed in data and expected number of background events in the different chargino search channels for all the data collected in 1999. The first errors are statistical and the second ones are systematic. The “re-weighting” method used to compute the systematics is described in section 6.2.1.

To study the systematic effect on the detection efficiency both the “shaking” method and the “smearing” method were used (see section 6.2.2).

$< E_{cm} > = 206 \text{ GeV}, \mathcal{L} = 164.4 \text{ pb}^{-1}$					
Topology:	$jj\ell$	$\ell\ell$	$jets$	rad	Total
$3 \leq \Delta M < 5 \text{ GeV}/c^2$					
Obs. events:	0	20	5	3	28
Expect. events:	$0.4 \pm 0.3^{+0.1}_{-0.0}$	$20.6 \pm 1.9^{+0.3}_{-2.4}$	$7.5 \pm 0.9^{+1.3}_{-0.6}$	$2.5 \pm 0.5^{+1.1}_{-0.1}$	$31.0 \pm 2.2^{+1.7}_{-2.5}$
$5 \leq \Delta M < 10 \text{ GeV}/c^2$					
Obs. events:	0	0	2	3	5
Expect. events:	$0.4 \pm 0.3^{+0.1}_{-0.0}$	$2.0 \pm 0.5^{+0.1}_{-0.5}$	$1.4 \pm 0.3^{+0.5}_{-0.3}$	$2.5 \pm 0.5^{+1.1}_{-0.1}$	$6.4 \pm 0.8^{+1.2}_{-0.6}$
$10 \leq \Delta M < 25 \text{ GeV}/c^2$					
Obs. events:	0	8	4	3	15
Expect. events:	$0.4 \pm 0.3^{+0.1}_{-0.0}$	$7.7 \pm 0.9^{+0.9}_{-0.4}$	$5.6 \pm 0.7^{+1.3}_{-0.5}$	$2.5 \pm 0.5^{+1.1}_{-0.1}$	$16.3 \pm 1.3^{+1.9}_{-0.6}$
$25 \leq \Delta M < 35 \text{ GeV}/c^2$					
Obs. events:	1	13	3	3	20
Expect. events:	$0.4 \pm 0.1^{+0.0}_{-0.0}$	$11.6 \pm 0.9^{+0.7}_{-2.1}$	$4.0 \pm 0.3^{+1.0}_{-0.0}$	$2.5 \pm 0.5^{+1.1}_{-0.1}$	$18.5 \pm 1.1^{+1.6}_{-2.1}$
$35 \leq \Delta M < 50 \text{ GeV}/c^2$					
Obs. events:	2	23	10	11	46
Expect. events:	$2.4 \pm 0.4^{+0.1}_{-0.1}$	$26.8 \pm 1.0^{+1.2}_{-2.8}$	$8.0 \pm 0.4^{+2.0}_{-0.0}$	$10.3 \pm 0.5^{+1.6}_{-0.5}$	$47.5 \pm 1.2^{+2.8}_{-2.8}$
$50 \text{ GeV}/c^2 \leq \Delta M$					
Obs. events:	3	40	22	11	76
Expect. events:	$3.8 \pm 0.4^{+0.4}_{-0.3}$	$38.9 \pm 1.0^{+4.3}_{-1.1}$	$18.7 \pm 0.5^{+4.2}_{-0.0}$	$10.3 \pm 0.5^{+1.6}_{-0.5}$	$71.7 \pm 1.3^{+6.2}_{-1.2}$
TOTAL (logical OR. between different $\Delta M$ windows)					
Obs. events:	4	76	31	11	122
Expect. events:	$5.0 \pm 0.5$	$69.7 \pm 2.2$	$29.0 \pm 1.3$	$10.9 \pm 0.7$	$114.6 \pm 2.7$

Table 14: Number of events observed in data and expected number of background events in the different chargino search channels for all the events recorded in 2000 with the detector fully operational ( $< E_{cm} > = 206 \text{ GeV}$ ). The first errors are statistical and the second ones are systematic. The “re-weighting” method used to compute the systematics is described in section 6.2.1.

For the high multiplicity topologies ( $jets$  &  $jj\ell$ ) the “shaking” method was used. The systematic uncertainty is larger in the two first  $\Delta M$  regions, due to the more problematic event reconstruction. For these  $\Delta M$  regions the relative systematic uncertainty on the detection efficiency determination is between 4% and 13%, but at larger  $\Delta M$  the effect is less than 4%. The relative difference for these two topologies can be seen in table 4. All the results from the “shaking” method for these topologies gave a higher efficiency, indicating that the “unshaken” efficiencies can be regarded as conservative.

For the leptonic ( $\ell\ell$ ) topology the “smearing” method was used. The results from this study did not give consistently higher efficiencies, but since the uncertainties are less than 1% for all the  $\Delta M$  regions it showed that this topology is much less sensitive to systematic effects.

In the case of the radiative topology, which consists of both high and low multiplicity events, both the “shaking” method and the “smearing” method were used to study the systematic uncertainty on the efficiency. The two methods gave compatible results in all the regions where they are both valid and the uncertainty is less than 2%.

## Limits

The simulated points were used to parameterise the efficiencies of the chargino selection criteria described in section 5.4.1 in terms of  $\Delta M$  and the mass of the chargino. The values of  $\Delta M$ , the chargino and neutralino masses, the cross-sections and the various decay branching ratios were then determined for a large number of points in the MSSM parameter space ( $\mu, M_2, \tan \beta$ ). From these values and the appropriate efficiencies, the number of expected signal events can be calculated. Taking into account the expected

$E_{cm} = 206.5 \text{ GeV}, \mathcal{L} = 60.0 \text{ pb}^{-1}$					
Topology:	$jj\ell$	$\ell\ell$	$\text{jets}$	rad	Total
$3 \leq \Delta M < 5 \text{ GeV}/c^2$					
Obs. events:	0	10	2	2	14
Expect. events:	$0.2 \pm 0.1^{+0.1}_{-0.0}$	$18.8 \pm 1.3^{+0.0}_{-4.0}$	$2.1 \pm 0.4^{+0.9}_{-0.0}$	$1.3 \pm 0.1^{+1.0}_{-0.0}$	$22.5 \pm 1.3^{+1.3}_{-4.0}$
$5 \leq \Delta M < 10 \text{ GeV}/c^2$					
Obs. events:	0	4	4	2	10
Expect. events:	$0.2 \pm 0.1^{+0.1}_{-0.0}$	$3.6 \pm 0.5^{+0.0}_{-0.5}$	$3.9 \pm 0.7^{+2.3}_{-0.1}$	$1.3 \pm 0.1^{+1.0}_{-0.0}$	$9.1 \pm 0.9^{+2.5}_{-0.5}$
$10 \leq \Delta M < 25 \text{ GeV}/c^2$					
Obs. events:	0	3	7	2	12
Expect. events:	$0.2 \pm 0.1^{+0.1}_{-0.0}$	$2.31 \pm 0.3^{+0.0}_{-0.4}$	$5.4 \pm 0.8^{+2.7}_{-0.0}$	$1.3 \pm 0.1^{+1.0}_{-0.0}$	$9.3 \pm 0.9^{+2.9}_{-0.4}$
$25 \leq \Delta M < 35 \text{ GeV}/c^2$					
Obs. events:	0	3	4	2	9
Expect. events:	$0.4 \pm 0.1^{+0.1}_{-0.1}$	$5.3 \pm 0.3^{+0.0}_{-2.2}$	$3.2 \pm 0.3^{+1.2}_{-0.0}$	$1.3 \pm 0.1^{+1.0}_{-0.0}$	$10.3 \pm 0.5^{+1.6}_{-2.2}$
$35 \leq \Delta M < 50 \text{ GeV}/c^2$					
Obs. events:	0	10	6	5	21
Expect. events:	$0.7 \pm 0.1^{+0.0}_{-0.1}$	$11.7 \pm 0.4^{+0.0}_{-5.2}$	$5.0 \pm 0.3^{+2.1}_{-0.0}$	$4.3 \pm 0.2^{+1.3}_{-0.0}$	$21.6 \pm 0.6^{+2.5}_{-5.2}$
$50 \text{ GeV}/c^2 \leq \Delta M$					
Obs. events:	1	16	9	5	31
Expect. events:	$2.0 \pm 0.1^{+0.0}_{-0.6}$	$14.2 \pm 0.4^{+4.1}_{-1.1}$	$6.3 \pm 0.3^{+2.4}_{-0.0}$	$4.3 \pm 0.2^{+1.3}_{-0.0}$	$26.8 \pm 0.5^{+4.9}_{-1.3}$
TOTAL (logical OR. between different $\Delta M$ windows)					
Obs. events:	1	31	16	5	53
Expect. events:	$2.3 \pm 0.1$	$38.8 \pm 1.4$	$13.1 \pm 1.0$	$4.5 \pm 0.2$	$58.7 \pm 1.8$

Table 15: Number of events observed in data and expected number of background events in the different chargino search channels for all the events recorded in 2000 with the TPC sector 6 off ( $\langle E_{cm} \rangle = 206.5 \text{ GeV}$ ). The first errors are statistical and the second ones are systematic. The “re-weighting” method used to compute the systematics is described in section 6.2.1.

background and the number of observed events, the corresponding point in the MSSM parameter space can be excluded, if the number of expected signal events is greater than the upper limit on the number of observed events of the corresponding  $\Delta M$  region, computed using the multichannel Bayesian formula (see section 6.1). Systematic errors were taken into account as described in section 6.2.3.

Figure 28 shows the chargino production cross-sections as obtained in the MSSM at  $\sqrt{s} = 208 \text{ GeV}$  for different chargino masses for the large  $\Delta M$  ( $\Delta M > 10 \text{ GeV}/c^2$ ) and low  $\Delta M$  ( $\Delta M = 3 \text{ GeV}/c^2$ ) cases. The parameters  $M_2$  and  $\mu$  were varied randomly in the ranges  $0 \text{ GeV}/c^2 < M_2 < 3000 \text{ GeV}/c^2$  and  $-200 \text{ GeV}/c^2 < \mu < 200 \text{ GeV}/c^2$  for three fixed different values of  $\tan \beta$ , namely 1, 1.5 and 35. The random generation of the parameters led to an accuracy on the mass limit computation of the order of  $50 \text{ MeV}/c^2$ . Two different cases were considered for the sneutrino mass:  $m_{\tilde{\nu}} > 1000 \text{ GeV}/c^2$  (for  $\Delta M > 10 \text{ GeV}/c^2$ ) and  $m_{\tilde{\nu}} > M_{\tilde{\chi}_1^\pm}$  (for  $\Delta M = 3 \text{ GeV}/c^2$ ). The mass limits are valid also for  $|\mu| > 200 \text{ GeV}/c^2$ , since in this case both the efficiency of the chargino search and the chargino branching fractions are largely independent of  $|\mu|$ , if  $m_{\tilde{\nu}} > M_{\tilde{\chi}_1^\pm}$ <sup>17</sup>.

The chargino mass limits are summarised in table 16. The dependence of the limit on  $\Delta M$  and  $M_2$  assuming a heavy sneutrino is shown in figures 29 and 30. The behaviour of the curve in figure 29 depends very weakly on the relation between  $M_1$  and  $M_2$ . Note that in figure 30, for a fixed large value of  $M_2$ , the chargino mass limit is lower for positive  $\mu$  than for negative  $\mu$ . This is due to the higher degree of mass degeneracy between the lightest chargino and the LSP found for positive  $\mu$  compared to negative  $\mu$ , for a fixed value of  $M_2$ .

<sup>17</sup>This was investigated by a coarse scan of random parameter sets with  $|\mu| > 200 \text{ GeV}/c^2$ , resulting in a mass limit greater than  $103 \text{ GeV}/c^2$ .

For  $\Delta M > 10 \text{ GeV}/c^2$  with a large sneutrino mass ( $> 1000 \text{ GeV}/c^2$ ), the lower limit on the chargino mass ranges between  $102.7 \text{ GeV}/c^2$  (for a mostly higgsino-like chargino) and  $103.4 \text{ GeV}/c^2$  (for a mostly wino-like chargino).

For  $\Delta M = 3 \text{ GeV}/c^2$ , the cross-section does not depend significantly on the sneutrino mass, since the region allowing small  $\Delta M$  values is located where the chargino is higgsino-like, due to the assumption of gaugino mass unification. The lower limit for the chargino mass, shown in figure 28, is  $97.1 \text{ GeV}/c^2$ .

Case	$m_{\tilde{\nu}}$ ( $\text{GeV}/c^2$ )	$M_{\chi^\pm}^{min}$ ( $\text{GeV}/c^2$ )	$\sigma_{min}^{208}$ (pb)	$N_{95\%}$
$\langle E_{cm} \rangle = 192\text{--}208 \text{ GeV}$				
$\Delta M > 10 \text{ GeV}/c^2$	$> 1000$	102.7	0.39	13.8
$\Delta M = 5 \text{ GeV}/c^2$	$> 1000$	101.7	0.57	7.3
$\Delta M = 3 \text{ GeV}/c^2$	$> M_{\tilde{\chi}_1^\pm}$	97.1	1.17	18.1

Table 16: Lower limits for the chargino mass, minimal pair-production cross-sections at 208 GeV for chargino masses below the limit and upper limits on the number of observed events.

The results can be translated into a limit on the mass of the lightest neutralino [4] also shown in the  $(M_{\tilde{\chi}_1^\pm}, M_{\tilde{\chi}_1^0})$  plane in figure 31. A lower limit of  $38.2 \text{ GeV}/c^2$  on the lightest neutralino mass is obtained, valid for  $\tan \beta \geq 1$  and a heavy sneutrino. This limit is reached for  $\tan \beta = 1$ ,  $\mu = -65.1 \text{ GeV}/c^2$ ,  $M_2 = 65.0 \text{ GeV}/c^2$ .

### 6.6.2 Nearly mass-degenerate scenarios

#### Efficiencies and selected events

In the search for heavy stable charged particles, the three windows described in section 5.4.2 were searched for mass-degenerate charginos. No events were found in the 1999 and 2000 data, where  $0.51 \pm 0.08$  and  $0.15 \pm 0.03$  events were expected, respectively. The efficiency for selecting a single chargino track by using this technique is shown in figure 32, as a function of the mass of the chargino and at the various centre-of-mass energies.

In the search for kinks, 42000 chargino events with masses between  $60$  and  $100 \text{ GeV}/c^2$  and mean decay length of  $50 \text{ cm}$  were generated at the centre-of-mass energies between  $192$  and  $206 \text{ GeV}$ . The events were used to map the selection and trigger efficiency for the single chargino, as a function of its mass and decay position. As an example, the efficiencies for a  $75 \text{ GeV}/c^2$  chargino at  $\sqrt{s}=196 \text{ GeV}$  are plotted in figure 33. In the data of 1999 (2000 with full TPC, 2000 without the sector 6 of TPC), 5 (3, 1) events passed the selection, while  $3.7 \pm 1.0$  ( $1.2 \pm 0.6$ ,  $0.5 \pm 0.2$ ) were expected from the standard sources.

In the search with the ISR photon tag a total of almost 3 million  $\tilde{\chi}_1^+ \tilde{\chi}_1^-$  events was generated at the centre-of-mass energies between  $192$  and  $206 \text{ GeV}$ ; about 100 000 of them

had a high  $p_t$  photon within the detector acceptance and were passed through the full detector simulation. The mass of the generated charginos ranged from 60 to 95  $\text{GeV}/c^2$ , and  $\Delta M$  from 150  $\text{MeV}/c^2$  to 3  $\text{GeV}/c^2$ . The selection efficiency was computed applying the selection cuts to the samples of simulated events. The trigger efficiency was parameterised on the real data, separately for the isolated photon and for the system of few low momentum particles. Compton and Bhabha events were used to assess the trigger efficiency for single photons, as a function of the photon energy and polar angle. To estimate the trigger efficiency in events with few soft charged particles, parameterised in terms of the transverse momentum of the single particles and the total transverse energy, the redundancy of the trigger in several classes of two-photon events was used instead. The overall trigger efficiency for the whole event was finally considered as the convolution of the trigger efficiency of the single photon and that of the system of low momentum charged particles. The parameterisation was then applied on the simulation (both signal and background events). Detection and trigger efficiency vary widely with  $M_{\tilde{\chi}_1^\pm}$  and  $\Delta M$ ; they also depend on the field composition of the chargino, since the spectrum of the ISR radiation is different for higgsinos and gauginos. The efficiency (including the trigger efficiency) for a signal (higgsino) at 206  $\text{GeV}$  is shown in figure 34. The small probability of radiating a photon with transverse energy  $E_T^\gamma$  above the chosen threshold is the main reason for having such a low efficiency. As the selection cuts varied across the plane ( $M_{\tilde{\chi}_1^\pm}, \Delta M$ ), so did the number of candidate events remaining in the data and the amount of background expected from the SM simulations available. Figure 35 shows, as an example, the number of events remaining in data and simulation for the year 2000 sample with fully operational TPC, as a function of the position in the plane ( $M_{\tilde{\chi}_1^\pm}, \Delta M$ ). In this sample, when  $\Delta M$  is below 1  $\text{GeV}/c^2$  additional candidates are selected in the data but none in the simulated background. The number of events remaining after the dedicated preselection and at the final step, after the logical OR of all selections, together with the integrated luminosity used for the analysis, are given in table 17. The excess of events seen in the data is of the same kind as the excess observed in the analyses done at lower energies [6] and, as in the past, it can be qualitatively explained by the incomplete phase space coverage of the standard simulation used, and possibly some noise events like beam-gas collisions, as already discussed at the end of section 5.4.2. The excess at the preselection level has been verified to be almost entirely due to the cuts done at the generator level in the (hadronic) two-photon simulation used (in 1999 tighter cuts in the generation were applied to the hadronic  $\gamma\gamma$  samples). After the final selection, the distribution of the 17 candidates in the data is compatible with the integrated luminosities shown in table 17. Fewer candidates are observed in the SM simulation than in the data. This is taken to indicate missing contributions in the modelling of two-photon background, or beam-gas interactions.

### Limits

Having no evidence for a signal in any of the three searches for charginos nearly mass-degenerate with the lightest neutralino, regions in the plane ( $M_{\tilde{\chi}_1^\pm}, \Delta M$ ) can be excluded. First, the two searches for long-lived charginos were combined, assuming that in a  $\tilde{\chi}_1^+ \tilde{\chi}_1^-$  event any of the two long-lived charginos can be tagged either as a kink or as a stable particle. Then the search with the ISR photon was considered for all events in which the chargino decay length was shorter than that required by the two other methods. In all cases, the data were combined with all previous data from the high energy phase of LEP [6].

$\sqrt{s}$ (GeV)	$\int \mathcal{L}$ (pb $^{-1}$ )	Preselection		Final sel.	
		Data	MC	Data	MC
192	25.4	75	$40 \pm 2$	0	$0.6 \pm 0.1$
196	76.2	162	$118 \pm 4$	4	$1.3 \pm 0.3$
200	84.0	201	$123 \pm 4$	0	$1.4 \pm 0.3$
202	40.4	109	$55 \pm 2$	0	$0.6 \pm 0.1$
206	163.0	423	$393 \pm 18$	11	$3.5 \pm 1.3$
206.5(*)	58.5	130	$113 \pm 4$	2	$1.0 \pm 0.4$
All		1100	$842 \pm 19$	17	$8.4 \pm 1.5$

Table 17: Number of events selected in data and expected from the SM simulation in the ISR photon search for charginos nearly mass-degenerate with the lightest neutralino. Numbers are given at the preselection and at the final selection level, for the different centre-of-mass energies. All year 2000 data were considered at the mean centre-of-mass energy of 206 GeV; (\*) indicates the data collected with the TPC sector 6 off. Simulation errors are statistical.

The limits obtained in this way are certainly model dependent: cross-sections, decay modes, and the spectrum of the ISR radiation itself all depend on the gauge composition of the chargino. They were obtained in the two SUSY scenarios in which a near mass-degeneracy between the lightest chargino and neutralino is possible: the  $M_2 \gg \mu$  scenario, in which the lightest chargino and neutralino are both almost pure higgsinos; and the  $\mu \gg M_2$  scenario, in which the lightest chargino and neutralino are both almost pure gauginos. In the gaugino scenario, the gaugino mass unification at large scale must be violated in order to obtain low  $\Delta M$ ; in the higgsino scenario this is not mandatory, therefore this is the scenario to be taken into account in the constrained SUSY models. These limits are shown in figure 36, separately for the different techniques. In the same figure, they are compared with the excluded region obtained in the search for larger  $\Delta M$  charginos.

With these new results, the  $\Delta M$ -independent lower limit on the mass of the chargino becomes  $M_{\tilde{\chi}_1^\pm} > 75 \text{ GeV}/c^2$  in the higgsino scenario and  $M_{\tilde{\chi}_1^\pm} > 70 \text{ GeV}/c^2$  in the gaugino scenario with heavy sneutrinos. Both limits take into account a variation of  $\tan \beta$  between 1 and 50, and a variation of  $M_1$ ,  $M_2$  and  $\mu$  such that the mass difference between the chargino and the neutralino remains below  $3 \text{ GeV}/c^2$  and  $M_2 \leq 2M_1 \leq 10M_2$ . In the higgsino scenario all sfermions are required to be heavier than the chargino, while in the gaugino scenario they must be heavy enough not to modify significantly the cross-section (only the sneutrino was required to be heavier than  $500 \text{ GeV}/c^2$ ) or the decay modes and widths.

Uncertainties in the selection efficiencies and in the expected background were included in the limits in a Bayesian way as described in section 6.2.3, using the method in [42]. The most important contributions to the systematic error is the uncertainty in the background content: depending on the point, the excluded regions may vary as much as 2-3  $\text{GeV}/c^2$ . Such an effect comes only from the uncertainty in the simulation available, since conservatively there was no attempt to increase the estimated background to take into account the regions of phase space not included in the simulation. Other systematics, like the uncertainties in the trigger efficiencies, were similarly taken into account by considering the configuration which leads to the weakest limits.

## 6.7 Neutralino searches

### 6.7.1 Efficiencies and selected events

More than 1.2 million  $\tilde{\chi}_1^0 \tilde{\chi}_2^0$  events were simulated for different combinations of masses with  $M_{\tilde{\chi}_1^0}$  and  $M_{\tilde{\chi}_2^0}$  ranging from 5  $\text{GeV}/c^2$  to 100  $\text{GeV}/c^2$  and from 10  $\text{GeV}/c^2$  to 200  $\text{GeV}/c^2$ , respectively, and for different  $\tilde{\chi}_2^0$  decay modes ( $q\bar{q}\tilde{\chi}_1^0$ ,  $\mu^+\mu^-\tilde{\chi}_1^0$ ,  $e^+e^-\tilde{\chi}_1^0$ ,  $\tilde{\tau}\tau$ ). The efficiencies were computed for each mass combination and parameterised as functions of the two masses. In addition, around 300 000  $\tilde{\chi}_2^0 \tilde{\chi}_{3,4}^0$  events with cascade decays were simulated. For cascade processes, the efficiencies were parameterised as functions of  $M_{\tilde{\chi}_1^0}$  and a second parameter, chosen to be either  $M_{\tilde{\chi}_{3,4}^0} - M_{\tilde{\chi}_2^0}$  when considering the decay modes  $\tilde{\chi}_2^0 \rightarrow \tilde{\chi}_1^0 \gamma$  and  $\tilde{\chi}_{3,4}^0 \rightarrow q\bar{q}\tilde{\chi}_2^0$ , or  $M_{\tilde{\chi}_{3,4}^0} + M_{\tilde{\chi}_2^0}$  when considering the decay modes  $\tilde{\chi}_2^0 \rightarrow q\bar{q}\tilde{\chi}_1^0$  and  $\tilde{\chi}_{3,4}^0 \rightarrow q\bar{q}\tilde{\chi}_2^0$ . The dependence on remaining parameters was found to be small in the relevant mass ranges and the efficiencies were averaged over them.

The efficiency for  $\tilde{\chi}_2^0 \tilde{\chi}_2^0 \rightarrow \tilde{\tau}\tau\tilde{\tau}\tau$  was evaluated in a number of points with  $M_{\tilde{\chi}_1^0}$  between 30 and 50  $\text{GeV}/c^2$  and mass differences between the stau and the  $\tilde{\chi}_1^0$  ranging from 2 to 5  $\text{GeV}/c^2$ . The  $\tilde{\chi}_2^0$  mass exceeded the  $\tilde{\chi}_1^0$  mass by 30 to 45  $\text{GeV}/c^2$ . These points were chosen because they correspond to a region in the CMSSM parameter space which cannot be covered by the chargino search nor, due to the small mass difference, by the stau search. Efficiencies between 10 and 20% were found, varying little with the chosen masses. These values were obtained with SGV and verified with DELSIM in a sub-set of points.

The number of events selected at different centre-of-mass energies and selection levels, together with the expected SM background, are given in tables 18 to 22 for the different neutralino search topologies discussed in section 5.5. The results of the sequential and likelihood ratio analyses for the acoplanar leptons and acoplanar jets were found to be comparable. The sequential analysis performed less well in the acoplanar jet search for large  $\Delta M$  values, whereas their results were very similar in the acoplanar lepton channels and in the low  $\Delta M$  region in general.

Tables 22 and 23 summarise the results at the final selection level of all neutralino searches. Table 24 shows the main background sources contributing in each channel and the typical efficiency of each search for MSSM points where it is relevant.

The effect of systematic uncertainties on background and efficiency evaluation was studied with the “shaking” method for high multiplicity topologies and with the “smearing” method for leptonic topologies (see section 6.2). The variations in the detection efficiencies were found to be small (the relative change was below 3% on average). The efficiencies for the “shaken” signal are typically larger than for the “unshaken” signal. The background estimated with the shaking method was typically 10% higher than the “unshaken” background. The variation of both background and efficiency is mostly due to a slightly higher observed missing energy in the “shaken” events.

### 6.7.2 Limits

In the absence of a signal, upper limits on neutralino production cross-sections were derived, using the dependence of the calculated efficiencies on the masses involved. The results obtained in different search topologies and at different centre-of-mass energies were combined using the Bayesian method [38] (see section 6.1).

The limits for  $\tilde{\chi}_1^0 \tilde{\chi}_2^0$  production, as obtained from the searches for acoplanar leptons and jets, are shown in figure 37 assuming different branching ratios.

$\sqrt{s}$ (GeV)	Acoplanar electrons search			
	Preselection		Final	
	Data	MC	Data	MC
192	65	$60 \pm 1$	5	$6.4 \pm 0.1$
196	135	$143 \pm 3$	19	$15.7 \pm 0.7$
200	192	$180 \pm 2$	12	$16.9 \pm 1.0$
202	68	$82 \pm 1$	8	$9.7 \pm 0.4$
205	64	$77 \pm 1$	18	$14.9 \pm 0.7$
207	72	$78 \pm 1$	9	$15.0 \pm 0.7$
208	10	$6.5 \pm 0.1$	4	$1.4 \pm 0.1$
206.5(*)	56	$62 \pm 1$	16	$12.6 \pm 0.7$
$\sqrt{s}$ (GeV)	Acoplanar muons search			
	Preselection		Final	
	Data	MC	Data	MC
192	102	$115 \pm 3$	13	$7.7 \pm 0.1$
196	298	$289 \pm 4$	18	$19.5 \pm 0.4$
200	340	$357 \pm 3$	15	$21.0 \pm 0.6$
202	200	$160 \pm 3$	14	$10.2 \pm 0.2$
205	179	$191 \pm 2$	18	$19.5 \pm 1.0$
207	180	$193 \pm 2$	20	$19.8 \pm 1.1$
208	24	$16 \pm 0.4$	3	$1.9 \pm 0.2$
206.5(*)	179	$191 \pm 2$	14	$16.3 \pm 0.3$
$\sqrt{s}$ (GeV)	Acoplanar jets search			
	Preselection		Final	
	Data	MC	Data	MC
192	927	$896 \pm 6$	3	$3.1 \pm 0.1$
196	2191	$2218 \pm 10$	13	$7.9 \pm 0.3$
200	2886	$2835 \pm 12$	9	$10.4 \pm 0.3$
202	1263	$1250 \pm 7$	7	$5.1 \pm 0.2$
205	1458	$1404 \pm 8$	14	$12.7 \pm 1.4$
207	1451	$1416 \pm 8$	15	$13.0 \pm 1.4$
208	133	$118 \pm 2$	2	$1.2 \pm 0.2$
206.5(*)	1066	$1014 \pm 8$	14	$7.8 \pm 0.4$

Table 18: Results of the likelihood ratio acoplanar jets and acoplanar leptons searches at the different selection levels and centre-of-mass energies. The number of events selected in data and expected from the SM simulation are given. Simulation errors are statistical. The systematic uncertainties on the background were estimated to be of the order of 3% for the acoplanar leptons topologies and of the order of 10% for the acoplanar jets topologies on the final level (see section 6.2); (\*) indicates the 2000 data taken with the sector 6 of the TPC off.

$\sqrt{s}$ (GeV)	ee selection		$\mu\mu$ selection		qq selection	
	Data	MC	Data	MC	Data	MC
192	0	$2.4 \pm 0.3$	3	$1.2 \pm 0.2$	1	$3.3 \pm 0.2$
196	11	$7.5 \pm 0.7$	4	$3.9 \pm 0.5$	9	$10.1 \pm 0.4$
200	6	$9.3 \pm 0.9$	0	$4.3 \pm 0.6$	5	$11.6 \pm 0.4$
202	5	$4.3 \pm 0.4$	1	$2.1 \pm 0.3$	5	$5.5 \pm 0.2$
205	5	$6.3 \pm 0.3$	5	$3.4 \pm 0.2$	7	$11.5 \pm 2.8$
207	6	$7.4 \pm 1.5$	3	$4.6 \pm 1.2$	12	$10.9 \pm 0.4$
208	2	$0.7 \pm 0.1$	1	$0.3 \pm 0.1$	4	$0.9 \pm 0.04$
206.5(*)	6	$4.4 \pm 0.6$	3	$2.5 \pm 0.4$	10	$8.0 \pm 0.5$
All	41	$42.3 \pm 2.1$	20	$22.3 \pm 1.5$	53	$61.8 \pm 3.0$

Table 19: Results of the acoplanar lepton and acoplanar jet sequential searches at the final selection level for the different flavours and centre-of-mass energies. The number of events selected in data and expected from the SM simulation are given. Simulation errors are statistical. The systematic uncertainties on the background were estimated to be of the order of 3% for the acoplanar leptons topologies and of the order of 10% for the acoplanar jets topologies (see section 6.2); (\*) indicates the 2000 data taken with the sector 6 of the TPC off.

Similarly, figures 38(a,b) show cross-section limits for  $\tilde{\chi}_2^0 \tilde{\chi}_i^0$  production ( $i = 3$  or 4). Figure 38(a) shows the limit obtained combining the results of the multijet and acoplanar jet searches in the case where  $\tilde{\chi}_i^0 \rightarrow \tilde{\chi}_2^0 q \bar{q}$  and  $\tilde{\chi}_2^0 \rightarrow \tilde{\chi}_1^0 q \bar{q}$ . Figure 38(b) gives the corre-

$\sqrt{s}$ (GeV)	Multijets without $\gamma$ search					
	Preselection		Intermediate		Final	
	Data	MC	Data	MC	Data	MC
192	873	$916 \pm 6$	114	$130.9 \pm 2.0$	3	$6.7 \pm 0.3$
196	2683	$2664 \pm 9$	383	$368.5 \pm 2.7$	23	$19.3 \pm 0.6$
200	2837	$2733 \pm 8$	417	$392.1 \pm 2.5$	20	$21.4 \pm 0.6$
202	1359	$1323 \pm 4$	208	$188.5 \pm 1.4$	8	$10.0 \pm 0.3$
205	2469	$2412 \pm 15$	378	$349.8 \pm 4.7$	15	$17.5 \pm 0.3$
207	2471	$2415 \pm 6$	405	$355.6 \pm 1.9$	20	$17.9 \pm 0.4$
208	213	$212 \pm 1$	33	$31.2 \pm 0.2$	3	$1.6 \pm 0.04$
206.5(*)	1701	$1248 \pm 6$	265	$225.3 \pm 1.8$	17	$12.9 \pm 0.5$
All	14606	$13923 \pm 22$	2203	$2042 \pm 7$	109	$107.3 \pm 1.2$
$\sqrt{s}$ (GeV)	Multijets with $\gamma$ search					
	Preselection		Intermediate		Final	
	Data	MC	Data	MC	Data	MC
192	11	$10.5 \pm 0.7$	4	$2.8 \pm 0.4$	0	$0.4 \pm 0.2$
196	29	$31.1 \pm 0.8$	6	$7.9 \pm 0.4$	0	$1.0 \pm 0.1$
200	33	$31.6 \pm 0.7$	8	$8.7 \pm 0.4$	1	$1.3 \pm 0.2$
202	17	$15.5 \pm 0.4$	4	$4.1 \pm 0.2$	0	$0.6 \pm 0.1$
205	28	$29.2 \pm 0.6$	8	$7.8 \pm 0.3$	2	$1.0 \pm 0.1$
207	28	$29.2 \pm 0.7$	7	$7.8 \pm 0.3$	0	$1.2 \pm 0.1$
208	1	$2.5 \pm 0.1$	0	$0.6 \pm 0.02$	0	$0.1 \pm 0.01$
206.5(*)	24	$14.2 \pm 0.5$	8	$4.0 \pm 0.2$	2	$0.7 \pm 0.1$
All	171	$164 \pm 2$	45	$44 \pm 1$	5	$6.3 \pm 0.4$

Table 20: Results of the multijets without  $\gamma$  and multijets with  $\gamma$  searches at the different selection levels and centre-of-mass energies. The numbers of events selected in data and expected from the SM simulation are given. Simulation errors are statistical. The systematic uncertainties on the background were estimated to be of the order of 10% on the final level (see section 6.2); (\*) indicates the 2000 data taken with the sector 6 of the TPC off.

$\sqrt{s}$ (GeV)	Multilepton search					
	Preselection		Intermediate		Final	
	Data	MC	Data	MC	Data	MC
192	1710	$1608 \pm 12$	26	$22.6 \pm 0.8$	3	$4.2 \pm 0.4$
196	5158	$4862 \pm 35$	64	$69.3 \pm 2.0$	13	$11.5 \pm 1.0$
200	5923	$5339 \pm 37$	61	$68.3 \pm 1.8$	11	$11.3 \pm 0.5$
202	2900	$2600 \pm 18$	36	$33.0 \pm 0.9$	4	$5.7 \pm 0.3$
205	5532	$5135 \pm 48$	57	$62.0 \pm 3.3$	13	$10.8 \pm 1.0$
207	5553	$5126 \pm 34$	55	$62.5 \pm 3.5$	13	$11.1 \pm 1.1$
208	486	$455 \pm 3$	7	$5.6 \pm 0.3$	0	$1.0 \pm 0.1$
206.5(*)	3911	$4135 \pm 26$	46	$44.8 \pm 1.3$	9	$8.7 \pm 0.7$
All	31173	$29260 \pm 85$	352	$368.1 \pm 5.8$	66	$64.3 \pm 2.1$
$\sqrt{s}$ (GeV)	Asymmetric tau search					
	Preselection		Intermediate		Final	
	Data	MC	Data	MC	Data	MC
192	1637	$1828 \pm 14$	23	$19.1 \pm 1.0$	1	$0.6 \pm 0.3$
196	5118	$5536 \pm 42$	57	$57.5 \pm 2.7$	4	$1.7 \pm 0.9$
200	5773	$6139 \pm 45$	58	$53.4 \pm 2.3$	1	$2.1 \pm 1.2$
202	2819	$2994 \pm 22$	34	$24.6 \pm 1.1$	2	$0.9 \pm 0.6$
205	5288	$5804 \pm 44$	45	$45.0 \pm 3.9$	0	$1.1 \pm 0.8$
207	5319	$5873 \pm 39$	48	$50.4 \pm 3.0$	4	$1.9 \pm 1.0$
208	491	$521 \pm 3$	4	$4.3 \pm 0.3$	0	$0.2 \pm 0.1$
206.5(*)	3318	$4613 \pm 29$	32	$31.1 \pm 1.6$	1	$1.5 \pm 0.6$
All	29763	$33308 \pm 94$	301	$285.4 \pm 6.5$	13	$10.0 \pm 2.2$

Table 21: Results of the multilepton and asymmetric tau searches at the different selection levels and centre-of-mass energies. The numbers of events selected in data and expected from the SM simulation are given. Simulation errors are statistical. The systematic uncertainties on the background were estimated to be of the order of 3% on the final level (see section 6.2); (\*) indicates the 2000 data taken with the sector 6 of the TPC off.

sponding limits when  $\tilde{\chi}_2^0 \rightarrow \tilde{\chi}_1^0 \gamma$ , as obtained from the search for multijet events with a photon signature.

$\sqrt{s}$ (GeV)	Data	Background
189	0	$0.42 \pm 0.17$
192	0	$0.02 \pm 0.06$
196	0	$0.06 \pm 0.02$
200	0	$0.25 \pm 0.11$
202	0	$0.13 \pm 0.05$
205–208	0	$0.21 \pm 0.04$
All	0	$1.10 \pm 0.19$

Table 22: Background and candidates in the  $\tilde{\chi}_2^0 \tilde{\chi}_2^0 \rightarrow \tilde{\tau}\tau\tilde{\tau}\tau$  analysis. This analysis did not include data from the period in 2000 when one sector of the TPC was off. The total expected background over the three years was  $1.10 \pm 0.19$  events, 55 % of which were two-fermion events, the remainder being four-fermion events. The systematic uncertainties on the background were estimated to be of the order of 5% on the final level (see section 6.2.2).

1999 Search	192 GeV		196 GeV		200 GeV		202 GeV	
	Data	MC.	Data	MC.	Data	MC.	Data	MC.
Acopl jets	3	$3.1 \pm 0.1$	13	$8.0 \pm 0.3$	9	$10.3 \pm 0.3$	7	$5.1 \pm 0.2$
Acopl electrons	5	$6.3 \pm 0.1$	19	$16.1 \pm 0.7$	12	$14.8 \pm 0.8$	8	$7.7 \pm 0.3$
Acopl muons	13	$7.7 \pm 0.1$	18	$19.5 \pm 0.4$	15	$21.0 \pm 0.5$	14	$10.2 \pm 0.2$
Multijets, $\gamma$ 's	0	$0.4 \pm 0.2$	0	$1.0 \pm 0.1$	1	$1.3 \pm 0.2$	0	$0.6 \pm 0.1$
Multijets, no $\gamma$	3	$6.7 \pm 0.3$	23	$19.3 \pm 0.6$	20	$21.4 \pm 0.6$	8	$10.0 \pm 0.3$
Multileptons	3	$4.2 \pm 0.4$	13	$11.5 \pm 1.0$	11	$11.3 \pm 0.5$	4	$5.7 \pm 0.3$
Asym tau cascades	1	$0.6 \pm 0.3$	4	$1.7 \pm 0.9$	1	$2.1 \pm 1.2$	2	$0.9 \pm 0.6$
All	28	$29 \pm 1$	90	$77 \pm 2$	69	$82 \pm 2$	43	$40 \pm 1$
2000 Search	205 GeV		207 GeV		208 GeV		206.5 GeV(*)	
	Data	MC.	Data	MC.	Data	MC.	Data	MC.
Acopl jets	14	$12.7 \pm 1.4$	15	$13.0 \pm 1.4$	2	$1.2 \pm 0.2$	14	$8.0 \pm 0.4$
Acopl electrons	18	$14.9 \pm 0.7$	9	$15.0 \pm 0.7$	3	$1.4 \pm 0.1$	16	$13.0 \pm 0.7$
Acopl muons	18	$19.5 \pm 1.0$	20	$19.8 \pm 1.1$	3	$1.8 \pm 0.2$	15	$15.4 \pm 0.3$
Multijets, $\gamma$ 's	2	$1.0 \pm 0.1$	0	$1.2 \pm 0.1$	0	$0.1 \pm 0.01$	2	$0.7 \pm 0.1$
Multijets, no $\gamma$	15	$17.5 \pm 0.3$	20	$17.9 \pm 0.4$	3	$1.6 \pm 0.04$	17	$12.9 \pm 0.5$
Multileptons	13	$10.8 \pm 1.0$	13	$11.1 \pm 1.1$	0	$1.0 \pm 0.1$	9	$8.7 \pm 0.7$
Asym tau cascades	0	$1.1 \pm 0.8$	4	$1.9 \pm 1.0$	0	$0.2 \pm 0.1$	1	$1.5 \pm 0.6$
All	80	$78 \pm 2$	81	$80 \pm 2$	11	$7.3 \pm 0.3$	74	$60 \pm 1$

Table 23: Results of the different neutralino searches. For any given search, events are explicitly rejected if accepted by one of the searches appearing earlier in the table; (\*) indicates the 2000 data taken with the sector 6 of the TPC off.

From the results of the search for  $\tilde{\chi}_2^0 \tilde{\chi}_2^0 \rightarrow \tilde{\tau}\tau\tilde{\tau}\tau$  described in section 5.2.3, an equivalent production cross-section at  $\sqrt{s} = 206.7$  GeV larger than 63 fb can be excluded. This limit is valid for  $30 \text{ GeV}/c^2 \leq M_{\tilde{\chi}_1^0} \leq 50 \text{ GeV}/c^2$  and  $M_{\tilde{\tau}} - M_{\tilde{\chi}_1^0} \leq 5 \text{ GeV}/c^2$  in the gaugino region  $|\mu| \gg M_2$ , where this channel is important for constraining the LSP mass. To combine data at different centre-of-mass energies the cross-section dependence on  $\sqrt{s}$  given by CMSSM in the neutralino and stau mass ranges indicated above was assumed. The corresponding expected limit was 68 fb.

The effect of the systematic and statistical errors of background and efficiency on the cross-section limits was evaluated using the method described in section 6.2.3 and found to be very small.

Search	Main SM bkg.	Eff. (%)
Acopl jets	$W^+W^-$ , $ZZ$	10 – 30
Acopl electrons	$W^+W^-$ , $\gamma\gamma \rightarrow e^+e^-$	10 – 40
Acopl muons	$W^+W^-$ , $\gamma\gamma \rightarrow \mu^+\mu^-$	10 – 40
Multijets, $\gamma$ 's	$Z\gamma$	10 – 20
Multijets, no $\gamma$	$W^+W^-$ , $Z\gamma$	10 – 40
Multileptons	$W^+W^-$	30 – 50
Asym tau cascades	$W^+W^-$ , $\gamma\gamma \rightarrow \mu^+\mu^-$	13 – 19
Double tau cascades	$ZZ$ , $ZZ^*$ , $Z\gamma^*$	10 – 20

Table 24: The main backgrounds and the typical efficiency of all of the neutralino searches for MSSM points where it is relevant is shown. The efficiencies depend typically on the masses of the sparticles involved in the process.

## 7 Combined exclusions and mass limits in the MSSM with gaugino and sfermion mass unification

### 7.1 The method

The method employed to set lower mass limits on the LSP mass and on the masses of other SUSY particles is to convert the negative results of the searches for charginos, neutralinos, sleptons and squarks into excluded regions in the  $(M_2, \mu)$  plane for different  $\tan \beta$  values, and then to find the minimal allowed sparticle masses as a function of  $\tan \beta$ . It is described in detail in [8,9]. The Higgs boson search in the maximal  $M_{h^0}$  scenario was used to exclude low values of  $\tan \beta$  [11].

Unless stated otherwise, the limits presented in the following are valid for  $M_2 \leq 1000$  GeV/ $c^2$  and for the  $\mu$  region in which the lightest neutralino is the LSP. The  $\mu$  range depends on the values of  $\tan \beta$  and  $m_0$ , and on the mixing parameters in the third family ( $A_\tau, A_t, A_b$ ). Unless stated otherwise, for high values of  $m_0$  (above 500 GeV/ $c^2$ ) the  $\mu$  range between –2000 and 2000 GeV/ $c^2$  was scanned, but the scan range was increased if any limit point was found to be close to the scan boundary.

#### 7.1.1 Method of combining different searches

In the scan of the SUSY parameter space the efficiencies of the different searches, as obtained in the previous sections, were parameterised for the dominant channels, and used together with the information on the number of events selected in data and the expected number of background events. The excluded regions obtained with the different searches were then simply superimposed.

In previous publications [8,9] it was verified that these parameterisations led to conservative results by comparing with a parallel approach, where these searches were applied to samples produced combining SGV with SUSYGEN (see section 4) to simulate simultaneously all channels of chargino, neutralino, slepton and squark production and decay.

The typical scan step size in  $\mu$  and  $M_2$  was 1 GeV/ $c^2$  except in the region of the LSP mass limit, where the step size was decreased to 0.5 GeV/ $c^2$ . The step size in  $m_0$  was variable, the density of points being increased in regions of potentially difficult mass configurations. Special care was taken to set up the scan logics in such a way that no such configuration was overlooked. In particular, whenever two nearby scan points were

excluded by different searches, the scan was performed with smaller steps between these points to check the continuity of the exclusion.

### 7.1.2 The influence of the $m_0$ value and of the mixing in the third family

The unification of sfermion masses to a common  $m_0$  at the GUT scale allows sfermion masses at the Electroweak Scale to be calculated as functions of  $\tan\beta$ ,  $M_2$  and  $m_0$ . In particular the masses of the sneutrino ( $\tilde{\nu}$ ), the left-handed selectron and smuon ( $\tilde{e}_L, \tilde{\mu}_L$ ), and the right-handed selectron and smuon ( $\tilde{e}_R, \tilde{\mu}_R$ ) can be expressed as<sup>18</sup>:

- (1)  $m_{\tilde{\nu}}^2 = m_0^2 + 0.77M_2^2 + 0.5m_Z^2 \cos 2\beta$
- (2)  $M_L^2 = m_0^2 + 0.77M_2^2 - 0.27m_Z^2 \cos 2\beta$
- (3)  $M_R^2 = m_0^2 + 0.22M_2^2 - 0.23m_Z^2 \cos 2\beta$

In the large  $m_0$  scenario,  $m_0 = 1000 \text{ GeV}/c^2$  was assumed, which implied sfermion masses of the same order. In this case only charginos, neutralinos and the Higgs boson could be produced at LEP<sup>19</sup> and the limits arise from a combination of the searches for these particles described in the previous sections of this paper and in [11].

For large  $m_0$ , the chargino pair-production cross-section is large and the chargino is excluded nearly up to the kinematic limit, provided  $M_2 < 200 \text{ GeV}/c^2$ .

It may also be remarked that at small  $M_2$ ,  $\Delta M = M_{\tilde{\chi}_1^\pm} - M_{\tilde{\chi}_1^0}$  is large, resulting in increased background from  $W^+W^-$  production. However, if  $|\mu|$  is small as well, the chargino tends to decay via  $\tilde{\chi}_1^\pm \rightarrow \tilde{\chi}_2^0 W^*$  to the next-to-lightest neutralino  $\tilde{\chi}_2^0$ , which then decays by  $\tilde{\chi}_2^0 \rightarrow \tilde{\chi}_1^0 \gamma$  or  $\tilde{\chi}_2^0 \rightarrow \tilde{\chi}_1^0 Z^*$ . For setting the mass limits, it is therefore important that the chargino search includes topologies with photons stemming from the decays  $\tilde{\chi}_1^\pm \rightarrow \tilde{\chi}_2^0 W^* \rightarrow \tilde{\chi}_1^0 \gamma W^*$ , since the search for topologies with photons does not suffer from  $W^+W^-$  background and is effective for large  $\Delta M$  (close to  $m_W$ ).

Of the detectable neutralino production channels (*i.e.* excluding  $\tilde{\chi}_1^0 \tilde{\chi}_1^0$ ), the  $\tilde{\chi}_1^0 \tilde{\chi}_2^0$  and  $\tilde{\chi}_1^0 \tilde{\chi}_3^0$  channels are dominant for large regions in the parameter space, but in order to cover as much as possible of the parameter space channels like  $\tilde{\chi}_2^0 \tilde{\chi}_3^0$  and  $\tilde{\chi}_2^0 \tilde{\chi}_4^0$  must also be considered, giving cascade decays with multiple jets or leptons in the final state. At large  $m_0$  the production cross-section for all these neutralino production channels drops to very small values for  $|\mu| \gtrsim 75 \text{ GeV}/c^2$ . This is because the two lightest neutralinos have very small higgsino component (photino  $\tilde{\chi}_1^0$  and zino  $\tilde{\chi}_2^0$ ) and their  $s$ -channel pair-production is therefore suppressed, while pair-production of heavier neutralinos is not kinematically accessible. Nevertheless, for  $\tan\beta < 1.5$  and  $M_2 > 68 \text{ GeV}/c^2$  the neutralino exclusion reaches beyond the kinematic limit for chargino production at negative  $\mu$  (see figure 39). This region of  $\tan\beta$  is now also excluded by the searches for the production of the lightest Higgs boson [11].

For medium  $m_0$ ,  $100 \text{ GeV}/c^2 \lesssim m_0 \lesssim 1000 \text{ GeV}/c^2$ , the  $\tilde{\chi}_1^0 \tilde{\chi}_2^0$  production cross-section in the gaugino-region ( $|\mu| \gtrsim 75 \text{ GeV}/c^2$ ) grows quickly as  $m_0$  falls, due to the rapidly rising contribution from the selectron  $t$ -channel exchange. Meanwhile, the chargino production cross-section in the gaugino region drops slowly, but it remains large enough to allow chargino exclusion nearly up to the kinematic limit for  $m_0 \gtrsim 200 \text{ GeV}/c^2$ . For lower  $m_0$  ( $\sim 100 \text{ GeV}/c^2$ ), the chargino production cross-section in the gaugino region is close to its minimum, while the neutralino production cross-section is very much enhanced. Consequently, the region of the  $(\mu, M_2)$  parameter space excluded by the

<sup>18</sup>It is worth noting that for  $\tan\beta \geq 1$  ( $\tan\beta < 1$ ) we have  $\cos 2\beta \leq 0$  ( $\cos 2\beta > 0$ ), so the  $\tilde{\nu}$  is never heavier (lighter) than the  $\tilde{e}_L$ .

<sup>19</sup>If  $|\mu|$  and/or mixing terms for the third family sfermions are sufficiently large, they can be light for large  $m_0$  as well, this case will be discussed further on.

searches for neutralino production at small  $m_0$  is larger than the one excluded by the search for chargino and neutralino production at large  $m_0$ , as shown in [7–9].

For small  $m_0$ ,  $m_0 \lesssim 100 \text{ GeV}/c^2$ , and small  $M_2$ ,  $M_2 \lesssim 200 \text{ GeV}/c^2$ , the situation is much more complicated because light sfermions affect not only the production cross-sections but also the decay patterns of charginos and neutralinos. Sleptons can also be searched for in direct pair-production. Excluded regions at small  $m_0$  arise from the combination of searches for chargino, neutralino and slepton production.

For small  $m_0$  and  $M_2$  the sneutrino is light, and for  $M_{\tilde{\chi}_1^\pm} > m_{\tilde{\nu}}$  the chargino decay mode  $\tilde{\chi}_1^\pm \rightarrow \tilde{\nu} \ell$  is dominant, leading to an experimentally undetectable final state if  $M_{\tilde{\chi}_1^\pm} \simeq m_{\tilde{\nu}}$ . In the gaugino region, for every value of  $M_2$  and  $\mu$ , an  $m_0$  can be found such that  $M_{\tilde{\chi}_1^\pm} \simeq m_{\tilde{\nu}}$ ; therefore the search for charginos cannot be used to exclude regions in the  $(\mu, M_2)$  plane if very small  $m_0$  values are allowed. The search for selectron production is used instead to put a limit on the sneutrino mass (and thus on the chargino mass), the selectron and the sneutrino masses being related by equations (1)–(3). The selectron pair-production cross-section is typically larger than the smuon pair-production cross-section, due to the contribution of  $t$ -channel neutralino exchange. However, at  $|\mu| \lesssim 200 \text{ GeV}/c^2$  the selectron production cross-section tends to be small and the exclusion arises mainly from the search for neutralino pair-production.

Mixing between the left-handed and right-handed sfermion states can be important for the third family sfermions and can lead to light  $\tilde{\tau}_1$ ,  $\tilde{b}_1$  and  $\tilde{t}_1$ . Mass splitting terms at the Electroweak Scale proportional to  $m_\tau(A_\tau - \mu \tan \beta)$ ,  $m_b(A_b - \mu \tan \beta)$ , and  $m_t(A_t - \mu / \tan \beta)$  were considered for  $\tilde{\tau}$ ,  $\tilde{b}$ , and  $\tilde{t}$  respectively (see section 2.2). In the first instance  $A_\tau = A_t = A_b = 0$  was assumed, then the dependence of the results on  $A_\tau$ ,  $A_b$  and  $A_t$  was studied. These terms lead to  $\tilde{\tau}_1$ ,  $\tilde{b}_1$  or  $\tilde{t}_1$  being degenerate in mass with  $\tilde{\chi}_1^0$ , or being the LSP for large values of  $|\mu|$ . The terms  $A_\tau, A_t, A_b$  are arbitrary unless further constraints on the model are imposed. To derive a conservative limit on the LSP mass, which is valid for any stau mixing scenario, a model was used with no mixing in the sbottom or stop sector, but only in the stau sector. This maximises the region in the parameter space where the stau can be close in mass to the LSP. Moreover the trilinear coupling  $A_\tau$  was adjusted in every point of the parameter space to get the stau close in mass to the LSP mass. For the stau to be degenerate with the LSP in the interesting mass range, the corresponding mixing term has to be of the order of  $12\,000 \text{ GeV}/c^2$ .

The results presented here are limited to the range of the  $\mu$  parameter where the lightest neutralino is the LSP.

## 7.2 Results

### 7.2.1 The LSP mass limit for large $m_0$

From charginos searches alone a limit of  $38.2 \text{ GeV}/c^2$  on the lightest neutralino mass is obtained, valid for  $\tan \beta \geq 1$  and a heavy sneutrino ( $m_{\tilde{\nu}} > 300 \text{ GeV}/c^2$ ). The limit is reached for  $\tan \beta = 1$ ,  $\mu = -65.7 \text{ GeV}/c^2$ ,  $M_2 = 65.0 \text{ GeV}/c^2$ . This limit improves by  $\sim 1 \text{ GeV}/c^2$  due to the constraint from the search for neutralino production; thus from chargino and neutralino searches the LSP mass can be constrained to be  $M_{\tilde{\chi}_1^0} > 39.2 \text{ GeV}/c^2$ , and the limit occurs at  $\tan \beta = 1$ . Figure 39 shows the region in the  $(\mu, M_2)$  plane for  $\tan \beta = 1$  excluded by the chargino and neutralino searches, relevant for the LSP mass limit at  $m_0 = 1000 \text{ GeV}/c^2$ . The lowest value of  $M_{\tilde{\chi}_1^0}$  not excluded by chargino and

neutralino searches occurs for  $\tan\beta=1$ ,  $\mu = -76.5 \text{ GeV}/c^2$  and  $M_2 = 67.0 \text{ GeV}/c^2$ . For these parameters,  $\tilde{\chi}_4^0\tilde{\chi}_2^0$  production and chargino pair-production are important.

Figure 40 gives the lower limit on  $M_{\tilde{\chi}_1^0}$  as a function of  $\tan\beta$ . At  $\tan\beta \gtrsim 1.2$  the neutralino search no longer contributes, the LSP limit is given by the chargino search, and its value reaches about half the limit on the chargino mass at large  $\tan\beta$ , where the isomass contours of  $\tilde{\chi}_1^\pm$  and  $\tilde{\chi}_1^0$  in the  $(\mu, M_2)$  plane become parallel. The rise of the LSP limit for small  $\tan\beta$  can be explained by the change of the shape of these contours with  $\tan\beta$ , as illustrated in [8,9]. It should be noted that, because the chargino and neutralino masses are invariant under the exchange  $\tan\beta \leftrightarrow 1/\tan\beta$ , the point  $\tan\beta = 1$  is the real minimum and the LSP limit for  $\tan\beta < 1$  can be obtained by replacing  $\tan\beta$  with  $1/\tan\beta$  in figure 40.

For  $M_A \leq 1000 \text{ GeV}/c^2$ ,  $A_t - \mu/\tan\beta = \sqrt{6} \text{ TeV}/c^2$  (maximal  $M_{h^0}$  scenario used in [11]), and  $m_t = 174.3 \text{ GeV}/c^2$ , the  $\tan\beta$  region  $0.5 \leq \tan\beta \leq 2.36$  is excluded by the Higgs searches. Thus including Higgs searches imposes a limit on  $M_{\tilde{\chi}_1^0}$  (see figure 40) of  $M_{\tilde{\chi}_1^0} > 49.0 \text{ GeV}/c^2$  for  $\tan\beta \geq 2.36$  and  $M_{\tilde{\chi}_1^0} > 48.5 \text{ GeV}/c^2$  for  $\tan\beta < 0.5$ .

Thus the lightest neutralino is constrained to have a mass:

$$M_{\tilde{\chi}_1^0} > 49.0 \text{ GeV}/c^2$$

for  $m_0 = 1000 \text{ GeV}/c^2$  and  $M_2 \leq 1000 \text{ GeV}/c^2$  and  $\tan\beta \geq 1.0$ . The limit occurs at the edge of the  $\tan\beta$  exclusion given by the searches for the Higgs boson. However, if  $m_t = 179 \text{ GeV}/c^2$ , the  $\tan\beta$  area excluded by searches for the Higgs boson shrinks to  $0.6 \leq \tan\beta \leq 2.0$  and these limits worsen to  $M_{\tilde{\chi}_1^0} > 48.5 \text{ GeV}/c^2$  for  $\tan\beta \geq 2.0$  and  $M_{\tilde{\chi}_1^0} > 47.0 \text{ GeV}/c^2$  for  $\tan\beta < 0.6$ . Thus the above limit worsens by 2 GeV if  $m_t = 179 \text{ GeV}/c^2$  and the  $\tan\beta < 1.0$  region is included.

It should be noted that the  $\tan\beta$  region excluded by Higgs boson searches is expected to shrink with the inclusion of complete one-loop corrections [49]. The LSP mass limit degrades in this case. Moreover, if there are sfermions lighter than  $M_{h^0}/2$ , the lightest Higgs boson will decay to them (see section 7.2.3). Such light sfermions are experimentally allowed only if they are degenerate in mass with the LSP. In this case, the lightest Higgs boson decays “invisibly”. The mass limit  $M_{h^0} > 112.1 \text{ GeV}/c^2$  set for an invisibly decaying Higgs boson [50] can be used to exclude small  $\tan\beta$ , and  $M_{\tilde{\chi}_1^0} > 48.5 \text{ GeV}/c^2$  for  $\tan\beta \geq 2.0$ .

### 7.2.2 The LSP mass limit for any $m_0$

Figure 40 also gives the lower limit on  $M_{\tilde{\chi}_1^0}$  as a function of  $\tan\beta$  for any  $m_0$ . The “any  $m_0$ ” limit resulting from chargino, neutralino and slepton searches follows the large  $m_0$  limit up to  $\tan\beta=1.4$ ; then it increases more slowly due to the opening of the possibility of the chargino-sneutrino degeneracy, reaching  $46 \text{ GeV}/c^2$  at  $\tan\beta \geq 2.36$  (edge of the region excluded by Higgs boson searches); finally, as discussed in more detail below, it falls to its lowest value,  $45.5 \text{ GeV}/c^2$ , at  $\tan\beta \geq 5$ , due to small  $M_{\tilde{\tau}_1} - M_{\tilde{\chi}_1^0}$ , if mixing in the stau sector is of the form  $A_\tau - \mu \tan\beta$ , and  $A_\tau = 0$ . This limit is set by searches for  $\tilde{\chi}_1^0\tilde{\chi}_2^0$  and  $\tilde{\chi}_2^0\tilde{\chi}_2^0$  production with  $\tilde{\chi}_2^0 \rightarrow \tilde{\tau}_1\tilde{\chi}_1^0$ .

Thus

$$M_{\tilde{\chi}_1^0} > 46.0 \text{ GeV}/c^2$$

independent of  $m_0$ , for  $\tan\beta \geq 1$  if there is no mixing in the third family ( $A_\tau = \mu \tan\beta$ ,  $A_b = \mu \tan\beta$ ,  $A_t = \mu/\tan\beta$ ), or if the mixing parameters leading to  $M_{\tilde{\tau}_1} - M_{\tilde{\chi}_1^0} < 6 \text{ GeV}/c^2$

are avoided. The Higgs boson search in the maximal  $M_{h^0}$  scenario was used to exclude  $0.5 \leq \tan \beta \leq 2.36$ .

LSP mass limits obtained with various assumptions are summarised in table 25.

### 7.2.3 The dependence of the LSP limit on the mixing in the third family.

Mixing in the third family affects in a complicated way the excluded regions obtained from Higgs, chargino, neutralino and squark searches, and a consistent discussion of the mixing is difficult.

For example, the maximal  $M_{h^0}$  scenario used to set  $\tan \beta$  limits from Higgs searches implies  $A_t - \mu/\tan \beta = \sqrt{6} \text{ TeV}/c^2$ , thus a different  $A_t$  for every  $\mu$ . Such a scenario implies as well that small  $m_0$  values are forbidden for  $M_2$  sufficiently small to be of interest from the point of view of the LSP mass limit<sup>20</sup>. Thus for consistency one should consider only the large  $m_0$  scenario for the LSP limit (thus higher limit), whenever  $\tan \beta$  limits from the maximal  $M_{h^0}$  scenario are used.

In the no-mixing scenario ( $A_\tau = \mu \tan \beta$ ,  $A_b = \mu \tan \beta$ ,  $A_t = \mu/\tan \beta$ ), the LSP limit occurs in the chargino-sneutrino degeneracy region, at  $\tan \beta > 1.5$ , where both the chargino and sneutrino mass limits are given by the selectron exclusion (see section 7.3). If there is no mixing in the stop sector, the  $\tan \beta$  region excluded by the Higgs searches grows to  $\tan \beta \leq 9.4$ , compared to  $0.5 \leq \tan \beta \leq 2.36$  for the maximal  $M_{h^0}$  scenario. However, there is no improvement of the LSP limit as compared to  $M_{\tilde{\chi}_1^0} > 46.0 \text{ GeV}/c^2$  given above, as the  $\tan \beta$  dependence of the limit “flattens out” at large  $\tan \beta$  (see figure 40).

As discussed in previous papers [8,9], mixing in the stau sector can lead to a configuration where  $M_{\tilde{\tau}_1} - M_{\tilde{\chi}_1^0}$  is small enough to make the  $\tilde{\tau}_1$  undetectable and cause a blind spot both in  $\tilde{\tau}_1$  and chargino exclusion. For  $A_t = A_\tau = A_b = 0$ , with the present data, the LSP mass limit occurs a) at large enough  $M_2$  that already for  $\tan \beta \geq 3$  both  $M_{\tilde{b}_1}$  and  $M_{\tilde{t}_1}$  are pushed above  $M_{\tilde{\tau}_1}$ <sup>21</sup>, and  $\tilde{\tau}_1$  can become degenerate in mass with  $\tilde{\chi}_1^0$ , and b) at large enough  $m_0$  that selectron and sneutrino pair-production are not allowed by kinematics.

For the above mixing assumptions, the mass of the lightest Higgs boson corresponding to the LSP limit point varies between 109 and 120  $\text{GeV}/c^2$ , depending on the  $\tan \beta$  region. However, when the stau is light the lightest Higgs boson decays predominantly to  $\tilde{\tau}_1 \tilde{\tau}_1$ , thus “invisibly”. The mass limit  $M_{h^0} > 112.1 \text{ GeV}/c^2$  set for an invisibly decaying Higgs boson [50] can be used to exclude some of these points, but it is enough to change slightly the mixing in the stop sector ( $A_t$ ) to push the Higgs mass above 112.1  $\text{GeV}/c^2$ .

For such a mixing configuration and for  $\tan \beta \gtrsim 3$ , the LSP limit is therefore set by the searches for stop and sbottom and those for  $\tilde{\chi}_1^0 \tilde{\chi}_2^0$  production with  $\tilde{\chi}_2^0 \rightarrow \tilde{\tau}_1 \tau$ , and it falls to  $M_{\tilde{\chi}_1^0} > 45.5 \text{ GeV}/c^2$  (see dot-dashed line in figure 40). This limit was verified to be robust when varying independently  $A_t, A_\tau$  and  $A_b$  in the range  $\pm 1000 \text{ GeV}/c^2$ .

As noted in previous papers [8,9], it is the appearance of the light sbottom and stop which protects the stau from being degenerate in mass with the LSP for very large  $m_0$  values, where the  $\tilde{\chi}_1^0 \tilde{\chi}_2^0$  and  $\tilde{\chi}_2^0 \tilde{\chi}_2^0$  production cross-sections are small. This is illustrated in figure 41, where the stop, sbottom, and stau masses at the largest allowed  $|\mu|$  value at

<sup>20</sup>To avoid “tachyonic” mass solutions for the squarks and sleptons we must have  $m_{ll} + m_{rr} > \sqrt{(m_{ll} - m_{rr})^2 + 4m_{lr}^2}$ , where  $m_{lr}$  is the off-diagonal mixing term, and  $m_{ll}, m_{rr}$  are the diagonal mass terms. For example, for the stop we have:  $m_{lr} = m_{top}(A_t - \mu/\tan \beta)$  and  $m_{ll} \simeq m_0^2 + 9M_2^2 + m_{top}^2 + m_Z^2 \cos 2\beta(0.5 - 2/3 \sin^2 \theta_W)$ ,  $m_{rr} \simeq m_0^2 + 8.3M_2^2 + m_{top}^2 + 2/3m_Z^2 \cos 2\beta \sin^2 \theta_W$ ; for an example value of  $A_t - \mu/\tan \beta = \sqrt{6} \text{ TeV}/c^2$ , the condition above sets a lower limit on a combination of  $m_0^2$  and  $M_2^2$ :  $m_0^2 + 8.5M_2^2 > 0.39 (\text{TeV}/c)^2$ . Thus, if  $M_2 < 190 \text{ GeV}/c^2$  we must have  $m_0 > 300 \text{ GeV}/c^2$ .

<sup>21</sup>The “mixing-independent” (diagonal) terms of the mass matrices grow faster with  $M_2$  for squarks than for sleptons, and they have different dependence on  $\tan \beta$ . For example, for  $A_t = A_\tau = A_b = 0$ ,  $\mu = 0$ , and  $\tan \beta = 1$ , both the  $\tilde{t}_1$  and  $\tilde{b}_1$  are heavier than the  $\tilde{\tau}_1$ ; but they become lighter than the  $\tilde{\tau}_1$  for large  $|\mu|$  values. The mass hierarchy between  $\tilde{\tau}_1$ ,  $\tilde{b}_1$ , and  $\tilde{t}_1$  depends on  $M_2$ ,  $\tan \beta$ ,  $\mu$ , and  $m_0$ .

the lowest non-excluded  $M_2$  are plotted. At large  $\tan \beta$ , the largest  $|\mu|$  value occurs when the sbottom and stop masses have their lowest non-excluded (see section 6.5) values. In a pathological model where there is no mixing in the sbottom or stop sector ( $A_b = \mu \tan \beta$ ,  $A_t = \mu / \tan \beta$ ) but only in the stau sector,  $\tilde{\tau}_1$  can be made degenerate with  $M_{\tilde{\chi}_1^0}$  even at large values of  $m_0$  and  $|\mu|$  so that the  $\tilde{\chi}_1^0 \tilde{\chi}_2^0$  and  $\tilde{\chi}_2^0 \tilde{\chi}_2^0$  production cross-sections at LEP are very small and the production of the Higgs boson and other sfermions is not accessible kinematically. However, for large  $m_0$  values the  $\tilde{\chi}_1^\pm \tilde{\chi}_1^\pm$  cross-section is sufficiently large to set a limit on the production of “invisibly” decaying charginos ( $\tilde{\chi}_1^\pm \rightarrow \tilde{\tau}_1 \nu$ ,  $\tilde{\tau}_1 \rightarrow \tilde{\chi}_1^0 \tau$ ) from the search with an ISR photon (see section 6.6.2). The limit set on the neutralino mass in such a scenario is 39  $\text{GeV}/c^2$  for  $\tan \beta > 2$  and is illustrated in figure 42.

In mSUGRA (as defined in section 2),  $|\mu|^2$  is in the range  $3.3 m_{1/2}^2 - 0.5 m_Z^2 < \mu^2 < m_0^2 + 3.8 m_{1/2}^2$  for  $\tan \beta > 2$  and a light stau cannot be degenerate with neutralino for large  $m_0$ . Neutralino production cross-section is thus large, and neutralino searches set a limit on the LSP mass for small  $M_{\tilde{\tau}_1} - M_{\tilde{\chi}_1^0}$  which is close to the one obtained for heavy sleptons (about 50  $\text{GeV}/c^2$ ).

#### 7.2.4 The influence of radiative corrections to the gaugino mass relations on the LSP limit.

The relations between chargino, neutralino and gluino masses and  $|\mu|$  and  $M_2$  are affected by radiative corrections of the order of 2%–20% [51]. However, only the relative relations between chargino, neutralino and gluino masses are important from the experimental point of view, and here the corrections are much smaller. For example, the relation  $M_{\tilde{\chi}_1^\pm}(M_{\tilde{\chi}_2^\pm})/M_{\tilde{\chi}_1^0} \simeq 2$  in the gaugino region, which is exploited to set a limit on the LSP mass, receives corrections only of the order of 2%. The ratio  $M_1/\alpha_1 : M_2/\alpha_2$  can receive corrections of similar order [52], thus affecting  $M_{\tilde{\chi}_1^\pm}(M_{\tilde{\chi}_2^\pm})/M_{\tilde{\chi}_1^0} \simeq 2$  in the same way.

It is enough to lower the LSP limits presented here by 1  $\text{GeV}/c^2$  (2%) to conservatively account for the 2% change of the  $M_{\tilde{\chi}_1^\pm}(M_{\tilde{\chi}_2^\pm})/M_{\tilde{\chi}_1^0}$  ratio.

### 7.3 $\tilde{\chi}_1^\pm$ mass limits for any $m_0$

Figure 43 shows the chargino mass limit as a function of  $\tan \beta$  for  $M_2 < 200 \text{ GeV}/c^2$ . The lowest non-excluded chargino mass is found at MSSM points very close to those giving the LSP mass limit, and the arguments presented in section 7.2.2 also apply to explain the dependence of the chargino mass limit on  $\tan \beta$ . For  $\tan \beta \lesssim 1.4$  the limit occurs at large  $m_0$  values. For  $1.4 \lesssim \tan \beta \lesssim 3$  and  $M_2 < 200 \text{ GeV}/c^2$ , the limit occurs at small  $m_0$  in the chargino-sneutrino degeneracy region. It falls at  $\tan \beta \gtrsim 4$  because of the small  $\Delta M = M_{\tilde{\tau}} - M_{\tilde{\chi}_1^0}$ .

The lightest chargino is constrained to have a mass:

$$M_{\tilde{\chi}_1^\pm} > 94 \text{ GeV}/c^2,$$

independently of  $m_0$ , for  $\tan \beta \leq 40$ ,  $M_2 \leq 1000 \text{ GeV}/c^2$ , if either there is no mixing in the third family ( $A_\tau = \mu \tan \beta$ ,  $A_b = \mu \tan \beta$ ,  $A_t = \mu / \tan \beta$ ) or the mixing parameters leading to  $M_{\tilde{\tau}_1} - M_{\tilde{\chi}_1^0} < 6 \text{ GeV}/c^2$  are avoided.

If mixing in the stau sector is of the form  $A_\tau - \mu \tan \beta$ , and  $A_\tau = 0$ , the limit falls to 90  $\text{GeV}/c^2$ , at  $\tan \beta \geq 3$ , due to small  $M_{\tilde{\tau}_1} - M_{\tilde{\chi}_1^0}$ . This limit is robust when varying  $A_t, A_\tau$

and  $A_b$  independently in the range  $\pm 1000$  GeV/ $c^2$ . In the “arbitrary” mixing scenario described above, where there is no mixing in the stop and sbottom sector, but only in the stau sector, this limit falls to 80 GeV/ $c^2$  and it is independent of the stau mixing.

The chargino mass limits for large  $M_2$  values, where the chargino can be degenerate in mass with the LSP are close to 75 GeV/ $c^2$  (see section 6.6.2).

Chargino mass limits obtained with various assumptions are summarised in table 25.

## 7.4 $\tilde{\nu}$ and $\tilde{e}_R$ mass limits for any $m_0$

The sneutrino and the  $\tilde{e}_R$  mass limits are:

$$m_{\tilde{\nu}} > 94 \text{ GeV}/c^2 \text{ and } M_{\tilde{e}_R} > 94 \text{ GeV}/c^2.$$

These limits, shown in figure 43, were obtained assuming no mass splitting in the third sfermion family ( $A_\tau = \mu \tan \beta$ ), implying  $M_{\tilde{e}_R} = M_{\tilde{\tau}_R} = M_{\tilde{\tau}_1} = M_{\tilde{\mu}_R}$ , as this gives the lowest values.

These limits result from the combination of slepton and neutralino searches. The selectron mass limit (see figure 43, dotted curve) is valid for  $-1000 \text{ GeV}/c^2 \leq \mu \leq 1000 \text{ GeV}/c^2$  and  $1 \leq \tan \beta \leq 40$  provided that  $M_{\tilde{e}_R} - M_{\tilde{\chi}_1^0} > 10 \text{ GeV}/c^2$ , and it allows a limit to be set on the sneutrino mass as shown in figure 43 (dashed curve). The sneutrino mass limit is expected to rise for  $\tan \beta < 1$ , the sneutrino being heavier than the  $\tilde{e}_R$  for small  $\tan \beta$ . The selectron mass limit for  $\tan \beta = 1.5$  and  $\mu = -200 \text{ GeV}/c^2$  is presented in section 6.4.1.

Slepton mass limits obtained with different assumptions are summarised in table 25.

## 7.5 MSSM parameter space exclusion

The limits on Higgs, chargino, neutralino, slepton and squark production used in the previous sections to set a mass limit on the LSP and other particles can be also used to exclude regions in a parameter space of the CMSSM. The excluded regions in the  $(\mu, M_2)$  plane for  $\tan \beta = 35$  and two assumptions about  $m_0$  and mixing in the third family are shown in figure 44.

# 8 Summary

Searches for charginos, neutralinos, sleptons and squarks in  $e^+e^-$  collisions at centre-of-mass energies up to 208 GeV were performed with the DELPHI detector at LEP. No evidence for a signal was found in any of the channels and 95% CL upper limits on the production cross-sections were derived. Under assumptions that depend on the channel lower limits on the masses of SUSY particles were set. In particular, in the framework of constrained MSSM scenarios with gravity-induced SUSY breaking, regions of the parameter space can be excluded, and these exclusions can be translated into limits on the masses of SUSY particles. The combination of the results of the different search channels is crucial to ensure the best possible coverage of the parameter space.

A summary of the obtained lower limits on the masses of SUSY particles is shown in table 25. The results presented extend and confirm previous exclusions set by DELPHI (see [2] to [9]) and by the other LEP experiments [53].

Particle	Validity conditions	Mass limit (GeV/c <sup>2</sup> )
$\tilde{e}_R$	$\tan\beta=1.5, \mu=-200, \Delta M>15$	94
	CMSSM, $\Delta M>10$	94
$\tilde{\mu}_R$	$\text{BR}(\tilde{\mu} \rightarrow \mu \tilde{\chi}^0)=1, \Delta M>5$	88
	CMSSM, $\Delta M>10$	94
$\tilde{\tau}$	$\text{BR}(\tilde{\tau} \rightarrow \tau \tilde{\chi}^0)=1, \Delta M \geq m_\tau$	26
$\tilde{\tau}_R$	$\text{BR}(\tilde{\tau} \rightarrow \tau \tilde{\chi}^0)=1, \Delta M>15, \text{no mixing}$	85
$\tilde{\tau}_{min}$	$\text{BR}(\tilde{\tau} \rightarrow \tau \tilde{\chi}^0)=1, \Delta M>15, \text{minimal cross-section}$	82
$\tilde{\nu}$	CMSSM, $(M_{\tilde{e}_R} - M_{\tilde{\chi}_1^0})>10$	94
$\tilde{b}$	$\text{BR}(\tilde{b} \rightarrow b \tilde{\chi}^0)=1, \Delta M>7, \text{no mixing}$	93
	$\text{BR}(\tilde{b} \rightarrow b \tilde{\chi}^0)=1, \Delta M>7, \text{minimal cross-section}$	76
$\tilde{t}$	$\text{BR}(\tilde{t} \rightarrow c \tilde{\chi}^0)=1, \Delta M>10, \text{no mixing}$	96
	$\text{BR}(\tilde{t} \rightarrow c \tilde{\chi}^0)=1, \Delta M>2, \text{no mixing}$	75
	$\text{BR}(\tilde{t} \rightarrow c \tilde{\chi}^0)=1, \Delta M>10, \text{minimal cross-section}$	92
	$\text{BR}(\tilde{t} \rightarrow c \tilde{\chi}^0)=1, \Delta M>2, \text{minimal cross-section}$	71
$\tilde{\chi}^\pm$	$m_{\tilde{\nu}}>1000, \Delta M>10, M_1 = \sim 0.5M_2,$	102.7
	$M_{\tilde{f}} > M_{\tilde{\chi}^\pm}, \Delta M>3$	97
	$M_{\tilde{f}} > M_{\tilde{\chi}^\pm}, \text{any } \Delta M, M_1 = \sim 0.5M_2$	75
	$m_{\tilde{\nu}}>300,  \mu  \geq M_2, \text{no gaugino mass unification, any } \Delta M$	70
	CMSSM, $\Delta M>3, \text{any } m_0, \text{no mixing or } \Delta M(\tilde{\tau}-\tilde{\chi}^0)>6$	94
	CMSSM, any $m_0, \text{any } M_2, \tan\beta < 40, \text{mixing } A_\tau=A_b=A_t=0$	90
$\tilde{\chi}^0$	CMSSM, high $m_0, \tan\beta > 1, \text{maximal mixing in } \tilde{t} \text{ sector}$	49
	CMSSM, any $m_0, \tan\beta < 40, \text{no mixing or } \Delta M(\tilde{\tau}-\tilde{\chi}^0)>6$	46
	CMSSM, any $m_0, \tan\beta < 40, \text{mixing } A_\tau=A_b=A_t=0$	46
	CMSSM, any $m_0, 1 < \tan\beta < 40, \text{mix. } A_\tau=A_b=0, A_t = \sqrt{6} \text{ TeV/c}^2$	49

Table 25: Summary of mass limits for supersymmetric particles and their validity conditions. In each line of the table  $\Delta M$  is the mass difference between the corresponding sparticle and the LSP. All masses and  $\Delta M$  values are in  $\text{GeV}/c^2$ . CMSSM refers to a model with gauge and sfermion mass unification, where  $\mu$  however is a free parameter (see section 2). Neutralino mass limits should be lowered by  $1 \text{ GeV}/c^2$  if the radiative corrections of [51] are taken into account.

## Acknowledgements

We are greatly indebted to our technical collaborators, to the members of the CERN-SL Division for the excellent performance of the LEP collider, and to the funding agencies for their

support in building and operating the DELPHI detector.

We acknowledge in particular the support of

Austrian Federal Ministry of Education, Science and Culture, GZ 616.364/2-III/2a/98,  
FNRS-FWO, Flanders Institute to encourage scientific and technological research in the industry (IWT), Federal Office for Scientific, Technical and Cultural affairs (OSTC), Belgium,

FINEP, CNPq, CAPES, FUJB and FAPERJ, Brazil,

Czech Ministry of Industry and Trade, GA CR 202/99/1362,

Commission of the European Communities (DG XII),

Direction des Sciences de la Matière, CEA, France,

Bundesministerium für Bildung, Wissenschaft, Forschung und Technologie, Germany,

General Secretariat for Research and Technology, Greece,

National Science Foundation (NWO) and Foundation for Research on Matter (FOM),  
The Netherlands,

Norwegian Research Council,

State Committee for Scientific Research, Poland, SPUB-M/CERN/PO3/DZ296/2000,  
SPUB-M/CERN/PO3/DZ297/2000 and 2P03B 104 19 and 2P03B 69 23(2002-2004)

JNICT–Junta Nacional de Investigaçāo Científica e Tecnológica, Portugal,

Vedecka grantova agentura MS SR, Slovakia, Nr. 95/5195/134,

Ministry of Science and Technology of the Republic of Slovenia,

CICYT, Spain, AEN99-0950 and AEN99-0761,

The Swedish Natural Science Research Council,

Particle Physics and Astronomy Research Council, UK,

Department of Energy, USA, DE-FG02-01ER41155,

EEC RTN contract HPRN-CT-00292-2002.

## References

- [1] P. Fayet and S. Ferrara, Phys. Rep. **32** (1977) 249;  
H.P. Nilles, Phys. Rep. **110** (1984) 1;  
H.E. Haber and G.L. Kane, Phys. Rep. **117** (1985) 75.
- [2] DELPHI Coll., P. Abreu *et al.*, E. Phys. J. **C19** (2001) 29;  
DELPHI Coll., P. Abreu *et al.*, E. Phys. J. **C6** (1999) 385.
- [3] DELPHI Coll., P. Abreu *et al.*, Phys. Lett. **B496** (2000) 59.
- [4] DELPHI Coll., P. Abreu *et al.*, Phys. Lett. **B479** (2000) 118;  
T. Alderweireld, I. Gil, P. Rebecchi, *Review of the chargino search in DELPHI. Latest results at  $E_{cm} = 189$  GeV*, CERN-OPEN-2002-031;  
DELPHI Coll., P. Abreu *et al.*, Phys. Lett. **B446** (1999) 75.
- [5] DELPHI Coll., J. Abdallah *et al.*, E. Phys. J. **C27** (2003) 153. DELPHI Coll., P. Abreu *et al.*, Phys. Lett. **B503** (2001) 34.
- [6] DELPHI Coll., P. Abreu *et al.*, Phys. Lett. **B485** (2000) 95;  
DELPHI Coll., P. Abreu *et al.*, E. Phys. J. **C11** (1999) 1.
- [7] DELPHI Coll., P. Abreu *et al.*, E. Phys. J. **C19** (2001) 201.

- [8] DELPHI Coll., P. Abreu *et al.*, Phys. Lett. **B489** (2000) 38.
- [9] M. Espirito Santo, K. Hultqvist, P. Johansson, A. Lipniacka, F. Mazzucato, *Limits on the masses of supersymmetric particles at  $\sqrt{s}$  up to 202 GeV*, CERN-OPEN-2002-014.
- [10] R. Arnowitt, A. Chamseddine and P. Nath, *N=1 Supergravity*, World Scientific, Singapore, 1984.
- [11] DELPHI Coll., *Final results from DELPHI on the searches for SM and MSSM Neutral Higgs bosons*, EP 2003-008 (11 February 2003), Submitted to Eur. Phys. J. C.
- [12] C.H. Chen, M. Drees, J.F. Gunion, Phys. Rev. **D55** (1997) 330, erratum/addendum *ibid.* **D60**:039901 (1999).
- [13] DELPHI Coll., P. Aarnio *et al.*, Nucl. Instr. and Meth. **303** (1991) 233; DELPHI Coll., P. Abreu *et al.*, Nucl. Instr. and Meth. **378** (1996) 57.
- [14] P. Rebecchi, *Optimisation de l'herméticité du détecteur DELPHI pour la recherche de particules supersymétriques à LEP2*, Ph.D. thesis, LAL 96-30 (May 1996), Université Paris XI Orsay, CERN THESIS-96-003.
- [15] T. Sjöstrand, Comp. Phys. Comm. **39** (1986) 347; T. Sjöstrand, PYTHIA 5.6 and JETSET 7.3, CERN-TH/6488-92.
- [16] J.E. Campagne and R. Zitoun, Z. Phys. **C43** (1989) 469.
- [17] S. Jadach, B.F.L. Ward and Z. Was, Comp. Phys. Comm. **79** (1994) 503.
- [18] S. Jadach, W. Placzek and B.F.L. Ward, Phys. Lett. **B390** (1997) 298.
- [19] F.A. Berends, R. Pittau, R. Kleiss, Comp. Phys. Comm. **85** (1995) 437.
- [20] J. Fujimoto *et al.*, Comp. Phys. Comm. **100** (1997) 128
- [21] S. Nova, A. Olshevski, and T. Todorov, *A Monte Carlo event generator for two photon physics*, DELPHI note 90-35 (1990).
- [22] R. Engel, Z. Phys. **C66** (1995) 203; R. Engel and J. Ranft, Phys. Rev. **D54** (1996) 4244.
- [23] F.A. Berends, P.H. Daverveldt, R. Kleiss, Comp. Phys. Comm. **40** (1986) 271, Comp. Phys. Comm. **40** (1986) 285, Comp. Phys. Comm. **40** (1986) 309.
- [24] S. Katsanevas and P. Morawitz, Comp. Phys. Comm. **112** (1998) 227.
- [25] G. Altarelli *et al.*, *Physics at LEP2*, Yellow Report CERN 96-01, vol. 2. (1996)
- [26] DELPHI Coll., P. Abreu *et al.*, Z. Phys. **C73** (1996) 11.
- [27] R. Keranen, A. Sopczak, H. Nowak, M. Berggren, E. Phys. J. **C7** (2000) 1.
- [28] S. Catani *et al.*, Phys. Lett. **B269** (1991) 432.
- [29] F. Cossutti, A. Tonazzo, F. Mazzucato, *REMCLU : a package for the Reconstruction of Electromagnetic CLusters at LEP200*, DELPHI note 2000-164 PROG 242 (2000).
- [30] DELPHI Coll., P. Abreu *et al.*, Z. Phys. **C70** (1996) 531; G. Borisov, C. Mariotti, Nucl. Instr. and Meth. **372** (1996) 181.
- [31] J. Neyman and K. Pearson, Phil. Trans. R. Soc. **A231** (1933) 289; T.W. Anderson, *An Introduction to multivariate analysis*, New York Wiley, 1958.
- [32] A. Zell *et al.*, SNNS user manual : Version 4.1 (1995), "<http://www.ra.informatik.uni-tuebingen.de/SNNS/>".
- [33] A. Read *et al.*, *1st Workshop on Confidence Limits*, Yellow report CERN 2000-005, (May 2000) 81-103; A. Read, note DELPHI 97-158 PHYS 737.
- [34] DELPHI Coll., P. Abreu *et al.*, Phys. Lett. **B444** (1998) 491.
- [35] T. Alderweireld, *Search for charginos in e+e- interactions with the DELPHI detector at LEP*, Ph.D. thesis, Université de Mons (Sept. 2002), CERN-THESIS-03-009.

- [36] A.V. Oppenheim and R.W. Schafer, *Discrete-time signal processing*, Prentice-Hall, 1989
- [37] Particle Data Group, R.M. Barnett *et al.*, Phys. Rev. **D54** (1996) .
- [38] V.F. Obraztsov, Nucl. Instr. and Meth. **316** (1992) 388;  
V.F. Obraztsov, Nucl. Instr. and Meth. **399** (1997) 500.
- [39] S. Jadach *et al.*, *LEP2 Monte Carlo Workshop : Report of the Working Groups on Precision Calculations for LEP2 Physics*, Yellow Report CERN 2000-009, (September 2000).
- [40] T. Alderweireld, S. Todorovova and P. Verdier, *Study of the hadronic  $\gamma\gamma$  interactions at  $\sqrt{s} = 200\text{GeV}$* , CERN-OPEN-2002-032.
- [41] DELPHI, Coll., J. Abdallah *et al.*, *ZZ production in  $e^+e^-$  interactions at  $\sqrt{s} = 183 - 209\text{ GeV}$* , to be submitted to E. Phys. J. C.
- [42] A. Perrotta, Int. J. Mod. Phys. **C13** (2002) 989.
- [43] ALEPH Coll., D.Decamp *et al.*, Phys. Rep. **216** (1992) 253;  
L3 Coll., M. Acciari *et al.*, Phys. Lett. **B350** (1995) 109;  
OPAL Coll., G. Alexander *et al.*, Phys. Lett. **B377** (1996) 273;  
DELPHI Coll., A. Lopez-Fernandez, *Search for  $Z^0$  decays into sleptons and neutralinos using the DELPHI detector*, DELPHI note 92-95 (Dallas) PHYS 206.
- [44] DELPHI Coll., P. Abreu *et al.*, E. Phys. J. **C16** (2000) 371;  
ALEPH, DELPHI, L3, OPAL Coll., D. Abbaneo *et al.*, *A combination of preliminary electroweak measurements and constraints on the Standard Model*, CERN-EP/2001-098.
- [45] Particle Data Group, J. Bartels *et al.*, E. Phys. J. **C15** (2000) 1.
- [46] K.Mönig, *Model independent limit of the Z-decay-width into unknown particles*, CERN-OPEN-97-040 and DELPHI 97-174 PHYS 748.
- [47] ASP Collaboration: C. Hearty *et al.*, Phys. Rev. **D39** (3207) 1989.
- [48] A. Bartl *et al.*, Z. Phys. **C76** (1997) 549.
- [49] M. Frank *et al.*, hep-ph/0212037.
- [50] DELPHI Coll., *Searches for Invisibly decaying Higgs bosons with the DELPHI detector at LEP*, to be submitted to E. Phys. J. C.;  
M. Stanitzki *et al.*, *Searches for Invisibly decaying Higgs bosons*, DELPHI note 2002-025 CONF 559, July 2002, contributed paper for ICHEP 2002, Amsterdam.
- [51] D. Pierce and A. Papadopoulos, Phys. Rev. D **50** (1994) 565; D. Pierce and A. Papadopoulos, Nucl. Phys. B **430** (1994) 278.
- [52] Graham D. Kribs, Nucl. Phys. B **535**(1998) 41.
- [53] ALEPH Coll., D. Abbaneo *et al.*, Phys. Lett. **B499** (2001) 67;  
ALEPH Coll., D. Abbaneo *et al.*, *Search for Charginos and Neutralinos in  $e + e^-$  Collisions at  $\sqrt{s}$  up to 208 GeV and Mass Limit for the Lightest Neutralino*, ALEPH 2001-009, February 2001;  
L3 Coll., P. Achard *et al.*, *Search for Supersymmetry in  $e + e^-$  collisions at  $\sqrt{s} = 202-208\text{ GeV}$* , L3 note 2644, February 2001;  
OPAL Coll., G. Abbiendi *et al.*, *New Particle Searches in  $e^+e^-$  Collisions at  $\sqrt{s} = 200-209\text{ GeV}$* , Opal Physics note PN470, February 2001.

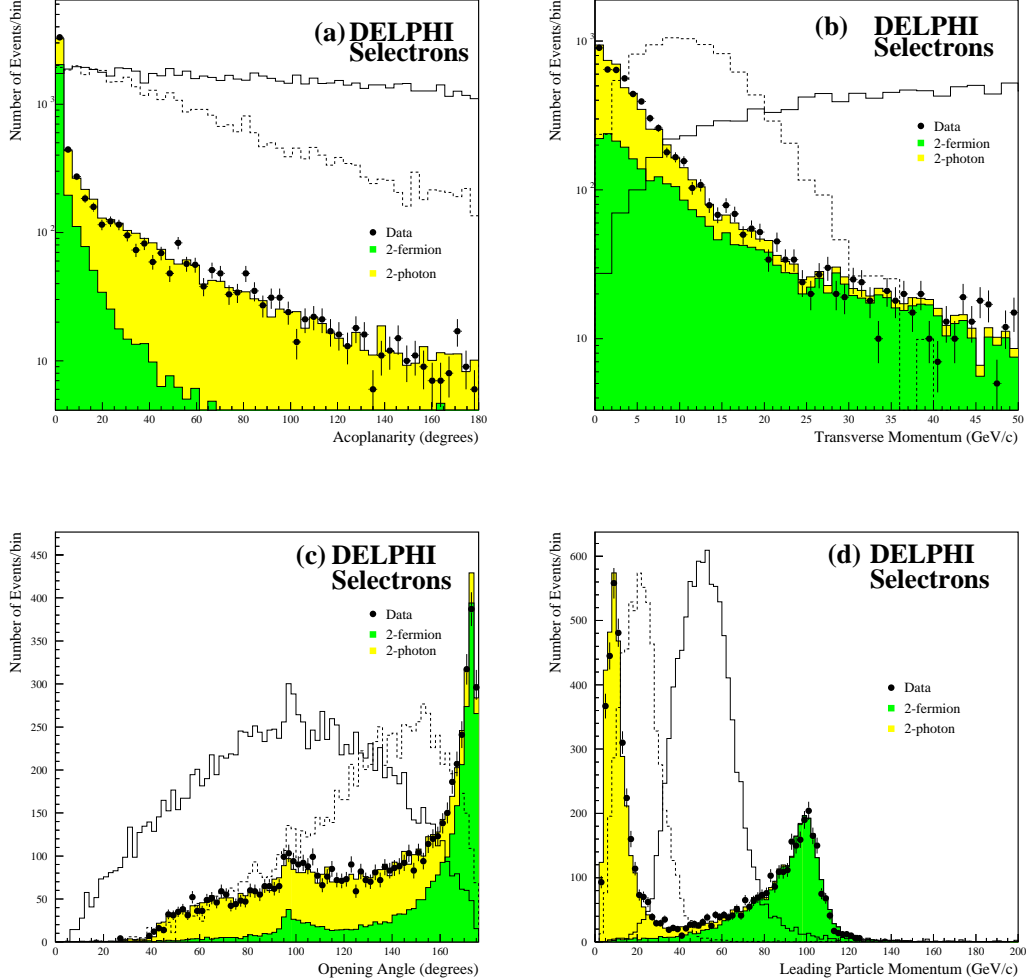


Figure 1: Comparison of data and simulation in the selectron channel at preselection level. The dots with error bars show the data, shaded histograms show the simulation. Plots include data taken in the year 2000 when the DELPHI detector was fully operational. The plots show: (a) the acoplanarity, (b) the transverse momentum, (c) the opening angle, (d) the momentum of the leading charged particle. Possible signals corresponding to the mass combinations  $M_{\tilde{e}}=90 \text{ GeV}/c^2, M_{\tilde{\chi}_1^0}=10 \text{ GeV}/c^2$  (solid) and  $M_{\tilde{e}}=50 \text{ GeV}/c^2, M_{\tilde{\chi}_1^0}=40 \text{ GeV}/c^2$  (dashed) are shown by the superimposed open histograms. The signal normalisation is arbitrary.

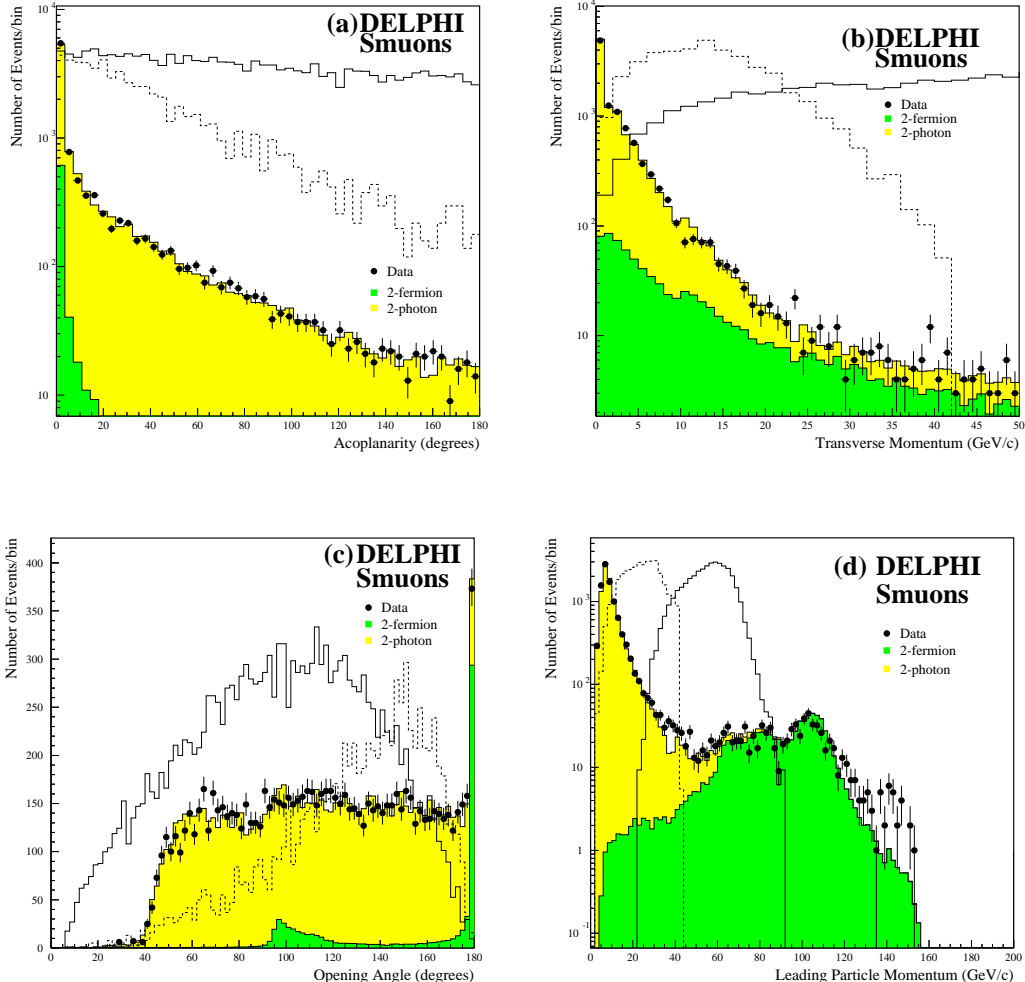


Figure 2: Comparison of data and simulation in the smuon channel at preselection level. The dots with error bars show the data, shaded histograms show the simulation. Plots include data taken in the year 2000 when the DELPHI detector was fully operational. The plots show: (a) the acoplanarity, (b) the transverse momentum, (c) the opening angle, (d) the momentum of the leading charged particle. Possible signals corresponding to the mass combinations  $M_{\tilde{\mu}}=90 \text{ GeV}/c^2, M_{\tilde{\chi}_1^0}=10 \text{ GeV}/c^2$  (solid) and  $M_{\tilde{\mu}}=50 \text{ GeV}/c^2, M_{\tilde{\chi}_1^0}=40 \text{ GeV}/c^2$  (dashed) are shown by the superimposed open histograms. The signal normalisation is arbitrary.

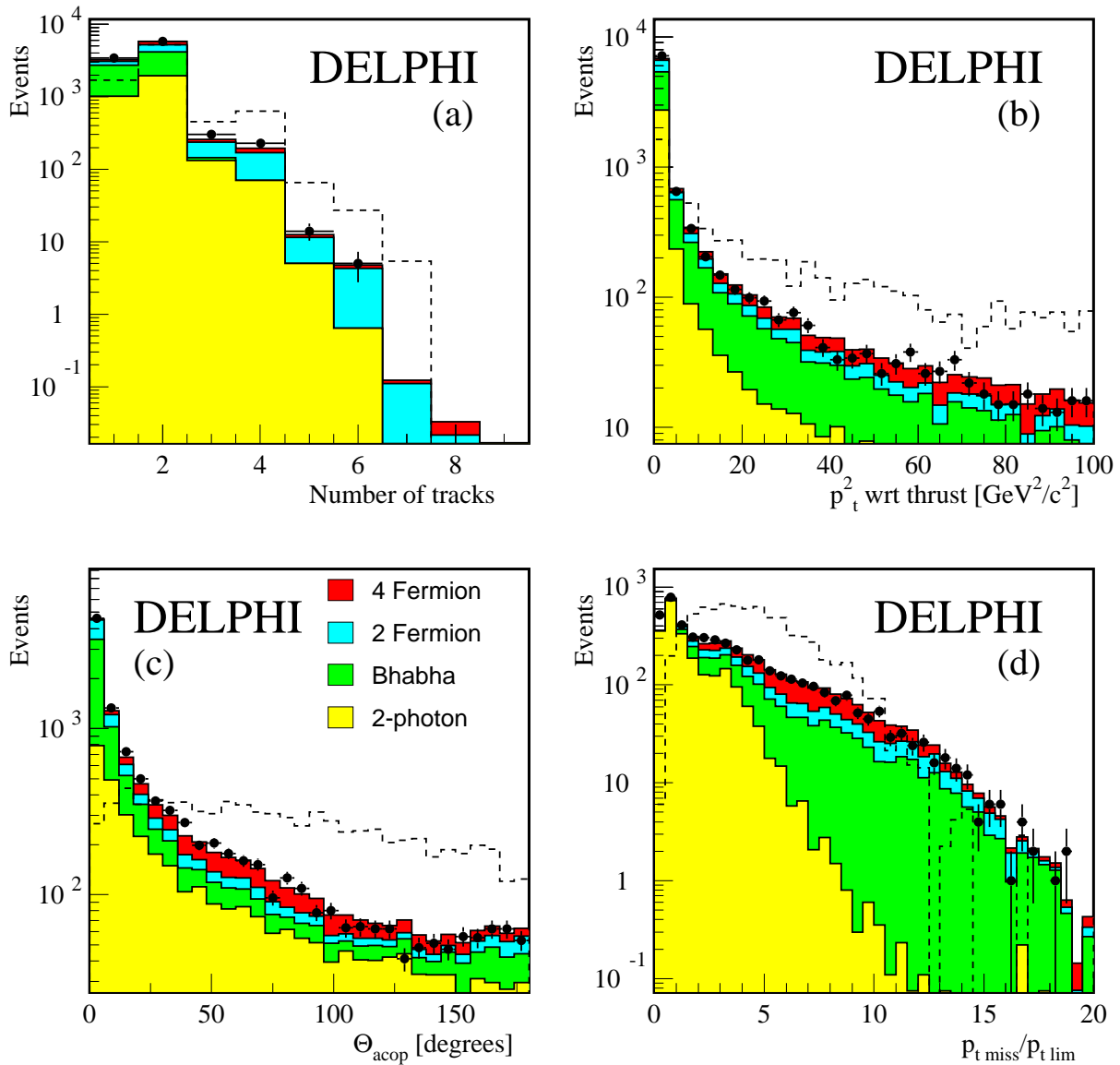


Figure 3: A preselection comparison of data and simulation in the stau analysis. The plots show: (a) the number of charged particles, (b) the square of the transverse momentum with respect to the thrust axis, (c) the acoplanarity, (d) the missing transverse momentum divided by the maximum missing transverse momentum in two-photon events with no beam-remnant electrons in the detector acceptance (ie. in “no-tag” events). The dots with error bars show the data, while the simulation is shown shaded. A typical signal ( $M_{\tilde{\tau}} = 83 \text{ GeV}/c^2$ ,  $M_{\text{LSP}} = 0 \text{ GeV}/c^2$ ) is shown by the superimposed open histogram, with arbitrary normalisation.

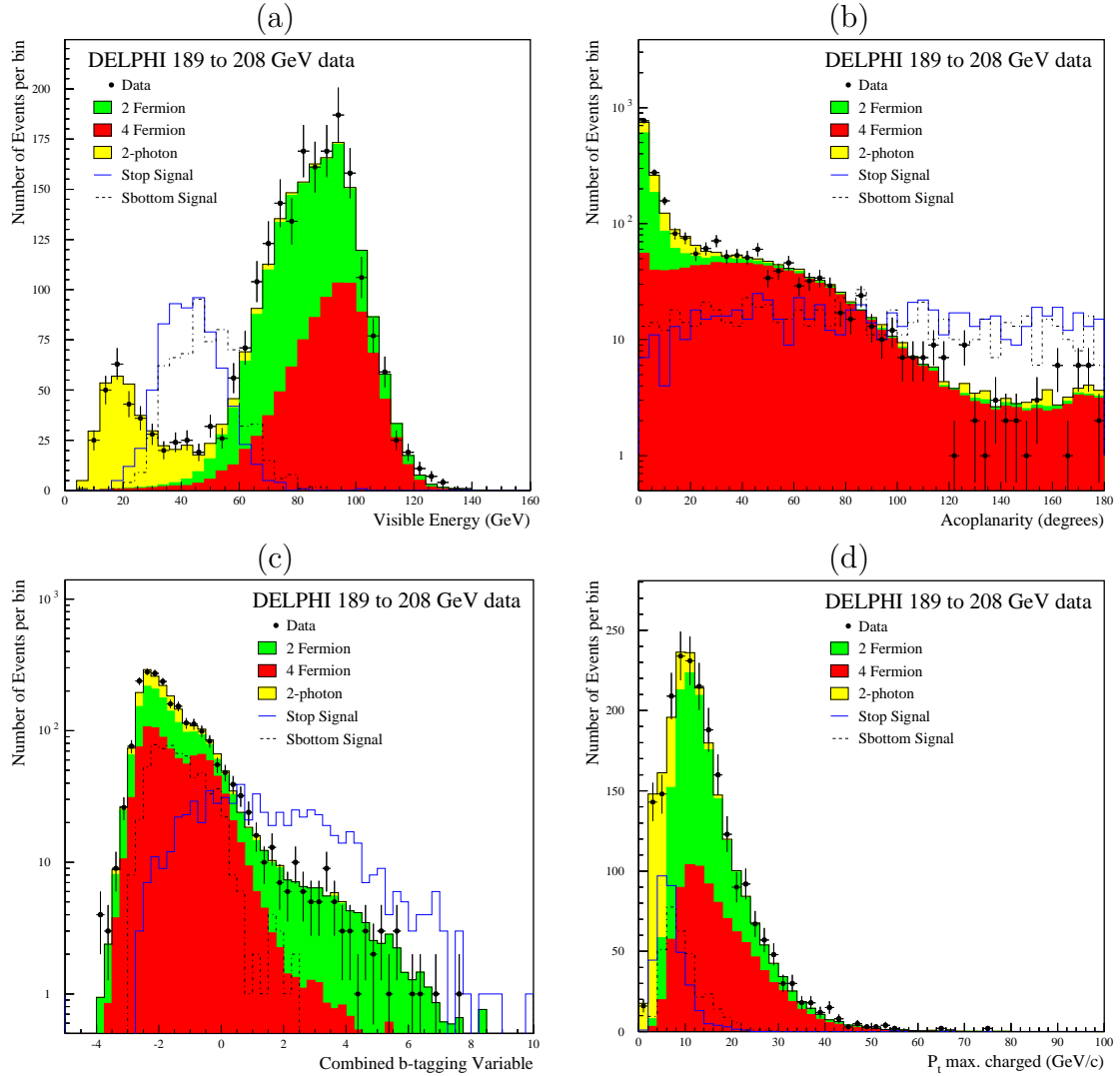


Figure 4: Comparison of data and simulation at the preselection level in the non-degenerate squark analysis. Plots include all DELPHI data from 189 to 208 GeV: (a) visible energy, (b) acoplanarity, (c) combined b-tagging variable, (d) maximal transverse momentum of a charged particle. The expected signal distributions at  $\sqrt{s} = 200$  GeV are shown for one possible stop and sbottom signal ( $M_{\tilde{q}}=90$  GeV/ $c^2$ ,  $M_{\tilde{\chi}_1^0} = 60$  GeV/ $c^2$ ), with arbitrary normalisation.

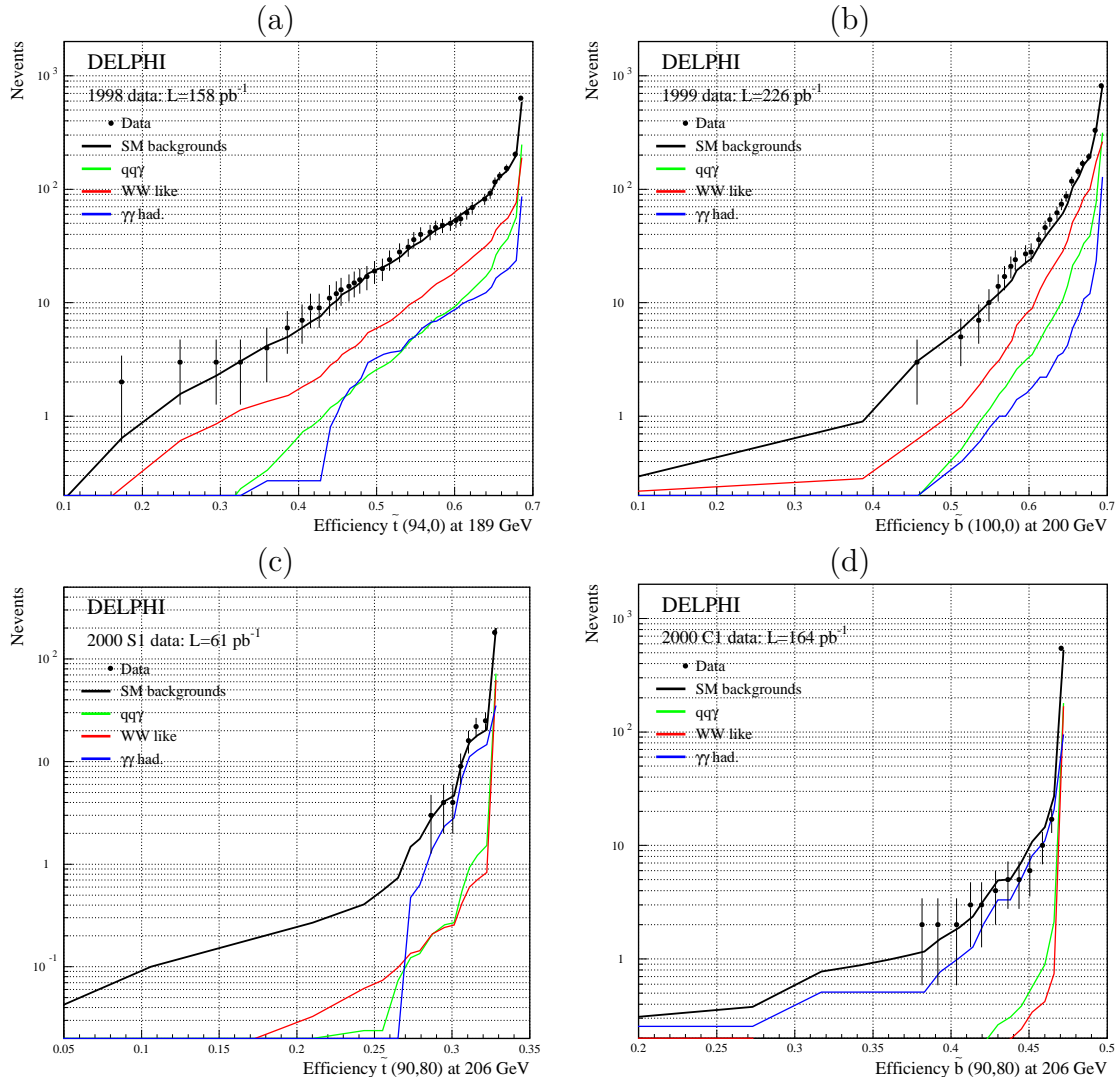


Figure 5: Number of events as a function of the signal detection efficiencies in the non-degenerate squark analysis: (a) 1998 data at 189 GeV: stop analysis for  $\Delta M > 20 \text{ GeV}/c^2$ , (b) 1999 data from 192 to 202 GeV: sbottom analysis for  $\Delta M > 20 \text{ GeV}/c^2$ , (c) 2000 data with TPC sector 6 off: stop analysis for  $5 \leq \Delta M \leq 20 \text{ GeV}/c^2$ , (d) 2000 data with TPC sector 6 on: sbottom analysis for  $5 \leq \Delta M \leq 20 \text{ GeV}/c^2$ . The efficiencies are for a given combination of squark and LSP masses, indicated in the parentheses.

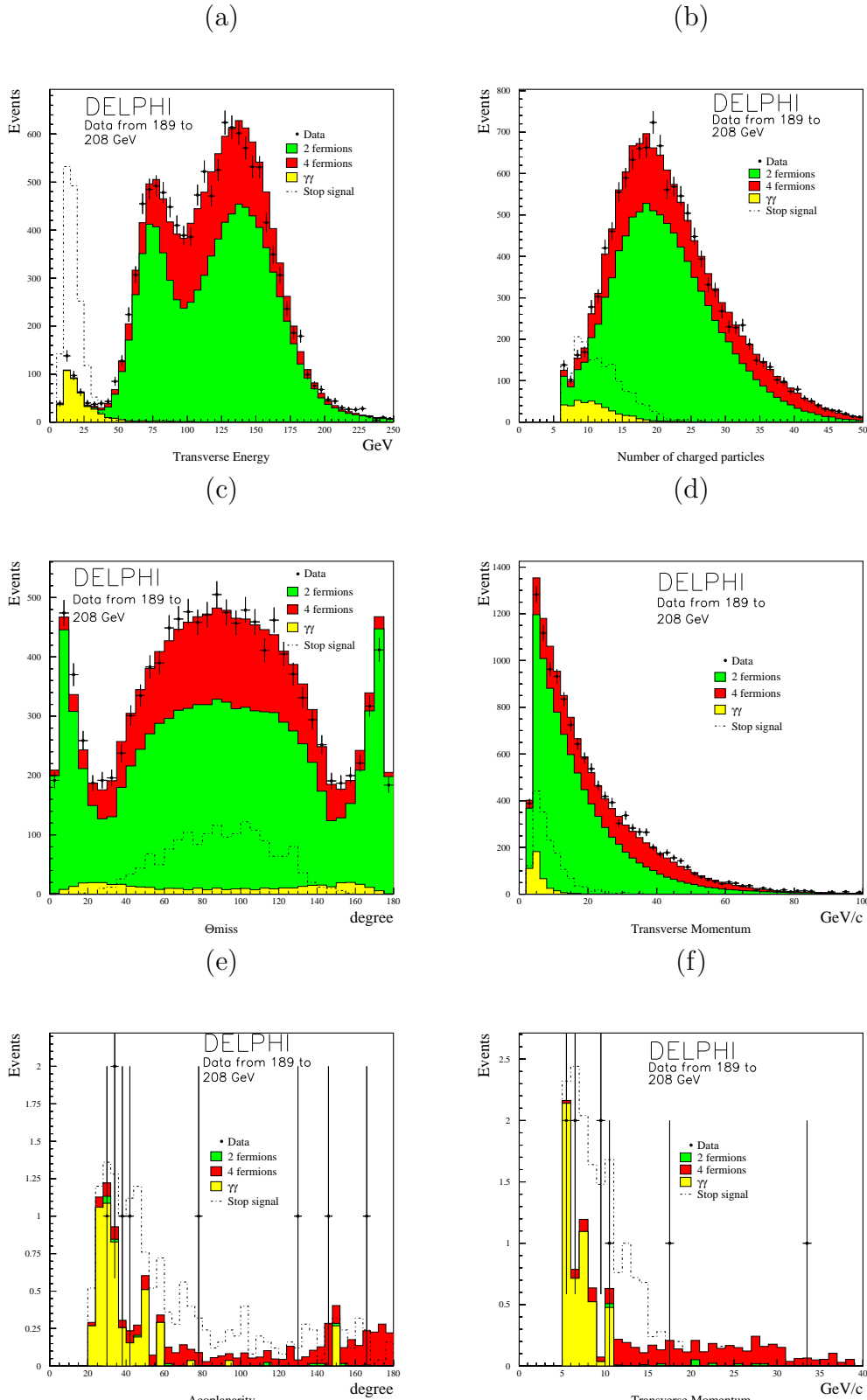


Figure 6: Comparison of data and simulation in the nearly degenerate squark analysis at preselection and final selection level. The distributions of (a) the total transverse energy, (b) total number of charged particles, (c) angle between the missing momentum and the beam axis and (d) transverse momentum are shown at preselection level. At the final selection level the distributions of (e) the acoplanarity and (f) the transverse momentum are shown. All DELPHI data from 189 to 208 GeV is included. A signal corresponding

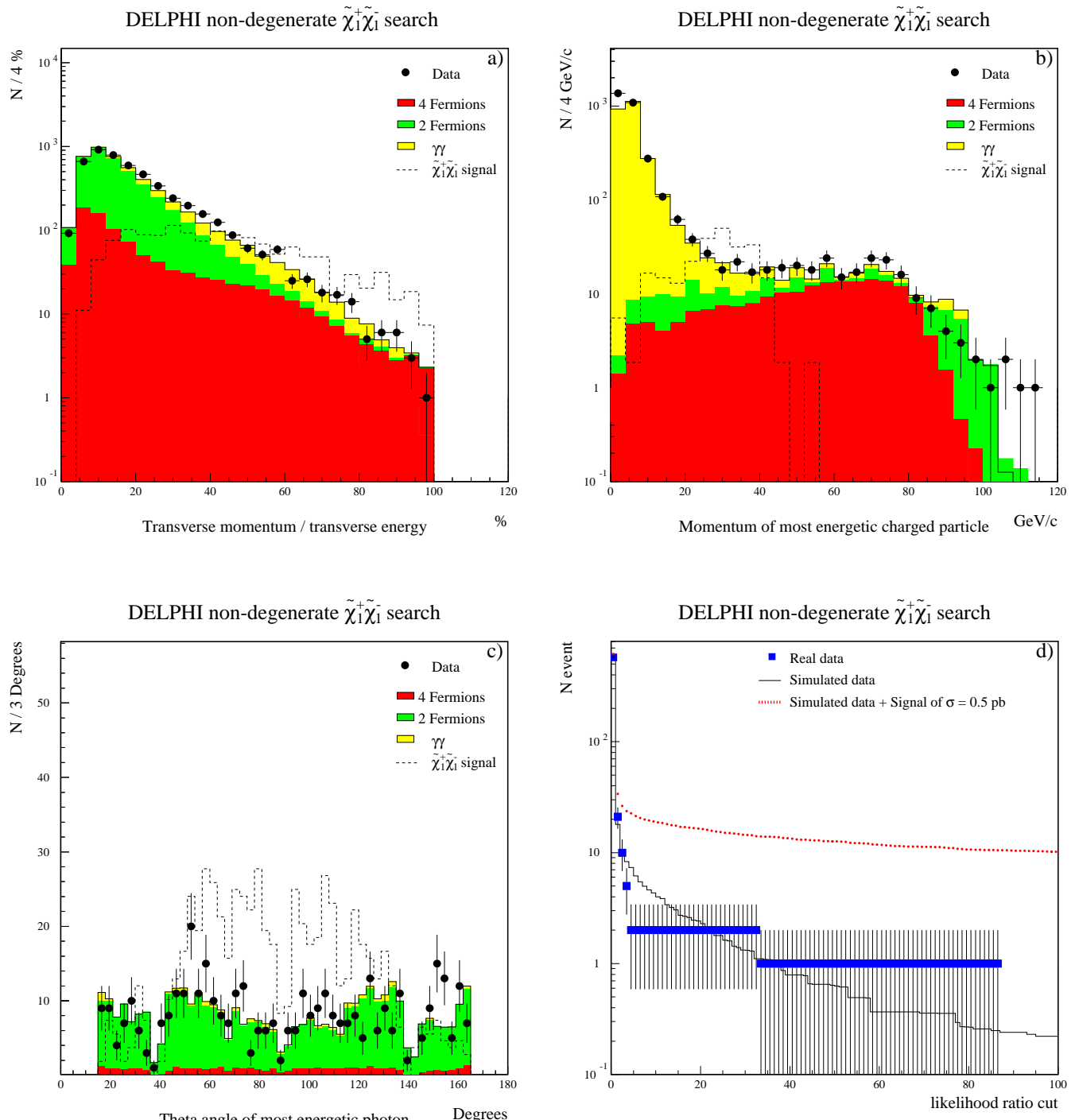


Figure 7: a), b) and c) show comparisons between real data (dots) and simulated background events (histogram) for the  $j\ell\ell$ ,  $\ell\ell$  and  $rad$  topologies respectively, using a logical OR of the 6 preselection cut functions of the corresponding topology. The dashed lines indicate how a characteristic chargino signal would appear (arbitrary normalisation). d) shows the number of events selected by the standard chargino analysis as a function of the  $\mathcal{L}_{R_{cut}}$  cut in the  $jj\ell$  topology for  $25 \leq \Delta M < 35 \text{ GeV}/c^2$ . The squares are the data and the solid line is the background simulation. The dotted curve shows a possible signal,  $M_{\tilde{\chi}_1^\pm} = 102.8 \text{ GeV}/c^2$   $M_{\tilde{\chi}_1^0} = 73 \text{ GeV}/c^2$ , of  $0.5 \text{ pb}$ . In all cases the data collected in the year 2000 with the TPC sector 6 on are shown.

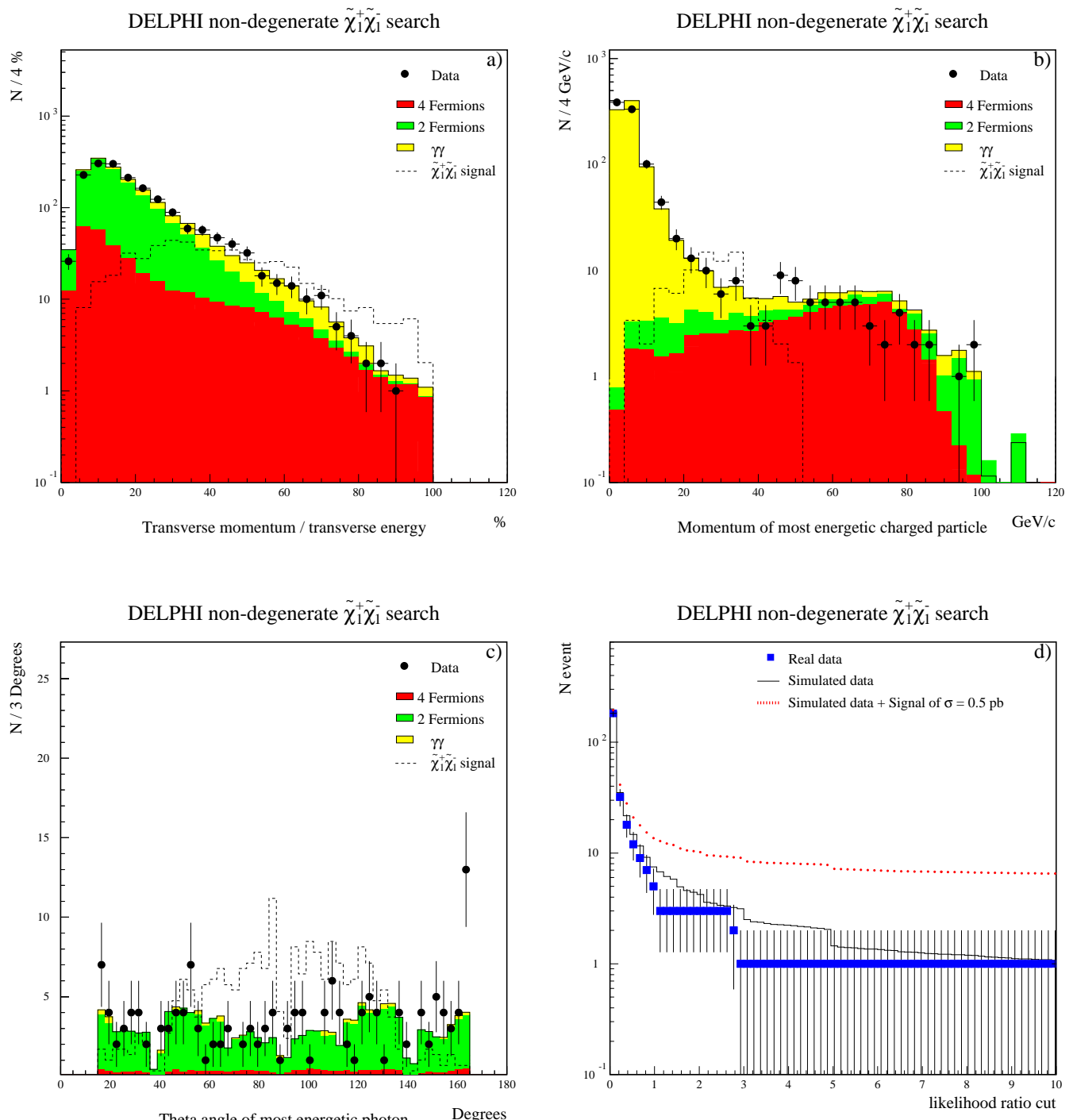


Figure 8: a), b) and c) show comparisons between real data (dots) and simulated background events (histogram) for the *jets*,  $\ell\ell$  and *rad* topologies respectively, using a logical OR of the 6 preselection cut functions of the corresponding topology. The dashed lines indicate how a characteristic chargino signal would appear (arbitrary normalisation). d) shows the number of events selected by the standard chargino analysis as a function of the  $\mathcal{L}_{\mathcal{R}_{cut}}$  cut in the  $jj\ell$  topology for  $25 \leq \Delta M < 35$   $\text{GeV}/c^2$ . The squares are the data and the solid line is the background simulation. The dotted curve shows a possible signal,  $M_{\tilde{\chi}_1^\pm} = 102.8$   $\text{GeV}/c^2$   $M_{\tilde{\chi}_1^0} = 73$   $\text{GeV}/c^2$ , of 0.5 pb. In all cases the data collected in the year 2000 with the TPC sector 6 off are shown.

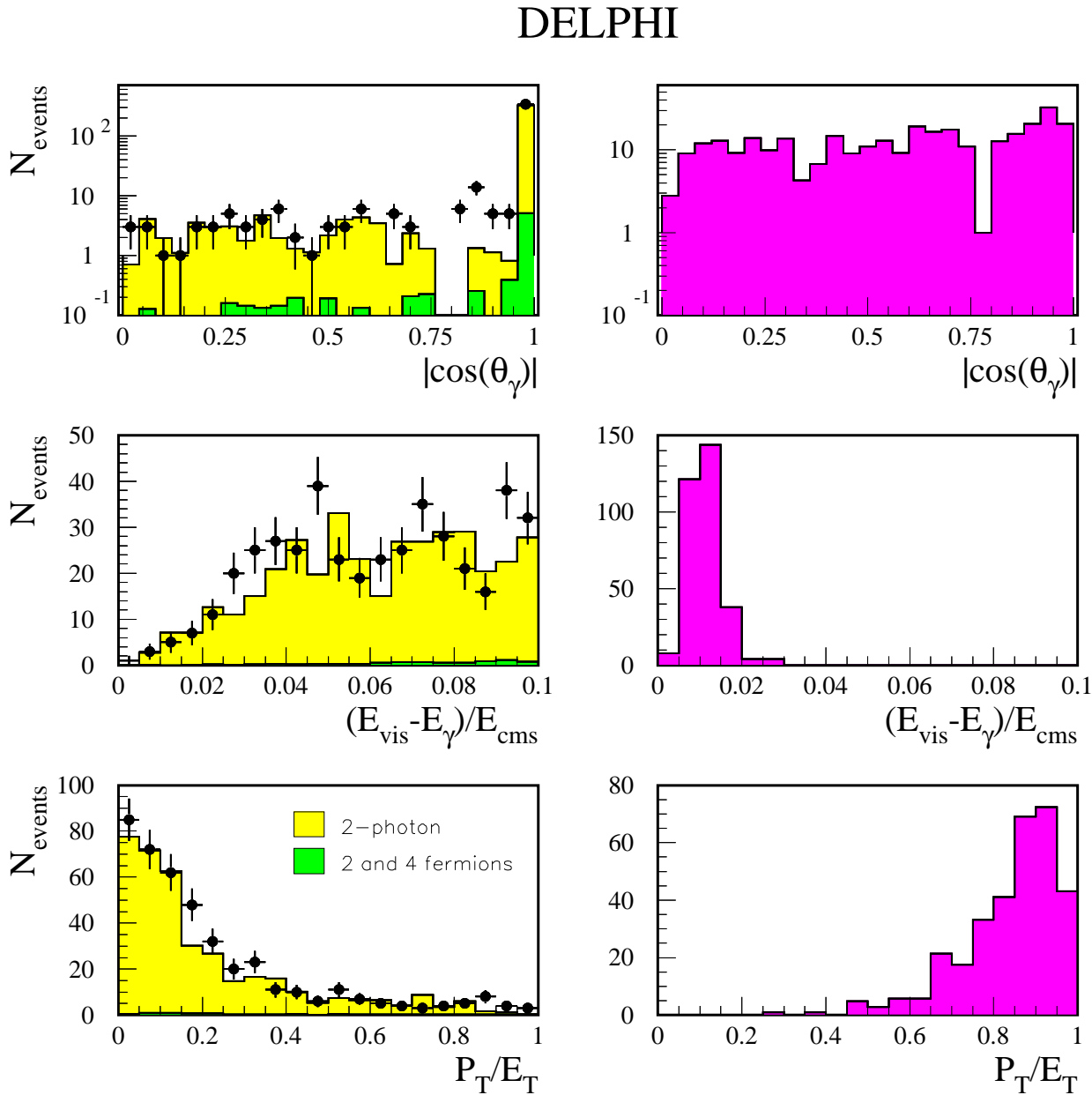


Figure 9: Some of the variables used in the selection for mass-degenerate charginos with an ISR photon tag. In the plots on the left the data (dots) are compared with the SM expectations. On the right, as an example, the corresponding distributions (with arbitrary normalisation) are shown for the signal with  $M(\tilde{\chi}_1^+) = 80 \text{ GeV}/c^2$  and  $\Delta M = 1 \text{ GeV}/c^2$ .

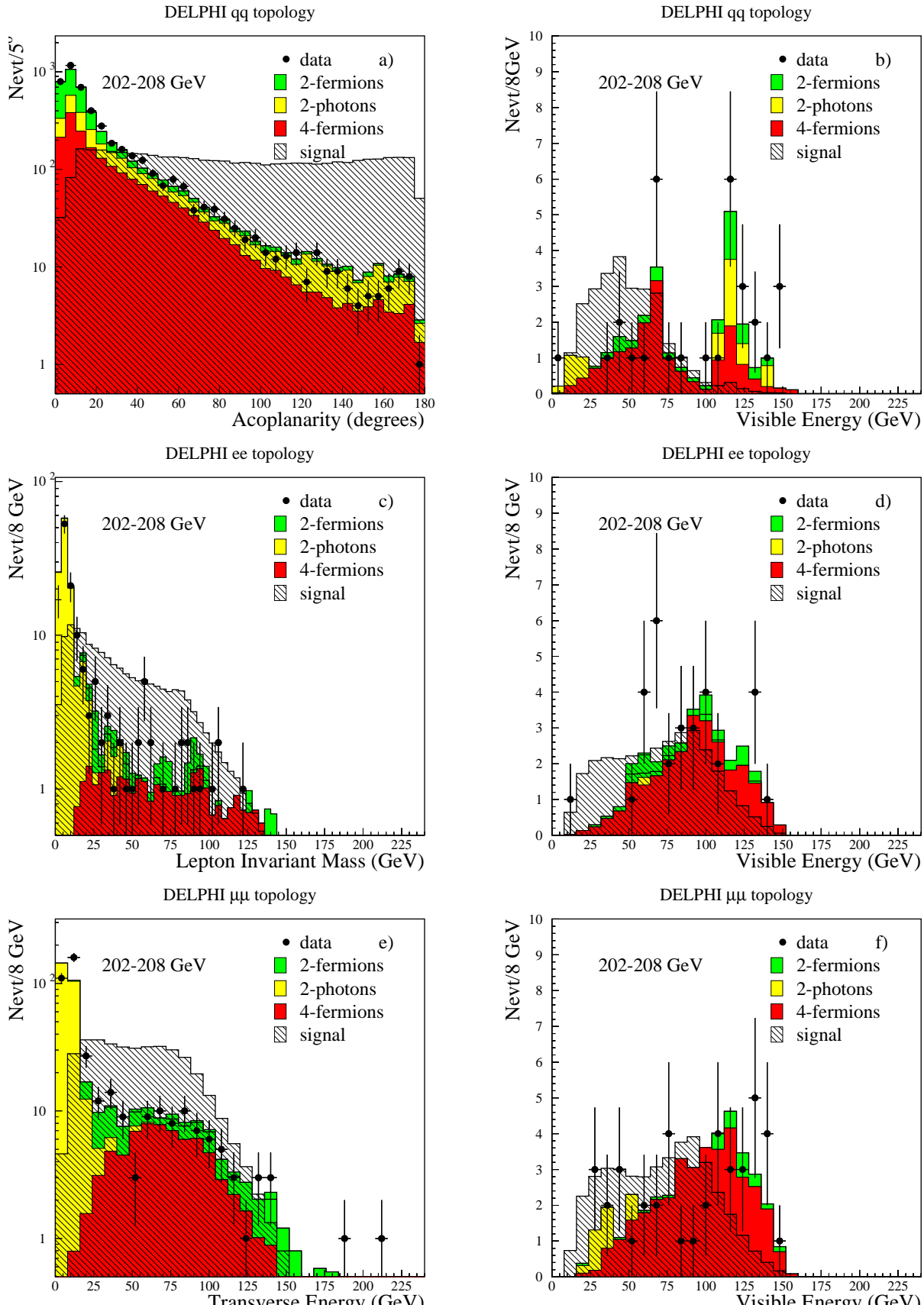


Figure 10: On the left the comparison between the real and simulated data is shown at preselection level for different variables for the  $q\bar{q}$ , ee, and  $\mu\mu$  topologies in the neutralino search. On the right the visible energy distribution is shown for the events selected at the final stage, after the likelihood selection. The signal distribution contains the contribution

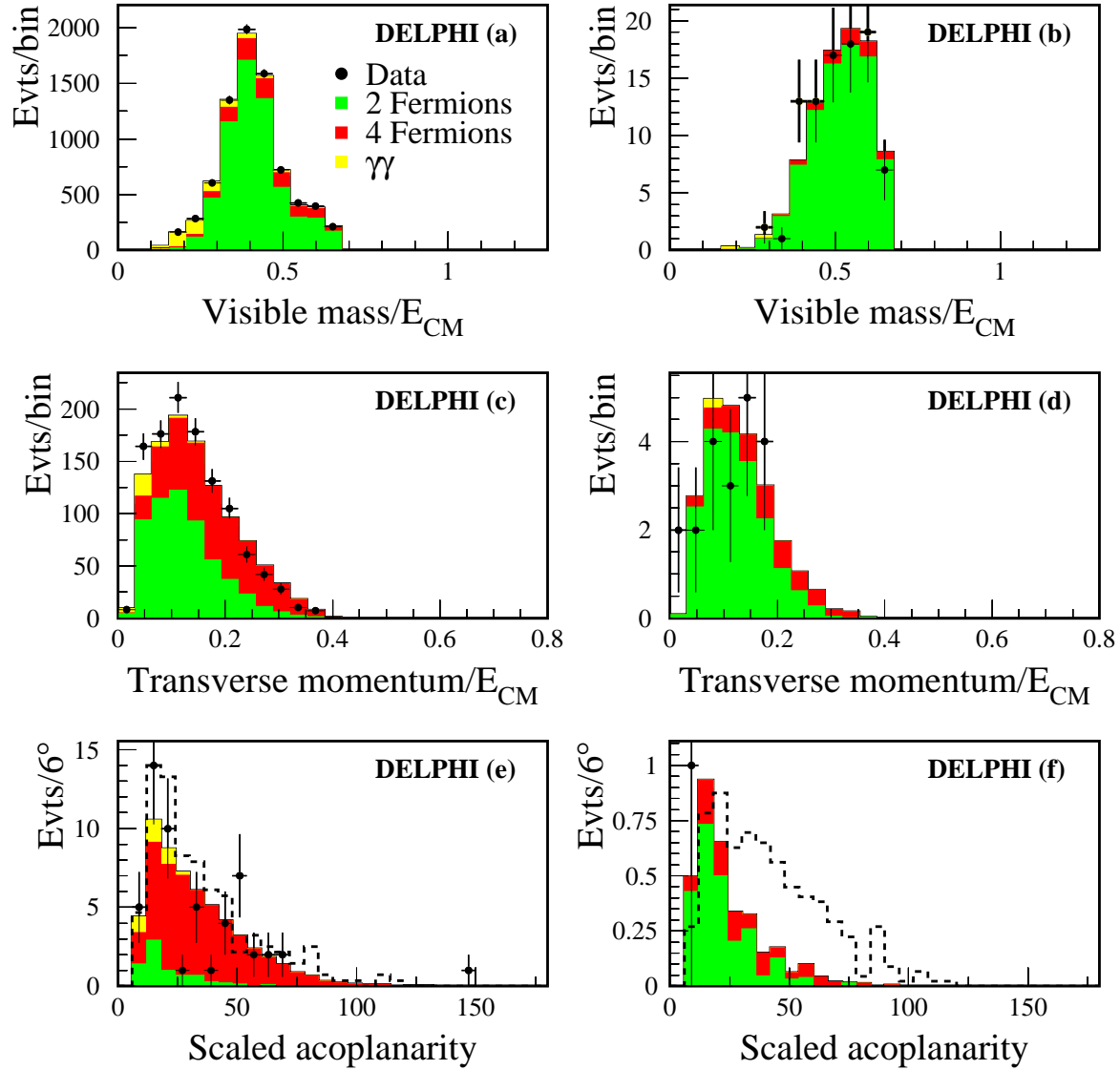


Figure 11: Comparison of real data from 1999 ( $\sqrt{s}$  in the range 192–202 GeV) and simulation for the neutralino multijet selection without photons (a,c,e) and with photons (b,d,f), at the preselection (a,b), intermediate (c,d), and final selection(e,f) stages. The distributions expected for  $\tilde{\chi}_3^0\tilde{\chi}_2^0$  production with  $\tilde{\chi}_3^0 \rightarrow \tilde{\chi}_2^0 q\bar{q}$  and  $\tilde{\chi}_2^0$  decaying to  $\tilde{\chi}_1^0 q\bar{q}$  or  $\tilde{\chi}_1^0\gamma$  are shown as dashed histograms where  $M_{\tilde{\chi}_3^0}=112$  GeV/ $c^2$ ,  $M_{\tilde{\chi}_2^0}=75$  GeV/ $c^2$  and  $M_{\tilde{\chi}_1^0}=41$  GeV/ $c^2$ . The signals are normalised to cross-sections of 0.8 pb (e) and 0.1 pb (f).

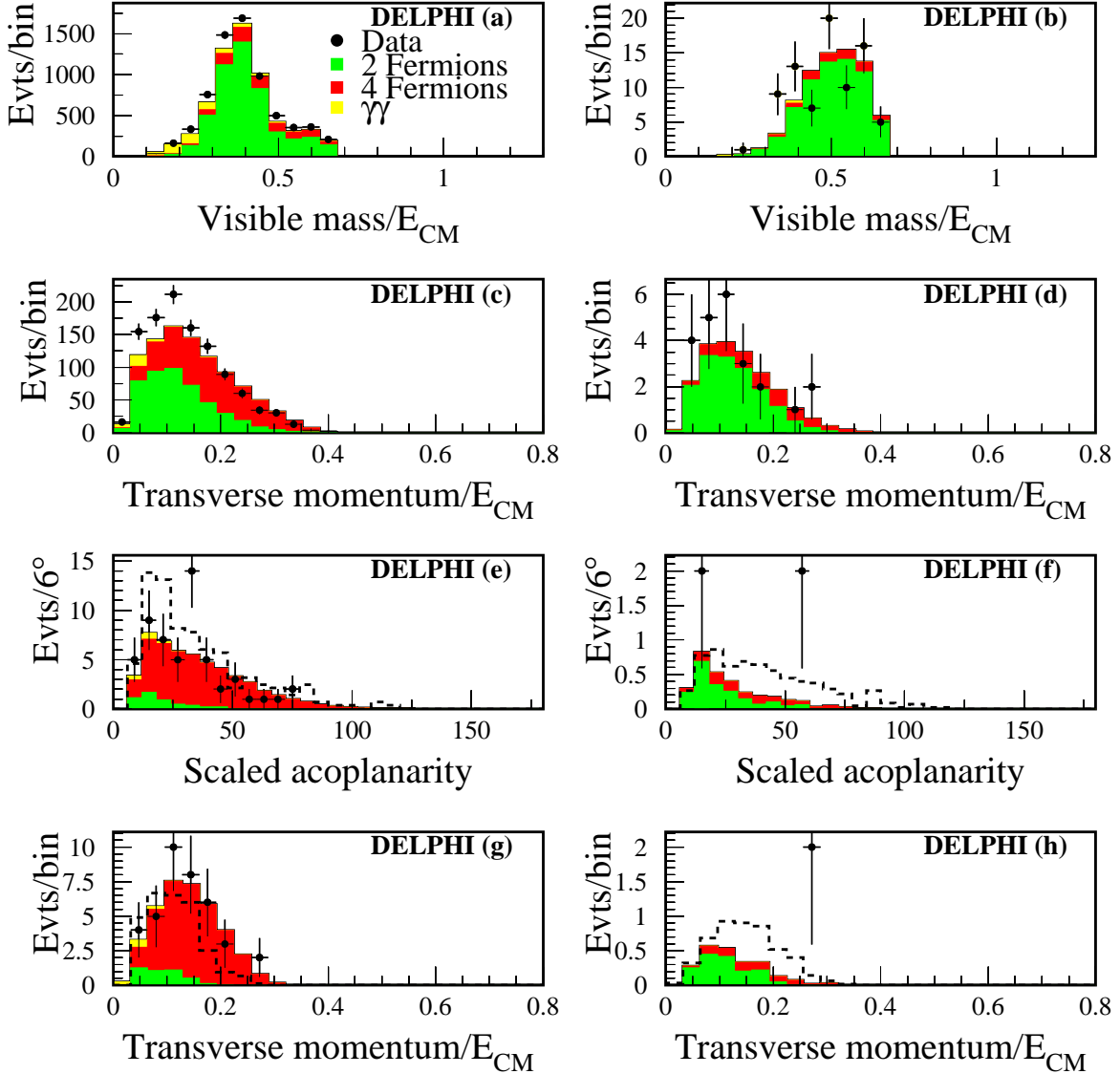


Figure 12: Comparison of real data from 2000 ( $\sqrt{s}$  in the range 204–208 GeV) and simulation for the neutralino multijet selection without photons (a,c,e,g) and with photons (b,d,f,h), at the preselection (a,b), intermediate (c,d), and final selection(e,f,g,h) stages. In (g,h) only the data collected with the TPC sector 6 on are shown. The distributions expected for  $\tilde{\chi}_3^0 \tilde{\chi}_2^0$  production with  $\tilde{\chi}_3^0 \rightarrow \tilde{\chi}_2^0 q \bar{q}$  and  $\tilde{\chi}_2^0$  decaying to  $\tilde{\chi}_1^0 q \bar{q}$  or  $\tilde{\chi}_1^0 \gamma$  are shown as dashed histograms where  $M_{\tilde{\chi}_3^0} = 112 \text{ GeV}/c^2$ ,  $M_{\tilde{\chi}_2^0} = 75 \text{ GeV}/c^2$  and  $M_{\tilde{\chi}_1^0} = 41 \text{ GeV}/c^2$ . The signals are normalised cross-sections of 0.8 pb (e), 0.1 pb (f,h) and 0.4 pb (g).

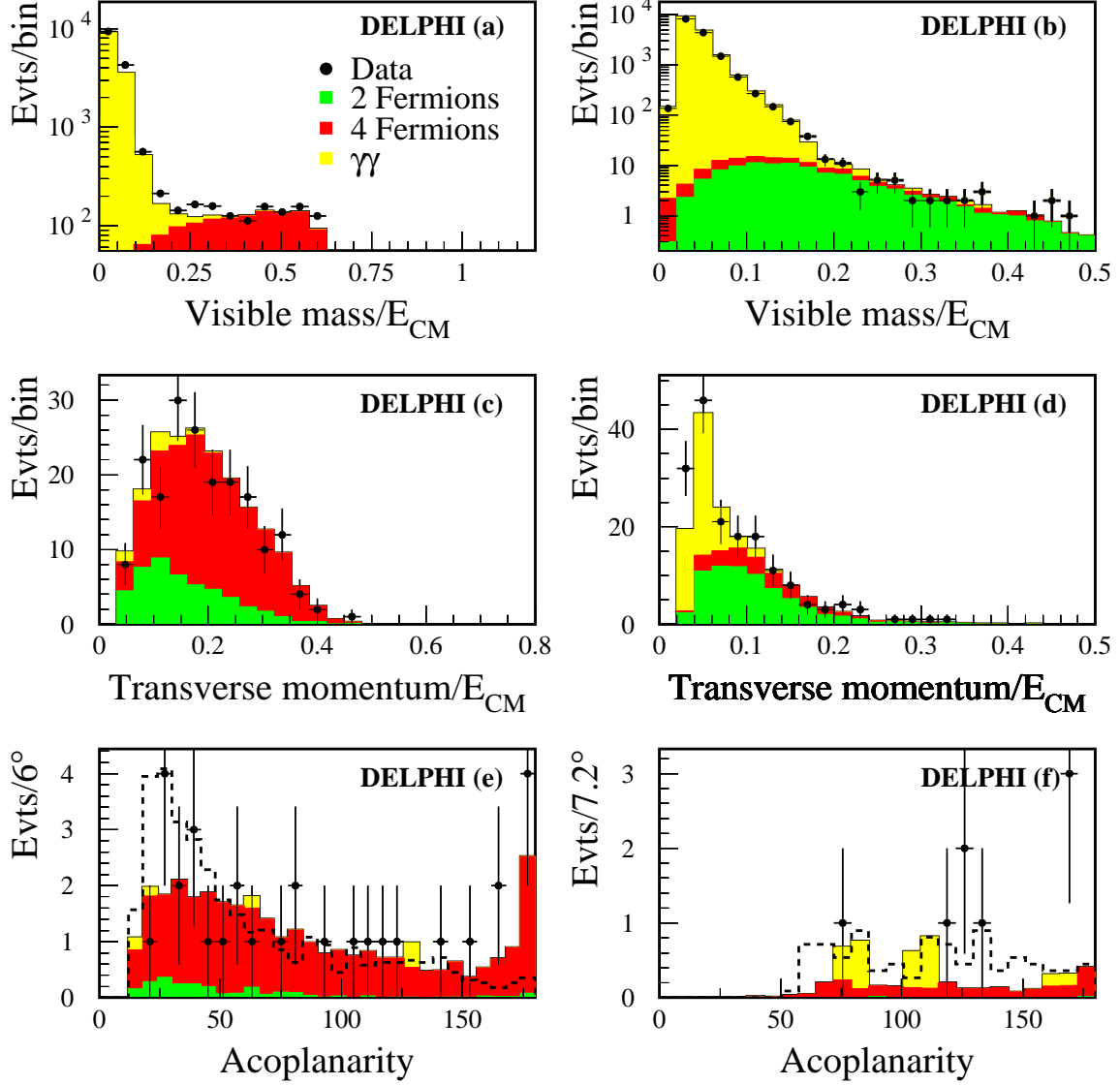


Figure 13: Comparison of real data from 1999 ( $\sqrt{s}$  in the range 192–202 GeV) and simulation for the neutralino multilepton search (a,c,e) and asymmetric tau search (b,d,f), at the preselection (a,b), intermediate (c,d), and final selection (e,f) stages. The dashed line in (e) shows the multilepton signal expected for  $\tilde{\chi}_3^0\tilde{\chi}_2^0$  production with  $\tilde{\chi}_3^0 \rightarrow \tilde{\chi}_2^0\ell^+\ell^-$  and  $\tilde{\chi}_2^0$  decaying to  $\tilde{\chi}_1^0\ell^+\ell^-$  where  $M_{\tilde{\chi}_3^0}=103$  GeV/ $c^2$ ,  $M_{\tilde{\chi}_2^0}=51$  GeV/ $c^2$  and  $M_{\tilde{\chi}_1^0}=45$  GeV/ $c^2$ . In (f) the dashed line shows the tau cascade signal for  $\tilde{\chi}_2^0\tilde{\chi}_1^0$  production with  $\tilde{\chi}_2^0 \rightarrow \tilde{\tau}\tau$  and  $\tilde{\tau} \rightarrow \tilde{\chi}_1^0\tau$  where  $M_{\tilde{\chi}_2^0}=75$  GeV/ $c^2$ ,  $M_{\tilde{\tau}}=44$  GeV/ $c^2$  and  $M_{\tilde{\chi}_1^0}=37.5$  GeV/ $c^2$ . The signals are normalised to a cross-section of 0.4 pb.

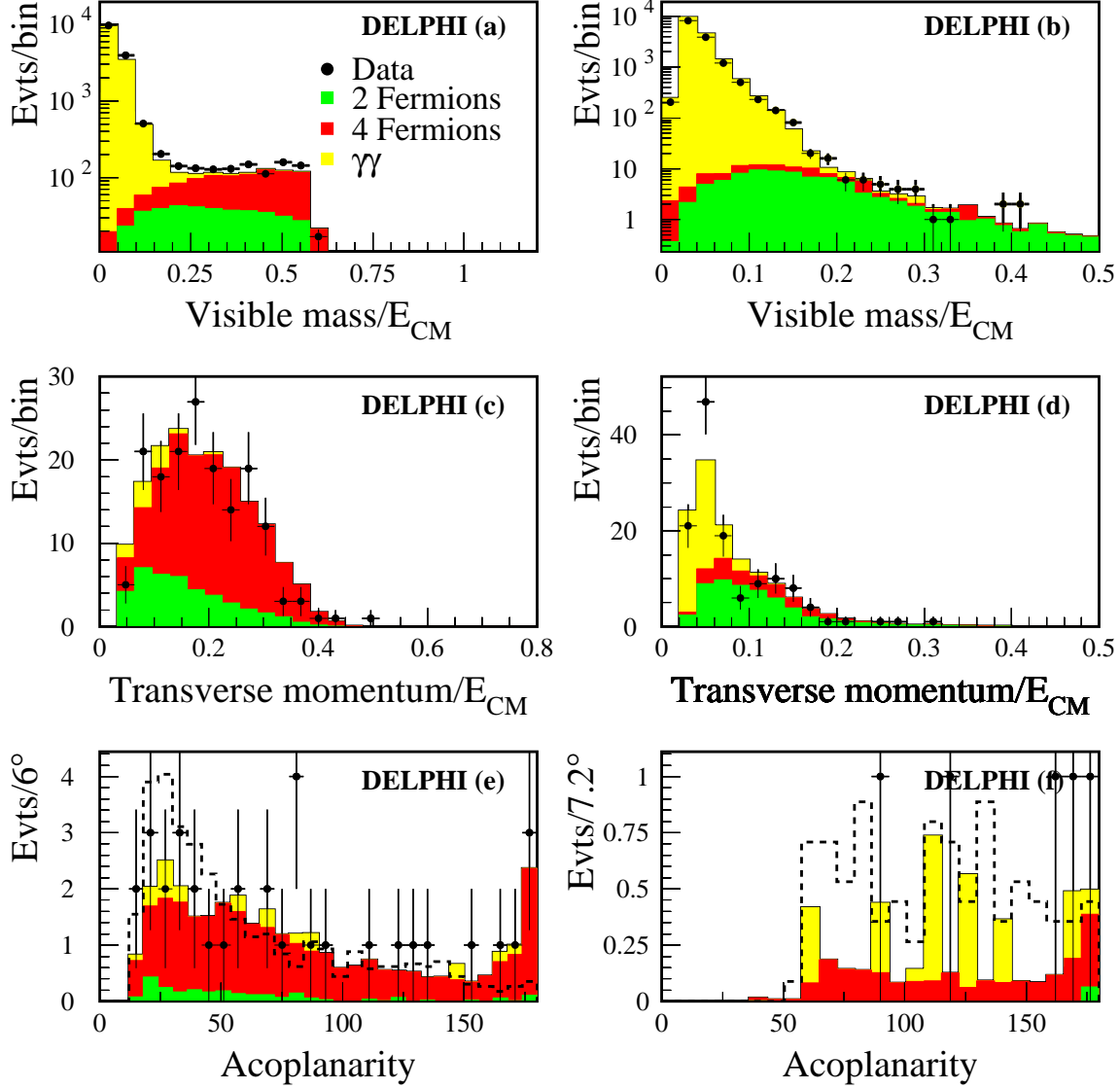


Figure 14: Comparison of real data from 2000 ( $\sqrt{s}$  in the range 204–208 GeV) and simulation for the neutralino multilepton search (a,c,e) and asymmetric tau search (b,d,f), at the preselection (a,b), intermediate (c,d), and final selection (e,f) stages. The dashed line in (e) shows the multilepton signal expected for  $\tilde{\chi}_3^0\tilde{\chi}_2^0$  production with  $\tilde{\chi}_3^0 \rightarrow \tilde{\chi}_2^0\ell^+\ell^-$  and  $\tilde{\chi}_2^0$  decaying to  $\tilde{\chi}_1^0\ell^+\ell^-$  where  $M_{\tilde{\chi}_3^0}=103$  GeV/ $c^2$ ,  $M_{\tilde{\chi}_2^0}=51$  GeV/ $c^2$  and  $M_{\tilde{\chi}_1^0}=45$  GeV/ $c^2$ . In (f) the dashed line shows the tau cascade signal for  $\tilde{\chi}_2^0\tilde{\chi}_1^0$  production with  $\tilde{\chi}_2^0 \rightarrow \tilde{\tau}\tau$  and  $\tilde{\tau} \rightarrow \tilde{\chi}_1^0\tau$  where  $M_{\tilde{\chi}_2^0}=75$  GeV/ $c^2$ ,  $M_{\tilde{\tau}}=44$  GeV/ $c^2$  and  $M_{\tilde{\chi}_1^0}=37.5$  GeV/ $c^2$ . The signals are normalised to a cross-section of 0.4 pb.

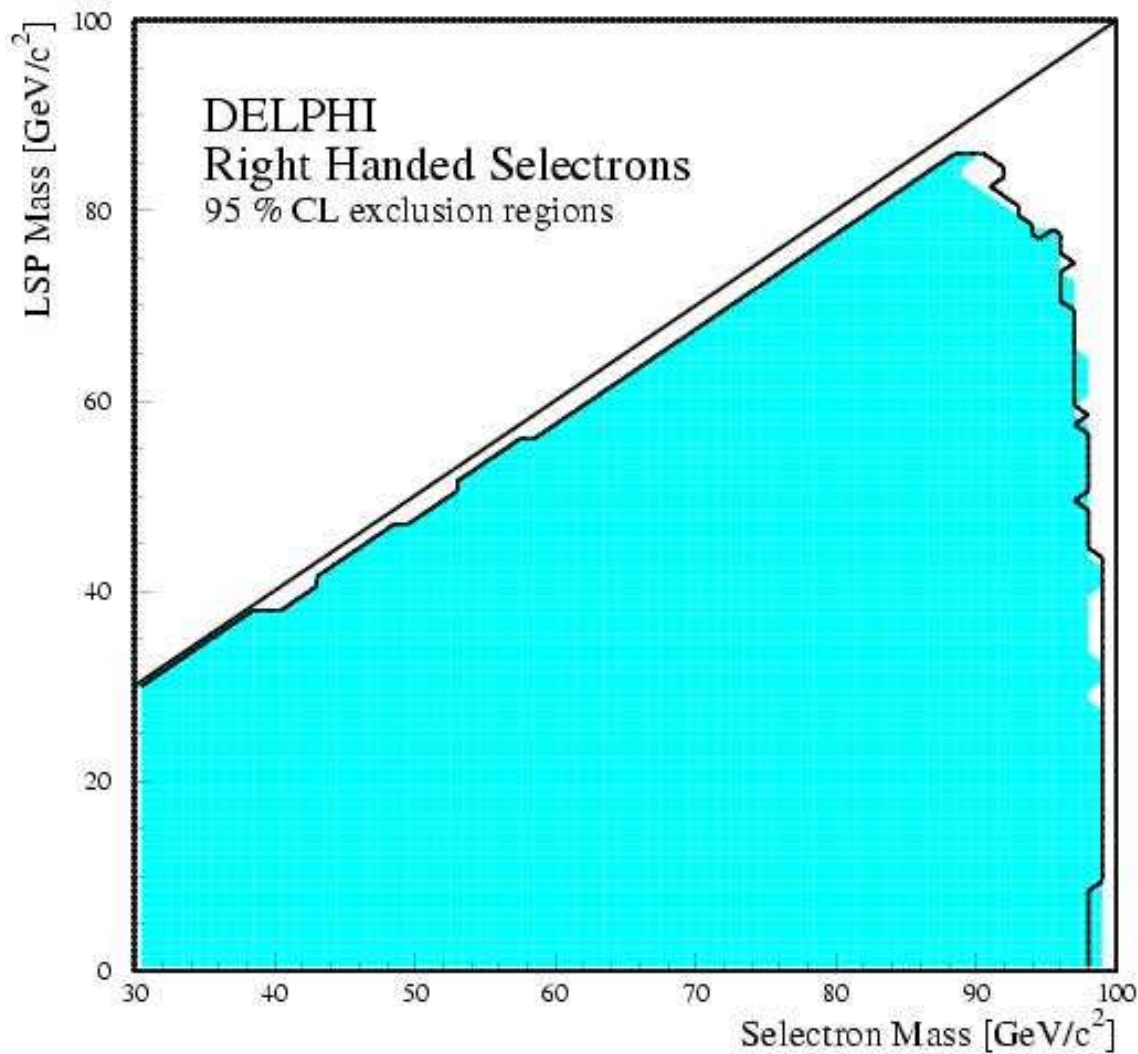


Figure 15: Excluded region in the  $(M_{\tilde{e}_R}, M_{LSP})$  plane. The solid line shows the expected limit and the shaded region shows the obtained limit. The cross-section and the branching ratios for each mass point were determined with the SUSY parameters  $\tan \beta = 1.5$  and  $\mu = -200 \text{ GeV}/c^2$  (for a discussion on the low selectron mass region see section 6.3).

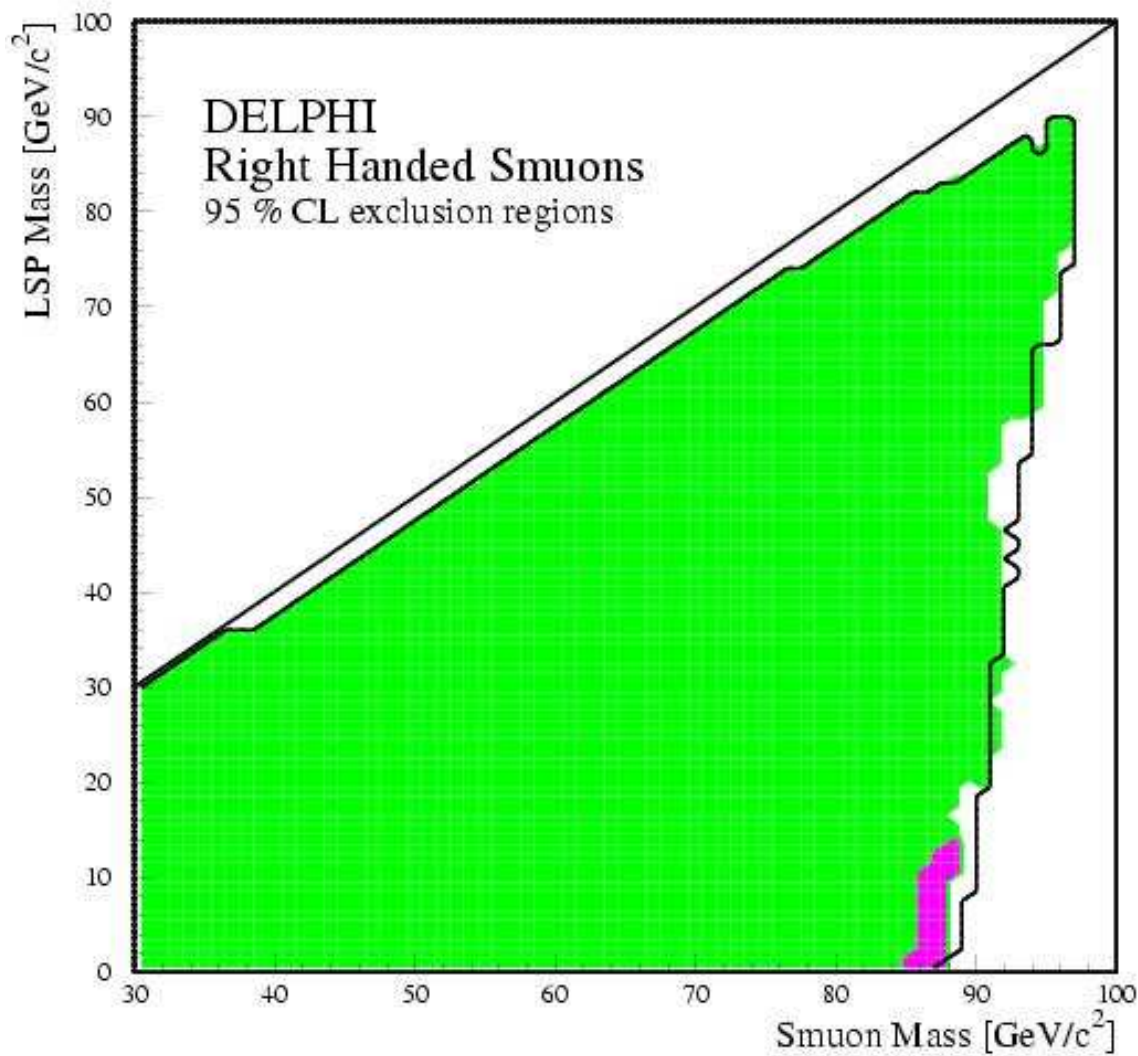


Figure 16: Excluded region in the  $(M_{\tilde{\mu}_R}, M_{LSP})$  plane. The shaded region shows the obtained limit. The lighter shaded region is excluded taking the branching ratios for each mass point with the SUSY parameters  $\tan \beta = 1.5$  and  $\mu = -200 \text{ GeV}/c^2$ . The solid line shows the corresponding expected limit. If the branching ratio of  $\tilde{\mu} \rightarrow \mu \chi_1^0$  is set to 1, the darker shaded region is also excluded (for a discussion on the low smuon mass region see section 6.3).

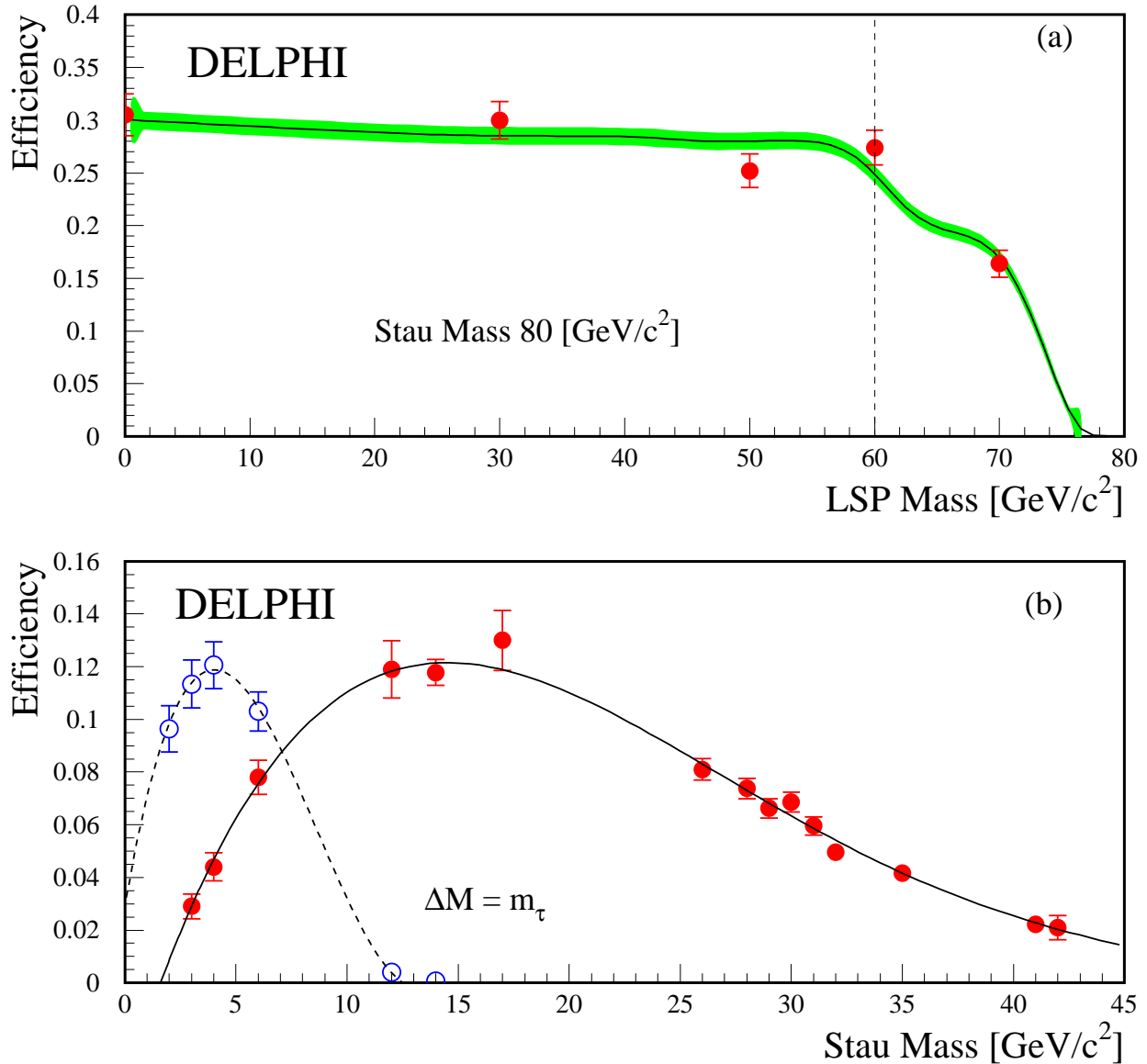


Figure 17: The selection efficiency in the stau analysis. The plots show: (a) Efficiency as a function of  $M_{LSP}$  at  $M_{\tilde{\tau}} = 80 \text{ GeV}/c^2$ . The line shows the result of SGV, and the points with error bars show the result of the full DELSIM simulation. The shaded area indicates the statistical uncertainty of the estimate, and the vertical line shows the position of the transition between the two  $\Delta M$ -regions. (b) Efficiency as a function of  $M_{\tilde{\tau}}$  at  $\Delta M = m_\tau$  for the low mass analysis (filled circles) and the very low mass analysis (open circles). The points show the results of the full simulation. The lines are polynomial fits to the points.

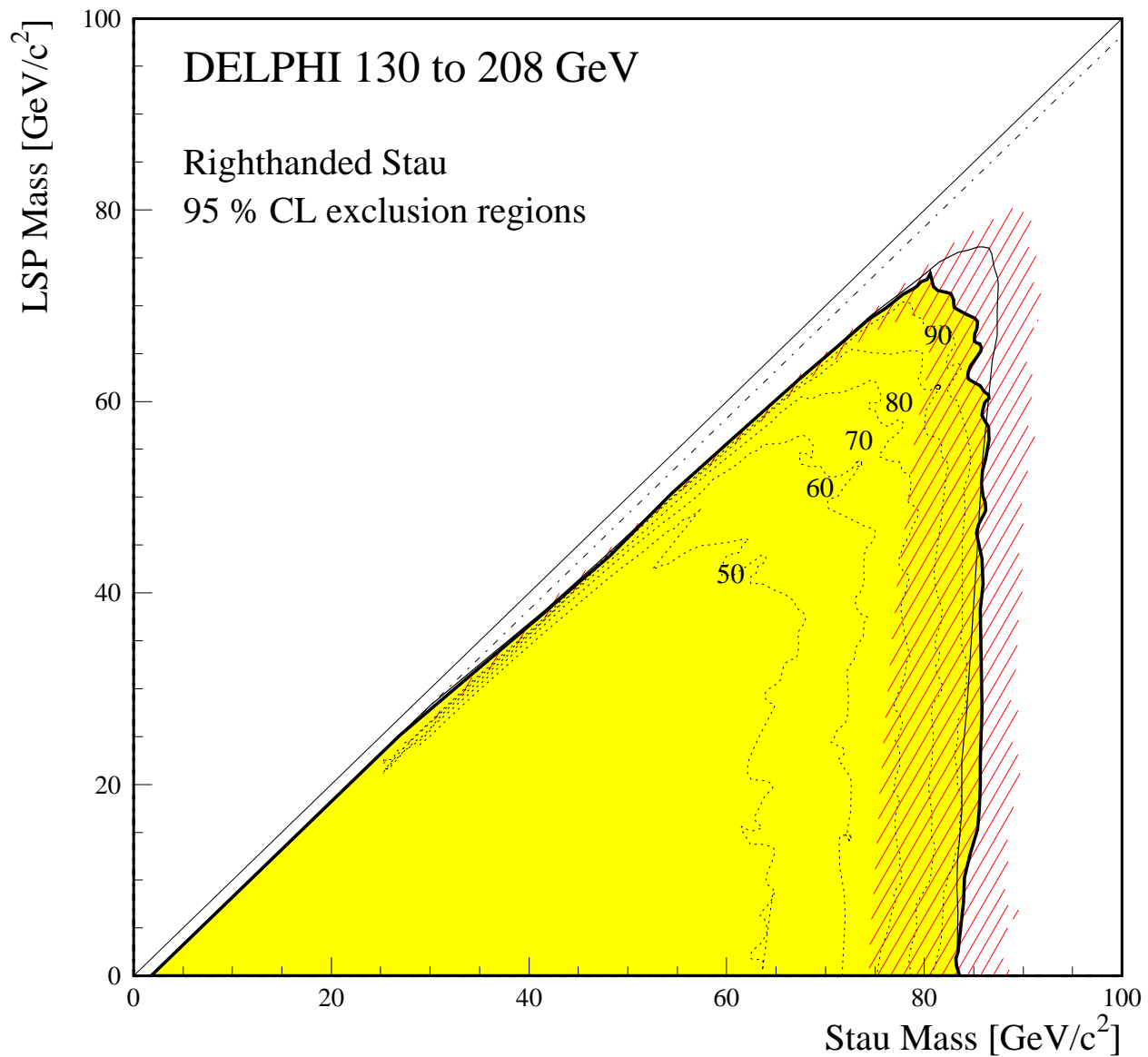


Figure 18: Excluded region in the  $(M_{\tilde{\tau}_R}, M_{LSP})$  plane. The shaded region shows the region excluded if  $\tilde{\tau} \rightarrow \tau$  LSP is the only allowed channel, and the thin solid line shows the corresponding expected limit. The dotted lines show the region excluded if the branching ratio of  $\tilde{\tau} \rightarrow \tau$  LSP has the values indicated in percent next to the lines, and it is assumed that the analysis has no sensitivity to other decay-modes. The dash-dotted line indicates  $\Delta M = m_\tau$ . The observed limit is everywhere within the 95% CL band for the expected limit shown as the hatched area.

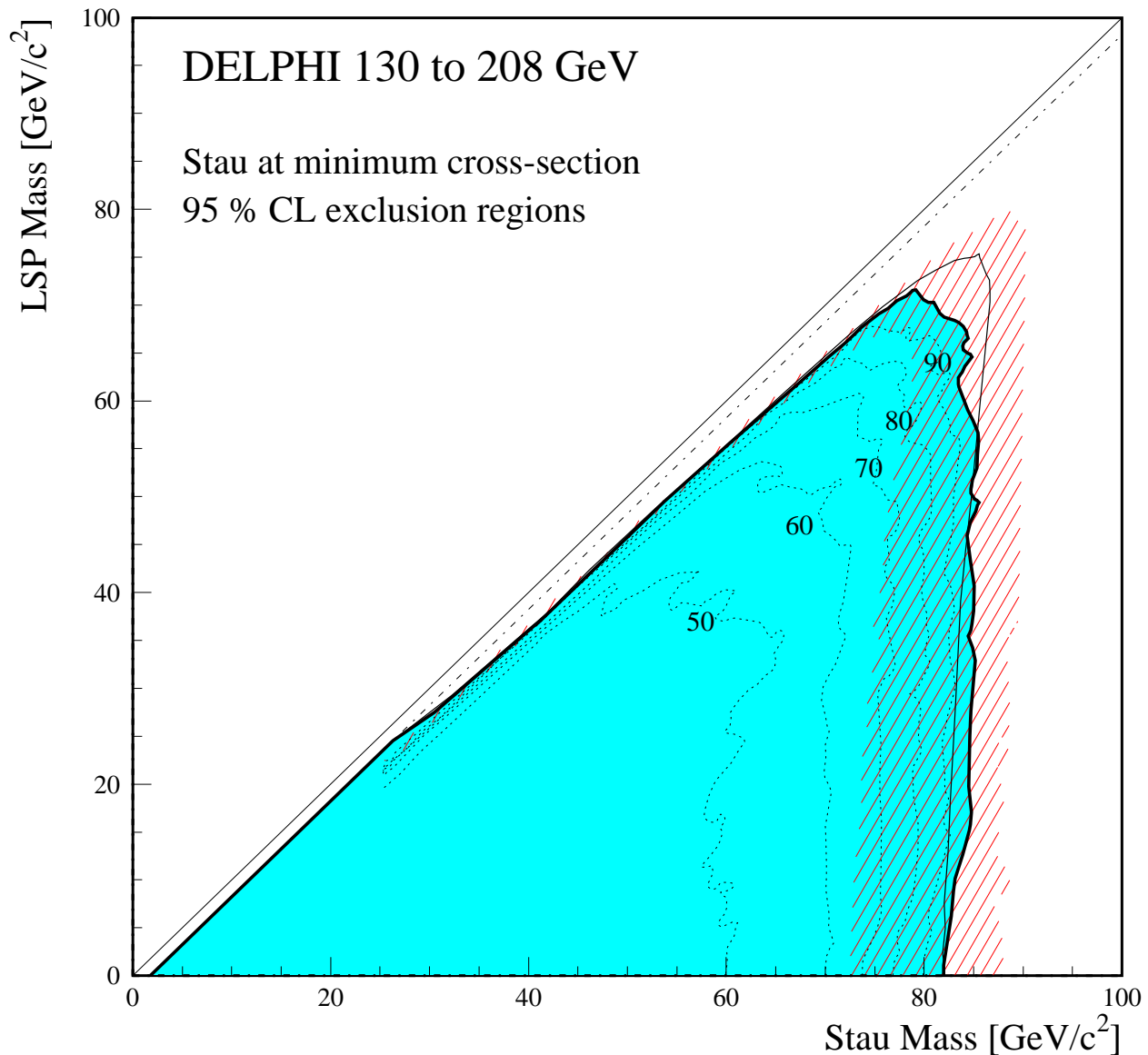


Figure 19: Excluded region in the  $(M_{\tilde{\tau}}, M_{LSP})$  plane obtained for the minimal  $\tilde{\tau}$  pair-production cross-section. The shaded region shows the region excluded if  $\tilde{\tau} \rightarrow \tau$  LSP is the only allowed channel, and the thin solid line shows the corresponding expected limit. The dotted lines show the region excluded if the branching ratio of  $\tilde{\tau} \rightarrow \tau$  LSP has the values indicated in percent next to the lines, and it is assumed that the analysis has no sensitivity to other decay-modes. The dash-dotted line indicates  $\Delta M = m_\tau$ . The observed limit is everywhere within the 95% CL band for the expected limit shown as the hatched area.

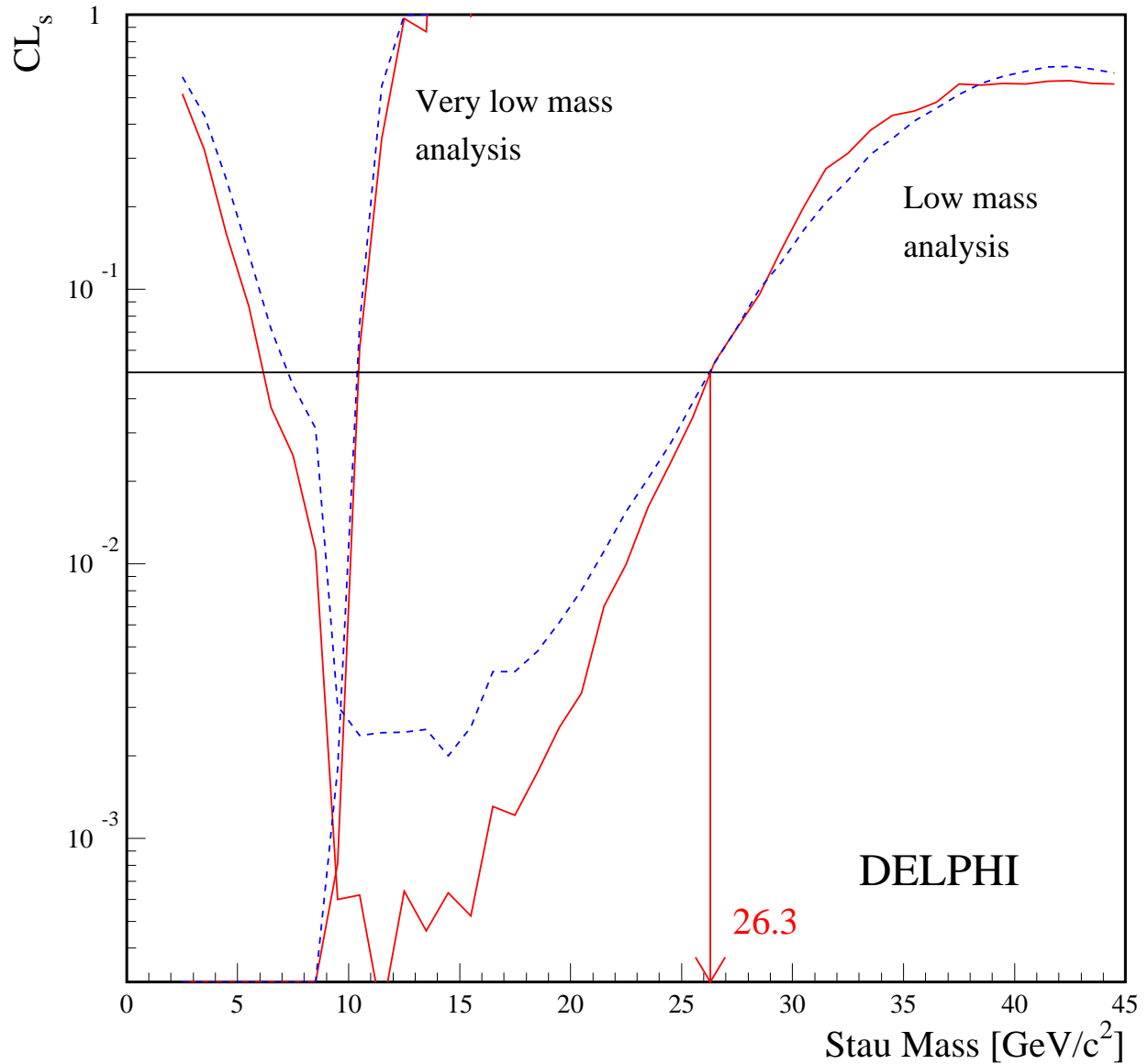


Figure 20: The value of  $CL_s$  versus  $M_{\tilde{\tau}}$  obtained for the minimal  $\tilde{\tau}$  pair-production cross-section, and  $\Delta M = m_{\tau}$ , which corresponds to the weakest limit. The solid curve shows the obtained  $CL_s$ , and the dashed line shows the corresponding expected value. The two sets of curves correspond to the “very low mass analysis” and the “low mass analysis”, as indicated in the figure.

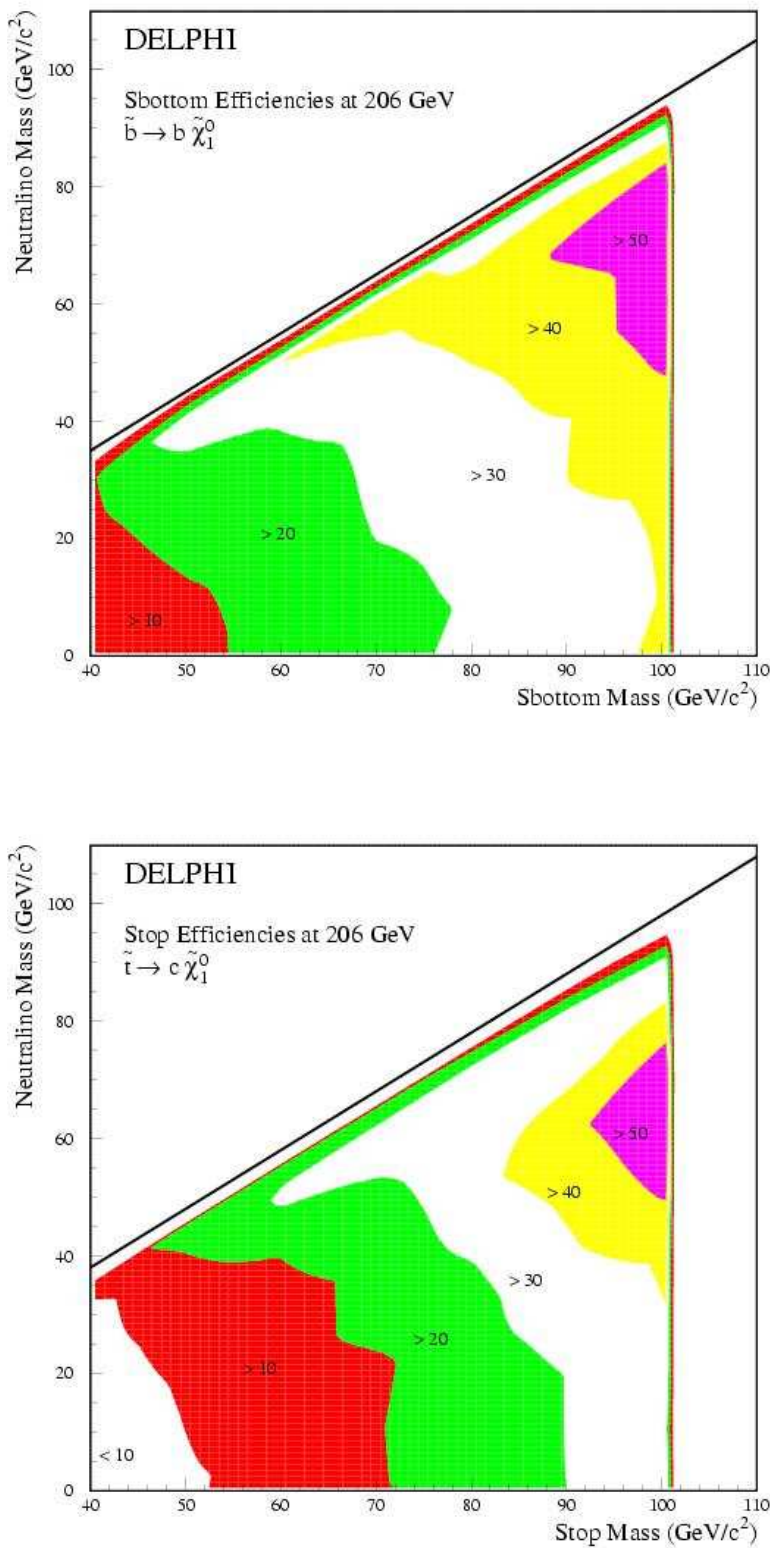


Figure 21: Squark signal detection efficiencies (in %) in the plane  $(M_{\tilde{q}_1}, M_{\tilde{\chi}_1^0})$  in the non-degenerate scenario.

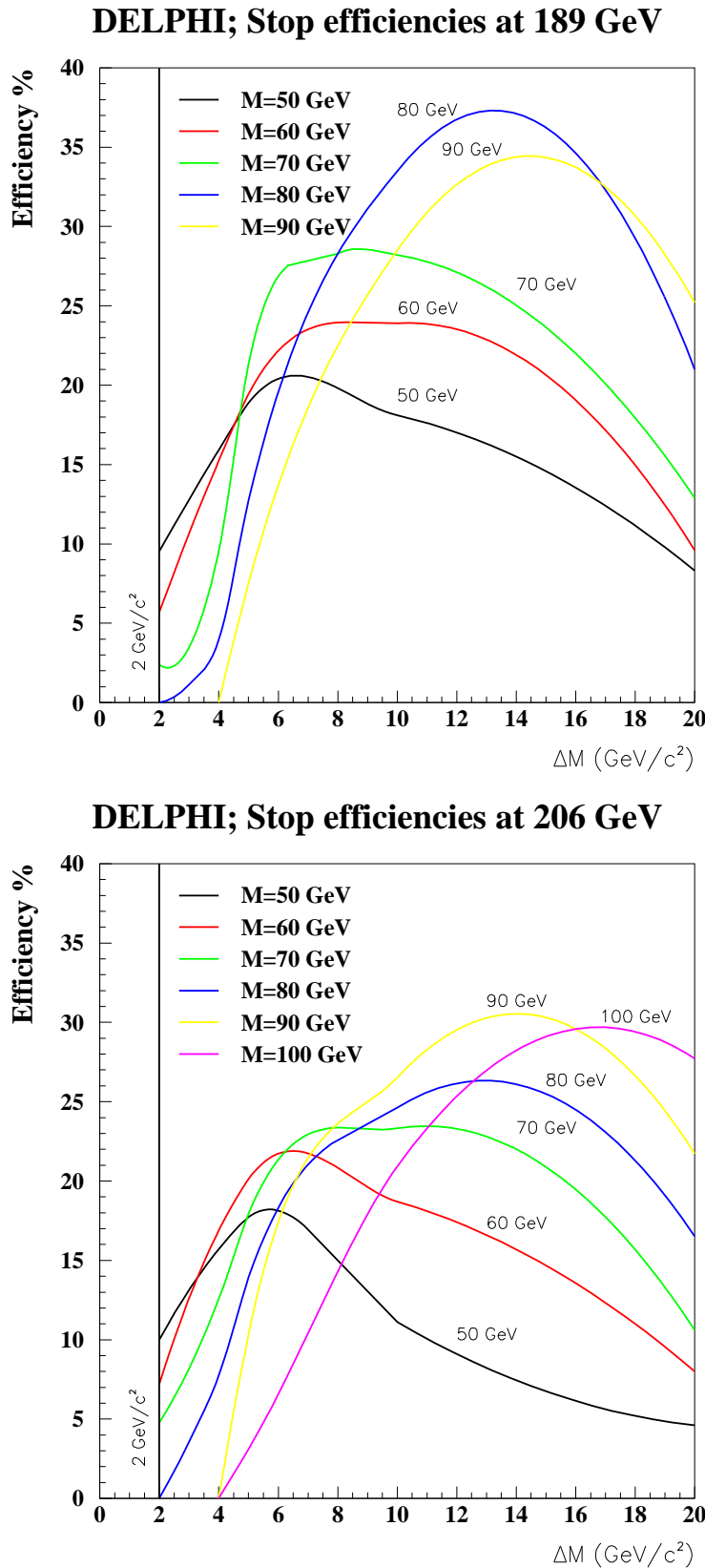


Figure 22: Signal efficiency of the stop search in the nearly degenerate scenario for different mass hypothesis as a function of  $\Delta M = M_{\tilde{t}_1} - M_{\tilde{\chi}_1^0}$ , for  $\sqrt{s}=189$  and 206 GeV.

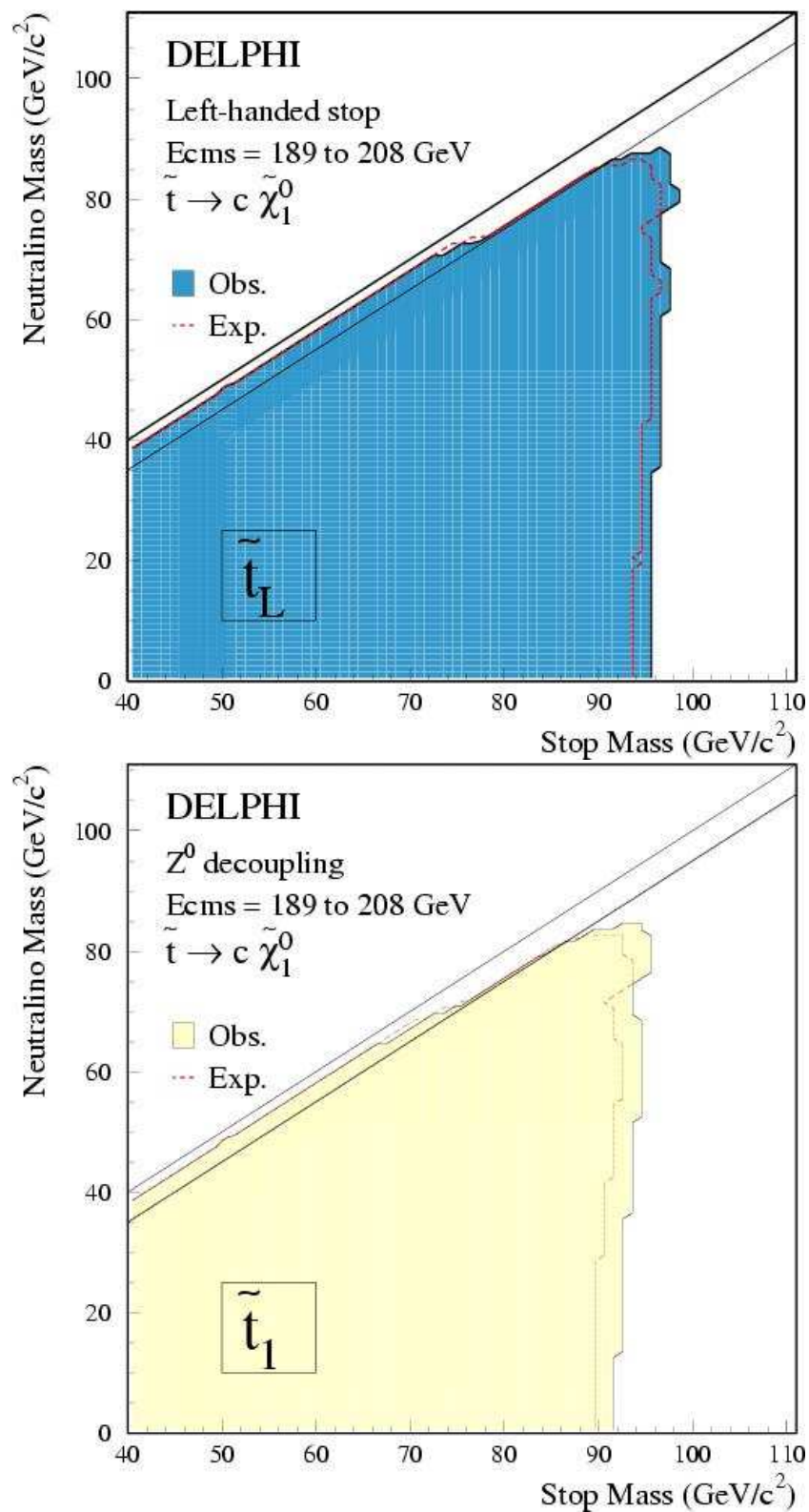


Figure 23: Excluded regions for the stop search in the plane  $(M_{\tilde{t}_1}, M_{\tilde{\chi}_1^0})$  for purely left handed stops (top) and for the states at the  $Z$  decoupling (bottom). The shaded areas show the observed excluded regions and the lines correspond to the expected exclusions (for a discussion on the low stop mass region see section 6.3).

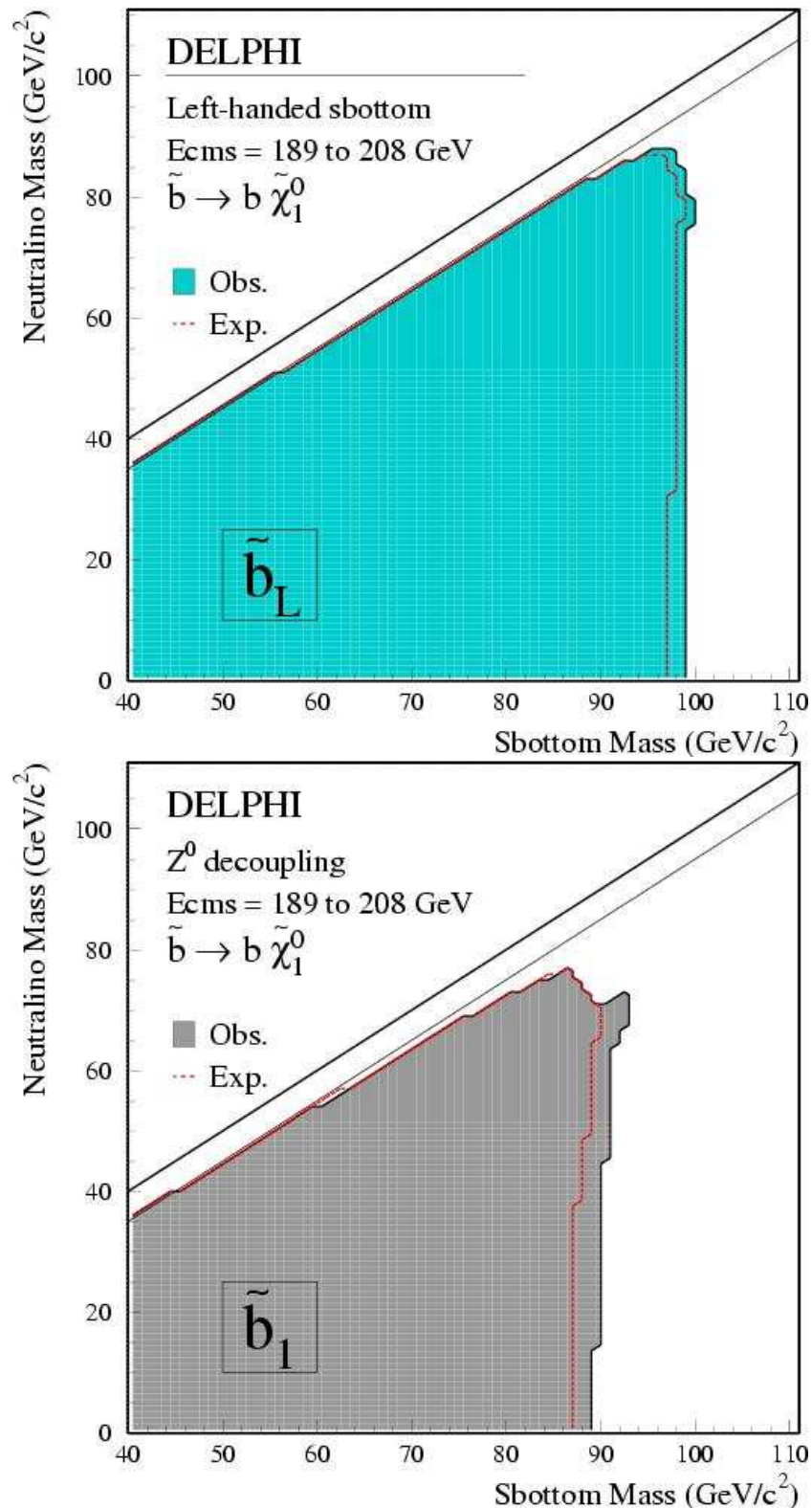


Figure 24: Excluded regions at for the sbottom search in the plane ( $M_{\tilde{b}_1}, M_{\tilde{\chi}_1^0}$ ) for purely left handed sbottoms (top) and for the states at the  $Z$  decoupling (bottom). The shaded areas show the observed excluded regions and the lines correspond to the expected exclusions (for a discussion on the low sbottom mass region see section 6.3).

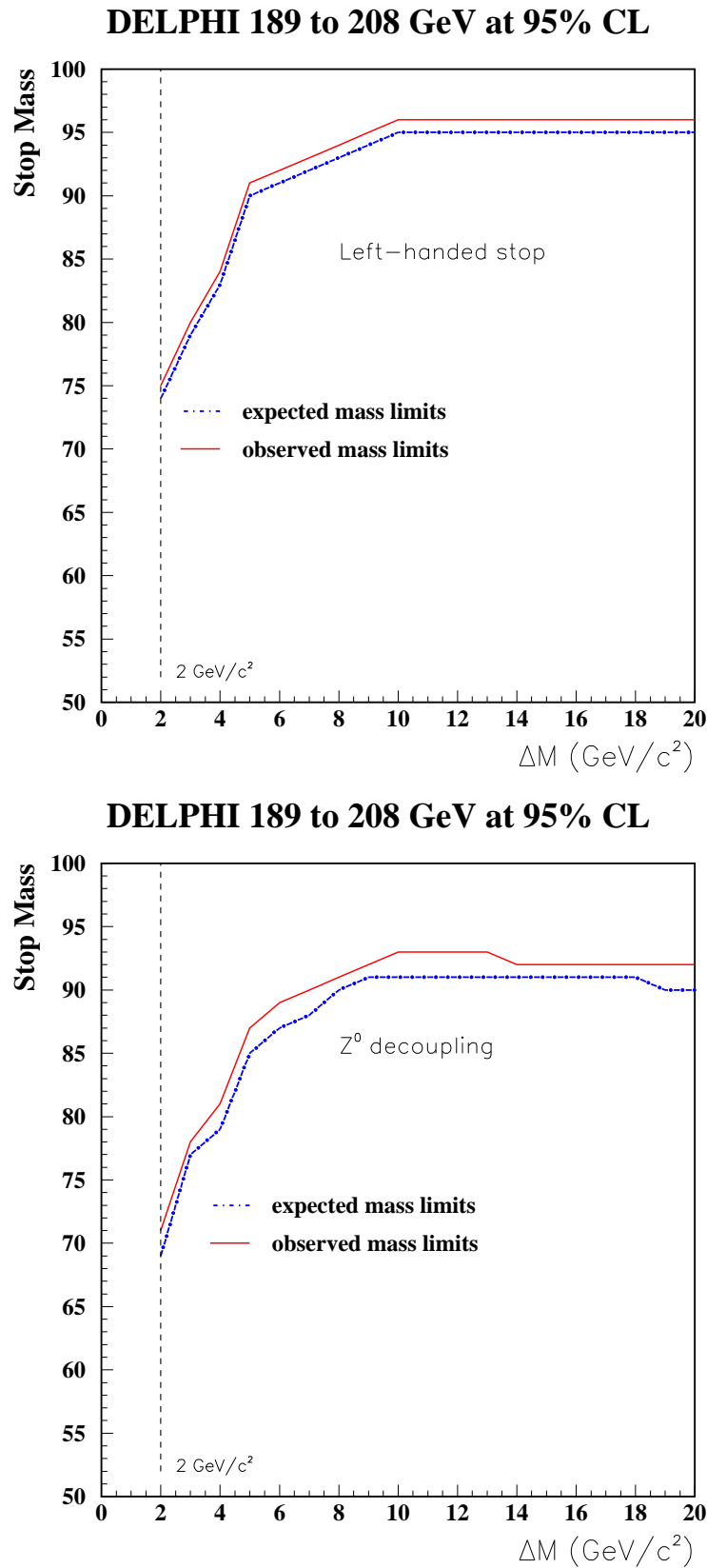


Figure 25: Stop mass limit as a function of  $\Delta M$  for a purely left-handed stop and for the stop mixing angle which minimises the cross-section.

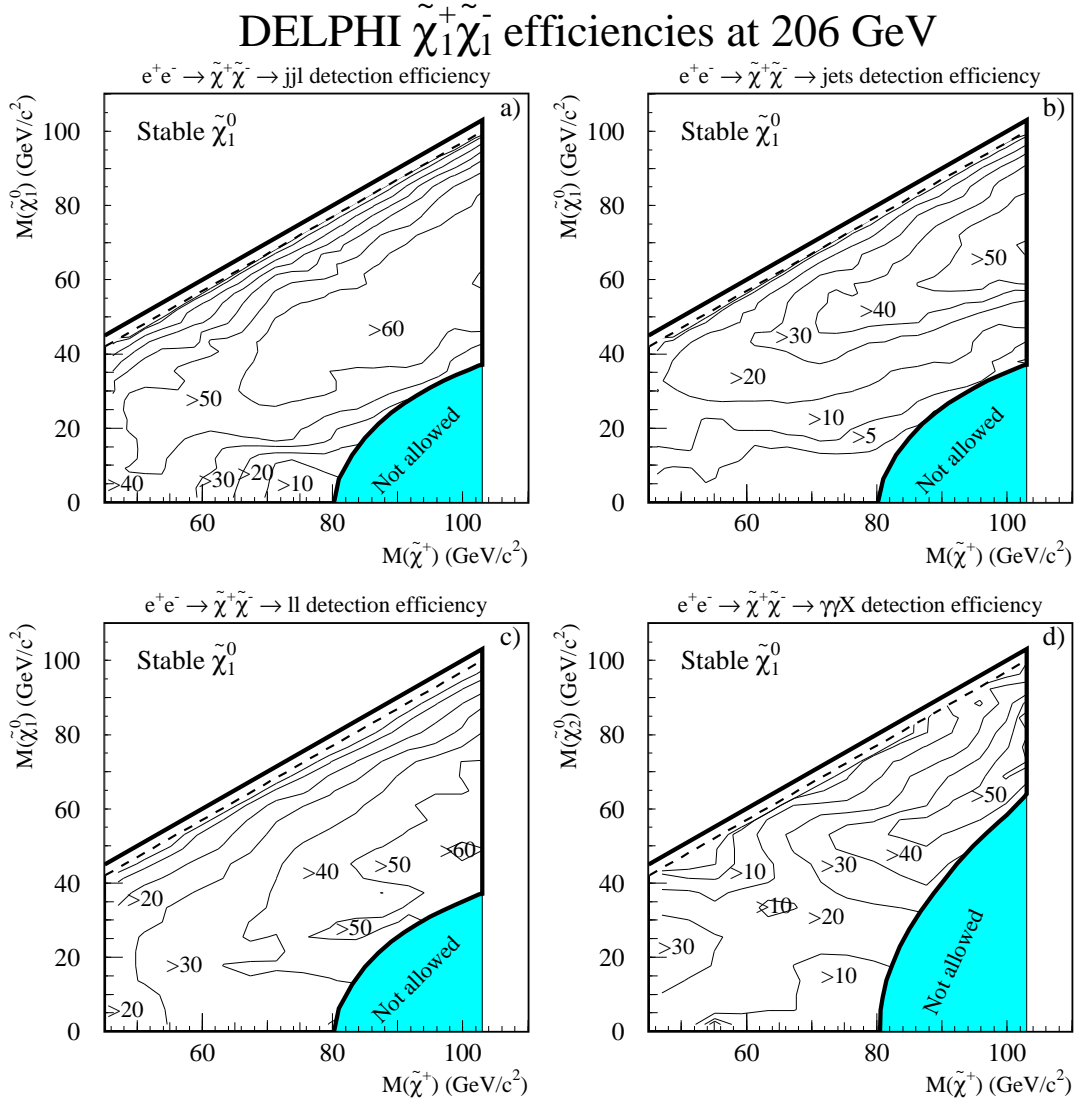


Figure 26: Chargino pair-production detection efficiencies (%) for the four decay channels a)  $jjl$ , b)  $\text{jets}$ , c)  $\ell\ell$  and d)  $\text{rad}$ , at 206 GeV in the  $(M_{\tilde{\chi}^\pm}, M_{\tilde{\chi}^0})$  plane. TPC sector 6 is on and a stable  $\tilde{\chi}_1^0$  is assumed. The shaded areas are disallowed in the MSSM scheme.

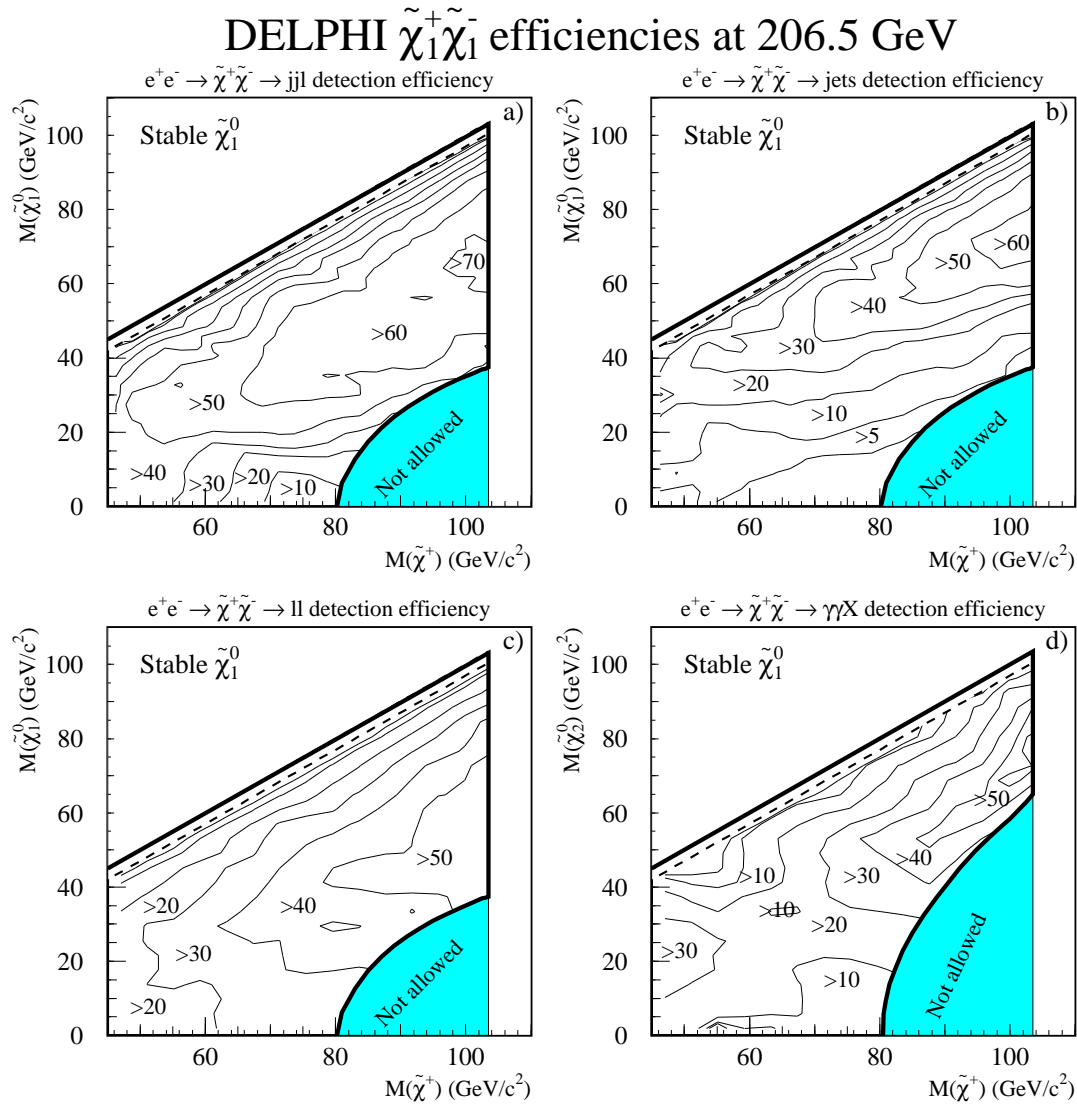


Figure 27: Chargino pair-production detection efficiencies (%) for the four decay channels a)  $jjl$ , b)  $\text{jets}$ , c)  $ll$  and d)  $\text{rad}$ , at 206.5 GeV in the  $(M_{\tilde{\chi}^\pm}, M_{\tilde{\chi}^0})$  plane. TPC sector 6 is off and a stable  $\tilde{\chi}_1^0$  is assumed. The shaded areas are disallowed in the MSSM scheme.

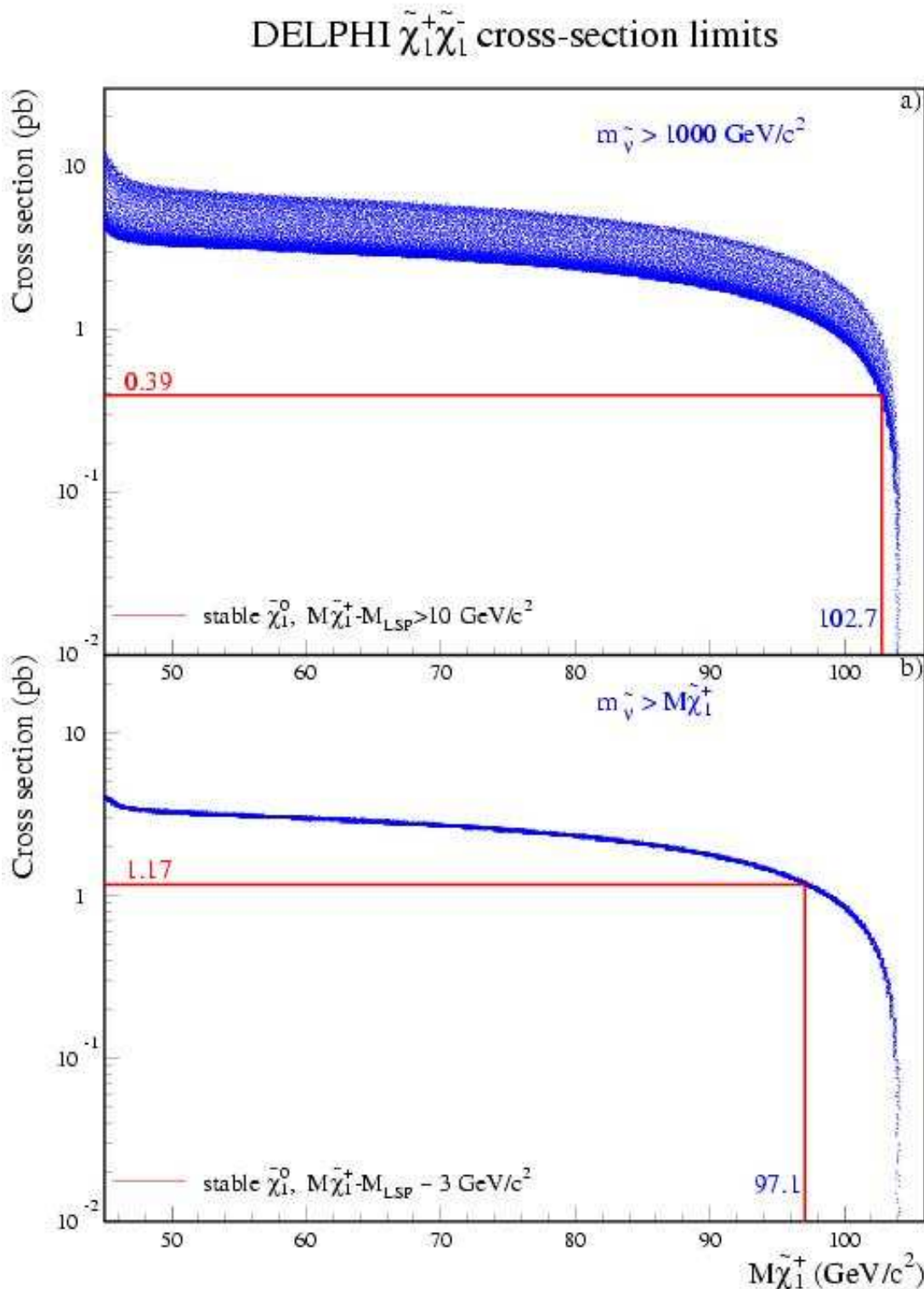


Figure 28: Expected cross-sections in pb at 208 GeV (dots) versus the chargino mass in a) for  $\Delta M > 10 \text{ GeV}/c^2$  and b) for  $\Delta M \sim 3 \text{ GeV}/c^2$ . The spread in the dots originates from the random scan over the parameters  $\mu$  and  $M_2$ . A heavy sneutrino ( $m_{\tilde{\nu}} > 1000 \text{ GeV}/c^2$ ) has been assumed in a) and  $m_{\tilde{\nu}} > M_{\tilde{\chi}_1^\pm}$  in b). The minimal cross-sections below the mass limits are indicated by the horizontal lines.

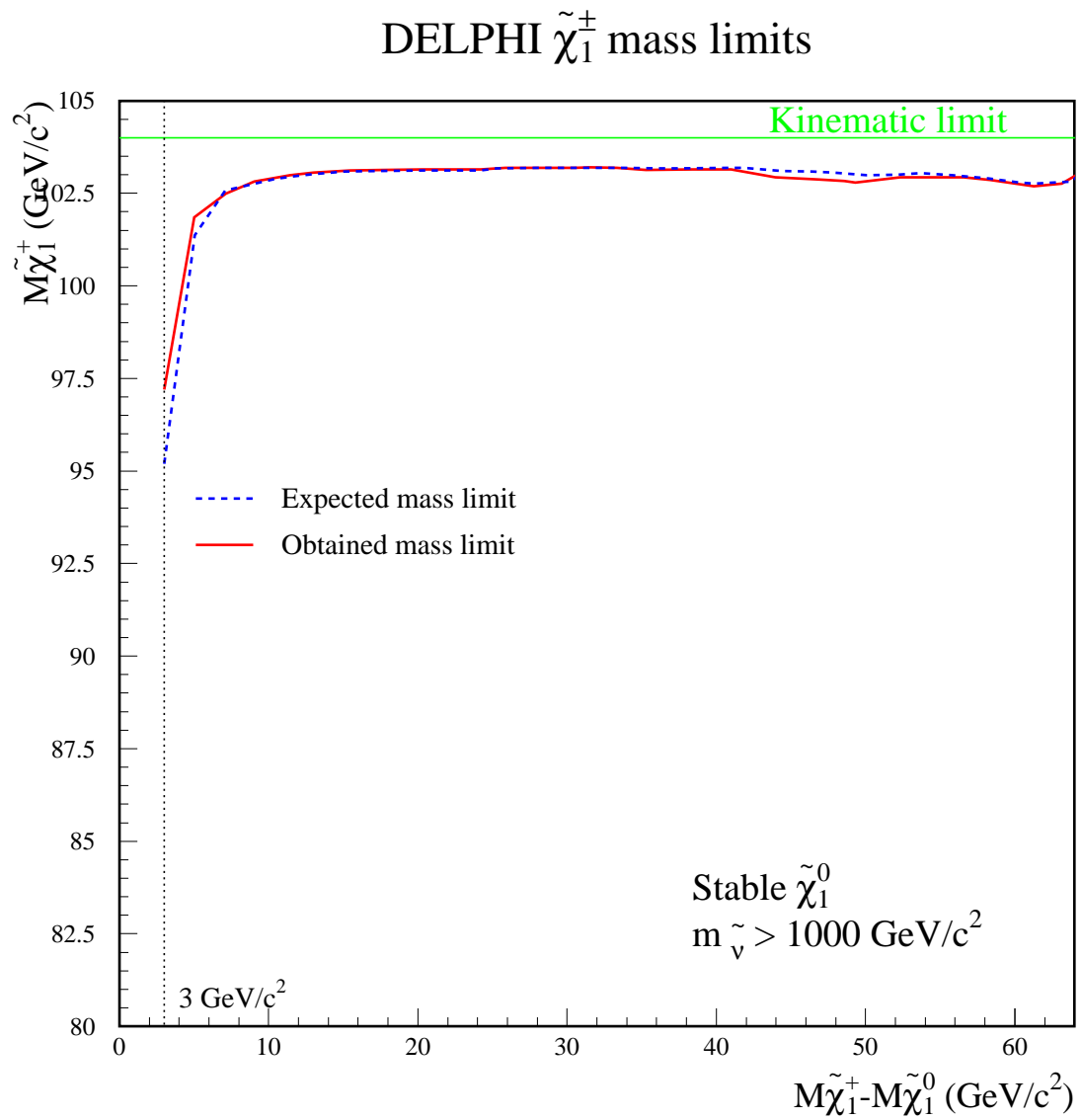


Figure 29: The chargino mass limit as function of the  $\Delta M$  value under the assumption of a heavy sneutrino. The limit applies to the case of a stable  $\tilde{\chi}_1^0$ . The straight horizontal line shows the kinematic limit.

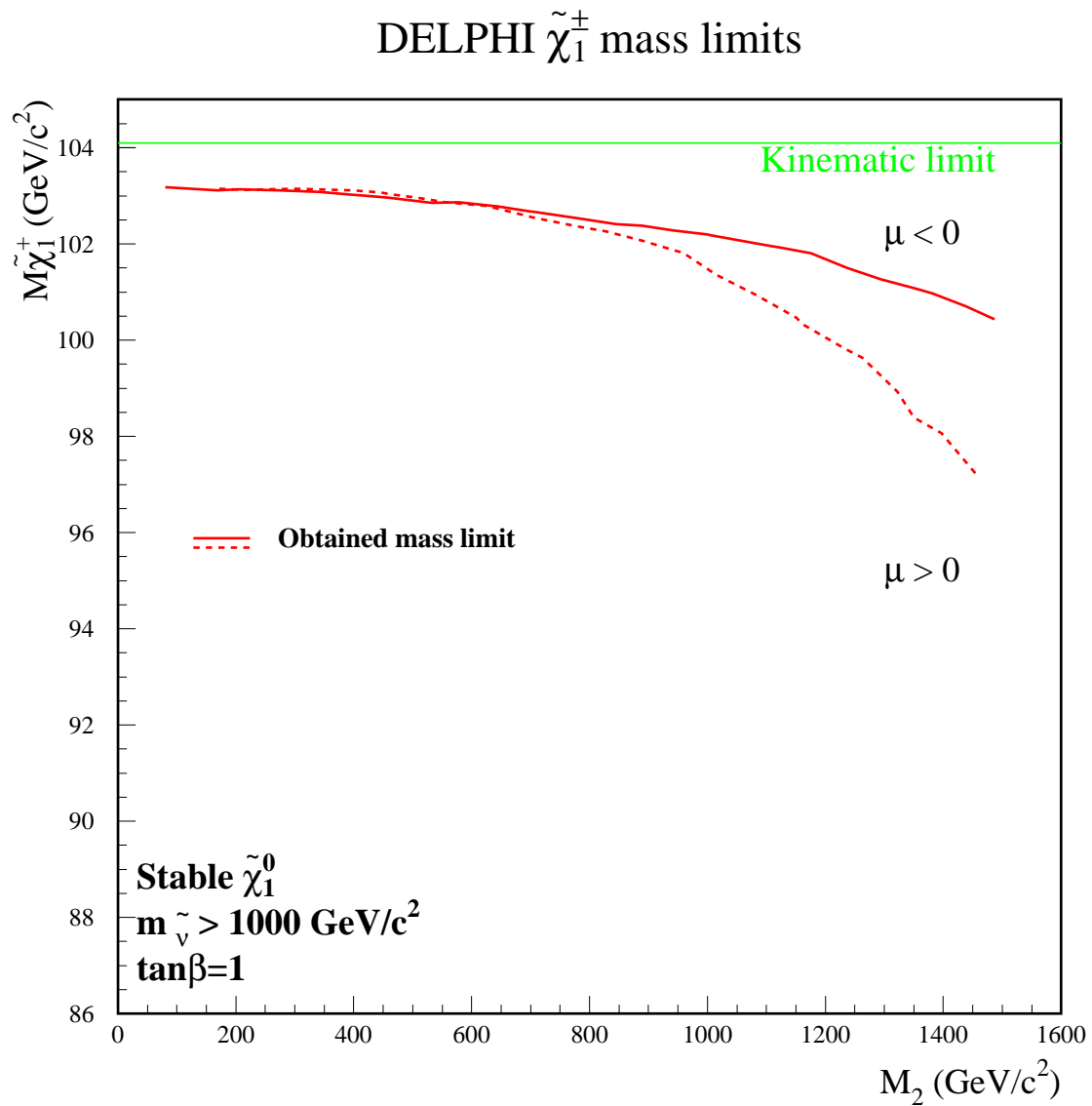


Figure 30: The chargino mass limit as function of  $M_2$  for  $\tan\beta = 1$ , under the assumption of a heavy sneutrino. The straight horizontal line shows the kinematic limit of the chargino production. The limit applies in the case of a stable  $\tilde{\chi}_1^0$ .

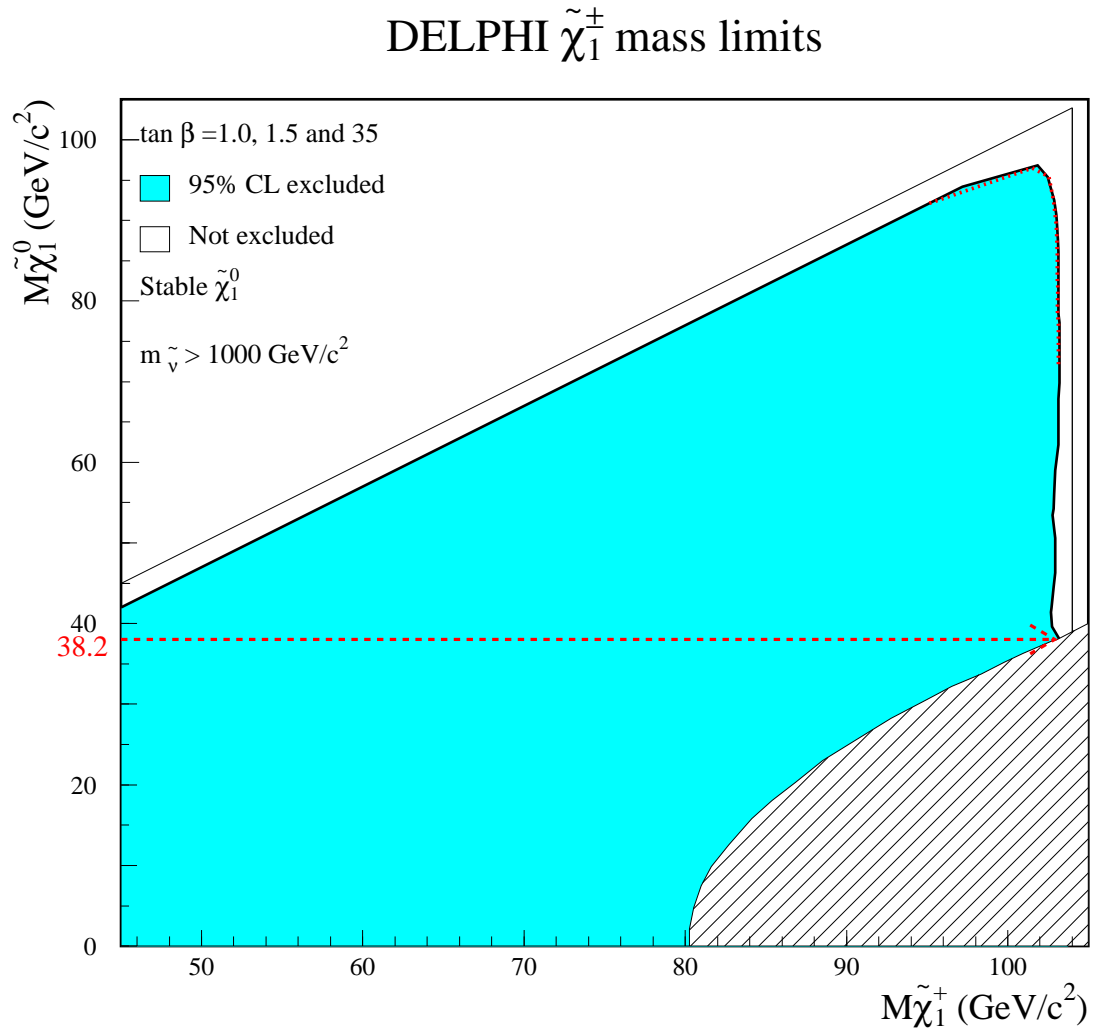


Figure 31: Region excluded in the plane of the mass of the lightest neutralino versus that of the lightest chargino under the assumption of a heavy sneutrino, for  $\tan \beta = 1.0, 1.5$  and  $35$ . The thin lines show the kinematic limits in the production and the decay. The dotted line (partly hidden by the shading) shows the expected exclusion. The dashed region is not allowed in the MSSM. The limit applies in the case of a stable  $\tilde{\chi}_1^0$ . The mass limit on the lightest neutralino is indicated by the horizontal dashed line (for a discussion on the low mass region see section 6.3).

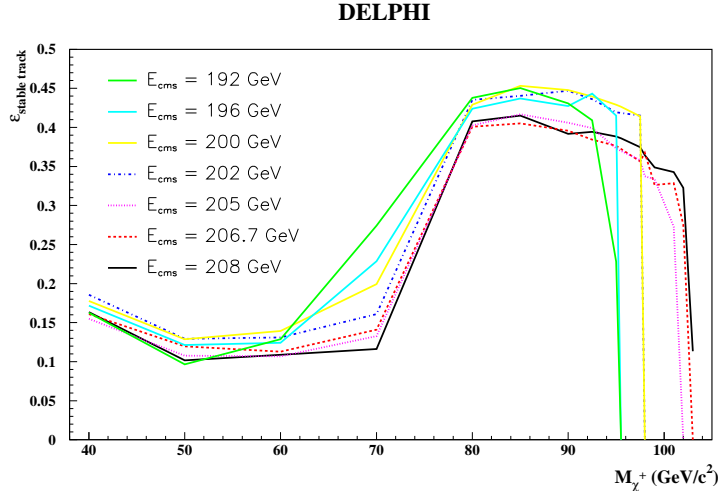


Figure 32: Efficiency for selecting a single almost stable chargino, as function of its mass, at the centre-of-mass energies of the years 1999 and 2000.

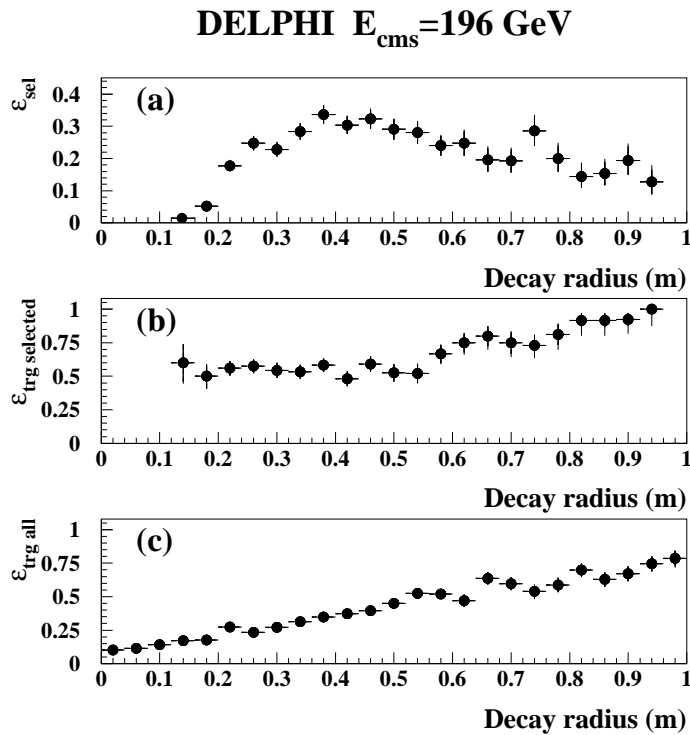


Figure 33: (a) Efficiency for selecting a single 75  $\text{GeV}/c^2$  chargino in the search for displaced decay vertices (kinks) at the centre-of-mass energy of 196 GeV, as function of its decay radius. (b) Trigger efficiency for the selected charginos. (c) Trigger efficiency for all 75  $\text{GeV}/c^2$  charginos, whether or not they were selected.

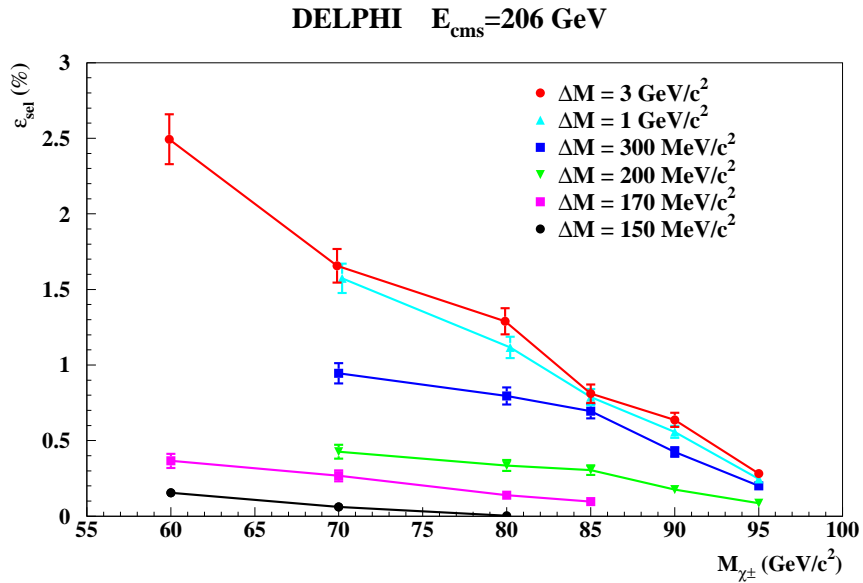


Figure 34: Selection times trigger efficiency in the search for nearly mass-degenerate charginos in the search with an ISR photon. The efficiency for higgsinos at  $\sqrt{s} = 206 \text{ GeV}$  at the different chargino masses and  $\Delta M$  values fully simulated is given as an example.

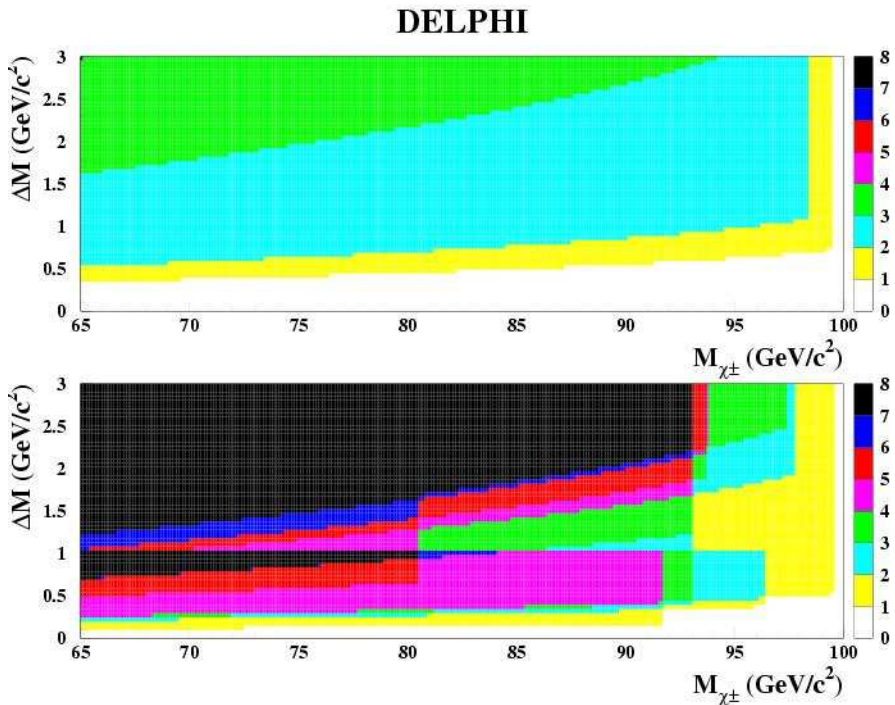


Figure 35: Expected number of background events (top) and number of selected events in the real data (bottom) after the final selection, for the year 2000 data with the TPC fully operational, as function of the points in the plane  $(M_{\tilde{\chi}_1^\pm}, \Delta M)$  considered in the chargino search with an ISR photon.

## DELPHI

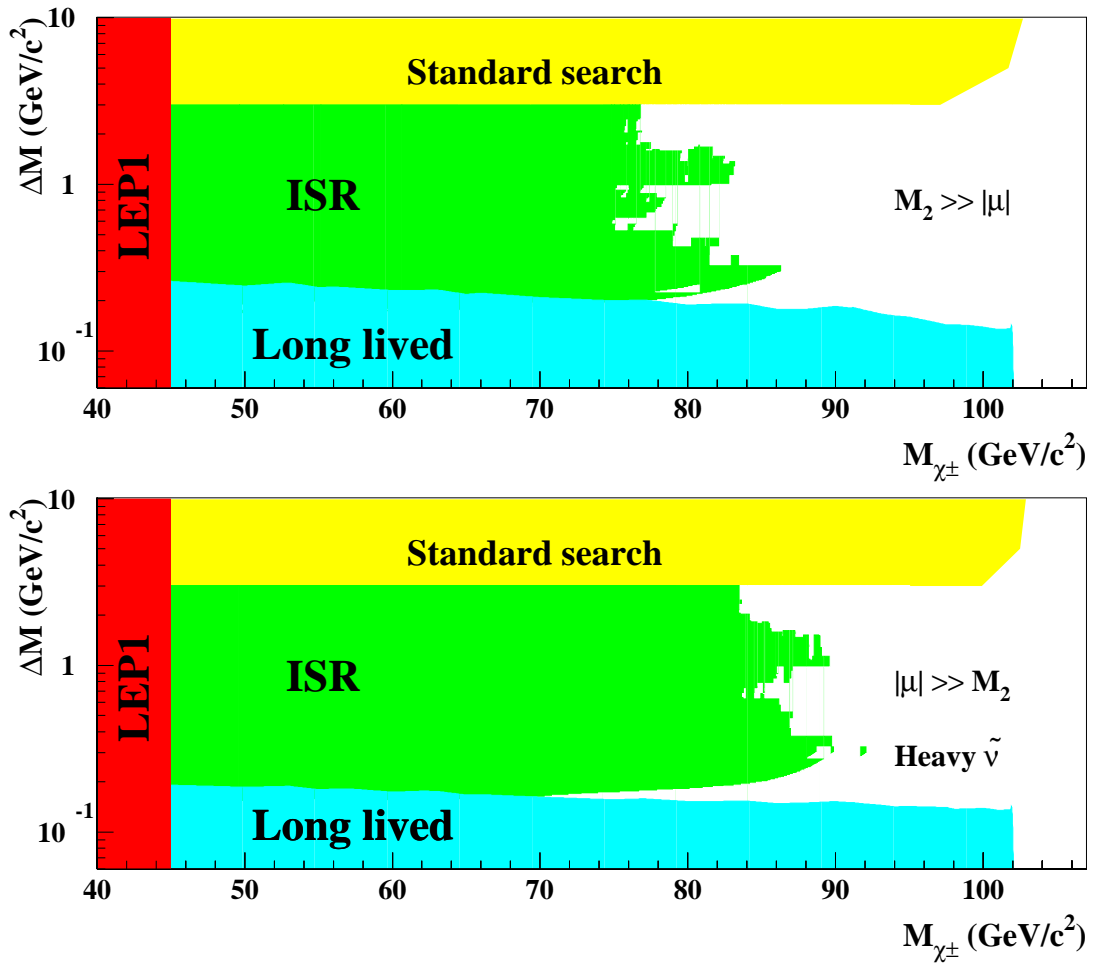


Figure 36: Regions in the plane ( $M_{\tilde{\chi}_1^+}$ ,  $\Delta M$ ) excluded using: the search for high  $\Delta M$  charginos; the search for soft particles accompanied by ISR; and the search for long-lived charginos. The two scenarios are (upper plot) the one in which the lightest chargino is a higgsino and (lower plot) the one in which the lightest chargino is a gaugino. For the second scenario, the limits are valid in the heavy sfermion approximation, while for the higgsino scenario it is sufficient that  $M_{\tilde{f}} > M_{\tilde{\chi}_1^+}$ .

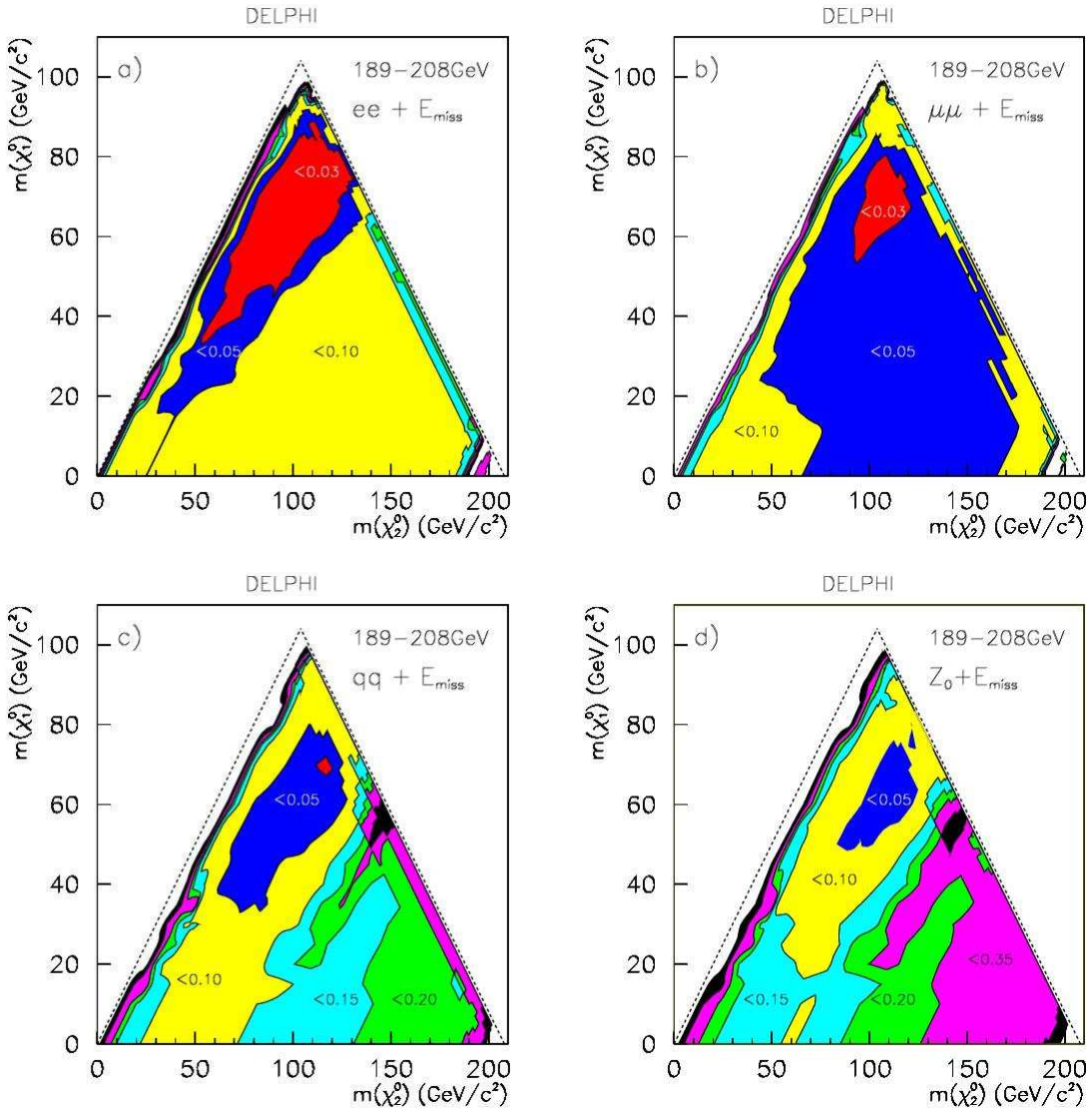


Figure 37: Contour plots of the upper limits obtained on the cross-sections for  $\tilde{\chi}_1^0\tilde{\chi}_2^0$  production at  $\sqrt{s} = 206$  GeV. The data at all energies were used, assuming the cross-section energy dependence expected at a chosen high  $m_0$  point in the higgsino region where the neutralino searches play an important role ( $m_0=1$  TeV/ $c^2$ ,  $\mu=-60$  GeV/ $c^2$ ,  $M_2=200$  GeV/ $c^2$ ). In each plot, the different shadings correspond to regions where the cross-section limit in picobarns is below the indicated number. For figures a), b), c),  $\tilde{\chi}_2^0$  decays into  $\tilde{\chi}_1^0$  and a)  $e^+e^-$ , b)  $\mu^+\mu^-$ , and c)  $q\bar{q}$ , while in d) the branching ratios of the  $Z$  were assumed, including invisible states. The dotted lines indicate the kinematic limit and the defining relation  $M_{\tilde{\chi}_2^0} > M_{\tilde{\chi}_1^0}$ .

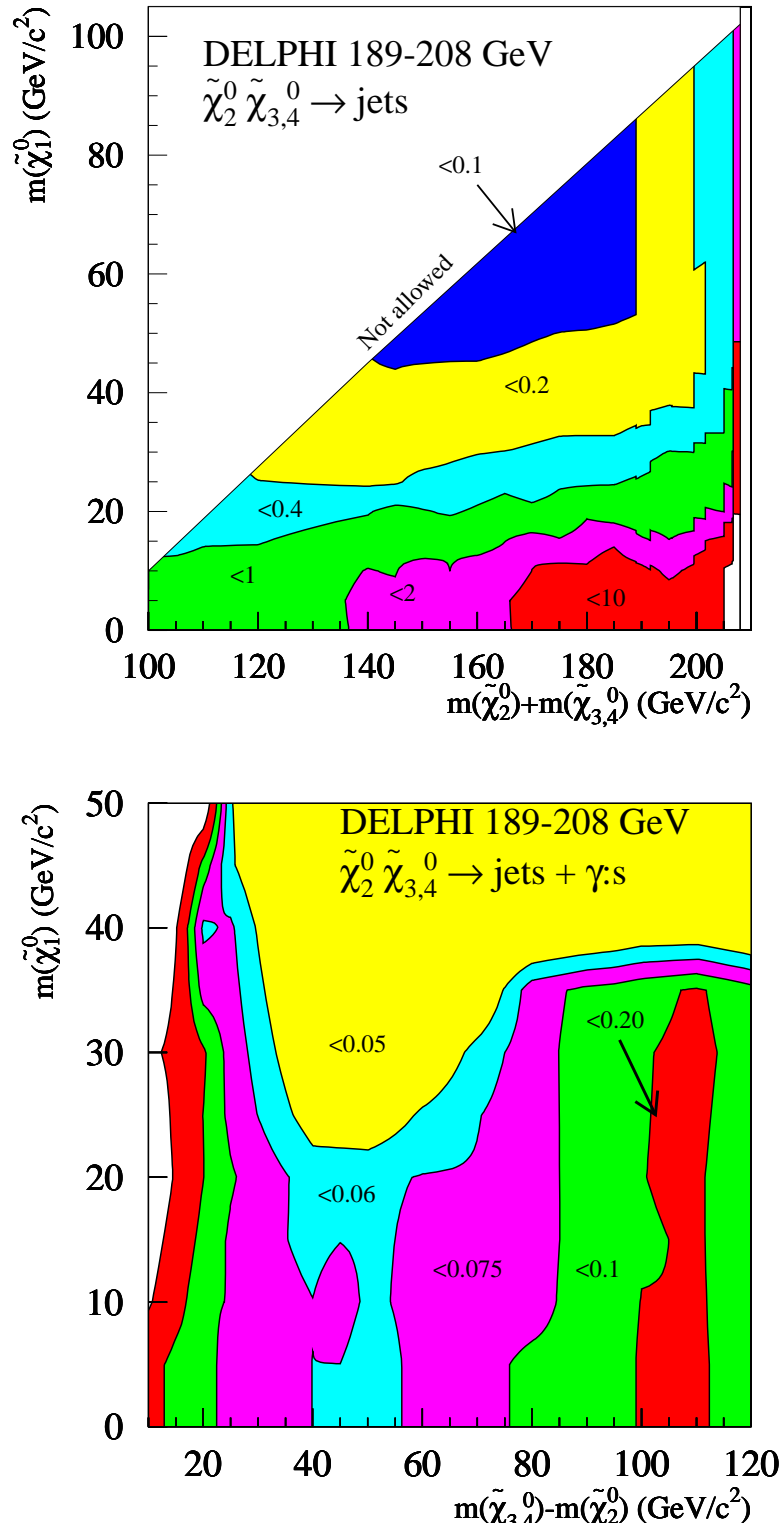


Figure 38: Upper limits on the cross-sections for  $\tilde{\chi}_2^0 \tilde{\chi}_i^0$  production with  $\tilde{\chi}_i^0 \rightarrow \tilde{\chi}_2^0 q \bar{q}$  ( $i=3,4$ ) including data up to  $\sqrt{s} = 208$  GeV. The different shadings correspond to regions where the cross-section limit in picobarns is below the indicated number. The  $\tilde{\chi}_2^0$  was assumed to decay 100% into  $\tilde{\chi}_1^0 q \bar{q}$  (left plot), and into  $\tilde{\chi}_1^0 \gamma$  (right plot). The limits in the left plot are based on the acoplanar jets and multijets selections, while those in the right plot derive from the search for multijets with photons.

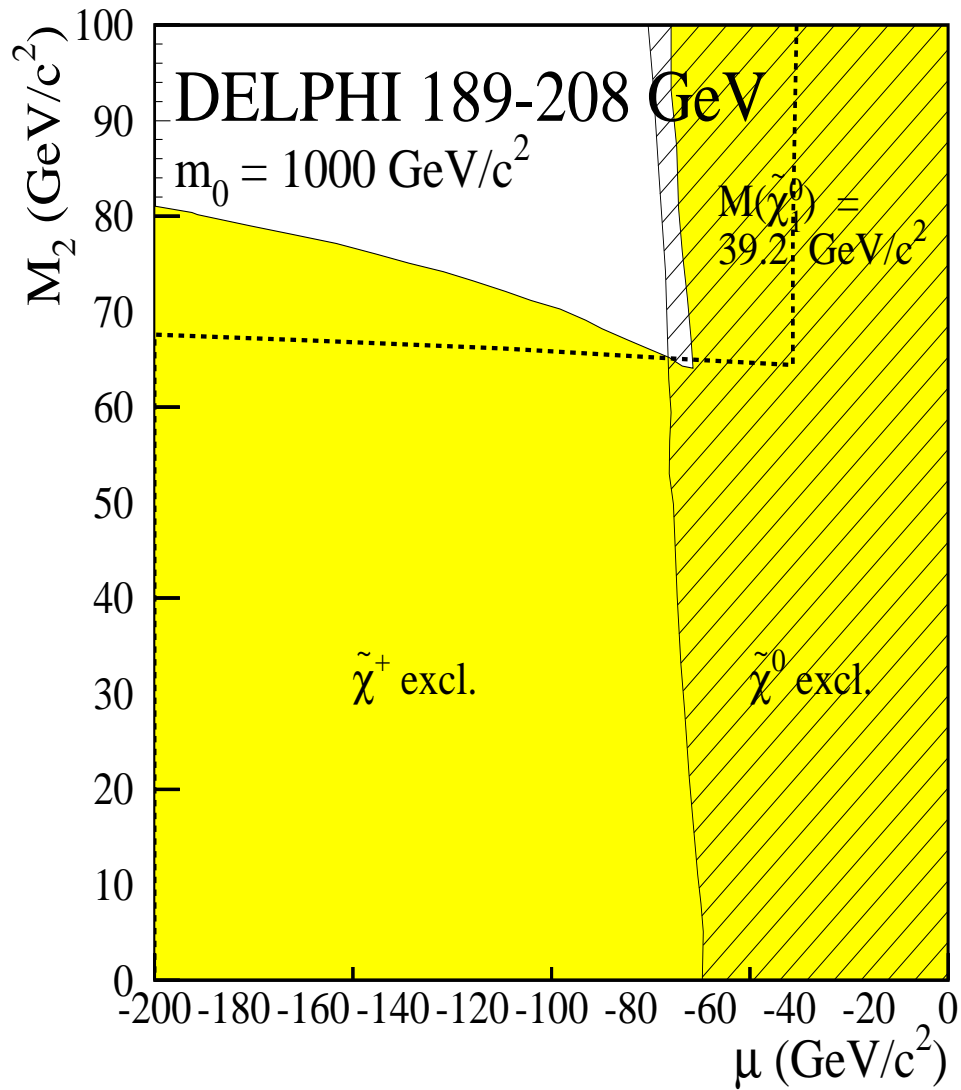


Figure 39: Excluded regions in the  $(\mu, M_2)$  plane for  $\tan \beta = 1$  for  $m_0 = 1000$  GeV/c<sup>2</sup>. The shaded areas show regions excluded by searches for charginos and the hatched areas show regions excluded by searches for neutralinos. The thick dashed curve shows the isomass contour for  $M_{\tilde{\chi}_1^0} = 39.2$  GeV/c<sup>2</sup>, the lower limit on the LSP mass obtained at  $\tan \beta = 1$ . The chargino exclusion is close to the isomass contour for  $M_{\tilde{\chi}_1^\pm}$  at the kinematic limit. From chargino searches alone the lower limit on  $M_{\tilde{\chi}_1^0}$  is  $M_{\tilde{\chi}_1^0} = 38.2$  GeV/c<sup>2</sup>.

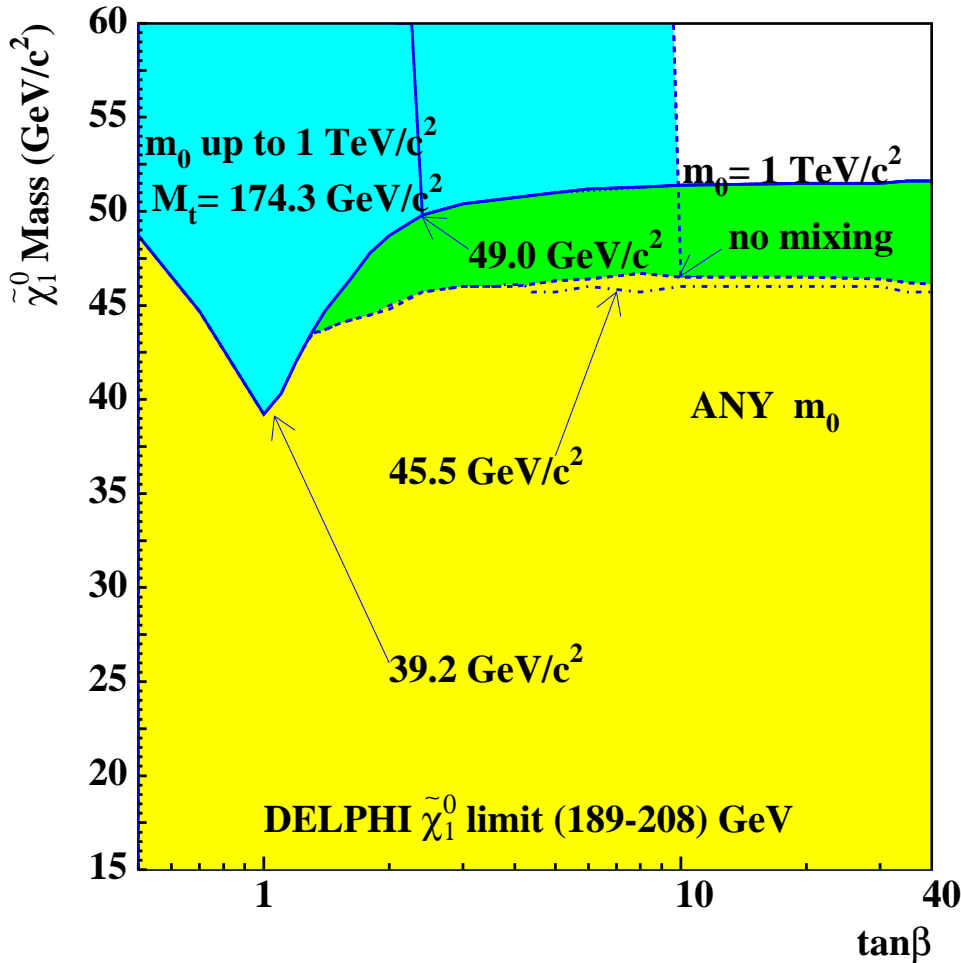


Figure 40: The lower limit on the mass of the lightest neutralino,  $\tilde{\chi}_1^0$ , as a function of  $\tan\beta$  assuming a stable  $\tilde{\chi}_1^0$ . The solid curve shows the limit obtained for  $m_0 = 1000 \text{ GeV}/c^2$ , the dashed curve shows the limit obtained allowing for any  $m_0$  assuming that there is no mixing in the third family ( $A_\tau = \mu \tan\beta$ ,  $A_b = \mu \tan\beta$ ,  $A_t = \mu/\tan\beta$ ), and the dash-dotted curve shows the limit obtained for any  $m_0$  allowing for mixing with  $A_\tau = A_b = A_t = 0$ . The steep solid (dashed) line shows the effect of the searches for the Higgs boson for the maximal  $M_{h^0}$  scenario (no mixing scenario),  $m_0 \leq 1000 \text{ GeV}/c^2$  and  $M_t = 174.3 \text{ GeV}/c^2$ , which amounts to excluding the region of  $\tan\beta < 2.36(9.7)$ .

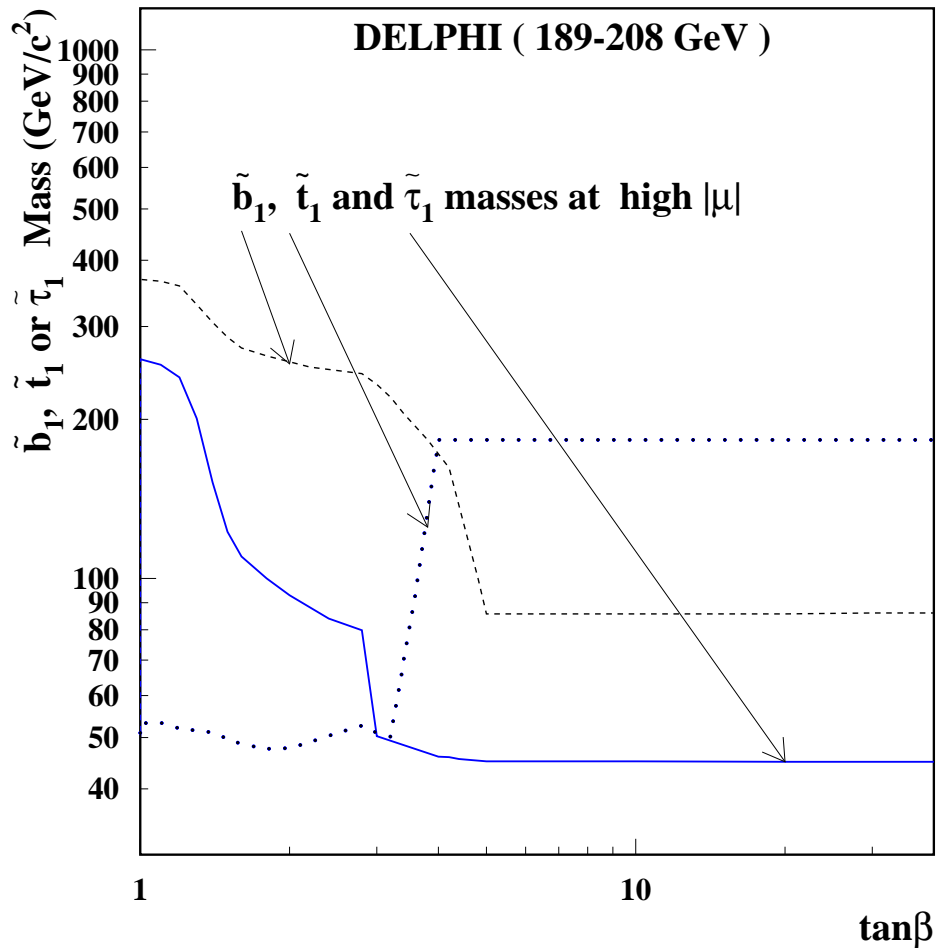


Figure 41: The masses as a function of  $\tan\beta$  of the lightest stau (solid curve), stop (dotted curve) and sbottom (dashed curve), at the largest allowed  $|\mu|$  for the smallest non-excluded  $M_2$  value. Mass splitting in the stau (sbottom, stop) sector in the form  $A_\tau - \mu \tan\beta$  ( $A_b - \mu \tan\beta$ ,  $A_t - \mu/\tan\beta$ ) was assumed, with  $A_\tau = 0$  ( $A_b = A_t = 0$ ).

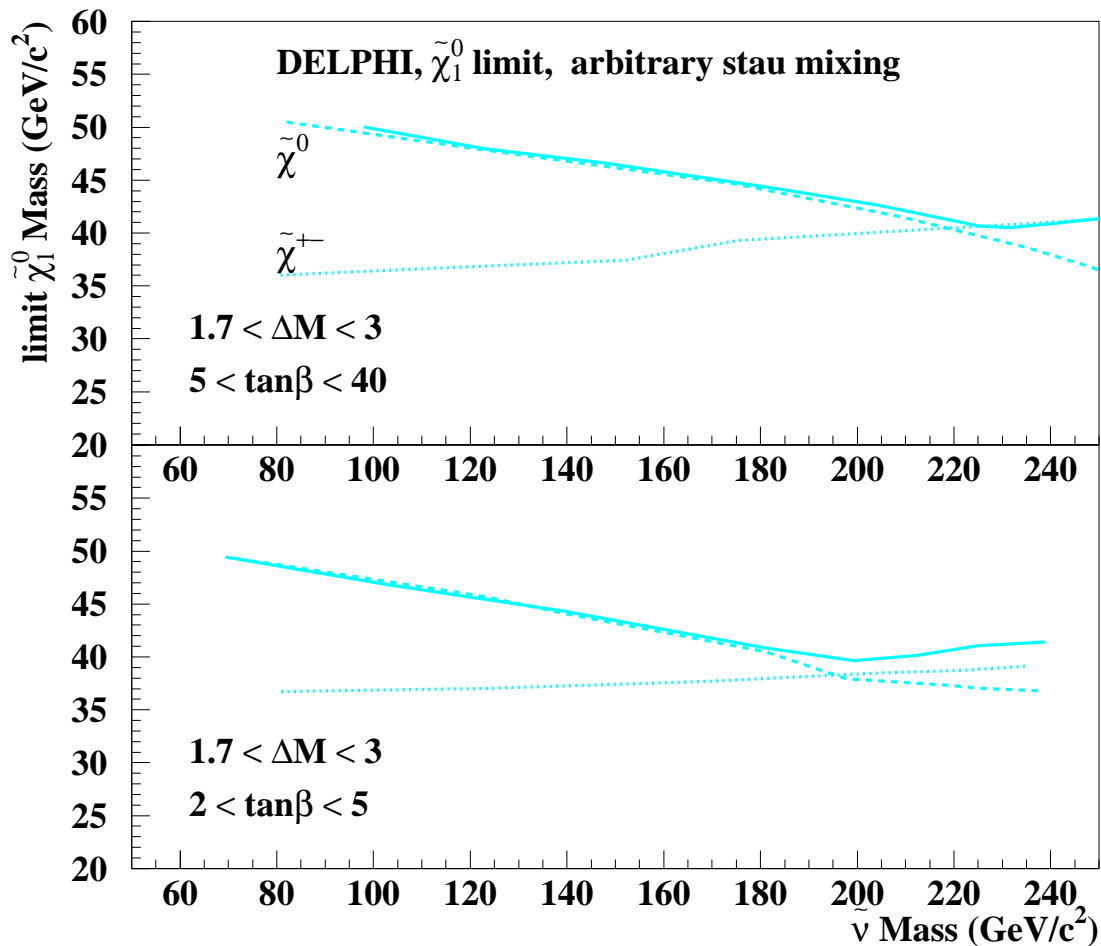


Figure 42: The limit set on the LSP mass by chargino (dotted line) and neutralino searches (dashed line) as a function of the sneutrino mass in the case when the lightest stau is degenerate in mass with the lightest neutralino. The combined limit is shown as solid line. These limits are valid for any model of stau mixing. In any particular model, in which mixing in the stau sector and in the sbottom and stop sector is related a more stringent limit on the LSP mass can be set.

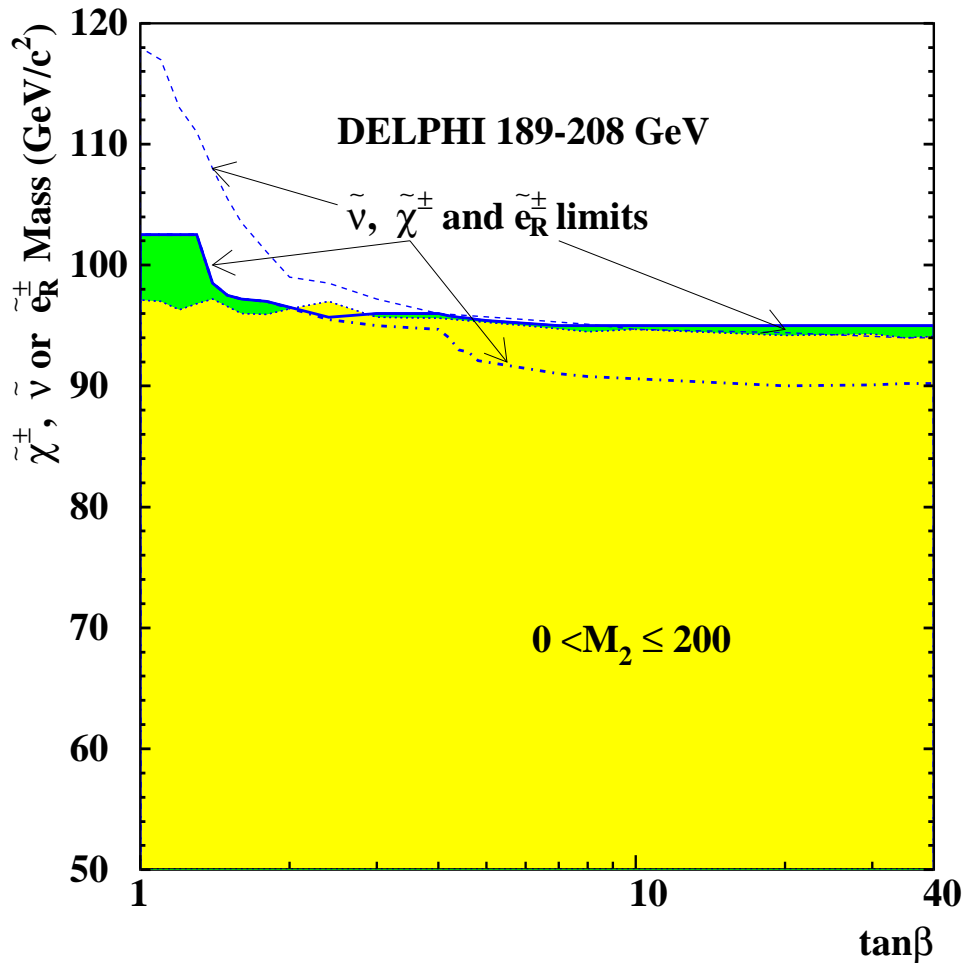


Figure 43: The minimum sneutrino mass (thin dashed curve) and the  $\tilde{e}_R$  mass (thin dotted curve and light shading) allowed by the slepton and neutralino searches, as a function of  $\tan\beta$ , together with the limits on the chargino mass (thick solid curve and dark shading, and thick dash-dotted curve). The chargino mass limit indicated by the solid curve and the sneutrino and selectron mass limits were obtained assuming no mass splitting in the third sfermion family ( $A_\tau - \mu \tan\beta = 0$  in particular). The selectron mass limit is valid for  $M_{\tilde{e}_R} - M_{\tilde{\chi}_1^0} > 10 \text{ GeV}/c^2$ . The chargino mass limit indicated with the dash-dotted curve was obtained allowing for mass splitting in the third sfermion family, with  $A_\tau = A_b = A_t = 0$ .

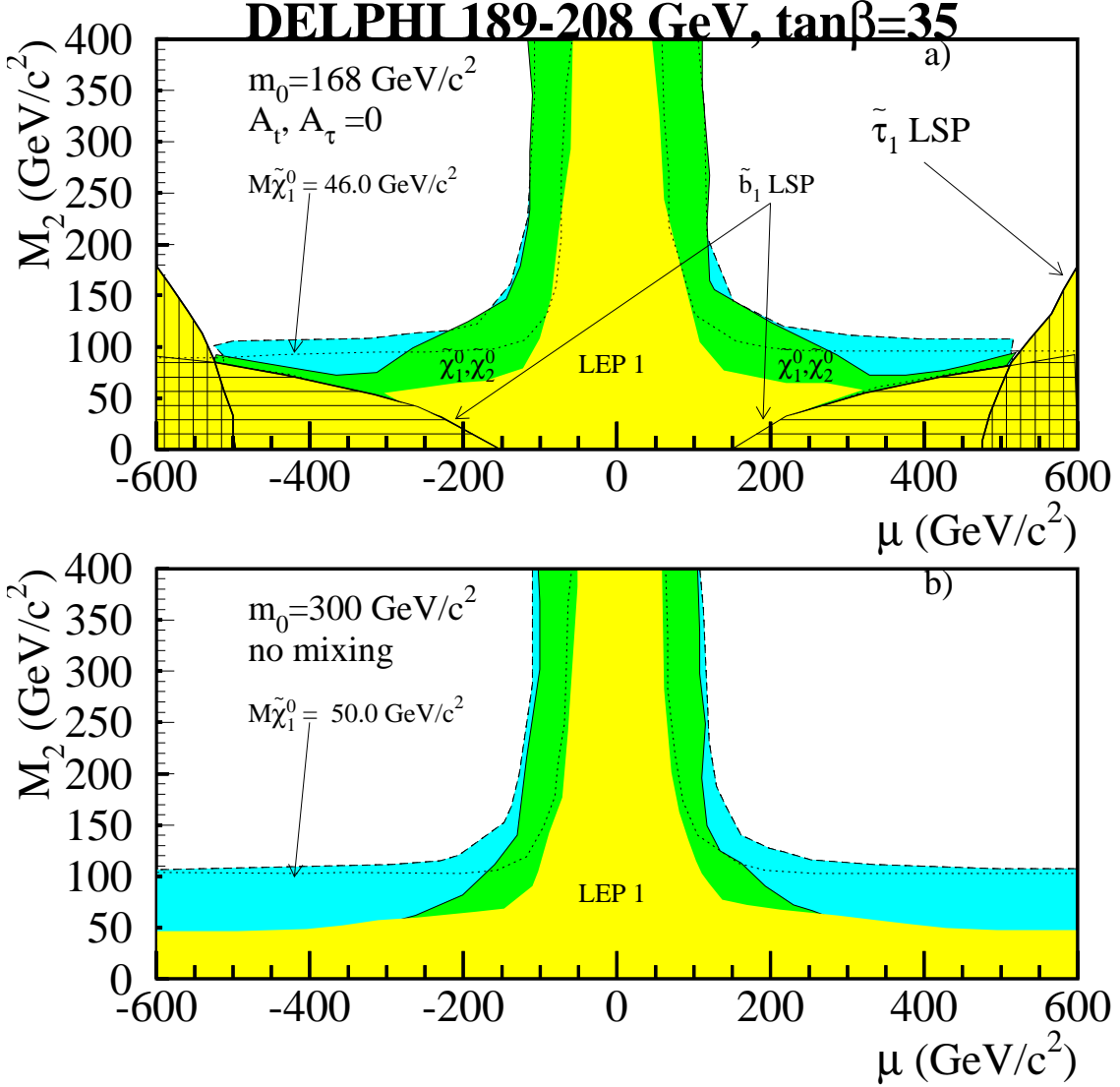


Figure 44: Regions excluded in the  $(\mu, M_2)$  plane for  $\tan\beta = 35$  and different assumptions of mixing in the third family. Light shaded regions are excluded by searches at LEP1 energies, darker shading bounded by the solid line marks regions which are excluded by neutralino searches, while intermediate shaded regions bounded by the thin dashed line are excluded by chargino searches. Mixing terms in the form  $A_\tau - \mu \tan\beta$  ( $A_b - \mu \tan\beta, A_t - \mu/\tan\beta$ ) were considered. For plot a)  $A_b = A_t = A_\tau = 0$  was assumed. The no-mixing scenario was used in b) ( $A_\tau - \mu \tan\beta = 0, A_b - \mu \tan\beta = 0, A_t - \mu/\tan\beta = 0$ ). Plot a) is for the  $m_0$  values giving the lowest non-excluded LSP mass. In the vertically (horizontally) hatched areas the stau (the sbottom) is the LSP. Relevant isomass contours of the lightest neutralino are also shown ( $M\tilde{\chi}_1^0 = 46 \text{ GeV}/c^2$  in a) and  $M\tilde{\chi}_1^0 = 50 \text{ GeV}/c^2$  in b)).